LOW TEMPERATURE MAGNETIC ORDERING OF FRUSTRATED RARE-EARTH PYROCHLORES

by

AMY K.R. BRIFFA

A thesis submitted to the
University of Birmingham
for the degree of
DOCTOR OF PHILOSOPHY

School of Physics And Astronomy
College of Engineering and Physical Sciences
University of Birmingham
30 September 2011

ABSTRACT

In this thesis we study the low temperature magnetic ordering of rare-earth pyrochlores. In these materials the dominant magnetic interaction: nearest neighbour antiferromagnetic Heisenberg exchange, is frustrated with a macroscopic ground-state degeneracy. We investigate how this degeneracy is lifted by weaker interactions which stabilise long-range magnetic order. We begin by considering the compound gadolinium stannate. This material can be understood by modeling it using the dipolar couplings with dominant nearest neighbour Heisenberg exchange. We first review existing theoretical work on this model and then extend it by including an external field. By factorising the Hamiltonian in terms of ten natural variables we are able to find exact solutions to the over-constrained model when the field is orientated along special highly symmetrical directions.

Next we study gadolinium titanate. Although this material has an equivalent structure to gadolinium stannate, the magnetic ordering is much more complex and indexed by a different propagation vector to gadolinium stannate. We believe this is because further neighbour exchange interactions compete with the dipole interactions in gadolinium titanate. There is some controversy surrounding the magnetically ordered phase of gadolinium titanate, in particular elastic neutron scattering and Mössbauer experiments have been explained using contradictory interpretations. We propose a new state which appears to resolve this inconsistency.

Finally we consider erbium titanate. This material requires rather different modeling as the crystal-field interaction has a dominant role. We re-examine existing elastic neutron scattering data and find that it is inconsistent with the state currently discussed in the literature. We therefore propose a new (and physically very different) state which

resolves this problem. The state we propose is unusual as the spins do not point along crystallographic directions despite the fact that the material has a very large anisotropy energy. We suggest this is because the Hamiltonian is extremely frustrated and use a phenomenological approach to investigate qualitatively how such a state might be energetically stabilised. Unusual gapless spin-wave modes have also been observed in erbium titanate. Our proposed multiple-q state offers the explanation that these gapless modes control the transfer of spin density between the different q-points of the state.

ACKNOWLEDGEMENTS

My thanks to my supervisor Professor Andy Schofield and also to Dr. Martin Long for giving me the opportunity to work with him.

CONTENTS

LIST OF FIGURES

LIST OF TABLES

CHAPTER 1

INTRODUCTION

1.1 Overview

In this thesis we will investigate the long-range magnetic ordering of a number of rare earth pyrochlores. These systems can develop unusual long-range order due to the fact that one of the dominant magnetic interactions: the nearest neighbour Heisenberg exchange is geometrically frustrated on the pyrochlore lattice. We will be focusing on how the macroscopic ground-state degeneracy that arises as a result of the geometric frustration is lifted by other interactions. We therefore begin this introduction by addressing the idea that geometric frustration can give rise to a ground-state degeneracy. We do this by discussing the behaviour of the nearest neighbour Heisenberg model on a variety of different lattices and consider the different types of magnetic behaviour that can occur. We then move on to discuss the origin of the Heisenberg interaction and other magnetic interactions in the context of rare earth oxides. Next we focus more closely on the rare earth pyrochlore materials. We describe their chemical structure and briefly consider the physical properties of some specific examples of this class of material in order to illustrate the wide range of magnetic behaviour that is observed. Finally, as we will be investigating long-range magnetic order, we introduce magnetic neutron diffraction as this is probably the key experimental technique for the study of long-range magnetic order and will be central to our later discussions. Then in the following chapters, we study

the low temperature magnetic ordering of gadolinium stannate, gadolinium titanate and erbium titanate.

1.2 Magnetic interactions and frustration

In this thesis we will investigate the low temperature magnetic ordering of geometrically frustrated systems, focusing on the zero-temperature properties. We will therefore begin by introducing one of the most common models used to describe magnetic spin systems: the classical Heisenberg model. We will then discuss the zero-temperature ground-state manifolds of a number of simple lattices with nearest neighbour Heisenberg interactions in order to introduce the idea of geometric frustration.

1.2.1 The Heisenberg model

The Heisenberg model describes the interaction between localised magnetic moments. The Hamiltonian is given by (see Section 1.2.4)[3]

$$H = \frac{1}{2}\sum_{ij} J_{ij}\mathbf{S}_i \cdot \mathbf{S}_j, \tag{1.1}$$

where $\mathbf{S}_i$ describes a classical spin-vector located at position $\mathbf{R}_i$, and J_{ij} is the interaction constant for the 'bond' between the spins at site $\mathbf{R}_i$ and site $\mathbf{R}_j$, which can be either positive or negative. We can see from looking at a single bond that for $J > 0$ the bond energy is minimised by antiparallelly aligned spins, i.e. the interaction is antiferromagnetic. Alternatively, if $J < 0$ then a parallel spin configuration is favoured and the interactions are therefore ferromagnetic. In this thesis we will only consider antiferromagnetic interactions ($J > 0$). We will discuss the microscopic origin of this interaction later in Section 1.2.4. The interaction strength, J_{ij}, depends on the details of the electronic orbital overlaps between the two moments at sites $\mathbf{R}_i$ and $\mathbf{R}_j$ (called the exchange pathway). Due to the crystal periodicity, moments at sites which are crystallographically equivalent therefore

have the same interaction strength. The interactions in the crystal are therefore usually grouped into 'shells' of neighbours, all bonds in the same shell having the same interaction strength. As the interaction strength decays rapidly with increasing complexity of the orbital exchange pathway, the behaviour of the system is usually dominated by the short range interactions (in particular the nearest neighbour interactions).

The Heisenberg model can be diagonalised by transforming to reciprocal space. We begin by writing the Hamiltonian as a sum over successive shells of neighbours (labeled by 's'):

$$H = \sum_s \frac{J_s}{2} \sum_{\langle jj' \rangle_s} \mathbf{S}_j \cdot \mathbf{S}_{j'}, \tag{1.2}$$

which for the classical-spin problem is also subject to the normalisation constraint

$$\mathbf{S}_j \cdot \mathbf{S}_j = S^2. \tag{1.3}$$

For the moment we assume that every spin lies on the Bravais lattice of the crystal. We make use of the Bloch periodicity of the crystal lattice[73] by defining the transformation

$$\begin{aligned} \mathbf{S}_{\mathbf{k}} &= \frac{1}{\sqrt{N}} \sum_j e^{i\mathbf{k}\cdot\mathbf{R}_j} \mathbf{S}_j, \\ \mathbf{S}_j &= \frac{1}{\sqrt{N}} \sum_{\mathbf{k}} e^{-i\mathbf{k}\cdot\mathbf{R}_j} \mathbf{S}_{\mathbf{k}}, \end{aligned} \tag{1.4}$$

where N is the number of lattice sites and $\mathbf{k}$ and $\mathbf{k}'$ range over the Brillouin zone of the reciprocal-space lattice. As we are working with real spins ($\mathbf{S}_j^\dagger = \mathbf{S}_j$) we notice, therefore, that

$$\mathbf{S}_{-\mathbf{k}} = \frac{1}{\sqrt{N}} \sum_j e^{-i\mathbf{k}\cdot\mathbf{R}_j} \mathbf{S}_j = \mathbf{S}_{\mathbf{k}}^*. \tag{1.5}$$

The Hamiltonian then becomes

$$H = \frac{1}{2N} \sum_s \sum_{\langle jj' \rangle_s} \sum_{\mathbf{k}\mathbf{k}'} J_s e^{-i\left(\mathbf{k}\cdot\mathbf{R}_j + \mathbf{k}'\cdot\mathbf{R}_{j'}\right)} \mathbf{S}_{\mathbf{k}} \cdot \mathbf{S}_{\mathbf{k}'}$$

$$= \frac{1}{2N}\sum_{s}\sum_{\langle jj'\rangle_s}\sum_{\mathbf{k}\mathbf{k}'} J_s e^{-i(\mathbf{k}+\mathbf{k}')\cdot\mathbf{R}_j} e^{-i\mathbf{k}'\cdot\left(\mathbf{R}_{j'}-\mathbf{R}_j\right)}\mathbf{S}_{\mathbf{k}}\cdot\mathbf{S}_{\mathbf{k}'}. \tag{1.6}$$

Using the periodicity of the lattice, we define $\mathbf{R}_{j'} - \mathbf{R}_j = \mathbf{R}_n$ and also use the identity

$$\frac{1}{N}\sum_{j} e^{-i(\mathbf{k}+\mathbf{k}')\cdot\mathbf{R}_j} = \delta_{\mathbf{k},-\mathbf{k}'}, \tag{1.7}$$

so that

$$\begin{aligned} H &= \frac{1}{2}\sum_{s}\sum_{\langle 0n\rangle_s} J_s e^{i\mathbf{k}\cdot\mathbf{R}_n}\mathbf{S}_{\mathbf{k}}\cdot\mathbf{S}_{-\mathbf{k}} \\ &= \frac{1}{2}\sum_{\mathbf{k}} J(\mathbf{k})\left|\mathbf{S}_{\mathbf{k}}\right|^2, \end{aligned} \tag{1.8}$$

where

$$J(\mathbf{k}) = \sum_{s} J_s z_s \gamma_s(\mathbf{k}), \tag{1.9}$$

and $\gamma_s(\mathbf{k})$ is the structure-factors for the s^{th} shell of spins, which has been normalised to the number of neighbours, z_s, in the s^{th} shell. We can see that the Hamiltonian is controlled by the structure-factor:

$$\gamma_s(\mathbf{k}) = \frac{1}{z_s}\sum_{\langle 0n\rangle_s} e^{i\mathbf{k}\cdot\mathbf{R}_n}, \tag{1.10}$$

which are determined by the geometry of the lattice. As $\left|\mathbf{S}_{\mathbf{k}}\right|^2 > 0$ (and $J_s > 0$ and $z_s > 0$) we need to find the minimum of the structure-factor and place all the reciprocal-space spin density ($\mathbf{S}_{\mathbf{k}}$) at this k-point ($\mathbf{k}_{min}$). As we will see later, if the crystal lattice has a non-trivial basis, the structure-factor actually becomes a matrix, which can then be diagonalised, so that all the spin-density is placed at the k-point which minimises the lowest energy eigenvalue.

We have not yet considered the classical-spin constraint, so we will address this next. Unfortunately minimising the Hamiltonian in reciprocal space considerably complicates the equal-length spin constraints as we will show[43]. We begin by multiplying Equa-

tion 1.3 on both sides by $e^{i\mathbf{q}\cdot\mathbf{R}_j}$, where $\mathbf{q}$ is some arbitrary wave-vector, and then sum over all lattice sites. Making use of the identity

$$\sum_j e^{i\mathbf{q}\cdot\mathbf{R}_j} = N\sum_{\mathbf{G}} \delta_{\mathbf{q},\mathbf{G}}, \tag{1.11}$$

(note that previously in Equation 1.7 we neglected the sum over the reciprocal-space lattice vectors, $\mathbf{G}$, as we had restricted $\mathbf{k}$ to lie within the first Brillouin zone only), the spin constraint then becomes

$$\begin{aligned} 0 &= \sum_j e^{i\mathbf{q}\cdot\mathbf{R}_j}\left[\mathbf{S}_j\cdot\mathbf{S}_j - S^2\right] \\ &= \frac{1}{N}\sum_j\sum_{\mathbf{k}\mathbf{k}'} e^{i(\mathbf{q}-\mathbf{k}-\mathbf{k}')\cdot\mathbf{R}_j}\mathbf{S}_{\mathbf{k}}\cdot\mathbf{S}_{\mathbf{k}'} - NS^2\sum_{\mathbf{G}}\delta_{\mathbf{q}-\mathbf{G}}, \end{aligned} \tag{1.12}$$

so that finally we get

$$\sum_{\mathbf{k}}\sum_{\mathbf{G}} \mathbf{S}_{\mathbf{k}}\cdot\mathbf{S}_{\mathbf{q}-\mathbf{k}+\mathbf{G}} = NS^2\sum_{\mathbf{G}}\delta_{\mathbf{q}-\mathbf{G}}. \tag{1.13}$$

It turns out, however, that for inversion symmetric lattices (as is the case for a Bravais lattice with only one atom per unit cell) the structure-factor is minimised by $\mathbf{k} = \pm\mathbf{k}_{min}$. In this case, for the isotropic Heisenberg model, we can construct solutions using all three of the spin-space dimensions and as a consequence it is usually possible to find a spiraling classical spin-state with the appropriate periodicity to minimise the structure-factor. However, this is by no-means the case for all models, so it is important to always check that a physical solution actually exists at this periodicity. We discuss this topic in more detail in Section 2.3.3 where we contrast the behaviour of a simple Heisenberg and Ising system. We will now move on to consider the nearest neighbour structure factors for the classical Heisenberg model on a number of simple lattices, with a view to introducing the idea of geometric frustration.

1.2.2 Geometric Frustration

For many magnetic spin systems nearest-neighbour Heisenberg exchange interactions dominates. As we will see in this section, for simple lattices minimising this interaction specifies a unique ground-state (up to global-spin rotations) in which every bond is independently minimised. In contrast, a geometrically frustrated system is one for which the ground-state does not minimise the energy of each individual bond[24]. This can give rise to a variety of different magnetic states, for example: Nèel bipartite; chiral; multiple-**q** and locally degenerate antiferromagnetism. We will introduce these different types of magnetism by discussing a number of model systems with the following geometries linear chain, simple-cubic, triangular, face-centered-cubic, Kagomé and pyrochlore (mostly focusing on nearest neighbour interactions). We will find that the different styles of magnetism can be classified by the form of the structure factor minima.

Bipartite Antiferromagnet: Linear chain

The simplest system the we can consider is the linear chain with nearest neighbour Heisenberg interactions. Spins are located at sites $\mathbf{R}_j = na\hat{\mathbf{x}}$ where n is an integer, as shown in Figure 1.1. The structure factor is given by

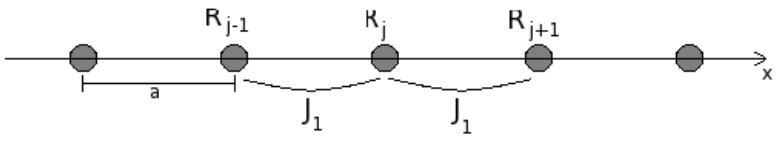

Figure 1.1: Linear chain with nearest neighbour Heisenberg interactions (which have an exchange constant of J_1)

$$\gamma(\mathbf{k}) = \frac{1}{2}\left(e^{iak_x} + e^{-iak_x}\right) = \cos(ak_x). \tag{1.14}$$

This is clearly minimised by $\mathbf{k}_{min} = \frac{\pi}{a}\hat{\mathbf{x}}$, which corresponds to a typical Nèel antiferromagnet:

$$\mathbf{S}_j = Se^{i\pi j}\hat{\mathbf{r}}, \tag{1.15}$$

where $\hat{\mathbf{r}}$ is an arbitrary unit vector. We see that after fixing the initial choice of $\hat{\mathbf{r}}$ (which provides two continuous global degrees of freedom) there is a unique ground-state. The corresponding energy is given by

$$E_0 = -J_1 NS^2, \tag{1.16}$$

i.e. every bond is minimised (and has an energy of $-J_1S^2$). This system is therefore not frustrated.

We can easily generalise this model to higher dimensions. For example, the simple-cubic lattice behaves completely analogously to the linear chain. The spins, $\mathbf{S}_j$, are located at sites $\mathbf{R}_j = a\left(n_1\hat{\mathbf{x}} + n_2\hat{\mathbf{y}} + n_3\hat{\mathbf{z}}\right)$ which corresponds to a structure factor of

$$\gamma\left(\mathbf{k}\right) = \frac{1}{3}\left[\cos(ak_x) + \cos(ak_y) + \cos(ak_z)\right]. \tag{1.17}$$

This time the structure factor is minimisd by $\mathbf{k}_{min} = \frac{\pi}{a}\left(\hat{\mathbf{x}} + \hat{\mathbf{y}} + \hat{\mathbf{z}}\right)$ and the ground-state is again a bipartite antiferromagnet described by

$$\mathbf{S}_j = Se^{i\pi(n_1+n_2+n_3)}\hat{\mathbf{r}}. \tag{1.18}$$

Chiral Magnet: Triangular Lattice

Next we will consider the triangular lattice, as it is the simplest example of a frustrated lattice. The positions of the spins are described by the lattice vectors

$$\mathbf{a}_1 = a\hat{\mathbf{x}}, \qquad \mathbf{a}_2 = \frac{a}{2}\left(\hat{\mathbf{x}} + \sqrt{3}\hat{\mathbf{y}}\right), \tag{1.19}$$

as shown in Fig. 1.2. There are six nearest neighbours and the structure factor is given

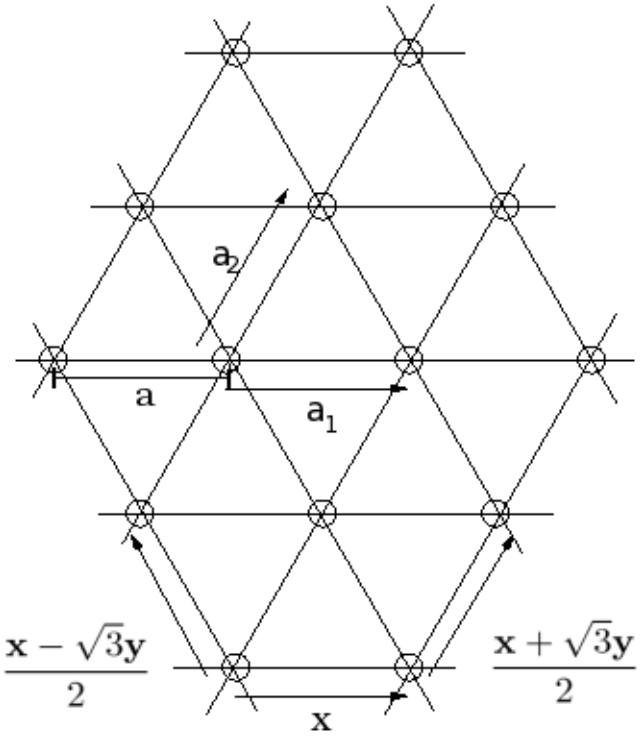

Figure 1.2: Triangular lattice

by

$$\begin{aligned}\gamma_1^t(\mathbf{k}) &= \frac{1}{3}\left[\cos(ak_x)+\cos\left(\frac{a(k_x+\sqrt{3}k_y)}{2}\right)+\cos\left(\frac{a(k_x-\sqrt{3}k_y)}{2}\right)\right] \\ &= \frac{1}{6}\left\{\left[2\cos\left(\frac{ak_x}{2}\right)+\cos\left(\frac{a\sqrt{3}k_y}{2}\right)\right]^2-\cos^2\left(\frac{a\sqrt{3}k_y}{2}\right)-2\right\}. \quad (1.20)\end{aligned}$$

which is minimised by $\mathbf{k}=\mathbf{K}=\pm\frac{2\pi}{3a}\hat{\mathbf{x}}$ (as can be seen in Fig. 1.3).

In real-space this corresponds to a 120° spiraling phase which can be described by:

$$\mathbf{S}_j = S\left[\hat{\mathbf{e}}_\mathbf{1}\cos(\mathbf{K}\cdot\mathbf{R}_j+\phi)+\hat{\mathbf{e}}_\mathbf{2}\sin(\mathbf{K}\cdot\mathbf{R}_j+\phi)\right], \quad (1.21)$$

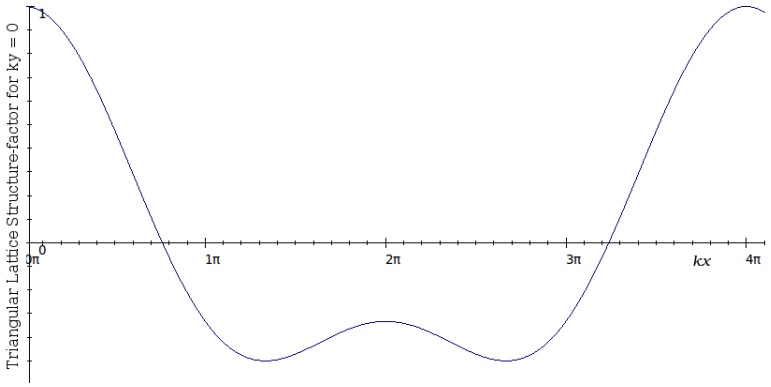

Figure 1.3: Triangular lattice structure factor plotted as a function of k_x, with $k_y = 0$ and $a = 1$

where $\hat{\mathbf{e}}_\mathbf{1}$ and $\hat{\mathbf{e}}_\mathbf{2}$ are orthonormal vectors and ϕ represents a free choice of phase (see Section 2.3.3 for a more detailed discussion on deriving a spiraling state from the reciprocal-space spin-constraints). Two chirally related examples of this state are depicted Fig. 1.4 These states have an energy of

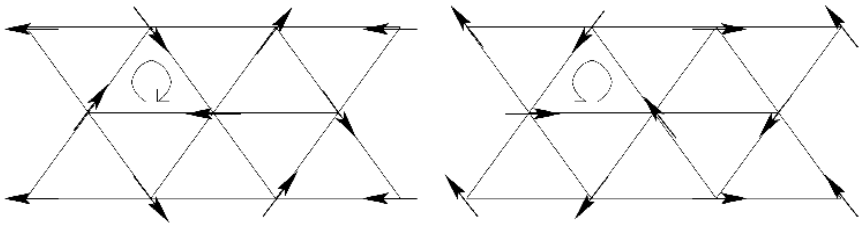

Figure 1.4: Two chirally related ground-states for nearest neighbour exchange on the triangular lattice

$$E_0 = -\frac{3}{2} J_1 N S^2, \tag{1.22}$$

which corresponds to an energy of $-J_1 S^2/2$ per bond. This model is clearly frustrated as this is only half the energy that can be gained by a single bond. The frustration exhibited by this model also shows up in the degeneracy of the ground-state. We have to be a little more careful, however, to assess the global degeneracy of this model than when we considered the simpler linear chain model. The vectors describing the spin directions form a planer state. In Fig. 1.4 we showed two states in which the spins lie in the plane of the lattice, however, this need not be the case. Consequently we can identify two continuous global degrees of freedom which are associated with this choice of plane. There is then

one more global continuous degree of freedom associated with fixing the direction of the initial spin within the chosen plane. So far this is analogous to the global degeneracy that was seen for the unfrustrated linear chain (or square lattice). For the triangular lattice, however, we still have on more choice to make before the spin state is completely specified: the second spin can make an angle of either $-2\pi/3$ or $+2\pi/3$ to the first spin. This gives rise to an additional discrete chiral degeneracy for the triangular lattice that is not present in the unfrustrated square lattice. We will see that the more frustrated a particular model is, the larger the ground-state degeneracy. Although the triangular lattice is one of the most frequently used examples to introduce the idea of geometric frustration, there are actually many models which are much more frustrated.

Multiple-q Magnet: Face-centred-cubic Lattice

Next we will consider multiple-**q** magnetism using the example of the face-centred-cubic lattice. Previously we saw that if the structure-factor was a minimum at two inversion symmetry related points then this lead to a chirally degenerate ground-state. In contrast, a multiple-**q** magnet occurs when the minima of the structure factor are related by a rotational symmetry. Solutions with an equal spin-density at all of these k-points are then degenerate with solutions that have unequal spin-densities at these k-points and solutions with only some or one of the k-points active. This allows the magnetism to break the rotational symmetry of the point-group of the underlying chemical lattice as we see in the following example of the face-centred-cubic lattice.

The face-centered-cubic lattice is generated by the lattice vectors

$$\mathbf{a}_1 = \frac{a}{2}\left(\hat{\mathbf{y}} + \hat{\mathbf{z}}\right), \qquad \mathbf{a}_2 = \frac{a}{2}\left(\hat{\mathbf{z}} + \hat{\mathbf{y}}\right), \qquad \mathbf{a}_3 = \frac{a}{2}\left(\hat{\mathbf{x}} + \hat{\mathbf{x}}\right), \tag{1.23}$$

and is shown in Fig. 1.5. This lattice has twelve nearest-neighbours and a corresponding

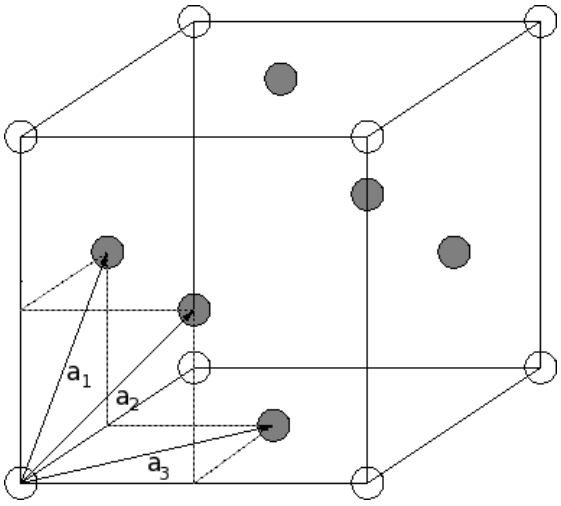

Figure 1.5: The face-centred-cubic lattice, where the cube shown has sides of length 'a.

structure factor given by

$$\gamma_1^f(\mathbf{k}) = \frac{1}{3}\left[\cos\left(\frac{ak_y}{2}\right)\cos\left(\frac{ak_z}{2}\right) + \cos\left(\frac{ak_z}{2}\right)\cos\left(\frac{ak_x}{2}\right) + \cos\left(\frac{ak_x}{2}\right)\cos\left(\frac{ak_y}{2}\right)\right]. \tag{1.24}$$

The minimum of this structure factor forms a degenerate line in reciprocal-space specified by the path

$$k_y = 0 \quad \text{and} \quad k_z = \frac{2\pi}{a}; \qquad k_x = \frac{2\pi}{a} \quad \text{and} \quad k_y = 0; \tag{1.25}$$

$$k_z = 0 \quad \text{and} \quad k_x = \frac{2\pi}{a}; \qquad k_y = \frac{2\pi}{a} \quad \text{and} \quad k_z = 0; \tag{1.26}$$

$$k_x = 0 \quad \text{and} \quad k_y = \frac{2\pi}{a}; \qquad k_z = \frac{2\pi}{a} \quad \text{and} \quad k_x = 0. \tag{1.27}$$

The reciprocal-space lattice is a body-centered lattice described by the reciprocal-lattice vectors

$$\mathbf{b}_1 = \frac{2\pi}{a}\left(\hat{\mathbf{y}} + \hat{\mathbf{z}} - \hat{\mathbf{x}}\right), \qquad \mathbf{b}_2 = \frac{2\pi}{a}\left(\hat{\mathbf{z}} + \hat{\mathbf{x}} - \hat{\mathbf{y}}\right), \qquad \mathbf{b}_3 = \frac{2\pi}{a}\left(\hat{\mathbf{x}} + \hat{\mathbf{y}} - \hat{\mathbf{z}}\right). \tag{1.28}$$

In Fig. 1.6 we show one quarter of the Brillouin zone, with the reciprocal-lattice points at the origin and the zone-centre ($\mathbf{k} = \frac{2\pi}{a}(1,1,1)$) shown in purple, and the path in red denotes the position of the minimum of the structure factor. We will return to further

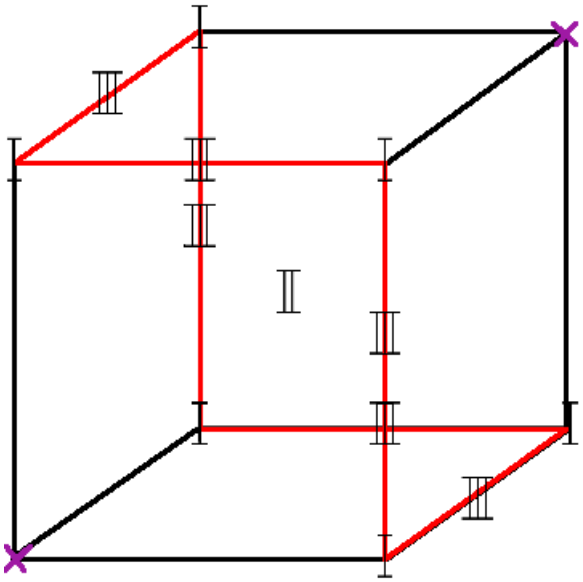

Figure 1.6: One quarter of the body-centred-cubic reciprocal space lattice (of the real-space face-centred-cubic lattice). Two of the reciprocal-lattice points are marked in purple. The location of the structure factor minimum for nearest-neighbour exchange is shown in red. The locations of the structure factor minima for type I, II and III antiferromagnetism (see text) are also marked.

consider this local degeneracy later. In experimentally realisable systems, however, there are usually weaker interactions present which greatly reduce the residual degeneracy. In this case, including second neighbour interactions gives rise to multiple-**q** magnetism. The second-neighbour structure factor is given by

$$\gamma_2^f = \frac{2}{3}\left[\cos^2\left(\frac{k_x a}{2}\right) + \cos^2\left(\frac{k_y a}{2}\right) + \cos^2\left(\frac{k_z a}{2}\right) - \frac{3}{2}\right], \tag{1.29}$$

and the corresponding Hamiltonian is

$$H = \frac{1}{2}\sum_{\mathbf{k}} |\mathbf{S}_{\mathbf{k}}|^2 \left[J_1 z_1 \gamma_1^f + J_2 z_2 \gamma_2^f\right]. \tag{1.30}$$

If $J_1 \gg |J_2|$, then we can minimise γ_1^f and then subsequently minimise γ_2^f. The simplest case is for $J_2 < 0$ (i.e. ferromagnetic second neighbour interactions) for which there are

three independent minima at

$$\mathbf{K}_1 = \frac{2\pi}{a}(0,1,1)\,, \qquad \mathbf{K}_2 = \frac{2\pi}{a}(1,0,1)\,, \qquad \mathbf{K}_3 = \frac{2\pi}{a}(1,1,0)\,. \tag{1.31}$$

This is commonly referred to as a 'Type I' antiferromagnet and the positions of the three active Bragg spots are indicated by 'I' in Fig. 1.6. As we have only three inequivalent k-points and three available spin degrees of freedom, we can construct a solution involving all three k-points which satisfy the classical spin constraints:

$$\mathbf{S}_\mathbf{k} = \sqrt{N}S\left[\delta_{\mathbf{k},\mathbf{K}_1}\sin\theta\cos\phi\hat{\mathbf{e}}_1 + \delta_{\mathbf{k},\mathbf{K}_2}\sin\theta\sin\phi\hat{\mathbf{e}}_2 + \delta_{\mathbf{k},\mathbf{K}_3}\cos\theta\hat{\mathbf{e}}_3\right], \tag{1.32}$$

which corresponds to the real-space solution

$$\mathbf{S}_j = S\left[\sin\theta\cos\phi e^{i\mathbf{K}_1\cdot\mathbf{R}_j}\hat{\mathbf{e}}_1 + \sin\theta\cos\phi e^{i\mathbf{K}_2\cdot\mathbf{R}_j}\hat{\mathbf{e}}_2 + \cos\theta e^{i\mathbf{K}_3\cdot\mathbf{R}_j}\hat{\mathbf{e}}_3\right]. \tag{1.33}$$

We can interpret the choice of how to orientate the orthonormal basis $\{\hat{\mathbf{e}}_1, \hat{\mathbf{e}}_2, \hat{\mathbf{e}}_3\}$ as the global degeneracy arising from rotating all the spins simultaneously. There are however also two continuous local degrees of freedom (governed by the angles θ and ϕ) which control the relative spin orientations. In Fig. 1.7 we depict one quarter of the unit cell

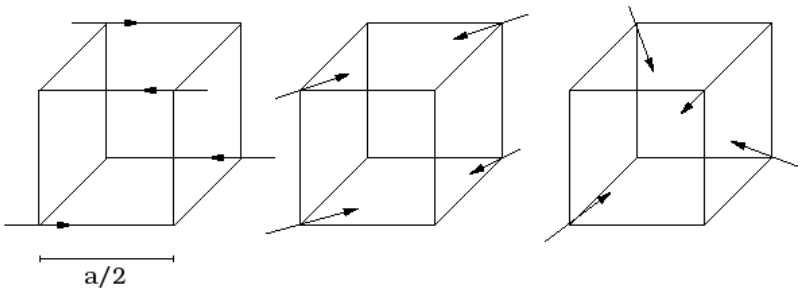

Figure 1.7: Three (highly symmetric) examples of possible Type I antiferromagnetic states. For each case one quarter of the conventional unit cell is shown.

of three highly symmetrical examples of possible states (where we have chosen $\hat{\mathbf{e}}_1 = \hat{\mathbf{x}}$, $\hat{\mathbf{e}}_2 = \hat{\mathbf{y}}$ and $\hat{\mathbf{e}}_3 = \hat{\mathbf{z}}$). The leftmost diagram shows the single-$\mathbf{q}$ state arising when $\theta = \pi/2$ and $\phi = 0$. The middle diagram has $\theta = \pi/2$ and $\phi = \pi/4$ which is a double-$\mathbf{q}$ state

with equal contributions from each of the two active **k**-points. Finally the right hand diagram is the triple-**q** state with $\cos\theta = 1/\sqrt{3}$ and $\phi = \pi/4$. Although states with unsymmetrical values of θ and ϕ are possible, experimentally they turn out to be extremely unlikely. This is because the crystal-field interaction usually stabilises spins lying along symmetric lattice directions. In experientially realisable systems, if the ground-state of the dominant interactions has a large degeneracy, it will usually by lifted by other weaker interactions which will be present (this idea will constitute a central topic of this thesis). One possibility that will be considered later is that quantum fluctuations will stabilise colinear states i.e. in this case ones that are indexed by a single wave-vector. Unlike the triple-**q** state, these single-**q** states break the point symmetry of the underlying chemical lattice.

One example of of a type I multiple-**q** magnet is γ-manganese[37]. Doping with nickel has been found to induce a number of phase transitions between cubic, tetragonal and orthorhombic antiferromagnetism. By means of elastic neutron scattering experiments, the different phases have been associated with different styles of type I antiferromagnetism[45].

For completeness we will briefly mention two other common forms of face-centred multiple-**q** magnetism. Type II antiferromagnetism can occur when $J_2 > J_1 > 0$ corresponding to structure factor minima at

$$\mathbf{K}_1 = \frac{\pi}{a}(1,1,1)\,, \qquad \mathbf{K}_2 = \frac{\pi}{a}(-1,1,1)\,, \qquad \mathbf{K}_3 = \frac{\pi}{a}(1,-1,1)\,, \qquad \mathbf{K}_4 = \frac{\pi}{a}(1,1,-1)\,, \tag{1.34}$$

(depicted using 'II' in Fig. 1.6). The other is type III antiferromagnetism, which can be stabilised for $J_1 > J_2 > 0$, giving rise to minima in the structure factor at

$$\begin{aligned} \mathbf{K}_1 &= \frac{\pi}{a}(0,1,2)\,, \qquad \mathbf{K}_2 = \frac{\pi}{a}(2,0,1)\,, \qquad \mathbf{K}_3 = \frac{\pi}{a}(1,2,0)\,, \\ \mathbf{K}_4 &= \frac{\pi}{a}(0,2,1)\,, \qquad \mathbf{K}_5 = \frac{\pi}{a}(1,0,2)\,, \qquad \mathbf{K}_5 = \frac{\pi}{a}(2,1,0)\,. \end{aligned} \tag{1.35}$$

Multiple-**q** antiferromagnetism is discussed in more detail in a review by M.W. Long[48]. Multiple-**q** magnetism will be a key topic of Chapter 5.

Locally degenerate antiferromagnets

As we established earlier, the structure factor minimum for the face-centred-cubic lattice with nearest neighbour Heisenberg interactions has a continuous degenerate minimum along the the path shown in Fig. 1.6. As a result the ground-state solutions to this model are macroscopically degenerate. This can be seen by considering the set of states which are indexed by a single wave-vector (which minimises the structure factor). We begin by just considering the spins in the xy-plane. Wave-vectors of the form $\mathbf{k} = (0, 2\pi/a, k)$, where k can take any value, are then consistent with the relative spin orientations shown in Fig. 1.8. There is no coupling however between successive planes along the z-axis

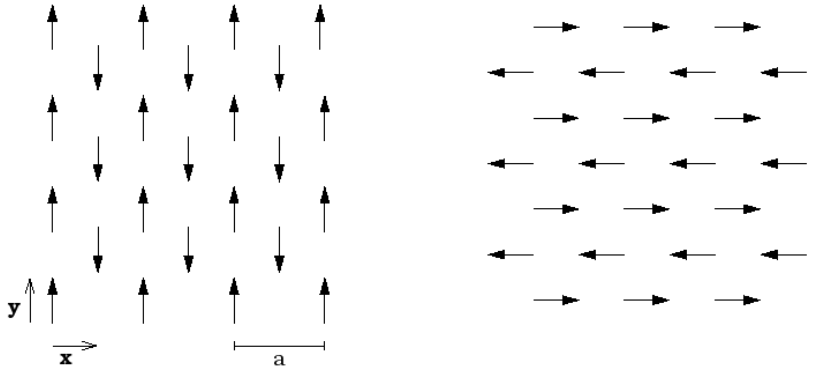

Figure 1.8: Relative spin orientations for the xy-plane of a type I antiferromagnet indexed by wave-vector $\mathbf{K} = (0, 2\pi/a, k)$, where k can take any value, i.e. all global rotations of the spins within one plane relative to the other planes are degenerate

(states with $k_z = k$ where k can take any value are degenerate). There are therefore two continuous degrees of freedom per plane of spins; these are associated with rotating all the spin orientations of just a single plane of the system. These states all have an energy of

$$E = -2J_1NS2, \tag{1.36}$$

which corresponds to an energy of $-J_1 S^2/3$ per bond. This is the most frustrated system that we have discussed so far. We can see that the magnitude of the ground-state degeneracy can be viewed as an alternative measure of how frustrated a system is. It is easier to assess the level of ground-state degeneracy in reciprocal-space rather than in real-space. For the chiral triangular lattice the structure factor had only two discrete inversion related minima. We then found that for the multiple-**q** model of first and second neighbour interactions on the face-centred-cubic lattice there were three, four or six rotationally related, though still discrete, minima of the structure factor. For just nearest neighbour interactions on the face-centred-cubic lattice, however, the structure factor minimum forms a continuous degenerate line in reciprocal space. Next we will go on to consider two more models which are even more frustrated: the Kagomé lattice and the pyrochlore lattice. Unlike the previously considered models both have multiple atoms per unit cell.

Firstly we will consider the Kagomé lattice with nearest neighbour interactions. The Kagomé lattice has an underlying triangular lattice with three atoms per unit cell and is depicted in Fig. 1.9. These are located at positions $\mathbf{R}_{\alpha j} = \mathbf{R}_j + \mathbf{c}_\alpha$, where $\alpha \in \{0, 1, 2\}$

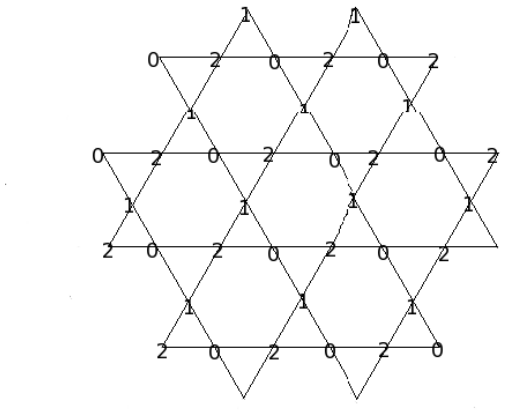

Figure 1.9: The Kagomé lattice with atoms on the three sub-lattices labeled by 0, 1 and 2

with $\mathbf{c}_\alpha$ describing the positions of the three spins within the unit cell:

$$\mathbf{c}_0 = \frac{a}{4}\left(\hat{\mathbf{x}} + \sqrt{3}\hat{\mathbf{y}}\right), \qquad \mathbf{c}_1 = -\frac{a}{2}\hat{\mathbf{x}}, \qquad \mathbf{c}_2 = \frac{a}{4}\left(\hat{\mathbf{x}} - \sqrt{3}\hat{\mathbf{y}}\right) \tag{1.37}$$

and the set of $\mathbf{R}_j$ form the triangular lattice.

As there is a basis of three sites per unit cell, the spins and the Block transforms gain the sub-lattice index α, so that

$$\mathbf{S}_{\alpha j} = \frac{1}{\sqrt{N}} \sum_{\mathbf{k}} e^{-i\mathbf{k}\cdot(\mathbf{R}_j + \mathbf{c}_\alpha)} \mathbf{S}_{\alpha\mathbf{k}}, \tag{1.38}$$

$$\mathbf{S}_{\alpha\mathbf{k}} = \frac{1}{\sqrt{N}} \sum_{j} e^{i\mathbf{k}\cdot(\mathbf{R}_j + \mathbf{c}_\alpha)} \mathbf{S}_{\alpha j}. \tag{1.39}$$

This means that the structure factor becomes a matrix (in this case 3×3) and the Hamiltonian is given by

$$H = \frac{J_1 z}{2} \sum_{\mathbf{k}} \sum_{\alpha\beta} \mathbf{S}^*_{\alpha\mathbf{k}} \gamma_{\alpha\beta}(\mathbf{k}) \mathbf{S}_{\beta\mathbf{k}}, \tag{1.40}$$

with

$$\gamma(\mathbf{k}) = \frac{1}{2} \begin{bmatrix} 0 & \cos\left(\frac{k_x - \sqrt{3}k_y}{4}\right) & \cos\left(\frac{k_x}{2}\right) \\ \cos\left(\frac{k_x - \sqrt{3}k_y}{4}\right) & 0 & \cos\left(\frac{k_x + \sqrt{3}k_y}{4}\right) \\ \cos\left(\frac{k_x}{2}\right) & \cos\left(\frac{k_x + \sqrt{3}k_y}{4}\right) & 0 \end{bmatrix}, \tag{1.41}$$

where we have set $a = 1$ to simplify the notation. To find the minimum energy solutions we need to diagonalise the structure factor. The characteristic equation for the eigenvalues, Γ, is given by

$$\begin{aligned} 4\Gamma^3 - \Gamma \left[\cos^2\left(\frac{k_x - \sqrt{3}k_y}{4}\right) + \cos^2\left(\frac{k_x}{2}\right) + \cos^2\left(\frac{k_x + \sqrt{3}k_y}{4}\right)\right] \\ - \cos\left(\frac{k_x - \sqrt{3}k_y}{4}\right) \cos\left(\frac{k_x}{2}\right) \cos\left(\frac{k_x + \sqrt{3}k_y}{4}\right) = 0. \end{aligned} \tag{1.42}$$

This can be written in terms of the triangular lattice structure factor, $\gamma_1^t(\mathbf{k})$, as

$$4\Gamma^3 - \frac{3}{2}\Gamma\left(\gamma_1^t + 1\right) - \frac{1}{4}\left(3\gamma_1^t + 1\right) = 0, \tag{1.43}$$

which factorises as

$$(2\Gamma + 1)\left(8\Gamma^2 - 4\Gamma - 3\gamma_1^t - 1\right) = 0, \tag{1.44}$$

The eigenvalues are therefore

$$\Gamma = -\frac{1}{2}, \frac{1}{4}\left(1 - \sqrt{6\gamma_1^t + 3}\right), \frac{1}{4}\left(1 + \sqrt{6\gamma_1^t + 3}\right), \tag{1.45}$$

where $-1/2 < \gamma_1^t < 1$. We find that the minimum energy eigenvalue is a flat dispersionless band. The ground-state of the Kagomé lattice is macroscopically degenerate[18]. To see this in real-space it is helpful to rewrite the Hamiltonian as a sum over triangles, t, as follows:

$$H = \frac{J_1}{2}\sum_t \left[(\mathbf{S}_0 + \mathbf{S}_1 + \mathbf{S}_2)^2 - 3S^2\right]. \tag{1.46}$$

This is minimised by ensuring that the total spin of each triangle vanishes (providing an energy of $-s^2/2$ per bond). As in the case of the triangular lattice, the minimum energy state of each triangle is the planar 120° phase. For the triangular lattice, as the triangles are edge sharing, selecting the spin state for one triangle also fixes the spin orientations for the entire lattice. The Kagomé lattice, however, consists of corner sharing triangles and therefore the plane in which the spins lie is nearly independent for each triangle (there are also some additional constraints associated with ensuring that the angles of the 'triangular planes' are chosen to close consistently around the hexagonal loops in the lattice). As a result the number of continuous degrees of freedom in the ground-state increases with the size of the lattice. We notice that although the triangular lattice an Kagomé lattice have the same energy per bond, the ground-state degeneracy of the two systems is completely different. For this reason it would seem that the extent of the ground-state degeneracy is a better measure of the level of frustration present in a system than the energy per bond.

Finally we will consider the pyrochlore lattice. This is one of the most geometrically frustrated systems that is experimentally accessible. Furthermore, the materials which we will study in this thesis have this structure. The pyrochlore lattice is formed from corner sharing tetrahedron as shown in Fig. 1.10. The lattice has four atoms per unit cell, located

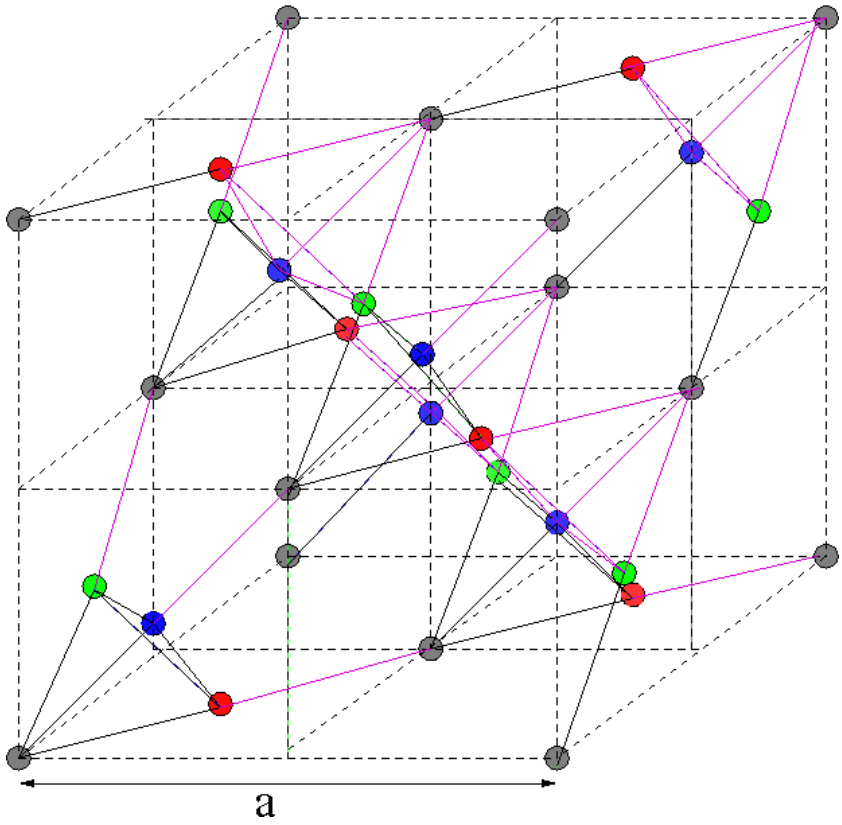

Figure 1.10: The pyrochlore lattice. The atoms forming the four sub-lattices are coloured gray, green, blue and red and the corner sharing tetrahedra are highlighted in black or pink.

at positions $\mathbf{R}_{\alpha j} = \mathbf{R}_j + \mathbf{c}_\alpha$, where $\mathbf{R}_j$ ranges over an underlying face-centred-cubic lattice and the locations of the four sub-lattices are given by:

$$\mathbf{c}_0 = -\frac{a}{8}\left(\hat{\mathbf{x}}+\hat{\mathbf{y}}+\hat{\mathbf{z}}\right), \quad \mathbf{c}_1 = \frac{a}{8}\left(\hat{\mathbf{y}}+\hat{\mathbf{z}}-\hat{\mathbf{x}}\right), \quad \mathbf{c}_2 = \frac{a}{8}\left(\hat{\mathbf{z}}+\hat{\mathbf{x}}-\hat{\mathbf{y}}\right), \quad \mathbf{c}_3 = \frac{a}{8}\left(\hat{\mathbf{x}}+\hat{\mathbf{y}}-\hat{\mathbf{z}}\right). \tag{1.47}$$

The four sub-lattices are coloured gray, green, blue and pink respectively in Fig. 1.10.

Setting $a = 1$ again, the structure factor is

$$\gamma(\mathbf{k}) = \frac{1}{3}\begin{bmatrix} 0 & X & Y & Z \\ X & 0 & z & y \\ Y & z & 0 & x \\ Z & y & x & 0 \end{bmatrix}, \tag{1.48}$$

where

$$\begin{aligned} X &= \cos\left(\frac{k_y + k_z}{4}\right), \quad Y = \cos\left(\frac{k_z + k_x}{4}\right), \quad Z = \cos\left(\frac{k_x + k_y}{4}\right) \\ x &= \cos\left(\frac{k_y - k_z}{4}\right), \quad y = \cos\left(\frac{k_z - k_x}{4}\right), \quad z = \cos\left(\frac{k_x - k_y}{4}\right). \end{aligned} \tag{1.49}$$

The characteristic equation for the eigenvalues, $\Gamma = \lambda/3$ is

$$\begin{aligned} \lambda^4 - \lambda^2\left(x^2 + y^2 + z^2 + X^2 + Y^2 + Z^2\right) - 2\lambda\left(xyz + xYZ + XyZ + XYz\right) \\ + \left(X^2x^2 + Y^2y^2 + Z^2z^2\right) - 2\left(YZyz + ZXzx + XYxy\right) = 0. \end{aligned} \tag{1.50}$$

Expressing this in terms of the face-centred-cubic structure factor simplifies things considerably:

$$\begin{aligned} \lambda^4 - 3\lambda^3\left(\gamma_1^f + 1\right) - 2\lambda\left(3\gamma_1^f + 1\right) - 3\gamma_1^f \\ (\lambda + 1)^2\left[(\lambda - 1)^2 - \left(3\gamma_1^f + 1\right)\right] = 0. \end{aligned} \tag{1.51}$$

This provides the eigenvalues

$$\Gamma = -\frac{1}{3}, -\frac{1}{3}, \frac{1}{3}\left(1 \pm \sqrt{3\gamma_1^f + 1}\right), \tag{1.52}$$

where $-\frac{1}{3} < \gamma_1^f < 1$. In Fig. 1.11 we plot the structure factor as a function of k_z with $k_x = k_y = 0$. We can see that two out of four of the eigenvalues are completely degenerate

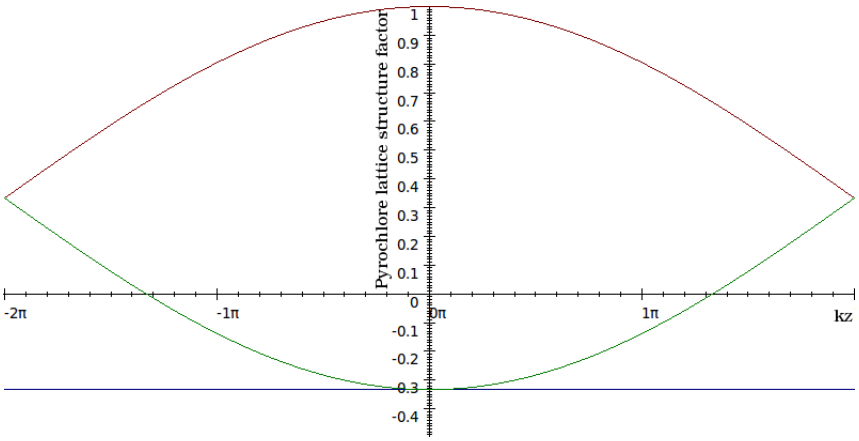

Figure 1.11: The pyrochlore lattice structure factor plotted as a function of k_z with $k_x = k_y = 0$

across the whole volume of reciprocal-space. We can assess this degeneracy in real-space using an equivalent method to that that was used previously for the Kagomé lattice. We write the Hamiltonian as a sum over tetrahedra, t, as described below:

$$H = \frac{J_1}{2} \sum_t \left[(\mathbf{S}_0 + \mathbf{S}_1 + \mathbf{S}_2 + \mathbf{S}_3)^2 - 4S^2 \right]. \tag{1.53}$$

The ground-state solutions are therefore all those for which the total spin of each tetrahedron vanishes and have an energy of $-J_1/3$ per bond. Each spin contributes two degrees of freedom and is shared between two tetrahedra. As a result there are four degrees of freedom per tetrahedron. If we treat the constraints that the total spin of every tetrahedron vanishes as independent (although this is not actually the case) then we have three constraints per tetrahedron and consequently one degree of freedom per tetrahedron. We note that this argument does not usually hold because the spin constraints for different units (e.g. tetrahedra, or triangles in the case of the Kagomé lattice) are not independent. For the Kagomé lattice, this argument predicts no macroscopic ground-state degeneracy, which as we discussed above is not the case. For the pyrochlore lattice, however, this argument has been shown to provide the correct degeneracy in the limit that the system size tends to infinity[58]. This thesis will investigate how this degeneracy is then lifted by other interactions by studying a number of magnetic materials which exhibit the

pyrochlore geometry.

More subtle models

As a final point in this section, we wish to mention a couple of more subtle systems. So far for every example that we have considered it has been possible to find a solution using the minimum of the structure factor and is also compatible with the equal-length spin constraints. We note, however, that this is not always the case. One situation in which this can occur is when there are multiple atoms per unit cell, as illustrated in the following example. We will consider the model depicted in Fig. 1.12, where we will use $J_1 = 2J_2$.

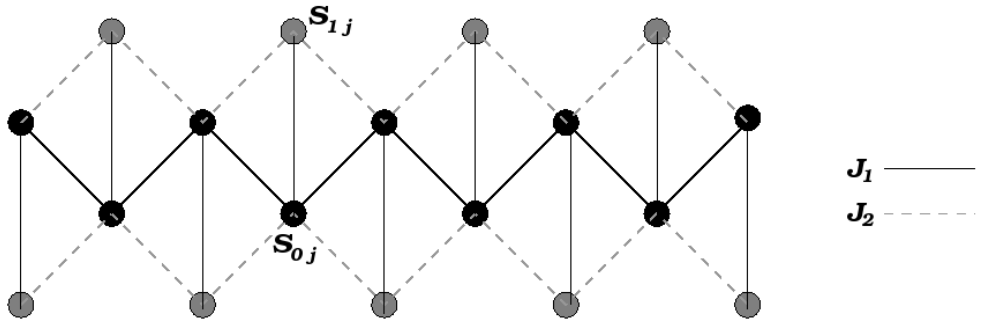

Figure 1.12: One dimensional Heisenberg model with two atoms per unit cell (shown in gray and black) and first and second neighbour interactions (indicated by the solid and dashed lines respectively).

The Hamiltonian is given by

$$H = \sum_j \frac{J_1}{2} \left(\mathbf{S}_{0,j-1} \cdot \mathbf{S}_{0,j} + \mathbf{S}_{0,j} \cdot \mathbf{S}_{0,j+1} \right) + J_1 \left(\mathbf{S}_{0,j} \cdot \mathbf{S}_{1,j} \right) + J_2 \left(\mathbf{S}_{0,j-1} \cdot \mathbf{S}_{1,j} + \mathbf{S}_{0,j+1} \cdot \mathbf{S}_{1,j} \right). \tag{1.54}$$

Block transforming then gives

$$H = \sum_k \left[\mathbf{S}^*_{0,k} \mathbf{S}^*_{1,k} \right] \begin{bmatrix} J_1 \cos ka & \frac{J_1}{2} \left(\cos ka + 1 \right) \\ \frac{J_1}{2} \left(\cos ka + 1 \right) & 0 \end{bmatrix} \begin{bmatrix} \mathbf{S}_{0,k} \\ \mathbf{S}_{1,k} \end{bmatrix}, \tag{1.55}$$

which has eigenvalues

$$\Gamma = \frac{J_1}{2}\left\{\cos ka \pm \left[\cos^2(ka) + (\cos ka + 1)^2\right]^{\frac{1}{2}}\right\}, \tag{1.56}$$

and $\Gamma_{min} = -J_1$ when $\cos ka = -1$. The Hamiltonian then becomes

$$H = -J_1 \sum_k |\mathbf{S}_{0,k}|^2, \tag{1.57}$$

which corresponds to the spin state

$$\mathbf{S}_{0,j} = Se^{ij\pi}\hat{\mathbf{r}}, \qquad \mathbf{S}_{1,j} = \mathbf{0}. \tag{1.58}$$

This state clearly does not satisfy the equal-length spin constraints. For the case of $J_1 = 2J_2$ it is actually straight forward to find the correct classical ground-state. The model can be broken down into edge sharing triangles, as shown in Fig. 1.13.

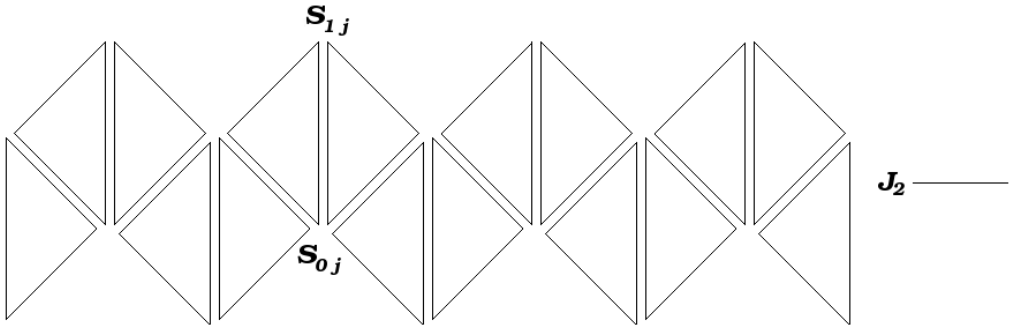

Figure 1.13: The same model as shown in Fig. 1.12 but for the case of $J_1 = 2J_2$, allowing the Hamiltonian to be interpreted as a sum over triangular plaquettes.

Then as for the Kagomé lattice the ground-state is found by ensuring that the total spin of each triangle vanishes and we get a planer 120° state like that of the triangular lattice.

Another instance of the structure factor minima failing to provide solutions which satisfy the equal-length spin constraints is when the model contains highly anisotropic interactions. This can result in there not being enough available spin components to con-

struct an equal-length spin state. An example is the nearest neighbour Ising model on the triangular lattice. To create the 120° spiraling phase that minimises the structure factor is not possible with only one (discrete) degree of freedom per spin. As a result the ground-state is actually much more frustrated: each triangle must have one up and one down spin while the third spin could be either up or down. This produces a macroscopically degenerate ground-state.

As these two examples illustrate, it is not guarantied that the structure factor minimum will be compatible with an equal-length spin state. This can make a model much more difficult to solve. As this issue forms a central theme of the next chapter when considering anisotropic interactions, we will return to this idea again in Section 2.3.3.

1.2.3 Rare-earth magnetism

In this thesis we will investigate the magnetic ordering of rare-earth pyrochlores: $R_2M_2O_7$. We will discuss their structure and behaviour in more detail in Section 1.3, however, here we will introduce some of the basic considerations of rare-earth magnetism (focusing on rare-earth oxides). The transition metal ions that we will consider are titanium and tin, both of which form M^{4+} ions. These have a closed outer shell (with the electron structure of argon and xenon respectively). The oxygen ions also form closed shell O^{2-} ions. Conserving charge then means that the rare-earth ions take the form R^{3+}. The rare-earth ions are therefore the only ones to have a non-zero magnetic moment. The valence electrons of the rare-earth ions lie in the $4f$-shell (with the particular number of electrons depending on which rare-earth ion is being considered). As the $4f$-orbitals are very localised, there is little overlap with the neighbouring oxygen $2p$-orbitals. Consequently rare-earth oxides are often insulators, with the $4f$-electrons forming local moments[39].

The total angular momentum and therefore the magnitude of the rare-earth ions can be found using Hund's rules[3]. Hund's first rule is to maximise the total spin of the ion and the second rule is to maximise the total orbital angular momentum of the ion, while always respecting Pauli's exclusion principle. By maximising the total spin of the ion,

the number of doubly occupied orbitals is minimised. As the orbitals are all orthogonal this reduces the probability of the electrons approaching each other and therefore reduces the Coulomb energy of the system. Similarly, maximising the orbital angular momentum reduces the chances of electrons approaching each other. Hund's third and final rule is that if the outer shell is under half filled then the total angular momentum, J, (where $|L-S| < J < L+S$) is maximised. On the other hand, if the outer shell is over half filled, then the total angular momentum is minimised. Hund's third rule arises from spin-orbit coupling[41], which has the Hamiltonian

$$H_{SO} = \frac{1}{2m^2c^4}\frac{Ze^2}{4\pi\epsilon_0}\frac{1}{r^3}\hat{\mathbf{S}}\cdot\hat{\mathbf{L}}, \tag{1.59}$$

where 'r' is the electron-nucleus distance and 'm' is the reduced mass of the electron and nucleus. Spin-orbit coupling arises from relativistic corrections to the Hamiltonian of the atom and is most significant for atoms with a large atomic number. As spin-orbit coupling is often a relatively weak effect, it can often be overturned by other weaker interactions, in particular the crystal-field interaction. In fact, for the transition metals the crystal-field interaction is usually in competition with Hund's first rule. For rare-earth ions, however, this is not the case and the magnetic moment calculated from the total angular momentum, J, is in excellent agreement with the experimentally measured values[6].

At low temperatures the rare-earth pyrochlores can develop long-range magnetic order. We wish to investigate the nature of this ordering in the low temperature limit and the interactions which control it. In the next section we will therefore discuss the most relevant interactions.

1.2.4 Magnetic Interactions

We will now discuss some of the interactions which drive magnetic ordering. Previously we discussed the properties of the ground-state of the Heisenberg interaction on a number of different lattices. As this interaction is usually dominant in many magnetic systems,

we will begin by outlining the electronic origin of this interaction. We will then go on to introduce the crystal-field interaction and the dipole interaction as these play an important role in the materials that we will discuss. Finally we will briefly mention some other effects.

The origin of the Heisenberg interaction

We will now discuss the electronic origin of the Heisenberg interaction. It can be derived from the Hubbard model in the limit that the Coulombic energy penalty arising from doubly occupying electronic orbitals dominates[2]. The Hubbard model is a highly simplified model used to capture the competition between the metallic and insulating character of a material. The Hamiltonian is given by

$$H = -\frac{t}{2} \sum_{\langle ij \rangle, \sigma} \left(c_{i\sigma}^{\dagger} c_{j\sigma} + c_{j\sigma}^{\dagger} c_{i\sigma} \right) + U \sum_{j} n_{j\uparrow} n_{j\downarrow}. \tag{1.60}$$

The first term constitutes the tight-binding model and describes the delocalisation of the electrons using the starting point of localised atomic orbitals[3]. The parameter 't' is a measure of the overlap between atomic orbitals on different sites. This overlap integral between two neighbouring orbitals a distance '$\mathbf{R}$' apart is given by

$$t = -\int \mathbf{dr}\ \phi_i^{*}(\mathbf{r})\, V \phi_j(\mathbf{r} + \mathbf{R}), \tag{1.61}$$

where $\phi_i(\mathbf{r})$ is the atomic orbital at site 'i' and '$V = V_{lat} - V_{at}$' is the difference between the periodic potential of the crystal (V_{lat}) and the potential of an isolated nucleus (V_{at}). We assume that only nearest neighbour hopping contributes, as the overlap integral decreases rapidly with increasing $\mathbf{R}$. The creation and annihilation of an electron on site 'i' with spin 'σ' are described by the operators '$c_i^{\dagger}$' and 'c_i' respectively. The second term represents the Coulomb energy penalty arising from doubly occupying an atomic orbital, the magnitude of which is given by the parameter 'U'. Finally, '$n_{i\sigma}$' is the number operator which counts

the number of electrons of spin 'σ' on site 'i'.

This Hubbard model is extremely difficult to solve in three dimensions with arbitrary values of 't' and 'U'. We will consider the limit that $U \gg t$ (which is not unreasonable for rare-earth magnets). For simplicity we will also assume that the model is at exactly half filling (i.e. the number of electrons is equal to the number of orbitals). In the limit that $U \mapsto \infty$, it becomes impossible to doubly occupy and orbital. In this case each of the electrons are localised to a single site. This state is called a Mott insulator. For a large but finite value of 'U', ionic solids can magnetically order. There is a negligible direct overlap between the orbitals of neighbouring rare-earth ions. Instead the dominant hopping pathway is via the intermediate oxygen $2p$-orbitals. The electrons on two neighbouring rare-earth ions can exchange by only temporally occupying an intermediate rare-earth orbital. This virtual hopping process is known as super-exchange. If the electrons on both rare-earth ions have the same spin then Pauli exclusion blocks the hopping onto the intermediate site. This means that the electrons on neighbouring rare-earth sites must have opposite spins in order to gain from super-exchange. For this reason Mott insulators are usually antiferromagnetic.

The concept of super-exchange can be used to obtain the Heisenberg model from the Hubbard model at half filling in the limit that $U \gg t$ [1]. As the valence electrons exchange via the intermediate oxygen site we require second order perturbation theory to calculate the matrix element of an effective Hamiltonian (H_{eff}). The energy (up to second order) is then given by[41]:

$$E = E_n^{(0)} + \lambda \langle n^{(0)}|V|n^{(0)}\rangle + \lambda^2 \sum_{k \neq n} \frac{|\langle k^{(0)}|V|n^{(0)}\rangle|^2}{E_n^{(0)} - E_k^{(0)}}, \tag{1.62}$$

where λ is a small parameter which we incorporate into the potential V, instead requiring that V itself is small. This is indeed the case for $V = V_{lat} - V_{at}$ if the atomic orbitals are highly localised. The first term is the energy of the unperturbed ground-state (i.e. all the rare-earth orbitals exactly half-filled), which we will take to be zero for convenience. The

second term is the direct overlap between the rare-earth orbitals which we will take to be negligible. In the third term, $\langle k^{(0)}|V|n^{(0)}\rangle$ is the overlap integral between the rare-earth and oxygen orbitals for which we will use the value '$-t$'. Finally, '$E_k^{(0)}$' is the energy of the intermediate state, i.e. the doubly occupied oxygen orbital which occurs an energy penalty of 'U' compared to the ground-state. We therefore find that the matrix element is given by $H_{eff} = \frac{-t^2}{U}$. The effective Hamiltonian for a single bond between neighbouring rare-earth sites is then given by summing over all possible spin states to give

$$H_{eff}^{\langle ij\rangle} = \frac{-t^2}{U}\sum_{\sigma\sigma'} c_{i\sigma}^\dagger c_{j\sigma} c_{j\sigma'}^\dagger c_{i\sigma'}, \tag{1.63}$$

which we can then express as

$$H_{eff}^{\langle ij\rangle} = \frac{-t^2}{U}\left[c_{i\uparrow}^\dagger c_{i\uparrow} c_{j\uparrow}^\dagger c_{j\uparrow} + c_{i\downarrow}^\dagger c_{i\downarrow} c_{j\downarrow}^\dagger c_{j\downarrow} + c_{i\uparrow}^\dagger c_{i\downarrow} c_{j\downarrow}^\dagger c_{j\uparrow} + c_{i\downarrow}^\dagger c_{i\uparrow} c_{j\uparrow}^\dagger c_{j\downarrow} + n_i\right]. \tag{1.64}$$

We then use

$$c_\uparrow^\dagger c_\uparrow = \frac{1}{2}+s^z, \qquad c_\downarrow^\dagger c_\downarrow = \frac{1}{2}-s^z, \qquad c_\uparrow^\dagger c_\downarrow = s^+ = s^x+is^y, \qquad c_\downarrow^\dagger c_\uparrow = s^- = s^x-is^y, \tag{1.65}$$

and $n_i = n_j = 1$ since we are considering half-filling and sum over all bonds to arrive at

$$\begin{aligned} H_{eff} &= \frac{t^2}{U}\sum_{<ij>}\left[\left(\frac{1}{2}+s_i^z\right)\left(\frac{1}{2}+s_j^z\right) + \left(\frac{1}{2}-s_i^z\right)\left(\frac{1}{2}-s_j^z\right) + s_i^+ s_j^- + s_i^- s_j^+ - 1\right], \\ &= \frac{J}{2}\sum_{<ij>}\left(\mathbf{S}_i\cdot\mathbf{S}_j - \frac{1}{4}\right), \end{aligned} \tag{1.66}$$

where we have defined $J = 4t^2/U$. If we neglect the final constant term, we have arrived at the nearest neighbour Heisenberg interaction. Further neighbour interactions are also possible, but require hopping pathways through a greater number of intermediate states. The exchange constant will therefore originate from a higher order of perturbation theory and consequently be much weaker. Although we have implicitly assumed only a single orbital per site in the above discussion, it can be easily generalised to multiple orbitals

per site. If however, the system is not exactly at half-filling the virtual hopping will be reduced as a result of Pauli blocking leading to a weaker interaction strength. Finally we note that the hopping matrix element may not necessary have the same value in all directions (especially for the case of non-spherically symmetrical orbitals) which will lead to an anisotropic Heisenberg interaction. We will now move on to consider other magnetic interactions, beginning with the crystal-field interaction.

The crystal-field interaction

In ionically bonded oxides the metal ions will often have an orbital degeneracy which will be lifted by various interactions. Hund's rules are one example, describing the effect of internal interactions within a single ion as we discussed earlier. Another possibility (which can be in competition with Hund's rules) is the crystal-field interaction. There is an electrostatic (Coulomb) repulsion between the valence electrons of the metal ion and the surrounding negatively charged O^{2-} ions. To minimises this energy the valence electrons of the metal ions can occupy the orbitals in the outer shell which have an average charge density that is as far as possible from the surrounding oxygen ions. In the case of the $4d$ and some of the $3d$ transition metals this effect can be strong enough to overturn Hund's rules. Although this is not the case for the f-block materials, the crystal-filed potential does lift the degeneracy of the $2J+1$ states which minimise Hund's third rule (except for the case of an exactly half-filled electron shell which has zero orbital angular momentum). This is because the orbitals with different l_z values will have a different spatial dependence far a given quantisation direction of the orbital angular momentum. In addition the spin-orbit interaction: $H_{SO} \propto \mathbf{L} \cdot \mathbf{S}$, couples the spin degree of freedom to the orbital angular momentum. The combination of the crystal-field interaction and spin-orbit coupling can then often be approximated by a single ion anisotropy term for each spin: $H = -D(\mathbf{S} \cdot \hat{\mathbf{z}})^2$, where '$\hat{\mathbf{z}}$' is the angular momentum quantisation direction (usually a symmetry axis of the crystal-field potential), and 'D' is a parameter describing the strength of the interaction.

Dipole interactions

Dipole interactions are present in all magnetic systems. They arise due to the magnetic field of one moment exerting a force on the other moments. The magnetic field at position '$\hat{\mathbf{r}}$' of a dipole moment '$\mathbf{m}_i$' centred on the origin is given by[42]

$$\mathbf{B} = \frac{-\mu_0}{4\pi}\left[\frac{\mathbf{m}_i - 3\hat{\mathbf{r}}\left(\mathbf{m}_i \cdot \hat{\mathbf{r}}\right)}{|\mathbf{r}|^3}\right], \tag{1.67}$$

where μ_0 is the permiativity of free space. The interaction between this moment and another moment '$\mathbf{m}_j$' is therefore given by

$$E_D = -\mathbf{m}_j \cdot \mathbf{B} = \frac{\mu_0}{4\pi}\left[\frac{\mathbf{m}_i \cdot \mathbf{m}_j - 3\left(\mathbf{m}_i \cdot \hat{\mathbf{r}}\right)\left(\mathbf{m}_j \cdot \hat{\mathbf{r}}\right)}{|\mathbf{r}|^3}\right], \tag{1.68}$$

where '$\mathbf{r}$' is the vector between the two dipoles. Summing over all moments in the system then gives the final form of

$$E_D = \frac{1}{2}\sum_{ij}\frac{\mu_0}{4\pi}\left[\frac{\mathbf{m}_i \cdot \mathbf{m}_j - 3\left(\mathbf{m}_i \cdot \hat{\mathbf{r}}\right)\left(\mathbf{m}_j \cdot \hat{\mathbf{r}}\right)}{|\mathbf{r}|^3}\right], \tag{1.69}$$

where the factor of one half prevents double counting in the summations. We note that by making use of the identity

$$\frac{\partial}{\partial \mathbf{x}}\left(\frac{1}{|\mathbf{x}|}\right) = -\frac{\mathbf{x}}{|\mathbf{x}|^3}, \tag{1.70}$$

we find the following alternative form of the dipole interaction:

$$E_D = -\frac{1}{2}\frac{\mu_0}{4\pi}\sum_{ij}\mathbf{m}_i \cdot \frac{\partial}{\partial \mathbf{x}}\,\mathbf{m}_j \cdot \frac{\partial}{\partial \mathbf{x}}\left(\frac{1}{|\mathbf{x}|}\right)\Big|_{\mathbf{x}=\mathbf{R}_i-\mathbf{R}_j}, \tag{1.71}$$

where '$\mathbf{R}_i$' denotes the position of the moment '$\mathbf{m}_i$'. In many magnetic systems the dipole interaction is much weaker than the Heisenberg exchange and can therefore safely be neglected. This is not always the case however, particularly for the systems that we will study. Firstly because we will be investigating the geometrically frustrated pyrochlore compounds. The dipole interaction is therefore instrumental lifting the degeneracy present

in the ground-state of the nearest neighbour Heisenberg interaction, as we will discuss in later chapters. In addition, the dipole interaction has a relatively strong interaction strength in lanthanide materials due to the large J values of the $4f$-moments. In the case of the spin-ice materials $Ho_2Ti_2O_7$ and $Dy_2Ti_2O_7$ (see Section 1.3.2).

The dipole interaction is rather more difficult to solve than the Heisenberg exchange interaction. Firstly because the interaction only decays as a power-law ($\propto 1/r^3$ where r is the distance between two moments) with increasing separation between magnetic moments. This means that accurately calculating the dipole energy of a system requires a long-range summation which is extremely taxing computationally. Secondly, the dipole interaction is highly anisotropic. This is because the interaction between two moments also depends on the direction of the lattice-vector joining the two moments. A consequence of this is that it can complicate finding classical equal-length spin solutions to the Hamiltonian. We address both of these issues in more detail in the next chapter.

Other magnetic interactions

There are many other magnetic effects which may play a part in determining the form of the ground-state which is stabilised. We will briefly mention three: quantum fluctuations, order from disorder and static disorder.

First we will consider quantum fluctuations. The quantum fluctuation energy of a system is defined as the difference between the total energy and the classical energy. We illustrate this for the simplest case of two spins interacting via Heisenberg exchange:

$$H = J\hat{\mathbf{S}}_1 \cdot \hat{\mathbf{S}}_2 = \frac{J}{2}\left[\left(\hat{\mathbf{S}}_1 + \hat{\mathbf{S}}_2\right)^2 - \left(\hat{\mathbf{S}}_1\right)^2 - \left(\hat{\mathbf{S}}_2\right)^2\right]. \tag{1.72}$$

The ground-state is the spin singlet with $\hat{\mathbf{S}}_1 + \hat{\mathbf{S}}_2 = \mathbf{0}$, which gives an energy of $E = -JS(S+1)$. The classical energy of the system is $E_{Cl} = -JS^2$ and therefore the quantum fluctuation energy is given by $E_Q = -JS$. For finite one-dimensional isotropic Heisenberg systems quantum fluctuations destroy long-range order[1]. This can also occur for certain

frustrated two-dimensional spin 1/2 Heisenberg systems[47]. More relevant to our work is the case when the classical ground-state manifold is degenerate (for example consisting of different multiple-**q** or single-**q** states). Quantum (or thermal) fluctuations prefer colinear (or sometimes coplaner) systems[44, 68]. This is because there are two (or one) transverse degrees of freedom to the ordering vector which can support coherent fluctuations without incurring an energy penalty from disrupting the classical magnetism. Quantum fluctuations will be discussed in more detail in Chapter 5 in the context of the material $Er_2Ti_2O_7$.

Order from disorder is another mechanism which has been proposed as a route to lifting a ground-state degeneracy[72]. In geometrically frustrated antiferromagnets the different ground-states are likely to have different excitation-spectra as the degeneracy is 'accidental' rather than resulting from a symmetry in of the Hamiltonian. This means that the system should favour on entropic grounds the states for which the low-energy excitations have the largest density of states [17]. Experimental systems which develop magnetic order through the order by disorder mechanism may however be very rare. It is likely that there will be other terms in the Hamiltonian, for example dipolar or longer-range Heisenberg interactions which will lift the ground-state degeneracy on energetic grounds.

Another mechanism which could stabilise one low energy state over another (for example different multiple-**q** states which all minimise the nearest neighbour Heisenberg interaction) is the presence of static disorder. In particular we are thinking of the substitution of non-magnetic ions for magnetic ions. This can stabilise a three-dimensional triple-**q** state over a colinear single-**q** state[46, 49]. Classically this is because it is energetically cheaper for the spins of the triple-**q** state to relax healing the 'defect' created in the local magnetic field caused by the non-magnetic impurity. This concludes our general discussion of various magnetic interactions. We will now move on to consider some specific examples of rare-earth pyrochlores and the magnetic behaviour that they display.

1.3 Rare Earth pyrochlores

In this section we will introduce the rare-earth pyrochlores in more detail, as this thesis will focus on studying the behaviour of a number of these materials. As mentioned previously they have the generic structure: $R_2M_2O_7$, where R represents a rare-earth ion and M represents a transition metal ion. There are a relatively large number of stable rare-earth pyrochlores[30]. We will focus on the compounds for which M is either Ti or Sn, and R is a rare-earth ion with an outer electron shell that is half filled or greater. This produces an insulating material, with local f-moments on the rare-earth sites[30]. These materials display a wide range of magnetic behaviors, examples of which are: long-range magnetically ordered phases; 'spin-ice' states; spin-glasses and spin-liquids. We will briefly introduce examples of these phenomenon in this section. First, however, we will describe the chemical structure of rare-earth pyrochlores.

1.3.1 Structure

As we discussed earlier, the pyrochlore lattice is formed of corner sharing tetrahedra and is specified by a face-centred-cubic lattice with four atoms per unit cell (see Fig. 1.10). The R_2M_2O7 structure is formed of two inter-penetrating pyrochlore lattices. This is depicted in Fig. 1.14, where the rare-earth ions are shown in black and the transition metal ions are shown in blue. The oxygen positions are slightly more complicated. There are two oxygen sites. One seventh of the oxygens lie at the first site, at the centre of the tetrahedra formed of four rare-earth ions. These sites are labeled by O1 in Fig. 1.14. The remaining six sevenths of the oxygens (labeled with O2 in Fig. 1.14) lie in the tetrahedra formed by two rare-earth ions and two transition metal ions. These oxygens however, do not lie in the centers of these tetrahedra. Instead they are shifted of centre by a distance of approximately a quarter of the length of the cube containing a tetrahedra. The result of this is that the O2 ions form octahedra around the transition metal ions[71]. the precise position of these oxygen atoms depends on the particular rare-earth atom present in the

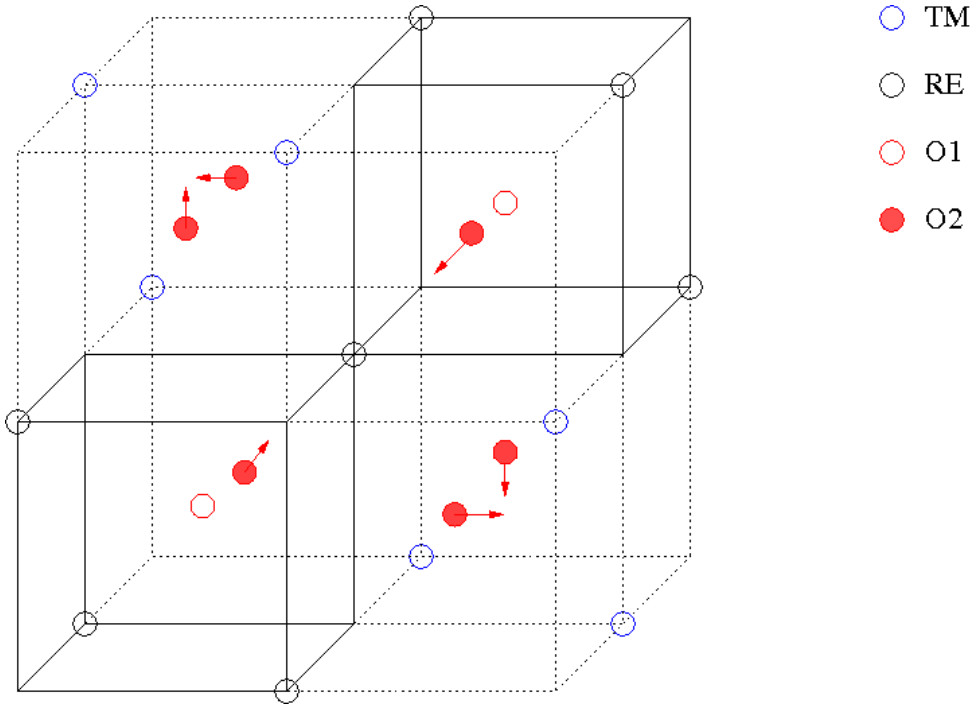

Figure 1.14: The chemical structure of $R_2M_2O_7$, with the rare-earth ions shown in black, the transition metal ions shown in blue and the oxygen ions shown in red. The oxygen ions labeled O1 lie in the centre of the rare-earth tetrahedra. The oxygen ions labeled O2 lie within the tetrahedra formed by two rare-earth ions and two transition metal ions. They are shifted off centre towards the two transition metal ions (in the directions indicated by the arrows).

system, although these differences are very small[71]. We will now go on to discuss the properties of some specific rare-earth pyrochlores.

1.3.2 Spin-ice materials

Currently the best known examples of rare-earth pyrochlores are the spin-ice materials. The most common examples are $Ho_2Ti_2O_7$ and $Dy_2Ti_2O_7$[30, 13]. The magnetic behaviour was first characterised by Harris *et. al*[35] for $Ho_2Ti_2O_7$. The crystal-field stabilises a ground-state doublet of states with $|m_j\rangle = |\pm J\rangle$. This produces a single-ion anisotropy (with an energy of about $50K$), that takes the form of an easy-axis along the local $\langle 1,1,1\rangle$ directions (i.e. the directions pointing into the centre of a tetrahedron) giving the spins an Ising character. $Ho_2Ti_2O_7$ has a Curie-Weiss temperature of $\theta_{CW} = 1.9K$, indicative of weak ferromagnetic correlations. The ferromagnetic correlations result from the dipole

interaction and when combined with the dominant crystal-field potential have been shown to stabilise the observed 'two-in-two-out' ground-state of spin-ice[23]. The state is known by this name because for each tetrahedron, two of the spins point towards the centre and the other two point away from the centre of the tetrahedron, as shown in Fig. 1.15 from Harris *et. al*[35]. This state was found to be consistent with diffuse neutron scattering and

Figure 1.15: An example of a 'two-in-two-out' state for a single tetrahedron from Bramwell *et. al*[35].

specific heat measurements by Bramwell *et. al*[12]. There are six possible ways to achieve a 'two-in-two-out' state for a single tetrahedron. Consequently, there are many different ways in which these six single-tetrahedron solutions can be combined to consistently cover the pyrochlore lattice, which gives rise to a macroscopic ground-state degeneracy. Muon spin resonance measurements find no transition to long-range magnetic order down to a temperature of $T = 0.05K$[35].

The residual degeneracy in the ground-state should give rise to a finite entropy as $T \mapsto 0$. This is known as the Pauling entropy by analogy to the equivalent phase of ice. The value of this entropy (which is also applicable to the spin-ice materials) was calculated by Pauling as: $S_P = \frac{R}{2}\ln(3/2)Jmol^{-1}K^{-1}$[61] and is compatible with that measured by Ramirez *et. al*[64] for $Dy_2Ti_2O_7$. A 'spin-freezing' transition between a paramagnetic Ising system and the two-in-two-out state occurs at a temperature of $T \sim 15K$[67]. The paramagnetic state is expected to have a magnetic entropy of $S = R\ln 2Jmol^{-1}K^{-1}$. Ramirez *et. al* measured the entropy change, ΔS, between $T = 12K$ and $T = 0.02K$ corresponding to the freezing of the spins into the two-in-two-out phase to be $\Delta S = (0.67 \pm 0.04)R\ln 2$. This gives a residual entropy of $S = 1.13S_P$ indicating that the ground-state does indeed display the expected degeneracy. Although no long-range order

is observed in $Dy_2Ti_2O_7$ down to a temperature of $T = 50mK$, the application of a magnetic field of around $0.8T$, parallel to one of the Cartesian directions can induce long-range order[26]. The field stabilises the $\mathbf{k} = 0$ structure in which every tetrahedron has the same spin state, with the ferromagnetic component aligned parallel to the applied field. More interesting though are the measurements on $Ho_2Ti_2O_7$ presented in the same paper by Fennell *et. al*[26]. They find that sweeping the magnetic field back and forth parallel to the $< 1, \bar{1}, 0 >$ direction induces short-range magnetic correlations indexed by $\mathbf{k} = (0, 0, 1)$. These coexist with ferromagnetism and indicate that antiferromagnetic correlations are being induced between the chains of spins which are uncoupled to the magnetic field. This could indicate that the energetic ground-state of spin-ice is actually a long-ranged ordered antiferromagnet (probably in order to minimise the long-range dipole interactions) and the fact that the low-energy observed state is the degenerate two-in-two-out state is due to the fact that the system is not in thermal equilibrium[52].

Finally, we note one aspect in particular of the behaviour of spin-ice which has recently generated a great deal of interest. This is the discovery that the low energy excitations produced by flipping a single spin in the two-in-two-out state can be very successfully modeled using effective magnetic monopoles [15, 11, 25]. As we will be focusing on the ground-state properties of rare-earth pyrochlores, however, we will not discuss this any further.

1.3.3 Long-range magnetically ordered phases

We will now consider examples of rare-earth pyrochlores for which long-range magnetic ordering has been observed. We will begin by introducing the materials $Gd_2Sn_2O_7$, $Gd_2Ti_2O_7$ and $Er_2Ti_2O_7$. As the low temperature behaviour of these three materials forms core content of this thesis, we will be returning to discuss them in much more detail later. Finally we will also briefly discuss the material $Tb_2Sn_2O_7$ for which long-range magnetic order has also been observed.

First we will consider $Gd_2Sn_2O_7$ and $Gd_2Ti_2O_7$. These two materials are of interest as

they have an identical electron structure but show rather different magnetic behaviour on cooling. As expected there are some similarities. Both have a Curie-Weiss temperature of $\theta_C W \sim 10K$ but only develop long-range magnetic order at temperatures of the order of $1K$[8]. This is consistent with the presence of strong antiferromagnetic interactions which are geometrically on the pyrochlore lattice. The Curie-Weiss data also indicates that for both materials the Gd^{3+} ions have magnetic moments close to the free-ion theoretical limit of $7.94\mu_B$ per ion[7]. Surprisingly, however, the nature of their magnetic ordering exhibits many differences. $Gd_2Sn_2O_7$ is the simpler of the two materials. There is a single transition at $T = 1.1K$[8] into a $\mathbf{k} = \mathbf{0}$ magnetically ordered state[75]. This state is believed to be stabilised by dipolar interactions in the presence of dominant antiferromagnetic exchange couplings[63, 60]. There is some confusion as to the exact mechanism, as we will discuss in the following chapter.

In contrast to the stanate compound, the behaviour of $Gd_2Ti_2O_7$ is more difficult to understand. The specific heat data shows that there are two different magnetically ordered phases stabilised. An intermediate phase exists for $0.7K < T < 0.97K$ and a low temperature phase of $T < 0.7K$[8]. Both phases are indexed by a wave-vector of $\mathbf{k} = (1/2, 1/2, 1/2)$[21]. There is some controversy over the structure of these ordered states. The elastic neutron scattering data has been fitted to an (almost) coplanar spin state for which one quarter of the spins remain disordered down to the lowest temperatures[69]. This description, however, is inconsistent with Mössbauer measurements by Bonville *et. al.* Their data indicates that all the spins order with essentially the full free ion moment and that they are orientated in the planes perpendicular to the local tetrahedral axes[8]. We discuss these issues in much more detail in Chapters 3 and 4, with the aim to resolve this controversy and also to understand the differences between the magnetic ordering of $Gd_2Ti_2O_7$ and $Gd_2Sn_2O_7$.

There is one final point which we wish to note about $Gd_2Ti_2O_7$. It has been suggested by Glazkov *et. al*[32] that the Gd^{3+} ions exhibit a strong single-ion anisotropy (with a strength comparable to that of the exchange coupling). This was investigated by using the

isostructural compound $Y_2Ti_2O_7$ and substituting $\sim 0.5\%$ of the Y^{3+} ions for Gd^{3+} (the crystal-lattice parameters of the two materials being very similar). Y^{3+} is a non-magnetic ion (having the same electron structure as a krypton atom). This allows the Gd^{3+} ions to be isolated from one another so that the Heisenberg exchange and dipolar interactions between Gd^{3+} ions become negligible. Electron paramagnetic resonance was then used to measure the crystal field splitting of the gadolinium energy levels. This was found to be consistent with a single-ion anisotropy term favouring spin orientations perpendicular to the local tetrahedral axes. This result is rather surprising because Gd^{3+} has a spherically symmetric $4f$-shell (as it is exactly half filled), so one would expect it to be isotropic. Independent studies of the material $Y_2Ti_2O_7$, however, have found an oxygen vacancy concentration of the order of 0.5% of the number of oxygen ions (and therefore considerably greater than the number of yttrium ions substituted for gadolinium)[33]. These vacancies are believed to be located in the tetrahedra formed by the yttrium ions (i.e. in the O1 position) and therefore do not form part of the TiO_6 octahedra. These oxygen vacancies are thought to give rise to a large ionic conductivity[33]. It therefore seems plausible that to relieve the strain on the crystal-lattice upon doing with the gadolinium ions the oxygen vacancies would preferentially occupy the O1 oxygen states which surround the Gd^{3+} ions (as Gd^{3+} has a greater ionic radius than Y^{3+}). If this is indeed the case then the single-ion anisotropy measured in this system would be unlikely to be representative of the true $Gd_2Ti_2O_7$ material. For this reason we choose not to consider a single-ion anisotropy term when we later discuss the energetics of $Gd_2Ti_2O_7$.

We will now move on to consider $Er_2Ti_2O_7$. As in the case of the gadolinium materials there are strong anti-ferromagnetic interactions (the Curie-Weiss temperature is $\theta_{CW} \sim 22K$[5]). The onset of long-range order is observed at $T = 1.2K$[5], an order of magnitude less than the Curie-Weiss temperature. Unlike the gadolinium materials, however, in $Er_2Ti_2O_7$ the crystal-field interaction also plays a key role and excited crystal-field levels have been observed at energies of $6.38meV$ and $7.39meV$[19]. The magnetically ordered state is indexed by the wave-vector $\mathbf{k} = \mathbf{0}$ and the Er^{3+} ions were found to have a

reduced moment of only $\sim 3\mu_B$ compared to the theoretically expected free ion moment of $9.59\mu_B$ per ion[19]. A magnetically ordered state in which the spins are orientated in the planes perpendicular to the local tetrahedral axes was proposed on the basis of a model consisting of antiferromagnetic Heisenberg exchange, dipolar couplings and an easy plane single-ion anisotropy, along with the data from the elastic neutron scattering experiments. As we discuss in Chapter 5, however, this proposed state does not actually appear to be consistent with all the neutron scattering data. It has been suggested on the basis of Monte Carlo simulations that this proposed state might be stabilised by quantum fluctuations[20]. There are also, however, a number of issues with this scenario. Firstly the simulations predict a first order transition into the magnetically ordered state, whereas it is in fact observed to be second order[19]. Secondly, the simulations predict a constant density of states as the energy, $\epsilon \mapsto 0$. This is not compatible with the observation that $C_v \propto T^3$[5]. In Chapter 5 we offer an alternative magnetically ordered state which is consistent with the neutron scattering data and then go on to consider how this state might be energetically stabilised. One final point of interest which we also discuss later is the observation of a gapless spin-wave mode in $Er_2Ti_2O_7$ by Ruff *et. al*[66].

The final compound showing long-range order that we consider is $Tb_2Ti_2O_7$. As in the case of the gadolinium pyrochlores, the Curie-Weiss data indicates that there are strong antiferromagnetic spin correlations ($\theta_{CW} \sim -12K$) and there is an observed effective moment of $9.8\mu_B$ per Tb^{3+} ion (which agrees well with the expected free ion moment of $9.72\mu_B$[7]. Diffuse neutron scattering experiments by Mirebeau *et. al* found that below $T = 2K$ the distribution of scattering intensity narrows and concentrates at low q-values which is indicative of the onset of ferromagnetic correlations[55].(The onset of the ferromagnetic correlations was initially suggested by Matsuhira *et. al* from low-temperature susceptibility measurements[53]). Then upon further cooling, at $T = 0.87K$ magnetic Bragg peaks appear at $\mathbf{q} = \mathbf{0}$. The ordered state is reminiscent of a long-range ordered version of the two-in-two-out spin-ice state. Instead of being aligned exactly along the the local tetrahedral axes, however, the spins are orientated at an angle of approximately

13° to these directions. The ferromagnetic component of all of the tetrahedra are aligned along one of the Cartesian directions. The ordered moment is found to be significantly reduced from the free-ion moment, having a value of $5.9\mu_B$ per ion[55]. This is believed to be a result of the crystal-field interaction. Surprisingly, however, the μ_{SR} spectra at temperatures above and below the ordering transition (measured at $T = 2.4K$ and $T = 0.17K$ respectively) can both be understood by assuming that there is no local-field present in the system, which would naively imply that there is no long-range order in the system[22]. The μ_{SR} data taken below the ordering temperature is consistent with spin-fluctuations on a time-scale of $\sim 10^{-10}s$. This was subsequently found to be compatible with further neutron scattering measurements by Mirebeau *et. al*[57] which found evidence of the coexistence of timescales of $10^{-9}s$ to $10^{-10}s$ with the long-range order.

1.3.4 Spin-glass and spin-liquid behaviour

Some of the rare-earth pyrochlores have been linked to more exotic magnetic behaviour, namely spin-glasses and spin-liquids. As these areas are rather outside the main focus of this thesis which is long-range order. We do not discuss these concepts in any detail therefore, but just give a very brief overview.

We will first consider spin-glasses. In these materials the spins "freeze" into a state with no (or negligible) dynamics, however, no long-range order is observed (i.e. there are no delta-function Bragg peaks observed in low-temperature neutron scattering experiments). The question as to whether a 'freezing transition' can actually occur at a non-zero temperature in a finite system is rather a subtle question[30]. Probably the simplest mechanism for spin-glass behaviour is when random disorder is introduced into a frustrated magnetically ordered system. This can be achieved by substituting diamagnetic atoms in the place of some of the paramagnetic ones. One example is the system $LiHo_xY_{1-x}F_4$[65]. For $x = 1$ the material is a ferromagnet in which the magnetic Ho^{3+} form Ising spins which are coupled via the dipole interaction. However, upon doping with the non-magnetic Y^{3+} ions at a concentration of $x \leq 0.2$ spin-glass behaviour has

been observed[65]. Though we will not discuss the details, the rare-earth pyrochlore materials $Yb_2Mo_2O_7$ and $Tb_2Mo_2O_7$ have been observed to show signatures of spin-glass behaviour[30].

Finally we will consider spin-liquid behaviour. This is the most dynamic (and therefore least ordered) phase that has been linked to the rare-earth pyrochlores. In a spin-liquid the moments continue to fluctuate down to the lowest temperatures experimentally accessible. The materials $Tb_2Ti_2O_7$, $Yb_2Ti_2O_7$ and $Er_2Sn_2O_7$ have all shown signs of spin-liquid behaviour, though further study is probably required[30]. We will discuss just $Tb_2Ti_2O_7$ in a little more detail.

For $Tb_2Ti_2O_7$, the magnetic susceptibility data is consistent with a Curie-Weiss temperature of $\theta_{CW} \sim -19K$ with the theoretically expected value of the free-ion magnetic moment down to temperatures of $T \sim 50K$ and from a crystal- field analysis the spins are believed to have an Ising character[31]. Short-range liquid-like correlations have been identified in diffuse neutron scattering data at $T = 2.4K$[29]. However, no long-range order has been observed in elastic neutron scattering data down to temperatures of at least $0.4K$, though there is evidence of the partial freezing of a small fraction of the spins (which maybe a result of the presence of defects in the sample)[76]. μ_{SR} measurements also indicate that the material remains paramagnetic down to temperatures of $70mK$[29]. Under the application of hydrostatic pressure, however, long-range order is stabilised, with the state indexed by the wave-vector $\mathbf{k} = (0, 0, 1)$. There are also Bragg spots seen at $\mathbf{k} = (1/4, 1/4, 1/4)$ which are suggested to be the result of a 'super-structure'[56]. This implies that in the absence of the applied field, the system is already energetically close to the long-range ordered state. However, no change in the crystal structure was observed upon application of hydrostatic pressure of up to $\sim 8GPa$ even though small magnetic Bragg spots appear at pressures of around $1.5GPa$. As a result this system merits further study, especially the origin of the magnetic Bragg spots attributed to a superstructure.

This concludes our introduction to the magnetic behaviour of a selection of the rare-earth pyrochlores. As we have seen a wide range of behaviour is observed in the various

materials. We will finish our introduction in the next section with an overview of the Bragg peak intensity measured by magnetic elastic neutron diffraction as this is a key tool in understanding the nature of the long-range magnetic order observed in the rare-earth pyrochlores.

1.4 Experimental Techniques

1.4.1 Elastic magnetic neutron scattering

In this thesis we will discuss (spin-only) elastic neutron scattering data in some detail. We will therefore discuss some of the basic principles, in particular a simple calculation of the magnetic Bragg peak intensities. Neutron scattering experiments are performed by measuring the energy and momentum change of neutrons which are scattered from a sample. We will only consider the elastic scattering from crystalline materials. At the most basic level, the neutrons can scatter coherently from the atoms in the crystal when they satisfy the Bragg condition[3]:

$$n\lambda = 2d\sin\theta, \tag{1.73}$$

where n is an integer, λ the wavelength of the neutron, d the separation between planes of atoms and θ is half the angle through which the neutron is deflected. An alternative way to express this condition is that coherent scattering occurs when the phase of the neutrons satisfy

$$e^{i(\mathbf{k}-\mathbf{k}')\cdot\mathbf{R}} = 1, \tag{1.74}$$

where $\mathbf{k}$ is the incident momentum, $\mathbf{k}'$ the outgoing momentum and $\mathbf{R}$ is a Bravais lattice vector. This means that when the momentum change, $\mathbf{k}-\mathbf{k}' = \mathbf{G}$, where $\mathbf{G}$ is a reciprocal-lattice vector we see a localised peak in the intensity of neutrons detected with this momentum change. This peak in k-space is usually referred to as a Bragg spot. By

observing the reciprocal-space locations of these peaks one can then infer the real-space structure of the sample.

In order to interpret the elastic scattering data we need to understand the scattering cross-section, $d\sigma/d\Omega$[50]. We describe the incident flux of neutrons traveling through a unit area in unit time by the variable 'N'. The number of neutrons scattered per unit time through an area element of solid angle '$d\Omega = \sin\theta d\theta d\phi$' is then given by:

$$N\left(\frac{d\sigma}{d\Omega}\right)d\Omega. \tag{1.75}$$

We assume that the interaction between the neutron and the target sample is weak so that the only change that takes place is a change in the direction of the wave-vector of the neutron. The energy of the neutron will remain constant; this is the condition for elastic scattering. To calculate the cross-section, we therefore need to know the probability of a transition ($W_{\mathbf{k}\mapsto\mathbf{k}'}$) from the incident plane-wave state, $\mathbf{k}$, of the neutron to a plane-wave state of wave-vector $\mathbf{k}'$, where both states have an energy $E = \hbar^2k^2/2m$. This is given by Fermi's Golden rule[41]

$$W_{\mathbf{k}\mapsto\mathbf{k}'} = \frac{2\pi}{\hbar}\left|\int d\ \mathbf{r}\psi^*_{\mathbf{k}'}\hat{V}\psi_{\mathbf{k}}\right|^2\rho_{\mathbf{k}'}, \tag{1.76}$$

where $\hat{V}$ is the interaction potential generated by the sample and $\rho_{\mathbf{k}'}(E)$ is the density of final states of the neutron. Somewhat arbitrarily, we fix the normalisation of the neutron wave-function, $\psi_{\mathbf{k}}$ by enclosing it in a box of side 'L', so that

$$\psi_{\mathbf{k}} = \frac{1}{L^{\frac{3}{2}}}e^{i\mathbf{k}\cdot\mathbf{r}}. \tag{1.77}$$

This allows us to obtain

$$\rho_{\mathbf{k}'}(E) = \left(\frac{L}{2\pi}\right)^3\frac{mk}{\hbar^2}d\Omega. \tag{1.78}$$

Finally, we also need to know the incident flux of neutrons which is given by

$$N = \frac{\hbar k}{mL^3}. \tag{1.79}$$

The cross-section is then given by

$$d\sigma = \frac{W_{\mathbf{k}\mapsto\mathbf{k}'}}{N} = L^6 \left(\frac{m}{2\pi\hbar^2}\right)^2 \left| \int d\ \mathbf{r}\psi^*_{\mathbf{k}'}\hat{V}\psi_{\mathbf{k}} \right|^2 d\Omega, \tag{1.80}$$

so that

$$\frac{d\sigma}{d\Omega} = \left| \langle \mathbf{k}' | \hat{V} | \mathbf{k} \rangle \right|^2, \tag{1.81}$$

where we have defined

$$2\pi\hbar^2 \langle \mathbf{k}' | \hat{V} | \mathbf{k} \rangle = \left(\frac{L^3 m}{2\pi\hbar^2}\right) \int d\mathbf{r}\ e^{-i\mathbf{k}'\cdot\mathbf{r}}\hat{V}e^{i\mathbf{k}\cdot\mathbf{r}}. \tag{1.82}$$

The next step is to consider the interaction potential. The magnetic field due to an electron is composed of two parts. The first is due to intrinsic spin of the electron, and is given by[42]

$$\mathbf{H}(\mathbf{R}) = \nabla \times \left(\frac{\mu_\mathbf{e} \times \mathbf{R}}{|\mathbf{R}|^3}\right), \tag{1.83}$$

where '$\mathbf{R}$' is the distance between the electron and the point of interest (for our purpose the neutron) and 'μ_e' is the magnetic moment of the electron and is given by

$$\mu_e = -2\mu_B \mathbf{s}_i, \tag{1.84}$$

where $\mathbf{s}_i$ is the spin of an electron at site $\mathbf{r}_i$. Similarly we define the magnetic moment of the neutron using

$$\mu = \gamma\mu_N\sigma, \tag{1.85}$$

where the gyro-magnetic ratio $\gamma = -1.91$. In general there is an additional component to the magnetic field, arising from the orbital angular momentum of the electron, however, we will assume this is zero and consider spin-only scattering. The interaction potential is then found by summing over the individual potentials from each electron in the lattice:

$$\hat{V} = -\sum_i \gamma\mu_N\sigma \cdot \mathbf{H} = 2\gamma\mu_N\mu_B \sum_i \sigma \cdot \left[\nabla \times \left(\frac{\mathbf{s}_i \times \mathbf{R}}{|\mathbf{R}|^3}\right)\right]. \tag{1.86}$$

Then using the identities

$$\frac{\mathbf{R}}{|\mathbf{R}|^3} = -\nabla\left(\frac{1}{\mathbf{R}}\right), \tag{1.87}$$

and

$$\frac{1}{\mathbf{R}} = \frac{1}{2\pi^2}\int d\mathbf{q}\ \frac{1}{q^2}e^{i\mathbf{q}\cdot\mathbf{R}}, \tag{1.88}$$

we find that

$$\nabla\times\left(\frac{\mathbf{s}_i\times\mathbf{R}}{|\mathbf{R}|^3}\right) = \frac{1}{2\pi^2}\int d\mathbf{q}\ \frac{1}{q^2}\left[\mathbf{q}\times(\mathbf{s_i}\times\mathbf{q})\right]e^{i\mathbf{q}\cdot\mathbf{R}}. \tag{1.89}$$

Using this result, and integrating twice, then provides us with the result:

$$\langle\mathbf{k}'|\,V\,|\mathbf{k}\rangle \propto \sum_i \sigma\cdot\left[\hat{\kappa}\times(\mathbf{s_i}\times\hat{\kappa})\right]e^{i\kappa\cdot\mathbf{r}_i}, \tag{1.90}$$

where we have defined the momentum transfer as $\mathbf{k}-\mathbf{k}'=\kappa$ and we have neglected the constant prefactor.

Next we assume that there is only one spin per site (though this might arise from a number of electrons) and consider the summation over the spins:

$$\sum_i \mathbf{S_i}e^{i\mathbf{k}\cdot\mathbf{r}_i}, \tag{1.91}$$

where we now use $\mathbf{k}$ instead of κ to represent the momentum transfer. We need to take into account that each spin should really be viewed as a finite region of spin density centered on site $\mathbf{r}_i$. We therefore use the mapping $\mathbf{r}_i \mapsto \mathbf{r}_i + \mathbf{r}'_{j(i)}$ where the vector $\mathbf{r}_{j(i)}$ ranges over the area of finite spin density around the site $\mathbf{r}_i$. Due to the periodicity of the lattice, the region of spin density around each atom is equivalent (with only the direction of the spin depending on the site index). We therefore use $\mathbf{S}_{\mathbf{r}_i+\mathbf{r}_{j(i)}} = \hat{\mathbf{S}}_{\mathbf{r}_i}S(\mathbf{r}'_j)$, where $\mathbf{S}_{\hat{r}_i}$ is a unit vector denoting the spin direction at site $\mathbf{r}_i$ and $S(\mathbf{r}'_j)$ is the spin density at position $\mathbf{r}'_j$. The summation then becomes

$$\sum_i e^{i\mathbf{k}\cdot\mathbf{r}_i}\hat{\mathbf{S}}_{\mathbf{r}_i}\sum_j e^{i\mathbf{k}\cdot\mathbf{r}'_j}S(\mathbf{r}'_j). \tag{1.92}$$

As the finite region of spin density is really continuous we let $\sum_j \mapsto \int \mathbf{d}^3\mathbf{r}'_j$ and let the integration limits extend to infinity which is equivalent to assuming the the spins are localised and therefore have a negligible (direct) overlap. As we will be considering f-shell electrons in this work, this assumption is not problematic. The summation has now become

$$\sum_i e^{i\mathbf{k}\cdot\mathbf{r}_i}\hat{\mathbf{S}}_{\mathbf{r}_i}\int \mathbf{d}^3\mathbf{r}'_j\ e^{i\mathbf{k}\cdot\mathbf{r}'_j}S(\mathbf{r}'_j), \tag{1.93}$$

and we notice that the integral is just the Fourier transform of the local spin density which we will represent using $f(\mathbf{k})$ and call the 'form factor'. The periodicity of the lattice means that $\hat{\mathbf{S}}_{\mathbf{r}_i+\mathbf{R}_i} = \hat{\mathbf{S}}_{\mathbf{r}_i}$, where we now use $\mathbf{R}_i$ to represent a lattice vector. Writing $\mathbf{r}_i = \mathbf{R}_i + \mathbf{c}_\alpha$ where $\mathbf{c}_\alpha$ describes the position of the atom within the unit cell, the summation finally becomes

$$\begin{aligned}
&\sum_\alpha\sum_j \mathbf{R}_i e^{i\mathbf{k}\cdot\mathbf{R}_i}e^{i\mathbf{k}\cdot\mathbf{c}_\alpha}\hat{\mathbf{S}}_\alpha f(\mathbf{k}) \\
&\quad = \frac{N}{N_0}\sum_\alpha e^{i\mathbf{k}\cdot\mathbf{r}_\alpha}\hat{\mathbf{S}}_\alpha f(\mathbf{k})\delta_{\mathbf{k},\mathbf{K}} \\
&\qquad = N\mathbf{S}_\mathbf{k} f(\mathbf{k})\delta_{\mathbf{k},\mathbf{K}},
\end{aligned} \tag{1.94}$$

where in the second line we use the fact that sum over lattice-lattice vectors averages to zero unless $\mathbf{k} = \mathbf{K}$, where $\mathbf{K}$ is a magnetic reciprocal lattice vector, N_0 represent the number of atoms in a unit cell and N the total number of atoms and finally we have defined the structure factor using

$$\mathbf{S}_\mathbf{k} = \frac{1}{N_0}\sum_\alpha e^{i\mathbf{k}\cdot\mathbf{r}_\alpha}\hat{\mathbf{S}}_\alpha. \tag{1.95}$$

Combining our results we now find that the scattering cross-section is given by

$$\frac{d\sigma}{d\Omega} \propto |f(\mathbf{k})|^2 \left|\hat{\mathbf{k}}\times\left(\mathbf{S}_\mathbf{k}\times\hat{\mathbf{k}}\right)\right|^2 \delta_{\mathbf{k},\mathbf{K}}, \tag{1.96}$$

where, since we will only consider unpolarised scattering, we assume that all possible

direction of the neutron magnetic moment are averaged over. This leads us to our final result. If we count the number of neutrons scattering through a small area of solid angle at a position corresponding to a momentum transfer of $\mathbf{k} = \mathbf{K}$, then the intensity of the beam will be given by

$$\begin{aligned} I(\mathbf{k}) &\propto |f(\mathbf{k})|^2 \left|\hat{\mathbf{k}} \times \left(\mathbf{S}_\mathbf{k} \times \hat{\mathbf{k}}\right)\right|^2 \\ &= |f(\mathbf{k})|^2 \left|\hat{\mathbf{k}} \times \mathbf{S}_\mathbf{k}\right|^2 \\ &= |f(\mathbf{k})|^2 \left[|\mathbf{S}_\mathbf{k}|^2 - \left|\hat{\mathbf{k}} \cdot \mathbf{S}_\mathbf{k}\right|^2\right]. \end{aligned} \tag{1.97}$$

The above expression for the Bragg peak intensities depends on three quantities. The first of these is the form factor, $f(\mathbf{k})$. This describes the Fourier transform of the real-space decay of the spin density. Many materials will contain different types of magnetic ion (for which the spin-density will have different spatial dependencies). The form factor can be used to determine which Bragg peaks are associated with which type of magnetic ion. For example, f-block moments are much more localised than d-block moments in real space. This means that in reciprocal space, the intensities of the f-block Bragg peaks will decay much more slowly as a function of 'k' than the intensities of the d-block Bragg peaks. In the rare earth pyrochlores that we will consider there is only one species of magnetic ion (the rare earth ion), however, so the main role of the form factor will be in quantitatively determining the relative Bragg peak intensities. The second quantity that appears in Equation 1.97 is the structure factor, $\mathbf{S}_\mathbf{k}$. Due to the periodicity of the magnetic ordering, there are usually only a small number of distinct magnetic structure factors. For powder samples, the Bragg peaks which all lie the same reciprocal distance 'k' from the origin are averaged over. This further reduces the information available from the magnetic structure factors. For example, as we will see in Chapter 4, for $Gd_2Ti_2O_7$ there are only sixteen unique magnetic structure factors. Four of these lie in the 'shell' closest to the origin (and all turn out to vanish). The remaining twelve also all lie at the same distance as each other from the origin (in the second shell) and are therefore averaged over in a powder spectrum

so that relatively little information about the magnetic structure is available from them. Finally, the third quantity in Equation 1.97 is the orientational factor, $\hat{\mathbf{k}} \cdot \mathbf{S}_{\mathbf{k}}$. The effect of the orientational factor is that magnetic Bragg peaks are only visible when the relevant momentum transfer 'k' is perpendicular to the structure factor. The orientational factors therefore provide the most information about the magnetic structure, though they can be difficult to interpret especially for a powder spectrum. One useful piece of information, however, is available from the Bragg peak with the weakest intensity (after form factor and structure factor contributions have been accounted for). As the orientational factor is responsible for the reduced intensity, it is likely that the structure factor is approximately parallel to the momentum transfer of this Bragg spot. In later chapters we will discuss the powder diffraction spectrum of $Gd_2Ti_2O_7$ and the single crystal scattering data of $Er_2Ti_2O_7$ in some detail.

CHAPTER 2

GADOLINIUM STANNATE (EXACT SOLUTIONS TO THE LONG-RANGE DIPOLE INTERACTION IN THE PRESENCE OF DOMINANT ANTIFERROMAGNETIC NEAREST NEIGHBOUR EXCHANGE AND AN EXTERNAL FIELD ON THE PYROCHLORE LATTICE).

2.1 Introduction

In this chapter we will study the properties of the dipolar interaction on the pyrochlore lattice. Dipole interactions are present in all magnetic systems. For the case of electronic spins, the Heisenberg exchange and crystal-field interactions are usually dominant and sufficient to describe the low temperature behaviour of classical magnets, rendering the effects of the dipolar interaction negligible. For the pyrochlore lattice, however, this is not the case. As was discussed in Section 1.2.2 , the nearest neighbour antiferromagnetic exchange interaction is geometrically frustrated on the pyrochlore lattice. This results in a macroscopic ground-state degeneracy, with one degree of freedom per tetrahedron, which will be lifted by other weaker interactions. An estimate of the interaction strength of Heisenberg exchange can be found from the Curie-Weiss temperature (θ_C). When normal systems are cooled down to the Curie-Weiss temperature, they are therefore expected to begin to develop long-range magnetic order. In systems for which the dominant interaction

is frustrated, however, the temperature at which long-range order begins to develop (T_N) is suppressed to the energy scale of the weaker interaction which actually lifts the residual degeneracy.

The pyrochlore compound $Gd_2Sn_2O_7$ shows precisely the behaviour described above. It is believed to be a model system for investigating the classical magnetic ordering driven by the dipole interaction. In the next section we therefore discuss the experimental evidence supporting this. There is some confusion in the literature over how the magnetically ordered ground-state of $Gd_2Sn_2O_7$ is energetically stabilised. We therefore also discuss some of the existing theoretical calculations on this topic. In particular, it was initially proposed that the minimum energy of the dipolar interaction matrix was degenerate along the line $\mathbf{k} = (q, q, q)$ in reciprocal space[63], and that the experimentally observed $\mathbf{k} = \mathbf{0}$ ground-state of $Gd_2Sn_2O_7$[75] is stabilised via an order from disorder mechanism[60]. Later calculations, however[43] find that dipolar interaction matrix actually has a unique minimum at $\mathbf{k} = (1/2, 1/2, 1/2)$ but the corresponding eigenvectors are incompatible with classical (equal-length spins) solutions. Instead it appears that the $\mathbf{k} = \mathbf{0}$ observed ground-state is the minimum energy state which is also compatible with classical spin constraints despite the fact that it does not coincide with the global minimum of the dipole interaction matrix. As this is not unusual for anisotropic spin systems, we then make a brief analogy to the simpler one dimensional Ising model.

We will then go on to consider the long-range dipolar problem on the pyrochlore lattice with a dominant antiferromagnetic Heisenberg exchange in the presence of an external magnetic field. We assume that the system remains with the $\mathbf{k} = \mathbf{0}$ subspace despite the presence of the external field and derive a real space approach to finding the ground-state solutions. This involves expressing the interactions in terms of the squares of ten natural variables. This formulation provides some physical insight into the states that are stabilised by the dipole interaction. This method also allows us find exact solutions to the problem for a set of special external field directions, which are highly symmetric (although for general field directions the problem is over constrained). As a result we also

discuss the possible observable phase transitions if the field takes these special orientations. Finally we also highlight a link between the dipole interaction and the intensity of elastic neutron scattering Bragg peaks which becomes evident during the investigation of the dipole interaction.

2.2 Experimentally observed properties of gadolinium stannate

The pyrochlore $Gd_2Sn_2O_7$ is believed to be an excellent material for studying the dipolar interaction. In this section, we will therefore summarise some of the experimentally observed properties of $Gd_2Sn_2O_7$, with a particular focus on the low temperature magnetic ordering.

As discussed in Section 1.2.3 only the Gd^{3+} ions have a non-zero magnetic moment. From Hund's rule's we find that $S = \frac{7}{2}, L = 0, J = \frac{7}{2}$, corresponding to an expected observed moment of $m = L + g_0 S \approx 7\mu_B$, where the electronic g-factor is given by $g_0 \approx 2$. The exactly half-filled $4f$-shell produces a spherically symmetric charge distribution, so that Gd^{3+} ions are isotropic and have no interaction with the crystal-field. The dominant interaction, therefore, is nearest neighbour Heisenberg exchange. Susceptibility measurements find a Curie-Weiss temperature of $\theta_C = -8.6K$[8], indicative of antiferromagnetic interactions. Using a simple mean-field estimate[40], this Curie-Weiss temperature corresponds to an exchange constant of:

$$\frac{|J_{\mathrm{Ex}}|}{k_B} \approx \frac{3\theta_C}{z} = 4.3K, \tag{2.1}$$

where nearest neighbour coordination number is given by $z = 6$ for the pyrochlore lattice. Low temperature specific heat measurements by Bonville *et al.* are shown in Fig. 2.1. There is a single singularity at $T_N = 1.015K$ which has been associated with the long-range magnetic ordering of the Gd^{3+} ions. As expected for a geometrically frustrated

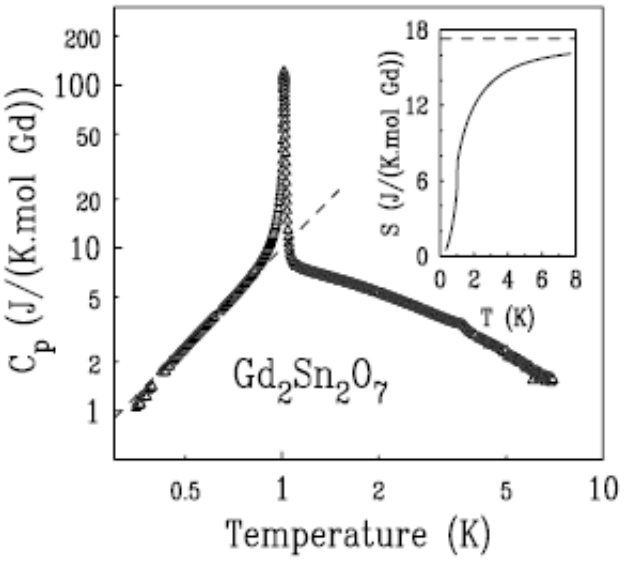

Figure 2.1: Specific heat and entropy (inset) variation with temperature for $Gd_2Sn_2O_7$ from Bonville *et. al*[8]

system, the magnetic ordering occurs at a temperature which is an order of magnitude lower than the Curie-Weiss temperature. The energy scale at which dipole-interactions become active can be estimated using:

$$\frac{|J_D|}{k_B} \approx \frac{\mu_0 g^2 S(S+1)}{4\pi r^3} = 0.84K, \tag{2.2}$$

where for Gd^{3+}, $S = 7/2$, and we use $r = a/2\sqrt{2}$ with $a = 10.184\mathring{A}$[63], indicating that the dipole interaction is instrumental in driving the magnetic ordering. As it is usual that $J_2 \ll J_1$ it appears safe to neglect the effects of further neighbour Heisenberg interactions, although we will return to this point in the next chapter. We will therefore investigate the behaviour of the dipolar interaction in the presence of a dominant nearest neighbour Heisenberg exchange on the pyrochlore lattice.

Elastic neutron scattering experiments by Wills *et al.*[75] show that the magnetically ordered state is indexed by the propagation vector $\mathbf{k} = \mathbf{0}$. Gadolinium stannate has a face centered cubic lattice with a basis of four Gd^{3+} ions per unit cell, which form a tetrahedron. A $\mathbf{k} = \mathbf{0}$ state can therefore be specified by defining the orientations of the four Gd^{3+} spins forming a single tetrahedron, and then translating this tetrahedron throughout the

lattice. The intensity of the observed Bragg spots has been fitted extremely well to a state where the spins in every tetrahedron form a planar spiral as shown in Fig. 2.2 from Wills *et. al*[75]. There are three degenerate states for which the axis of the spiral is parallel to

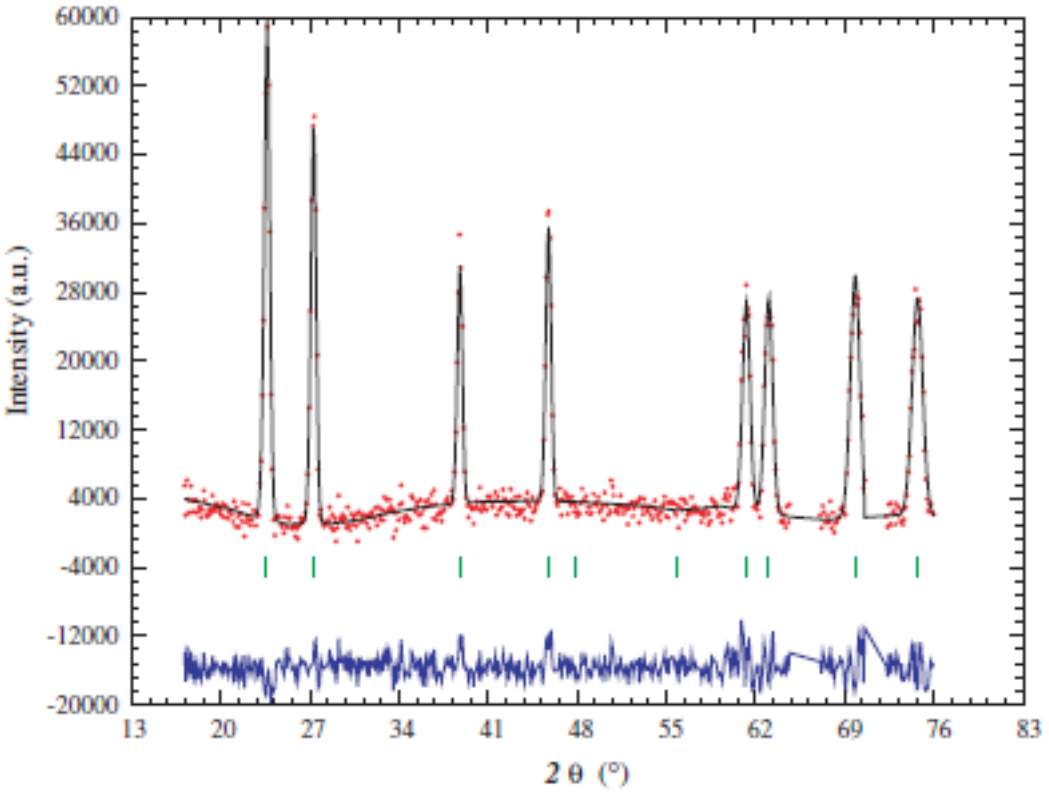

Figure 2.2: Fit to the powder magnetic neutron diffraction data reproduced from the paper by Wills *et. al*[75]. Red points: experimental data obtained by subtracting the measured intensity in the paramagnetic phase ($T = 1.4K$) from that in the magnetically ordered phase ($T = 0.1K$) in order to isolate the magnetic scattering intensity. Black line: fit to the $\mathbf{k} = \mathbf{0}$ spiral states shown in Fig. 2.3. Blue line: difference between the calculated Bragg peak intensities (black line) and the experimentally measured data.

one of the three Cartesian directions as is shown in Fig. 2.3. (In addition there are also the chirally related domains obtained by inverting all of the spins). We show an example of one of these states in Fig 2.4 in which we have highlighted half of the tetrahedra in green to make the spirals easier to spot.

Finally we will briefly discuss the Mössbauer experiments[54, 74] , also by Bonville *et al.*[8]. The data shows an excellent fit if it is assumed that all spins have the same magnitude and are orientated in planes that are perpendicular to the local tetrahedral

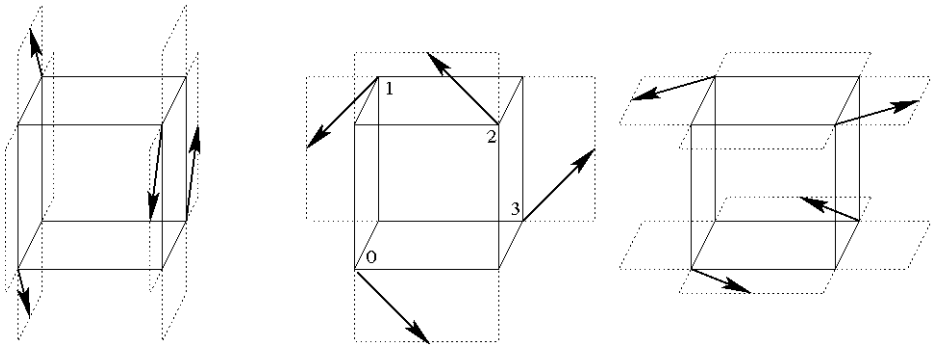

Figure 2.3: The three spiral states shown for a single tetrahedron

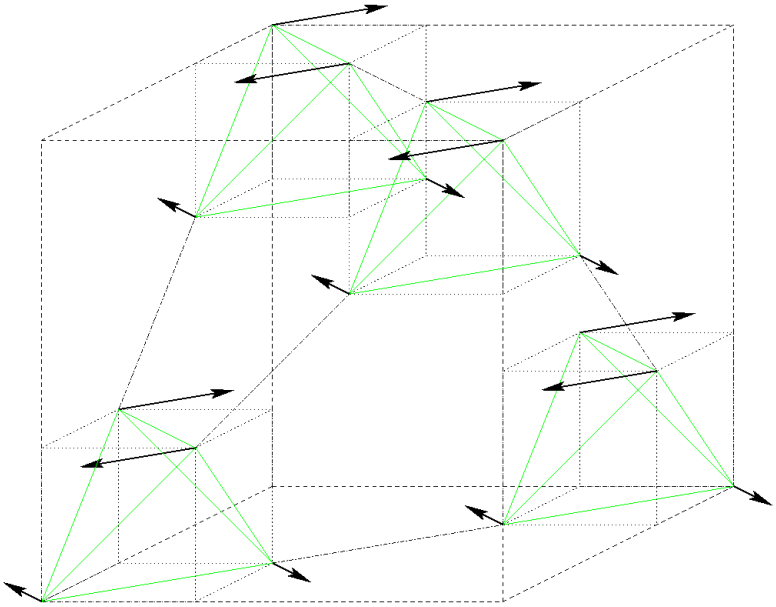

Figure 2.4: The $\mathbf{k} = \mathbf{0}$ 'spiral' ground-state of $Gd_2Sn_2O_7$. Half of the tetrahedra have been highlighted in green in order to make the spirals stand out (in this case with the axis parallel to the Cartesian z-axis).

axes (which are specified by: $\langle 1,1,1\rangle$, $\langle 1,-1,-1\rangle$, $\langle -1,1,-1\rangle$ and $\langle -1,-1,1\rangle$). The spins depicted in the three spiral states above are indeed orientated in these planes and are therefore consistent with this observation. As the sample is cooled below $T \approx 0.8K$, the magnitude of the Gd^{3+} moments is seen to saturate at the classically expected value of $m = 7\mu_B$ per spin (see Fig. 2.5). This reinforces the idea that gadolinium stannate can be modeled as a classical magnet, and that quantum fluctuations do not play a significant role.

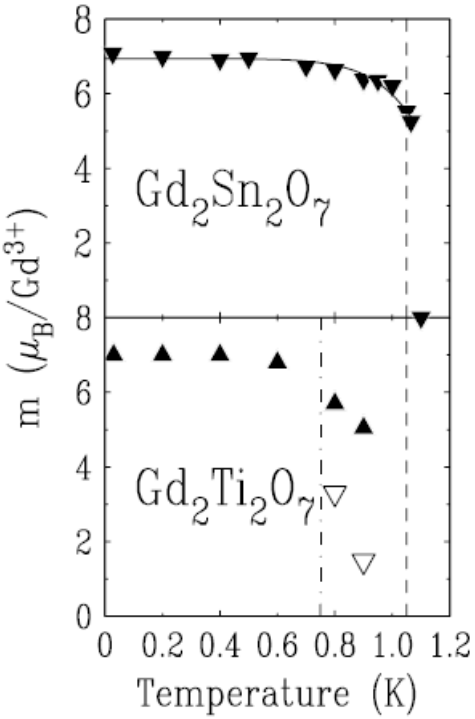

Figure 2.5: Temperature dependence of the Gd^{3+} moments in $Gd_2Sn_2O_2$(top) and $Gd_2Ti_2O_7$(bottom) from ^{155}Gd Mössbauer measurements by Bonville *et. al*[8]. See the end of Section 3.2 for a discussion of the $Gd_2Ti_2O_7$ data.

2.3 Theoretical Background

2.3.1 Previous numerical work

We will now briefly discuss a few of the previous theoretical studies of the dipolar interaction, which had a particular focus of gadolinium stannate. The first paper we will consider is by Raju *et al.*[63]. They calculate the spin-spin interaction matrix for the nearest neighbour antiferromagnetic Heisenberg exchange and (long-range) dipolar interactions. As there are four atoms per unit cell, the space is of dimensions: $\mathcal{D}_S \otimes \mathcal{D}_{sl}$, where $\mathcal{D}_S = 3$ is the dimension of the spin-component subspace and $\mathcal{D}_{sl} = 4$ denotes the sub-lattice degree of freedom, which gives a 12×12 matrix. This was calculated by summing the dipolar interaction (in real space) up to the 500th neighbour. After transforming to reciprocal space, the minimum eigenvalue of the matrix was calculated. A plot from Raju *et al.* of a slice through k-space of the modulus of this eigenvalue is shown in

Fig. 2.6[63]. The interaction matrix appears to be minimum along the degenerate lines

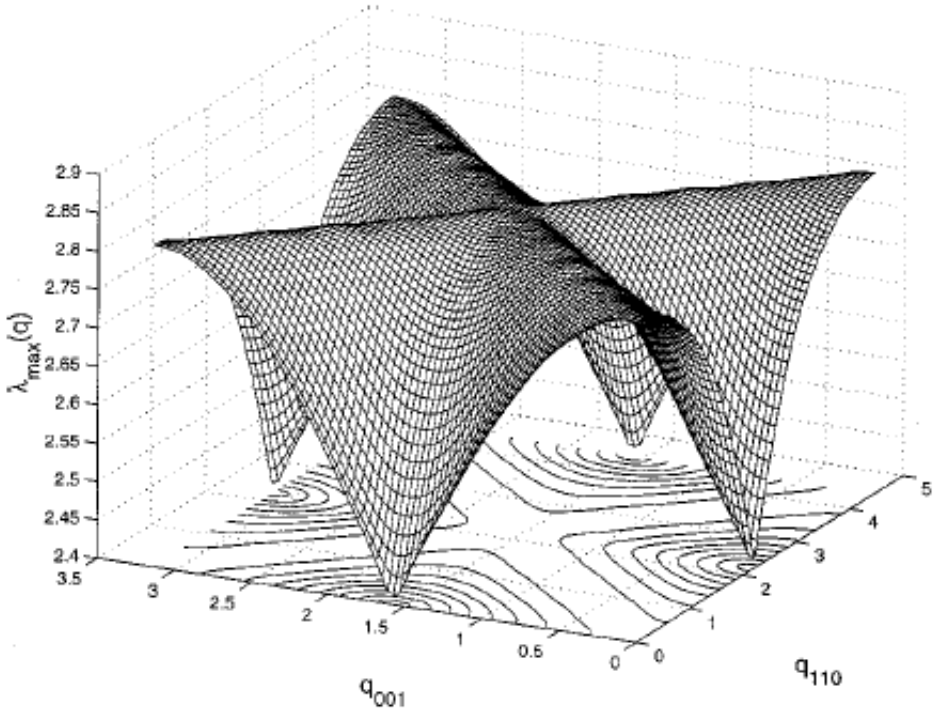

Figure 2.6: Plot of the wave-vector dependence of the modulus of the minimum energy eigenvalue of the dipole interaction matrix with dominant nearest neighbour Heisenberg interaction on the pyrochlore lattice calculated by Raju *et. al*[63]. The faint ripples along the (111) and $(11\bar{1})$ directions are attributed to truncating the dipolar sum after a finite number (500) of nearest neighbours.

of $\mathbf{k} \propto (1,1,1), (1,\bar{1},\bar{1}), (\bar{1},1,\bar{1})$ and $(\bar{1},\bar{1},1)$. The faint ripples that can be seen along these directions are attributed to truncation of the dipolar sum. Subsequent order from disorder calculations[60] based on this degeneracy conclude that there is a fluctuation induced transition at $T \approx 1K$ to the $\mathbf{k} = \mathbf{0}$ magnetically ordered state depicted above in Fig 2.4. Finally we will consider Monte Carlo calculations by Cépas *et al.*[16]. They simulate the nearest neighbour antiferromagnetic Heisenberg exchange with long-range dipolar interactions for classical spins on the pyrochlore lattice, considering periodic systems of up to $N = 4^5$ spins. The simulations are interpreted by calculating two order parameters, which evaluate the 'overlap' with two different magnetically ordered states. The two states that they focus on lie on the apparently degenerate $\mathbf{k} \propto (1,1,1)$ line. The first is the $\mathbf{k} = \mathbf{0}$ state, and the second is a $\mathbf{k} = (1/2, 1/2, 1/2)$ state which we will discuss later

in Section 3.2. They find that for temperatures below about $0.7K$ the order-parameter for the $\mathbf{k} = \mathbf{0}$ state rapidly increases by about two orders of magnitude, whereas the order-parameter for the $\mathbf{k} = (1/2, 1/2, 1/2)$ state plummets to zero and conclude that the system magnetically orders in the $\mathbf{k} = \mathbf{0}$ state that is observed in $Gd_2Sn_2O_7$. This supports the idea that the low temperature energetics of gadolinium stanate is governed by nearest neighbour exchange and dipolar couplings.

2.3.2 Using Sub-band representation to minimise the dipolar structure factor

Precise dipolar calculations can require lengthy computations in order to do the long-range summations required. Preforming the calculation for a pyrochlore lattice in real space also requires the summation to be done twelve times (as mentioned in the previous section) due to the four sub-lattice degrees of freedom. However, instead of using the sub-lattice-representation, we can use the alternative sub-band representation which we will discuss in this section. Although using sub-lattice representation is the simplest way of understanding the real-space spin orientations, sub-band representation has other advantages. These will be discussed later in this section, but one is that using the sub-band representation halves the number of summations over the lattice required, which in turn allows calculations to be carried out to a greater precision in a reasonable time-frame.

Sub-band representation is used to describe systems with multiple atoms per unit cell. It is only applicable to crystal structures in which all atoms lie at positions which are commensurate with the underlying lattice. Extra lattice sites can then be added to form a finer periodic array for which every atom lies on a lattice site of this new 'super-lattice'. For the pyrochlore lattice this is achieved by including the position of the tin atoms as lattice sites (even though we will then later treat them as having zero magnetic moment), which gives rise to a face-centre-cubic lattice with a standard unit cell volume of one eighth of the unit cell of the original lattice. The structure factors (defined by Equation 1.95) specified at points related by reciprocal super-lattice vectors are all identical. In sub-band

representation, the spin-structure is described using the non-equivalent reciprocal-space spin densities (i.e. the non-equivalent structure factors of the original (large-scale) face-centre-cubic lattice).

To express the dipole energy of the system using sub-band representation we start from the expression given in Equation 1.71:

$$E_D = -\frac{\mu}{2}\sum_{jj'}\mathbf{S}_j \cdot \frac{\partial}{\partial \mathbf{X}}\mathbf{S}_{j'} \cdot \frac{\partial}{\partial \mathbf{X}}\, V\left(|\mathbf{x}|\right)\big|_{\mathbf{x}=\mathbf{R}_j-\mathbf{R}_{j'}}, \tag{2.3}$$

where $\mathbf{R}_j$ ranges over the face-centre-cubic super-lattice so that we have at present included the gadolinium and tin atoms in the summation on an equal footing. The potential is given by

$$V\left(X\right) = \frac{1}{X} \tag{2.4}$$

for all lattice vectors, except that $V(X) \mapsto 0$ as $X \mapsto 0$, including sufficient spatial derivatives to ensure that there is no self-interaction contribution, and $\mu = \frac{\mu_0}{4\pi}$. We then apply a Bloch transform, again using the periodicity of the super-lattice and with $\mathbf{k}$ ranging over the associated Brillouin zone:

$$\begin{aligned} \tilde{\mathbf{S}}_{\mathbf{k}} &= \frac{1}{\sqrt{N}}\sum_j e^{i\mathbf{k}\cdot\mathbf{R}_j}\mathbf{S}_j \\ \mathbf{S}_j &= \frac{1}{\sqrt{N}}\sum_{\mathbf{k}} e^{-i\mathbf{k}\cdot\mathbf{R}_j}\tilde{\mathbf{S}}_{\mathbf{k}}. \end{aligned} \tag{2.5}$$

We can then transform the expression for the dipole energy into reciprocal space. This is described in Appendix A and provides:

$$E_D = \sum_{\mathbf{k}} \mathbf{S}^*_{\mathbf{k}} \cdot \mathbf{M}_{D\mathbf{k}} \cdot \mathbf{S}_{\mathbf{k}}, \tag{2.6}$$

where the 3×3 matrix controlling the energetics is given by:

$$M^{\alpha\beta}_{D\mathbf{k}} = \frac{1}{2\mathcal{V}(\Omega)}\sum_i (\mathbf{k}+\mathbf{G}_i)^\alpha (\mathbf{k}+\mathbf{G}_i)^\beta \tilde{V}(|\mathbf{k}+\mathbf{G}_i|), \tag{2.7}$$

where $\mathbf{G}_i$ ranges over the reciprocal super-lattice. This matrix can then be calculated for each $\mathbf{k}$ value in the Brillouin zone. At present, however, we are still treating the gadolinium and tin ions as equivalent.

We wish to enforce zero moment on the tin ions, so that we are just considering the spins on the tin sites. We therefore need to return to the original periodicity of the pyrochlore lattice. There are eight $\mathbf{k}$ values that quotient out the pyrochlore reciprocal lattice from the current reciprocal super-lattice, which we will label as:

$$\begin{aligned} &\mathbf{Q}_0 = (0,0,0), \qquad \mathbf{Q}_1 = (2,0,0), \qquad \mathbf{Q}_2 = (0,2,0), \qquad \mathbf{Q}_3 = (0,0,2), \\ &\mathbf{K}_0 = (1,1,1), \qquad \mathbf{K}_1 = (1,\bar{1},\bar{1}), \qquad K_2 = (\bar{1},1,\bar{1}), \qquad \mathbf{K}_3 = (\bar{1},\bar{1},1). \end{aligned} \tag{2.8}$$

The expression for the dipole energy then becomes

$$E_D = \sum_{\mathbf{k}} \sum_{m} \left[\mathbf{S}^*_{\mathbf{k}+\mathbf{Q}_m} \cdot \mathbf{M}_{D\mathbf{k}+\mathbf{Q}_m} \cdot \mathbf{S}_{\mathbf{k}+\mathbf{Q}_m} + \mathbf{S}^*_{\mathbf{k}+\mathbf{K}_m} \cdot \mathbf{M}_{D\mathbf{k}+\mathbf{K}_m} \cdot \mathbf{S}_{\mathbf{k}+\mathbf{K}_m} \right], \tag{2.9}$$

where $m \in \{0,1,2,3\}$. We can see that the degrees of freedom are now the Bragg spot structure factors. As these are quantities which are experimentally accessible via neutron scattering experiments it can be useful to use a representation in which they are transparent. If the tin atoms have zero moment then the following four linear relationships between structure factors hold (this is explained later in more detail in Section 5.3:

$$\begin{aligned} \mathbf{S}_{\mathbf{k}+\mathbf{K}_0} &= \frac{1}{2}\left[-\mathbf{S}_{\mathbf{k}+\mathbf{Q}_0} + \mathbf{S}_{\mathbf{k}+\mathbf{Q}_1} + \mathbf{S}_{\mathbf{k}+\mathbf{Q}_2} + \mathbf{S}_{\mathbf{k}+\mathbf{Q}_3}\right] \\ \mathbf{S}_{\mathbf{k}+\mathbf{K}_1} &= \frac{1}{2}\left[+\mathbf{S}_{\mathbf{k}+\mathbf{Q}_0} - \mathbf{S}_{\mathbf{k}+\mathbf{Q}_1} + \mathbf{S}_{\mathbf{k}+\mathbf{Q}_2} + \mathbf{S}_{\mathbf{k}+\mathbf{Q}_3}\right] \\ \mathbf{S}_{\mathbf{k}+\mathbf{K}_2} &= \frac{1}{2}\left[+\mathbf{S}_{\mathbf{k}+\mathbf{Q}_0} + \mathbf{S}_{\mathbf{k}+\mathbf{Q}_1} - \mathbf{S}_{\mathbf{k}+\mathbf{Q}_2} + \mathbf{S}_{\mathbf{k}+\mathbf{Q}_3}\right] \\ \mathbf{S}_{\mathbf{k}+\mathbf{K}_3} &= \frac{1}{2}\left[+\mathbf{S}_{\mathbf{k}+\mathbf{Q}_0} + \mathbf{S}_{\mathbf{k}+\mathbf{Q}_1} + \mathbf{S}_{\mathbf{k}+\mathbf{Q}_2} - \mathbf{S}_{\mathbf{k}+\mathbf{Q}_3}\right]. \end{aligned} \tag{2.10}$$

Finally, to provide the sub-band representation for the dipole energy of a pyrochlore, we substitute these expressions for $\mathbf{K}_m$ into Equation 2.9. This now generates cross terms

between the $\mathbf{S}_{\mathbf{k}+\mathbf{Q}_m}$'s giving a 12×12 interaction matrix. To calculate this interaction matrix it is necessary to perform the long-range summation for each element of eight 3×3 matrices in Equation 2.9 (which can then be 'slotted' together to form the required 12×12). This is, however, only half the work required to calculate each element of the 12×12 matrix individually, as is required if one works in sub-lattice representation. Finally, for completeness, we note that we can recover the more usual sub-lattice representation of the interaction matrix by using the unitary transformation:

$$\mathbf{U} = \begin{bmatrix} 1 & 1 & 1 & 1 \\ 1 & 1 & -1 & -1 \\ 1 & -1 & 1 & -1 \\ 1 & -1 & -1 & 1 \end{bmatrix} \tag{2.11}$$

The interaction matrix for long-range dipolar couplings in the presence of a dominant antiferromagnetic nearest neighbour Heisenberg exchange on the pyrochlore lattice was calculated by M.W. Long[43] using Ewald summations in sub-band representation. Ewald techniques involve splitting the summation into both a real-space and a reciprocal-space part in order to simultaneously capture the short-range and long-range behaviour of the interactions as accurately as possible. The calculated dispersion of the minimum eigenvalue of the interaction matrix is shown in Fig. 2.7[43], for three slices through k-space.

In particular the $\mathbf{k} = (q, q, q)$ direction which was found by Raju *et al.*[63] to be degenerate is shown, in addition to two other highly symmetrical directions: $\mathbf{k} = (q, 0, 0)$ and $\mathbf{k} = (q, q, 0)$. As was seen in the calculations by Raju *et al.* the dispersions along the $\mathbf{k} = (q, 0, 0)$ and $\mathbf{k} = (q, q, 0)$ directions are huge compared to that along the $\mathbf{k} = (q, q, q)$ direction. However, in contrast to the calculations by Raju *et al.*, Long does find a small dispersion along the $\mathbf{k} = (q, q, q)$, with a clear minimum at $\mathbf{k} = (1/2, 1/2, 1/2)$. One might think that the system should therefore automatically order at this wave-vector. However, we are interested in the solution to the classical problem which gives rise to additional

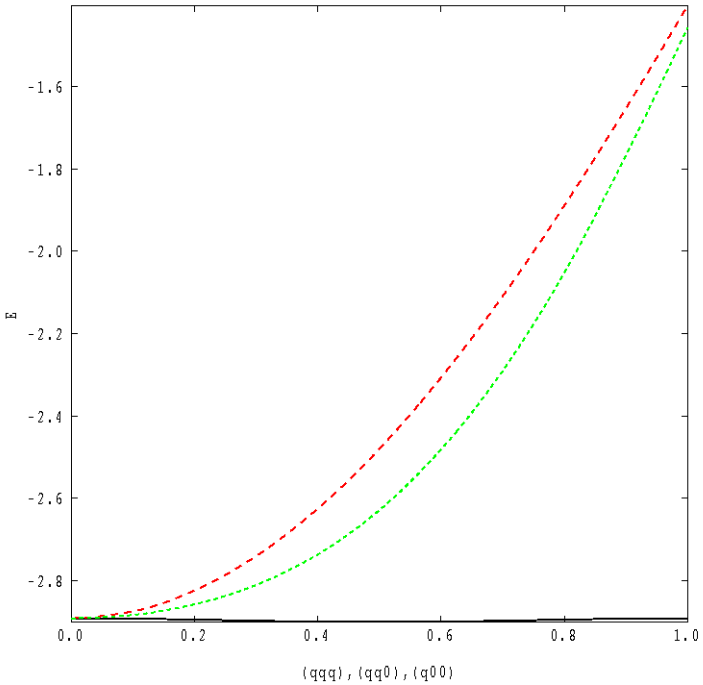

Figure 2.7: The dispersion of the minimum energy eigenvalue of the long-range dipolar interaction matrix for the pyrochlore lattice. Calculation preformed by M.W. Long using Ewald summation[43]. The dispersion is plotted in units of 2π for three symmetrical reciprocal space directions: (q,q,q) (black), (q,q,0) (red) and (0,0,q) (green).

constraints to ensure that all spins have equal magnitude. The eigenstate corresponding to the minimum energy eigenvalue at $\mathbf{k} = (1/2, 1/2, 1/2)$ unfortunately turns out to be incompatible with the equal length spin constraints making this state unphysical. As this state will also be relevant later, however, we will pause to explain its structure.

The easiest way to understand the $\mathbf{k} = (1/2, 1/2, 1/2)$ eigenstate is to consider the structure of the pyrochlore lattice in terms of the planes perpendicular to the $\langle 1, 1, 1 \rangle$ direction. The pyrochlore lattice is formed from stacking alternating planes of Kagomé and 'sparse triangular' lattices as shown in Fig 2.8 (where we have labeled the four atoms per unit cell). The eigenstate has the spins on the Kagomé planes orientated in an in-plane, 120° phase (all with equal magnitude), while the spins on the sparse triangular planes have zero magnitude. This is shown in Fig. 2.9 where we have drawn the orientations of the moments with a non-zero magnitude in red.

If the minimum eigenvalue of the structure factor does not provide a physical solution,

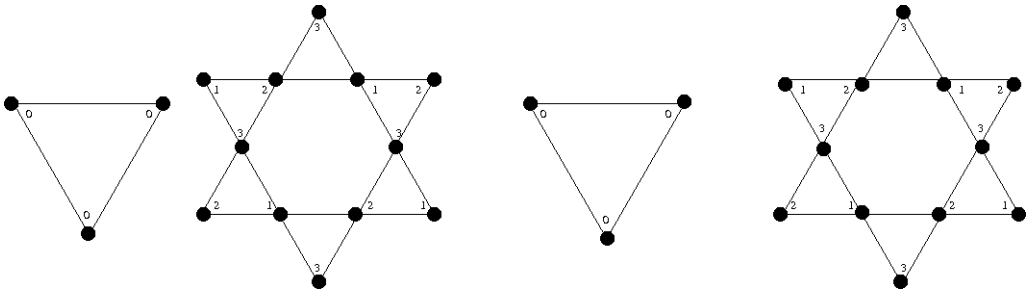

Figure 2.8: The pyrochlore lattice viewed perpendicular to the $\langle 111 \rangle$ direction takes the form of alternating sparse triangular planes and Kagomé planes as shown. The labels $0, 1, 2$ and 3 indicate the locations of the four sub-lattices.

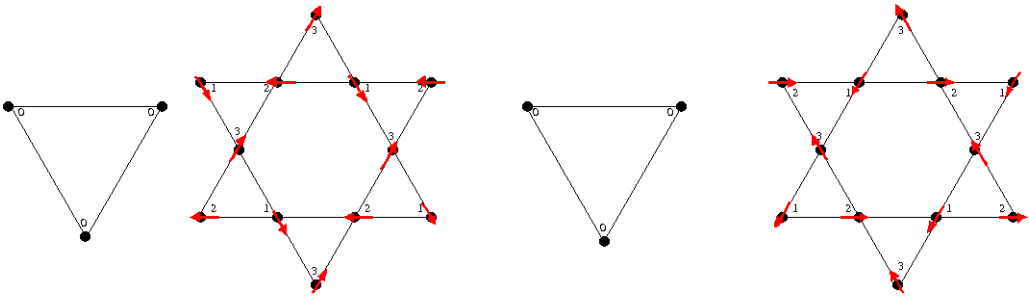

Figure 2.9: The minimum energy eigenstate (indexed by $\mathbf{k} = (1/2, 1/2, 1/2)$) of the long-range dipole interaction in the presence of dominant nearest neighbour Heisenberg exchange on the pyrochlore lattice. The sites on sub-lattice '0' have zero ordered moment, while the spins on the other three sub-lattices have ordered moments of equal magnitude which form a 120° phase with the spins lying within the Kagomé planes (shown by the red arrows). The 120° states on neighbouring Kagomé planes have the opposite chirallity. We note that this state does not satisfy the classical equal-length spin constraint.

the problem becomes much more difficult. In principle the classical ground-state solution could be some linear combination of eigenstates making it extremely difficult to prove which is the correct ground-state. Ewald calculations by M.W. Long [43] find that the eigenstates of the lowest energy eigenvalue along the $\mathbf{k} = (q, q, q)$ direction from $\mathbf{k} \mapsto (1/2, 1/2, 1/2)$ to $\mathbf{k} \mapsto (0, 0, 0)$ all have an incommensurate magnetic ordering vector and give rise to states for which the magnitude of the spins varies slowly across the lattice. Although not proved, it is believed to be impossible to combine these eigenstates into a classical state with equal magnitude spins. However, this band is only weakly dispersive, and at $\mathbf{k} = \mathbf{0}$ we find the spiral states shown in Fig. 2.3 which do have equal magnitude spins. These states are therefore believed to be the classical-ground states of the dipolar interaction in the presence of a dominant Heisenberg exchange on

the pyrochlore lattice [43], although they are not at the global minimum of the dipolar structure factor (which is found at $\mathbf{k} = (1/2, 1/2, 1/2)$).

2.3.3 Anisotropic vs. isotropic forces

In the previous section we discussed the dispersion of the minimum energy eigenvalue of the dipolar interaction matrix on the pyrochlore lattice. The corresponding eigenstate however is incompatible with the classical spin problem as all the spins do not have the same magnitude. In contrast, for the isotropic Heisenberg interaction it is usually (though not always) possible to find a classical solution that minimises the structure factor of the interaction. In this section we will discuss a couple of simple classical models to illustrate this difference between the magnetic ordering of isotropic and anisotropic classical spin systems. For simplicity, instead of the dipolar interaction, we will consider the second neighbour one-dimensional Ising model and contrast this with the second neighbour one dimensional Heisenberg model.

We will begin with the one dimensional second neighbour Heisenberg model. This is described by the Hamiltonian:

$$H = \frac{J_1}{2} \sum_{\langle ij \rangle_1} \mathbf{S}_i \cdot \mathbf{S}_j + \frac{J_2}{2} \sum_{\langle ij \rangle_2} \mathbf{S}_i \cdot \mathbf{S}_j, \tag{2.12}$$

where $J_1 > 0$ and $J_2 > 0$. Bloch transforming this Hamiltonian using:

$$\mathbf{S}_\mathbf{k} = \frac{1}{\sqrt{N}} \sum_j e^{i\mathbf{k}\cdot\mathbf{R}_j} \mathbf{S}_j \tag{2.13}$$

gives

$$H = \sum_\mathbf{k} \gamma_\mathbf{k} \left| \mathbf{S}_k \right|^2, \tag{2.14}$$

with the structure factor:

$$\gamma_\mathbf{k} \quad = \quad J_1 \cos k_x + J_2 \cos 2k_x$$

$$= \quad 2J_2 \left[\cos k_x + \frac{J_1}{4J_2}\right]^2 - \frac{J_1^2}{8J_2} - J_2. \tag{2.15}$$

If $\frac{J_1}{4J_2} > 1$, then this is clearly minimised by $\mathbf{k} = \pm\pi\hat{\mathbf{x}}$ and the ground-state is the bipartite ferromagnetic described by $\mathbf{S}_j = Se^{i\pi j}\hat{\mathbf{e}}$, where $\hat{\mathbf{e}}$ is an arbitrary unit vector as the Hamiltonian is invariant under global spin rotations. However, if $\frac{J_1}{4J_2} < 1$ then the structure factor is minimal for the incommensurate wave-vector $\mathbf{k} = \mathbf{k}_s = \pm k_s\hat{\mathbf{x}}$ (where $\cos k_s = \frac{J_1}{4J_2} < 1$). To find classical solutions with this ordering vector we next need to apply the reciprocal-space spin-constraint given in Equation 1.13, which we reproduce below:

$$\sum_{\mathbf{kG}} \mathbf{S}_{\mathbf{k}} \cdot \mathbf{S}_{\mathbf{q-k+G}} = NS^2 \sum_{\mathbf{G}} \delta_{\mathbf{q-G}}. \tag{2.16}$$

$\mathbf{S}_{\mathbf{k}}$ is zero unless $\mathbf{k} = \pm\mathbf{k}_s$ (up to some reciprocal lattice vector) which gives us

$$\sum_{\mathbf{G}} \left[\mathbf{S}_{\mathbf{k}_s} \cdot \mathbf{S}_{\mathbf{q-k}_s+\mathbf{G}} + \mathbf{S}_{-\mathbf{k}_s} \cdot \mathbf{S}_{\mathbf{q+k}_s+\mathbf{G}}\right] = NS^2 \sum_{\mathbf{G}} \delta_{\mathbf{q-G}}. \tag{2.17}$$

If $\mathbf{q} = \mathbf{G}$, then using $\mathbf{S}_{\mathbf{k+G}} = \mathbf{S}_{\mathbf{k}}$ and $\mathbf{S}_{\mathbf{k}}^* = \mathbf{S}_{-\mathbf{k}}$ (a property of real spins), the constraint simplifies to a normalisation condition:

$$|\mathbf{S}_{\mathbf{k}_s}|^2 = \frac{NS^2}{2}. \tag{2.18}$$

For the other case, where $\mathbf{q} \neq \mathbf{G}$, we find:

$$\mathbf{S}_{\mathbf{k}_s} \cdot \mathbf{S}_{\mathbf{q-k}_s} + \mathbf{S}_{-\mathbf{k}_s} \cdot \mathbf{S}_{\mathbf{q+k}_s} = 0, \tag{2.19}$$

which is non-zero only when $\mathbf{q} = 2\mathbf{k}_s$ (or $\mathbf{q} = -2\mathbf{k}_s$) providing

$$\mathbf{S}_{\mathbf{k}_s} \cdot \mathbf{S}_{\mathbf{k}_s} = 0. \tag{2.20}$$

As we are free to make $\mathbf{S_k}$ complex, we arrive at the non-trivial solution of

$$\mathbf{S}_{\mathbf{k}_s} = \frac{1}{\sqrt{2}} \left[\hat{\mathbf{e}}_1 + i\hat{\mathbf{e}}_2\right] e^{-i\phi} \sqrt{\frac{N}{2}} S \tag{2.21}$$

(which also satisfies the normalisation condition in Equation 2.18), where ϕ is an arbitrary phase and $\hat{\mathbf{e}}_1$ and $\hat{\mathbf{e}}_2$ are orthonormal vectors. The real-space spin orientations are then described by:

$$\mathbf{S}_j = \hat{\mathbf{e}}_1 \cos(\mathbf{k}_s \cdot \mathbf{R}_j + \phi) + \hat{\mathbf{e}}_2 \sin(\mathbf{k}_s \cdot \mathbf{R}_j + \phi), \tag{2.22}$$

which is an incommensurate spin-spiral, with an energy of

$$E = NS^2 \gamma_{min}, \tag{2.23}$$

where

$$\gamma_{min} = -\frac{J_1^2}{8J_2} - J_2. \tag{2.24}$$

We will now move on to consider an analogous but anisotropic model: the one dimensional second neighbour Ising model. Hamiltonian is:

$$H = \frac{J_1}{2} \sum_{\langle ij \rangle_1} S_i^z S_j^z + \frac{J_2}{2} \sum_{\langle ij \rangle_2} S_i^z S_j^z. \tag{2.25}$$

Using the same procedure as previously we can transform to reciprocal space to get

$$H = \sum_{\mathbf{k}} \gamma_{\mathbf{k}} \left|S_{\mathbf{k}}^z\right|^2, \tag{2.26}$$

where $\gamma_{\mathbf{k}}$ is the same as for the second neighbour one dimensional Heisenberg model, and therefore also minimised by the incommensurate wave-vectors $\mathbf{k} = \pm k_x \hat{\mathbf{x}}$. If we tried to minimise the Hamiltonian by placing all the spin-density at these $\mathbf{k}$-points, in the z-direction we get a state in which the magnitude of the spins has a periodic modulation along the lattice. This clearly violates the classical-spin constraints in a similar way to

that which is seen for the 'Kagomé planes' state (Fig. 2.9) which minimises the structure factor of the long-range dipole interaction on the pyrochlore lattice. We can of course construct the spiral state state given in Equation 2.22. It is however not the ground-state for this model. As only the z-component of the spins contribute, the energy of the spiral for the Ising model is given by

$$E = \frac{NS^2}{2}\gamma_{min}. \tag{2.27}$$

An alternative option is to consider states of different periodicities in which the spins are pinned along the z-axis. In the limit that $J_2 \mapsto 0$ the ground state is clearly a bipartite antiferromagnet with

$$H\left|\uparrow\downarrow\uparrow\downarrow\uparrow\downarrow ...\right\rangle = -N(J_1 - J_2)\left|\uparrow\downarrow\uparrow\downarrow\uparrow\downarrow ...\right\rangle, \tag{2.28}$$

while for $J_1 \mapsto 0$ the ground-state and corresponding energy is given by:

$$H\left|\uparrow\uparrow\downarrow\downarrow\uparrow\uparrow ...\right\rangle = -NJ_2\left|\uparrow\uparrow\downarrow\downarrow\uparrow\uparrow ...\right\rangle. \tag{2.29}$$

For intermediate values of J_1 and J_2 the ground-state cannot contain more than two adjacent spins of the same type as this would incur an energy penalty from both the first and second neighbour interaction. The only other option is to consider states of larger periodicity such as:

$$H\left|\uparrow\uparrow\downarrow\uparrow\downarrow\uparrow\uparrow\downarrow\uparrow\downarrow\right\rangle = -\frac{N}{5}(3J_1 - J_2)\left|\uparrow\uparrow\downarrow\uparrow\downarrow\uparrow\uparrow\downarrow\uparrow\downarrow\right\rangle, \tag{2.30}$$

however, solutions of this type can be interpreted as domains of the solutions in Equations 2.28and 2.29 (which we will refer to here as 'State 1' and 'State 2' respectively). The simplest example of these types of states is to add one domain wall to State 1 this gives rise to an energy change of $\Delta E = 2(J_1 - 2J_2)$ and therefore only becomes favorable when $J_2 > J_1/2$, however, we also notice that this is precisely the condition that stabilises State 2 over State 1. When the relative interaction strength reaches this value, the ground-state

will therefore jump straight from State 1 to State 2. Finally we note that if an external field is applied parallel to the z-axis to the one dimensional Ising model with long range convex antiferromagnetic interactions, then the ground state can be tuned by the field to access states of all possible commensurate periodicities[4], resulting in a Devil's staircase of plateaux at all rational values of the magnetisation as the external field strength is increased.

To summarise, for isotropic models it is usually possible to construct a classical solution with the periodicity that minimises the structure factor. In contrast, for anisotropic models this is not the case. This is exactly what is seen for the dipole interaction on the pyrochlore lattice. As a result anisotropic interactions can give rise to rather exotic long-range magnetically ordered states. In the next section we will investigate the effect of adding an external field to the problem of a long-range dipole coupling and dominant Heisenberg exchange on the pyrochlore lattice, with the assumption that the system remains within the $\mathbf{k} = \mathbf{0}$ subspace that is stabilised for zero external field.

2.4 Exact solution in $\mathbf{k} = 0$ subspace

In this section we will discuss the minimisation of the dipole interaction on the pyrochlore lattice in the presence of a dominant antiferromagnetic nearest neighbour Heisenberg exchange and an external magnetic field. Restricting ourselves to the $\mathbf{k} = \mathbf{0}$ subspace, we will begin by considering only the nearest neighbour dipole interaction and then go on to discuss how this can be generalised to the long-range dipolar problem. As we wish to study classical magnetism, we will work with normalised spins such that $|\mathbf{S}| = 1$. Although the problem turns out to be over-constrained we are able to find some exact solutions for certain special external field directions.

We will start with the Hamiltonian for the dominant nearest neighbour Heisenberg exchange and external magnetic field. As discussed earlier, the pyrochlore lattice is formed from four inter-penetrating face-centre-cubic sub-lattices. In the $\mathbf{k} = \mathbf{0}$ subspace all the

spins on a sub-lattice are parallel. As the four spins forming a tetrahedron each lie on a different sub-lattice, in the $\mathbf{k} = \mathbf{0}$ sub-space we need only consider a single tetrahedron and then sum over the number of tetrahedra in the lattice. We label the four spins forming a tetrahedron using $\mathbf{S}_\alpha$ where $\alpha \in \{0, 1, 2, 3\}$ as indicated in Fig. 2.3, and define the scaled total spin of each tetrahedron as:

$$\mathbf{T} = \frac{1}{2}\left[\mathbf{S}_0 + \mathbf{S}_1 + \mathbf{S}_2 + \mathbf{S}_3\right], \tag{2.31}$$

so that we can write the Heisenberg interaction as:

$$H_0 = 2J_0 \sum_t \mathbf{T} \cdot \mathbf{T}, \tag{2.32}$$

where we have neglected the constant and the sum over 't' indicates a sum over the tetrahedra forming the pyrochlore lattice.

Next we will turn to the dipole interaction. Focusing on the nearest neighbour contribution, the dipolar Hamiltonian takes the form:

$$H_D = -\frac{1}{2}\sum_{\langle ij \rangle} \frac{\mu_0}{4\pi}\left[\frac{3(\mathbf{S}_i \cdot \hat{\mathbf{r}}_{ij})(\mathbf{S}_j \cdot \hat{\mathbf{r}}_{ij}) - \mathbf{S}_i \cdot \mathbf{S}_j}{|\mathbf{r}_{ij}|^3}\right], \tag{2.33}$$

where $\mathbf{r}_{ij} = \mathbf{r}_i - \mathbf{r}_j$ and $\mathbf{S}_i$ represents a classical spin at position $\mathbf{r}_i$. Defining $\mu = \frac{3\mu_0}{4\pi r_{ij}^3}$ we again focus on a single tetrahedron so that the dipolar Hamiltonian (in the $\mathbf{k} = \mathbf{0}$ can be written as:

$$\begin{aligned} H_1 \;=\; & -\frac{\mu}{2}\sum_t \left[\left(S_0^y + S_0^z\right)\left(S_1^y + S_1^z\right) + \left(S_2^y - S_2^z\right)\left(S_3^y - S_3^z\right)\right. \\ & + \left(S_0^z + S_0^x\right)\left(S_2^z + S_2^x\right) + \left(S_1^z - S_1^x\right)\left(S_3^z - S_3^x\right) \\ & \left. + \left(S_0^x + S_0^y\right)\left(S_3^x + S_3^y\right) + \left(S_1^x - S_1^y\right)\left(S_2^x - S_2^y\right) - \frac{4}{3}\mathbf{T}\cdot\mathbf{T}\right]. \end{aligned} \tag{2.34}$$

We recognise that this expression can be factorised in terms of the squares of seven natural variables. One method of obtaining this result is given in Appendix B, however, here we

will just quote it:

$$\begin{aligned} H_1 &= \sum_t \Big\{ \frac{\mu_a}{4} \Big[(S_0^x + S_0^y + S_0^z - [T^x + T^y + T^z])^2 + (S_0^x - S_1^y - S_1^z - [T^x - T^y - T^z])^2 \\ &\quad + (-S_2^x + S_2^y - S_2^z - [-T^x + T^y - T^z])^2 + (-S_3^x - S_3^y + S_3^z - [-T^x - T^y + T^z])^2 \Big] \\ &\quad + \frac{\mu_b}{8} \Big[(S_0^x + S_1^x - S_2^x - S_3^x)^2 + \left(S_0^y - S_y^x + S_y^x - S_3^y\right)^2 + (S_0^z - S_1^z - S_2^z + S_3^z)^2 \Big] \\ &\quad + \frac{\mu_b}{6} \mathbf{T} \cdot \mathbf{T} \Big\}, \end{aligned} \tag{2.35}$$

where we have neglected a constant term. For the nearest neighbour dipole interaction $\mu_a = \mu_b = \mu$. However, the Ewald calculations by M.W. Long[43] (discussed at the end of Section 2.3.2) find that in the $\mathbf{k} = \mathbf{0}$ subspace, the long-range dipolar energy can be written precisely in the form given above with $\mu_b = 0.899105\mu_a$. We can see that this Hamiltonian is clearly minimised by making each of the seven quadratic terms equal to zero. If such solutions exist they are then independent of the precise dipolar interaction strength.

Finally we will include the external magnetic field using

$$H_2 = -\mathbf{B} \cdot \sum_t \mathbf{T}. \tag{2.36}$$

In addition we also combine the Heisenberg type term from Equation 2.35 into H_0 to give

$$H_0 = 2J \sum_t \mathbf{T} \cdot \mathbf{T} \tag{2.37}$$

where $J = J_0 + \mu_B/12$, so that we can combine the two Hamiltonians as:

$$H_0 + H_2 = 2J \sum_t \left[(T^x - \beta^x)^2 + (T^y - \beta^y)^2 + (T^z - \beta^z)^2 \right], \tag{2.38}$$

where β^x, β^y and β^z are the components of the rescaled external field (such that $\beta = \mathbf{B}/4J$.

Our final Hamiltonian therefore becomes

$$\begin{aligned} H &= \sum_t \Big\{ 2J \left[(T^x - \beta^x)^2 + (T^y - \beta^y)^2 + (T^z - \beta^z)^2 \right] \\ &\quad + \frac{\mu_a}{4} \Big[\left(S_0^x + S_0^y + S_0^z - [T^x + T^y + T^z] \right)^2 + \left(S_0^x - S_1^y - S_1^z - [T^x - T^y - T^z] \right)^2 \\ &\quad + \left(-S_2^x + S_2^y - S_2^z - [-T^x + T^y - T^z] \right)^2 + \left(-S_3^x - S_3^y + S_3^z - [-T^x - T^y + T^z] \right)^2 \Big] \\ &\quad + \frac{\mu_b}{8} \Big[\left(S_0^x + S_1^x - S_2^x - S_3^x \right)^2 + \left(S_0^y - S_1^y + S_2^y - S_3^y \right)^2 + \left(S_0^z - S_1^z - S_2^z + S_3^z \right)^2 \Big] \Big\} \end{aligned} \tag{2.39}$$

.

Using Equation 2.39 to express the dipolar energy also leads to some physical insights as to how this energy can be minimised. Assuming the exchange energy is dominant, the spin structure becomes a saturated ferromagnet for external field of strength $\beta > 2$. Otherwise the total spin of the tetrahedron is equal to 2β. We notice two points about the term in μ_a, the first being that the spin component parallel to the local tetrahedral axis is required to be twice the value (per spin) induced by the magnetic field. Secondly, there is an induced effective crystal field that forces any additional spin component into the plane perpendicular to the local tetrahedral axis. We wish to highlight that in the case of no external magnetic field, minimising these terms is therefore consistent with the planer spin orientations observed in the Mössbauer data for $Gd_2Sn_2O_7$ (discussed in Section 2.2).The terms in μ_b however are somewhat more subtle. They describe the three ways of pairing the atoms in a tetrahedron and provide an energy penalty for an antiferromagnetic coupling in the direction of the relevant spin component.

We wish to look for 'unfrustrated' solutions to the problem of minimising Equation 2.39, i.e. solutions which make all of the ten quadratic terms vanish. For a single tetrahedron, it appears therefore that we have ten constraints. There is, however, one linear dependency between the ten arguments: the sum of the four arguments of the 'μ_a' terms is equal to the sum of the three arguments of the 'μ_b' terms. This gives us nine constraints, but as we are working with four, normalised spins, there are only eight degrees of freedom. Our problem is therefore over-constrained. Surprisingly, for a special

set magnetic fields we are able to find solutions. These occur when the field lies in one of the Cartesian planes (e.g. $\beta^z = 0$) or when $|\beta| = 1$, and will be discussed in the following sections.

Finally we note that the spiral ground-states observed for $Gd_2Sn_2O_7$ (see Fig. 2.3) is consistent with minimising the ten quadratics in Equation 2.39 in the absence of an external field. This is further confirmation that the dipole interaction is instrumental in controlling the energetics of gadolinium stannate.

2.5 Solutions for an external field in the $z = 0$ plane

In this section we discuss the solutions when the magnetic field lies in one of the Cartesian planes. We will focus on the case where the field is in the $z = 0$ plane (i.e. $\beta^z = 0$), as the solutions for the other two case can be found using symmetry.

Equation 2.39 gives us ten constraint equations, from which we can eliminate T^x, T^y and T^z to give us:

$$S_0^x + S_1^x + S_2^x + S_3^x = 2\beta^x, \qquad S_0^y + S_1^y + S_2^y + S_3^y = 2\beta^y, \qquad S_0^z + S_1^z + S_2^z + S_3^z = 2\beta^z, \tag{2.40}$$

$$S_0^x + S_1^x - S_2^x - S_3^x = 0, \qquad S_0^y - S_1^y + S_2^y - S_3^y = 0, \qquad S_0^z - S_1^z - S_2^z + S_3^z = 0, \tag{2.41}$$

$$S_0^x + S_0^y + S_0^z = \beta^x + \beta^y + \beta^z, \qquad S_1^x - S_1^y - S_1^z = \beta^x - \beta^y - \beta^z, \tag{2.42}$$

$$-S_2^x + S_2^y - S_0^z = -\beta^x + \beta^y - \beta^z, \qquad -S_3^x - S_3^y + S_3^z = -\beta^x - \beta^y + \beta^z. \tag{2.43}$$

These relationships can also be expressed as:

$$S_0^x + S_1^x \;=\; \beta^x, \qquad , S_0^y + S_2^y = \beta^y, \qquad S_0^z + S_3^z = \beta^z$$

$$S_2^x + S_3^x = \beta^x, \qquad , S_1^y + S_3^y = \beta^y, \qquad S_1^z + S_1^z = \beta^z$$

$$S_1^x + S_2^y + S_3^z = 0, \qquad S_0^x - S_3^y - S_2^z = 0, \qquad -S_3^x + S_0^y - S_1^z = 0, \qquad -S_2^x - S_1^y + S_0^z = 0 \tag{2.44}$$

which provides an alternative perspective on how the spin coefficients are inter-related. If, for the moment, we neglect the spin normalisation, then we have twelve spin degrees of freedom and only nine linearly independent constraints. We therefore parameterise the spins in terms of the variables: x, y and z. There are many possible ways of doing this. If the field is confined to the xy-plane, this marks out the z-direction as special. We will therefore choose

$$S_1^x = z + \frac{\beta^x}{2}, \qquad S_1^y = y + \frac{\beta^y}{2}, \qquad S_2^x = x + \frac{\beta^x}{2}, \tag{2.45}$$

which gives:

$$\begin{aligned}
\mathbf{S}_0 &= \left(\frac{\beta^x}{2} - z, \frac{\beta^y}{2} - y + z - x, \frac{\beta^x}{2} + x + \frac{\beta^y}{2} + y\right) \\
\mathbf{S}_1 &= \left(\frac{\beta^x}{2} + z, \frac{\beta^y}{2} + y, \frac{\beta^y}{2} - y - \frac{\beta^x}{2} + z\right) \\
\mathbf{S}_2 &= \left(\frac{\beta^x}{2} + x, \frac{\beta^y}{2} + y - z + x, \frac{\beta^x}{2} - z - \frac{\beta^y}{2} + y\right) \\
\mathbf{S}_3 &= \left(\frac{\beta^x}{2} - x, \frac{\beta^y}{2} - y, -\frac{\beta^x}{2} - x - \frac{\beta^y}{2} - y\right),
\end{aligned} \tag{2.46}$$

where we have used $\beta^z = 0$. Using this parameterisation ensures that all of the ten constraint equations are satisfied. We therefore now move on to consider normalising these spins. Although this might seem difficult as we have the four normalisation constraints, but only three variables. We notice however that if we put $z = x$, such that:

$$\begin{aligned}
\mathbf{S}_0 &= \left(\frac{\beta^x}{2} - x, \frac{\beta^y}{2} - y, \frac{\beta^x}{2} + x + \frac{\beta^y}{2} + y\right) \\
\mathbf{S}_1 &= \left(\frac{\beta^x}{2} + x, \frac{\beta^y}{2} + y, -\frac{\beta^x}{2} + x + \frac{\beta^y}{2} - y\right)
\end{aligned}$$

$$\begin{aligned}
\mathbf{S}_2 &= \left(\frac{\beta^x}{2}+x, \frac{\beta^y}{2}+y, \frac{\beta^x}{2}-x-\frac{\beta^y}{2}+y\right) \\
\mathbf{S}_3 &= \left(\frac{\beta^x}{2}-x, \frac{\beta^y}{2}-y, -\frac{\beta^x}{2}-x-\frac{\beta^y}{2}-y\right),
\end{aligned} \tag{2.47}$$

then we have automatically satisfied: $|\mathbf{S}_0|^2 = |\mathbf{S}_3|^2$ and $|\mathbf{S}_1|^2 = |\mathbf{S}_2|^2$, which reduces us to only two normalisation constraints and two variables. We find that:

$$|\mathbf{S}_0|^2 - |\mathbf{S}_1|^2 = \frac{\beta^x}{2}\frac{\beta^y}{2} + xy = 0, \tag{2.48}$$

which can be substituted into $|\mathbf{S}_0|^2 + |\mathbf{S}_1|^2 = 2$ to provide the quartic equation:

$$x^4 + \frac{\beta^y}{2}x^3 + \left[\left(\frac{\beta^x}{2}\right)^2 + \left(\frac{\beta^y}{2}\right)^2 - \frac{1}{2}\right]x^2 - \left(\frac{\beta^x}{2}\right)^2\frac{\beta^y}{2}x + \left(\frac{\beta^x}{2}\right)^2\left(\frac{\beta^y}{2}\right)^2 = 0. \tag{2.49}$$

For general values of β^x and β^y the above equation would have to be solved numerically. In. Fig. 2.10 we plot the values of β^x and β^y for which the discriminant of this equation vanishes. This tells us the value of the external field at which the exact solutions cease to exist (i.e. when the roots of Equation 2.49 become imaginary). We can see that for the field in the Cartesian $\beta^z = 0$ there are two types of solution, one of which is more stable to the external field than the other (except for when $\beta^x = \pm\beta^y$, where the two types of solutions are lost simultaneously). We can see from Equations 2.47 that the general form of these solutions can be written as:

$$\begin{aligned}
\mathbf{S}_0 &= \left[\frac{\beta^x}{2}\hat{\mathbf{x}} + \frac{\beta^y}{2}\hat{\mathbf{y}}\right] + \left[-y\hat{\mathbf{y}} + \left(y+\frac{\beta^x}{2}\right)\hat{\mathbf{z}}\right] + \left[-x\hat{\mathbf{x}} + \left(x+\frac{\beta^y}{2}\right)\hat{\mathbf{z}}\right], \\
\mathbf{S}_1 &= \left[\frac{\beta^x}{2}\hat{\mathbf{x}} + \frac{\beta^y}{2}\hat{\mathbf{y}}\right] + \left[+y\hat{\mathbf{y}} - \left(y+\frac{\beta^x}{2}\right)\hat{\mathbf{z}}\right] + \left[+x\hat{\mathbf{x}} + \left(x+\frac{\beta^y}{2}\right)\hat{\mathbf{z}}\right], \\
\mathbf{S}_2 &= \left[\frac{\beta^x}{2}\hat{\mathbf{x}} + \frac{\beta^y}{2}\hat{\mathbf{y}}\right] + \left[+y\hat{\mathbf{y}} + \left(y+\frac{\beta^x}{2}\right)\hat{\mathbf{z}}\right] + \left[+x\hat{\mathbf{x}} - \left(x+\frac{\beta^y}{2}\right)\hat{\mathbf{z}}\right], \\
\mathbf{S}_3 &= \left[\frac{\beta^x}{2}\hat{\mathbf{x}} + \frac{\beta^y}{2}\hat{\mathbf{y}}\right] + \left[-y\hat{\mathbf{y}} - \left(y+\frac{\beta^x}{2}\right)\hat{\mathbf{z}}\right] + \left[-x\hat{\mathbf{x}} - \left(x+\frac{\beta^y}{2}\right)\hat{\mathbf{z}}\right].
\end{aligned} \tag{2.50}$$

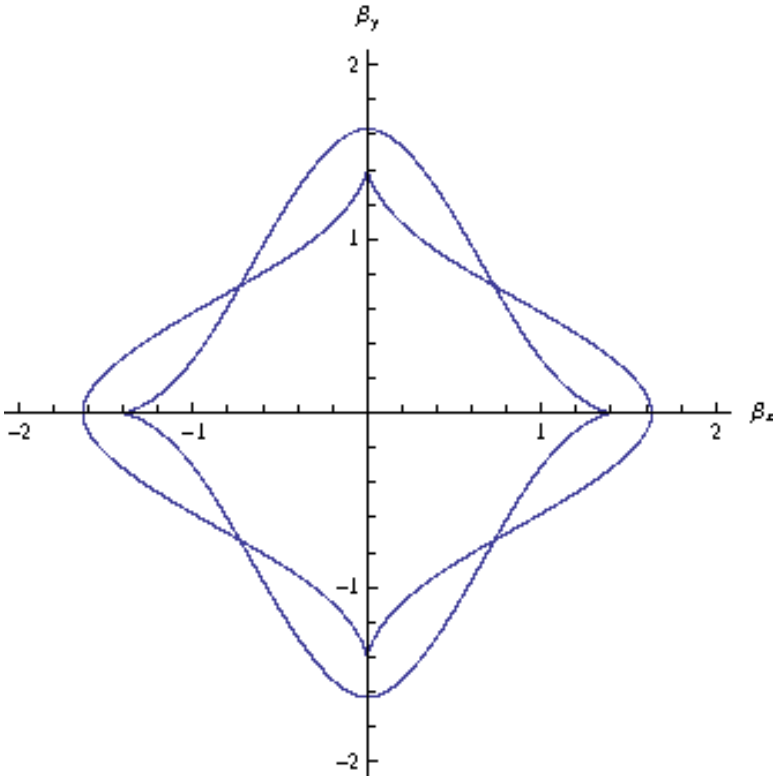

Figure 2.10: The values of β^x and β^y (describing the scaled external magnetic field defined in Equation 2.38) for which the discriminant of Equation 2.49 vanishes. This is equivalent to the external field values for which exact solutions to the Hamiltonian shown in Equation 2.39 for the case that $\beta^z = 0$ (and the external filed therefore lies within the xy-plane) cease to exist.

Spin states of this form can be interpreted as a sum of three components: the first is a contribution proportional to the external field ; the second is a distorted spiral perpendicular to the x-axis and the third is a distorted spiral perpendicular to the y-axis. The distorted spiral perpendicular to the x-axis is shown in Fig. 2.11 and its projection onto the x-axis in Fig. 2.12. The two spin components have magnitudes 'y' and '$y + \frac{\beta^x}{2}$'.

If we also enforce that $\beta^y = 0$ in Equation 2.49 we find:

$$x^2 \left(x^2 + \left(\frac{\beta^x}{2} \right)^2 - \frac{1}{2} \right) = 0, \tag{2.51}$$

which is trivial to solve. There are a number of possible solutions to this (along with Equation 2.48), though not all are compatible with the normalisation condition. We find

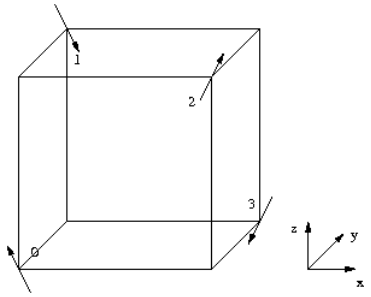

Figure 2.11: The component of the spin state described in Equations 2.50 which forms a distorted spiral perpendicular to the x-axis.

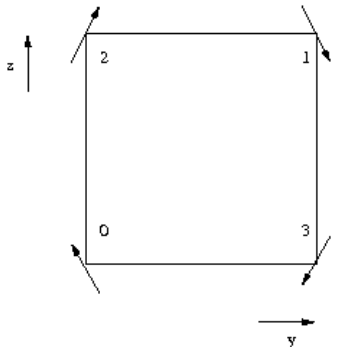

Figure 2.12: The projection of the distorted spiral shown in Fig. 2.11 onto the yz-plane. The spins are numbered according to the convention used in Figs. 2.3 and 2.11.

two types of solution which are compatible:

$$x = \pm\frac{1}{\sqrt{2}}\sqrt{1-\frac{(\beta^x)^2}{2}}, \qquad y = 0 \tag{2.52}$$

and

$$x = 0, \qquad y = -\frac{\beta^x}{4} \pm \frac{1}{2}\sqrt{2-3\left(\frac{\beta^x}{2}\right)^2}. \tag{2.53}$$

First we will consider the chirally related pair of solutions given in Equation 2.52. The spins are confined to the zx-plane and have the orientations given below:

$$\begin{aligned}
\mathbf{S}_0 &= \left(\frac{\beta^x}{2} \mp \frac{1}{\sqrt{2}}\sqrt{1-\frac{(\beta^x)^2}{2}}, 0, \frac{\beta^x}{2} \pm \frac{1}{\sqrt{2}}\sqrt{1-\frac{(\beta^x)^2}{2}}\right), \\
\mathbf{S}_1 &= \left(\frac{\beta^x}{2} \pm \frac{1}{\sqrt{2}}\sqrt{1-\frac{(\beta^x)^2}{2}}, 0, -\frac{\beta^x}{2} \pm \frac{1}{\sqrt{2}}\sqrt{1-\frac{(\beta^x)^2}{2}}\right),
\end{aligned}$$

$$\begin{aligned}
\mathbf{S}_2 &= \left(\frac{\beta^x}{2} \pm \frac{1}{\sqrt{2}} \sqrt{1 - \frac{(\beta^x)^2}{2}}, 0, \frac{\beta^x}{2} \mp \frac{1}{\sqrt{2}} \sqrt{1 - \frac{(\beta^x)^2}{2}} \right), \\
\mathbf{S}_3 &= \left(\frac{\beta^x}{2} \mp \frac{1}{\sqrt{2}} \sqrt{1 - \frac{(\beta^x)^2}{2}}, 0, -\frac{\beta^x}{2} \mp \frac{1}{\sqrt{2}} \sqrt{1 - \frac{(\beta^x)^2}{2}} \right),
\end{aligned} \tag{2.54}$$

and we can see that as $\beta^x \mapsto 0$ we recover the undistorted spiral in the zx-plane, shown in Fig. 2.13a) and projected onto the zx-plane in Fig. 2.14a). The spin components are

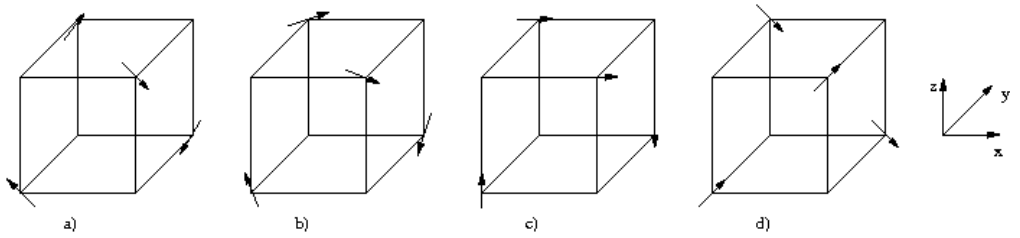

Figure 2.13: The evolution of the state described in Equation 2.54 (for the case that the external field lies parallel to the x-axis) with increasing β^x. a) $\beta^x = 0$, b) $0 < \beta^x < 1$, c) $\beta^x = 1$, d) $\beta^x = \sqrt{2}$.

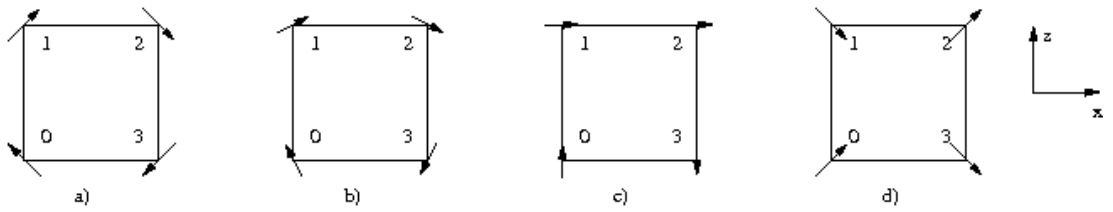

Figure 2.14: The projection of the states depicted in Fig. 2.13 onto the zx-plane. The spins are numbered according to the convention used in Figs. 2.3 and 2.11.

plotted as a function of β^x in Fig 2.15. For small β^x we get the distorted spiral shown in Figs. 2.13b) and 2.14b). As β^x is increased the spiral further distorts until at exactly half-saturation (i.e. $\beta^x = 1$ we get the state shown in Figs. 2.13c) and 2.14c). Here two spins are parallel to the field, with the other two spins forming an antiferromagnetically aligned pair perpendicular to the field direction. As the field is further increased the two spins that are parallel to the field then distort somewhat away from the field direction and finally we arrive at the planer 'two-in-two-out' state shown in Figs. 2.13d) and 2.14d). This state occurs at $\beta^x = \sqrt{2}$ which is the point where the chirallity is lost, as the two states become

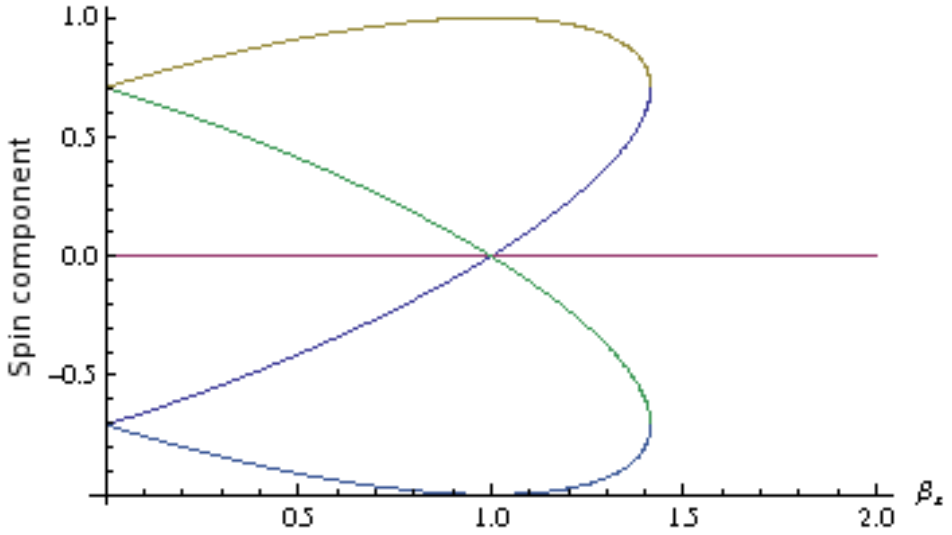

Figure 2.15: The spin components of the normalised state given in Equation 2.54. Yellow: $S_0^z = S_1^x = S_2^x$, Green: S_1^z, Purple: $S_0^y = S_1^y = S_2^y = S_3^y$, Dark blue: $S_0^x = S_2^z = S_3^x$, Light blue (bottom curve): S_3^z.

equivalent. At this point the solution also becomes imaginary if the field is increased any more. Finally we note that this type of solution is actually four-fold degenerate. There are also a chirally related pair of solutions which form an equivalent distorted spiral in the xy-plane. These can be found by substituting $z = -x$ in Equations 2.46. This extra degeneracy exists because the external field lies both in the $\beta^y = 0$ plane and the $\beta^z = 0$ plane.

We will now move on to describe the other style of solutions, given by Equation 2.53. This leads to the following spin orientations:

$$\begin{aligned}
\mathbf{S}_0 &= \left(\frac{\beta^x}{2}, \frac{\beta^x}{4} \mp \frac{1}{2}\sqrt{2-3\left(\frac{\beta^x}{2}\right)^2}, \frac{\beta^x}{4} \pm \frac{1}{2}\sqrt{2-3\left(\frac{\beta^x}{2}\right)^2}\right), \\
\mathbf{S}_1 &= \left(\frac{\beta^x}{2}, -\frac{\beta^x}{4} \pm \frac{1}{2}\sqrt{2-3\left(\frac{\beta^x}{2}\right)^2}, -\frac{\beta^x}{4} \mp \frac{1}{2}\sqrt{2-3\left(\frac{\beta^x}{2}\right)^2}\right), \\
\mathbf{S}_2 &= \left(\frac{\beta^x}{2}, -\frac{\beta^x}{4} \pm \frac{1}{2}\sqrt{2-3\left(\frac{\beta^x}{2}\right)^2}, \frac{\beta^x}{4} \pm \frac{1}{2}\sqrt{2-3\left(\frac{\beta^x}{2}\right)^2}\right), \\
\mathbf{S}_3 &= \left(\frac{\beta^x}{2}, \frac{\beta^x}{4} \mp \frac{1}{2}\sqrt{2-3\left(\frac{\beta^x}{2}\right)^2}, -\frac{\beta^x}{4} \mp \frac{1}{2}\sqrt{2-3\left(\frac{\beta^x}{2}\right)^2}\right),
\end{aligned}$$

(2.55)

and the spin components are plotted as a function of β^x in Fig. 2.16. We see that for

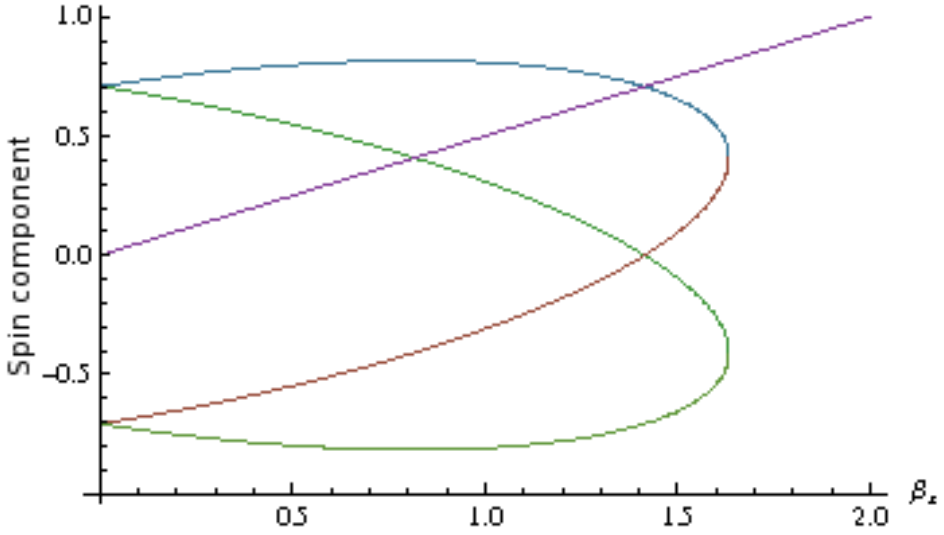

Figure 2.16: The spin components of the normalised state given in Equation 2.55. Light blue: $S_0^z = S_2^z$, Dark green: $S_1^y = S_2^y$, Purple: $S_0^x = S_1^x = S_2^x = S_3^x$, Brown: $S_0^y = S_3^y$, Light green (bottom curve): $S_1^z = S_3^z$.

$\beta^x \mapsto 0$ we recover the chirally related pair of spirals in the yz-plane. When β^x is increased, all four spins develop a component parallel to the field. If this component is subtracted off, then the two states are again chirally related distorted spirals. Increasing the field increases the distortion until at $\beta^x = \sqrt{2}$, the spiral collapses onto a single component. At this field value, these two states are actually identical to the two states found for the other style of solution (also at $\beta^x = \sqrt{2}$), one of which was shown in Figs. 2.13d) and 2.14d). The two styles of solutions therefore merge at this point, and the degeneracy is reduced from six states down to only two. As the field is then further increased the states continue to distort until at $\beta^x = 2\sqrt{2/3}$ the final two chirally related states merge to produce the spin configuration shown in Fig. 2.17. At this point the solutions also become imaginary.

To find the ground-state for fields of $\beta^x > 2\sqrt{2/3}$ requires a general minimisation of the ten arguments of Equation 2.39 (which will no longer be all equal to zero). This is not something that we attempt here, however, numerical minimisation calculations by M.W. Long[43] show that there is a unique ground-state in which all the spins continuously

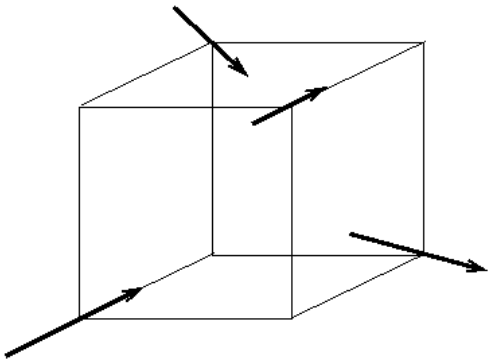

Figure 2.17: The spin configuration for an external field parallel to the x-axis, with $\beta^x = 2\sqrt{2/3}$. This is the field value at which the exact solutions cease to exist.

collapse onto the direction of the external field, so that at $\beta^x = 2$ the system becomes a saturated ferromagnet. For fields orientated along the x-axis we therefore expect three transitions. The first two at $\beta^x = \sqrt{2}$ and $\beta^x = 2\sqrt{2/3}$ which are associated with a reduction in the degeneracy from six states down to two, and then to a single state. The third transition is the loss of antiferromagnetism at the saturation field. Although we have not proved it, similar behaviour is expected for less symmetric field orientations in the $\beta^z = 0$ plane. The initial degeneracy, however, will probably be four rather then six. We will now move on to consider the other exactly solvable case: when $|\beta| = 1$.

2.6 Solutions for a scaled external field of unit magnitude

In this section we will discuss exact solutions when the scaled external field has unit magnitude ($|\beta| = 1$. As was done in previous section, we begin by choosing a parameterisation of the four spins. In this case we wish to make the parameterisation as symmetric as possible. Initially we define six parameters: Xy, Xz, Yx, Yz, Zx, Zy and choose the signs with which they appear in the spin orientations given below so as to satisfy the constraints expressed in Equations 2.40 and 2.41:

$$\mathbf{S}_0 \;=\; \left(\frac{\beta^x}{2} + Yx + Zx, \frac{\beta^y}{2} + Xy + Zy, \frac{\beta^z}{2} + Xz + Yz\right),$$

$$
\begin{aligned}
\mathbf{S}_1 &= \left(\frac{\beta^x}{2} - Yx - Zx, \frac{\beta^y}{2} + Xy - Zy, \frac{\beta^z}{2} + Xz - Yz\right), \\
\mathbf{S}_2 &= \left(\frac{\beta^x}{2} + Yx - Zx, \frac{\beta^y}{2} - Xy + Zy, \frac{\beta^z}{2} - Xz + Yz\right), \\
\mathbf{S}_3 &= \left(\frac{\beta^x}{2} - Yx + Zx, \frac{\beta^y}{2} - Xy - Zy, \frac{\beta^z}{2} - Xz - Yz\right).
\end{aligned}
\tag{2.56}
$$

Substituting the above parameterisation into the remaining four constraints (Equations 2.42 and 2.43) provides us with the following relationships:

$$
\begin{aligned}
Yx + Zx + Zy + Xy + Xz + Yz &= \frac{\beta^x}{2} + \frac{\beta^y}{2} + \frac{\beta^z}{2}, \\
-Yx - Zx + Zy - Xy - Xz + Yz &= \frac{\beta^x}{2} - \frac{\beta^y}{2} - \frac{\beta^z}{2}, \\
-Yx + Zx - Zy + Xy + Xz - Yz &= -\frac{\beta^x}{2} + \frac{\beta^y}{2} - \frac{\beta^z}{2}, \\
Yx - Zx - Zy - Xy - Xz - Yz &= -\frac{\beta^x}{2} - \frac{\beta^y}{2} + \frac{\beta^z}{2},
\end{aligned}
\tag{2.57}
$$

which we can see are satisfied by:

$$
\frac{\beta^x}{2} = Yz + Zy, \qquad , \frac{\beta^y}{2} = Zx + Xz, \qquad , \frac{\beta^z}{2} = Xy + Yx. \tag{2.58}
$$

Consequently we define the three independent parameters using:

$$
x = Yz - Zy, \qquad y = Zx - Xz, \qquad z = Xy - Yx, \tag{2.59}
$$

so that:

$$
\begin{aligned}
\mathbf{S}_0 &= \frac{1}{2}\left(\frac{2\beta^x + \beta^y + \beta^z}{2} + y - z, \frac{\beta^x + 2\beta^y + \beta^z}{2} + z - x, \frac{\beta^x + \beta^y + 2\beta^z}{2} + x - y\right) \\
\mathbf{S}_1 &= \frac{1}{2}\left(\frac{2\beta^x - \beta^y - \beta^z}{2} - y + z, \frac{-\beta^x + 2\beta^y + \beta^z}{2} + z + x, \frac{-\beta^x + \beta^y + 2\beta^z}{2} - x - y\right) \\
\mathbf{S}_2 &= \frac{1}{2}\left(\frac{2\beta^x - \beta^y + \beta^z}{2} - y - z, \frac{-\beta^x + 2\beta^y - \beta^z}{2} - z + x, \frac{\beta^x - \beta^y + 2\beta^z}{2} + x + y\right)
\end{aligned}
$$

$$\mathbf{S}_3 = \frac{1}{2}\left(\frac{2\beta^x+\beta^y-\beta^z}{2}+y+z, \frac{\beta^x+2\beta^y-\beta^z}{2}-z-x, \frac{-\beta^x-\beta^y+2\beta^z}{2}-x+y\right). \tag{2.60}$$

If we then employ the four normalisation constraints in the form:

$$\begin{aligned} |\mathbf{S}_0|^2+|\mathbf{S}_1|^2+|\mathbf{S}_2|^2+|\mathbf{S}_3|^2-4 &= 0, \\ |\mathbf{S}_0|^2+|\mathbf{S}_1|^2-|\mathbf{S}_2|^2-|\mathbf{S}_3|^2 &= 0, \\ |\mathbf{S}_0|^2-|\mathbf{S}_1|^2+|\mathbf{S}_2|^2-|\mathbf{S}_3|^2 &= 0, \\ |\mathbf{S}_0|^2-|\mathbf{S}_1|^2-|\mathbf{S}_2|^2+|\mathbf{S}_3|^2 &= 0, \end{aligned} \tag{2.61}$$

we get the following four relationships:

$$x^2+y^2+z^2 = 2-\frac{3}{4}\left[(\beta^x)^2+(\beta^y)^2+(\beta^z)^2\right],$$

$$\begin{aligned} \left(y-\frac{\beta^y}{2}\right)\left(z+\frac{\beta^z}{2}\right) &= \beta^y\beta^z, \\ \left(z-\frac{\beta^z}{2}\right)\left(x+\frac{\beta^x}{2}\right) &= \beta^z\beta^x, \\ \left(x-\frac{\beta^x}{2}\right)\left(y+\frac{\beta^y}{2}\right) &= \beta^x\beta^y. \end{aligned} \tag{2.62}$$

We can then rewrite the final three equations as:

$$\begin{aligned} \beta^y\beta^z\left(x^2-\frac{5}{4}(\beta^x)^2\right) &= 0, \\ \beta^z\beta^x\left(y^2-\frac{5}{4}(\beta^y)^2\right) &= 0, \\ \beta^x\beta^y\left(z^2-\frac{5}{4}(\beta^z)^2\right) &= 0. \end{aligned} \tag{2.63}$$

Despite the problem being over constrained, we can see two types of solution. Firstly there is:

$$x^2+y^2=2-\frac{3}{4}\left[(\beta^x)^2+(\beta^y)^2\right], \qquad \left(x-\frac{\beta^x}{2}\right)\left(y+\frac{\beta^y}{2}\right)=\beta^x\beta^y,$$

$$z=0, \qquad \beta^z=0, \tag{2.64}$$

(and cyclic permutations), which provides an alternative route to find the solutions consistent with the external field lying in a plane perpendicular to one of the Cartesian axes (which were discussed in the previous section). Secondly, we find the independent solutions specified by:

$$x=\pm\frac{\sqrt{5}}{2}\beta^x, \qquad y=\pm\frac{\sqrt{5}}{2}\beta^y, \qquad z=\pm\frac{\sqrt{5}}{2}\beta^z,$$

$$|\beta|=(\beta^x)^2+(\beta^y)^2+(\beta^z)^2=1, \tag{2.65}$$

where the scaled external field lies on the unit sphere. We note that this external field strength is exactly half that required for the ferromagnetic moment to saturate.

There are two solutions for $|\beta|=1$ which can both be understood physically as a sum of four terms. Firstly, each spin had a contribution proportional to the external field. The other three terms are distorted spirals perpendicular to the three Cartesian axes. The three spirals each have a magnitude proportional to the external field strength along the corresponding Cartesian axis. For each spiral, the two components have relative magnitudes of $\left\{\frac{\pm\sqrt{5}+1}{2}, \frac{\pm\sqrt{5}-1}{2}\right\}$. Finally we note that for the particular case of $\beta=(\pm1,\pm1,\pm1)/\sqrt{3}$, i.e. when the field is orientated along one of the tetrahedral axes, there is a much simpler description of the two states. The spin lying on the appropriate tetrahedral axis points parallel to the field, while the remaining three spins spiral symmetrically (either clockwise or anticlockwise) around the field direction. One of the pair of states for $\beta=(1,1,1)/\sqrt{3}$ is shown in Fig. 2.18.

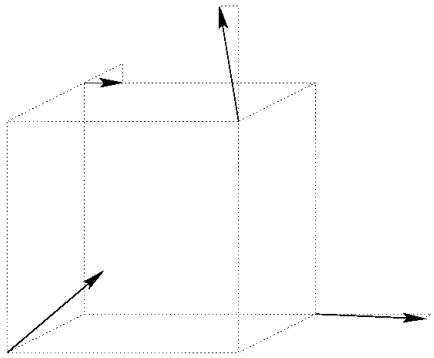

Figure 2.18: The spin configuration for a scaled external field of $\beta = (1,1,1)/\sqrt{3}$.

2.7 Connections to neutron scattering

Neutron scattering is a key tool for experimentally studying magnetic ordering. In this final section we will therefore discuss some links between the dipole interaction and elastic neutron scattering. As explained in Section 1.4.1 the scattering intensity at a Bragg spot at position $\mathbf{k}$ in reciprocal space is given by:

$$I \propto |f(\mathbf{k})|^2 \left[|\mathbf{S}_\mathbf{k}|^2 - |A_\mathbf{k}|^2 \right], \tag{2.66}$$

where $f(\mathbf{k})$ is the form factor, $\mathbf{S}_\mathbf{k}$ is the structure factor and

$$A_\mathbf{k} = \hat{\mathbf{k}} \cdot \mathbf{S}_\mathbf{k}, \tag{2.67}$$

represents the orientational factor.

We return to the sub-band representation of the dipolar energy and recall that

$$\frac{\mu}{2\mathcal{V}(\Omega)} \sum_\mathbf{k} \sum_\mathbf{G} |\mathbf{S}_\mathbf{k} \cdot (\mathbf{k}+\mathbf{G})|^2 \tilde{V}(|\mathbf{k}+\mathbf{G}|), \tag{2.68}$$

which was derived in Appendix A. In this expression,

$$\mathbf{S}_\mathbf{k} = \frac{1}{\sqrt{N}} \sum_j e^{i\mathbf{k}\cdot\mathbf{R}_j} \mathbf{S}_j, \tag{2.69}$$

where $\mathbf{R}_j$ ranges over the small-scale face-centre-cubic lattice, $\mathbf{k}$ ranges over the associated Brillouin zone and $\mathbf{G}$ over the large-scale body-centre reciprocal-space super-lattice. If the spins on the titanium sites are set to zero, $\mathbf{S_k}$ then provides the structure factors for the pyrochlore lattice. Finally, $\tilde{V}(K)$, the Fourier transform of the potential $V(X) = \frac{1}{X}$ but with $V(X) \mapsto 0$ as $X \mapsto 0$, is a positive monotonically decreasing function. To minimise the dipole interaction we therefore need to make $\mathbf{S_k} \cdot (\mathbf{k} + \mathbf{G}) = 0$, in particular for the Bragg spots closest to the origin, as their contributions are dominant. However, as $\mathbf{S_k} \cdot (\mathbf{k} + \mathbf{G})$ is also proportional to the orientational factor given in Equation 2.67, we have a direct link between the Bragg peak intensities and the dipole interaction. Physically, this is because magnetic neutron scattering occurs as a result of the magnetic moment of the neutron and a magnetic moment in the target system experiencing a dipole interaction. For systems in which the dipole energy is minimised we expect the Bragg spots closest to the origin to be of maximal intensity subject to the value of the structure factor. In other words we expect the orientational factors to vanish for the Bragg spots closest to the origin. This is indeed the case for $Gd_2Sn_2O_7$, as can be seen in Fig. 2.2. In contrast, for the compound $Er_2Ti_2O_2$ (which we will discuss in detail in Chapter 5), the eight Bragg spots closest to the origin are found to be either quite weak or vanishingly small[66]. This implies that for $Er_2Ti_2O_7$ the dipolar interaction is frustrated.

In the case of the $\mathbf{k} = \mathbf{0}$ system, $Gd_2Sn_2O_7$, the eight Bragg spots closest to the origin are located at wave-vectors of:

$$\begin{aligned} &\mathbf{Q}_0 = (000), \qquad \mathbf{Q}_1 = (200), \qquad \mathbf{Q}_2 = (020), \qquad \mathbf{Q}_3 = (002), \\ &\mathbf{K}_0 = (111), \qquad \mathbf{K}_1 = (1\bar{1}\bar{1}), \qquad \mathbf{K}_2 = (\bar{1}1\bar{1}), \qquad \mathbf{K}_3 = (\bar{1}\bar{1}1), \end{aligned} \tag{2.70}$$

which have the following structure factors:

$$\begin{aligned} \mathbf{S}_{\mathbf{Q}_0} &= \frac{1}{4}(\mathbf{S}_0 + \mathbf{S}_1 + \mathbf{S}_2 + \mathbf{S}_3) = \frac{1}{2}\mathbf{T}, \qquad \mathbf{S}_{\mathbf{K}_0} = +\frac{1}{2}(\mathbf{S}_0 - \mathbf{T}), \\ \mathbf{S}_{\mathbf{Q}_1} &= \frac{1}{4}(\mathbf{S}_0 + \mathbf{S}_1 - \mathbf{S}_2 - \mathbf{S}_3), \qquad \mathbf{S}_{\mathbf{K}_1} = -\frac{1}{2}(\mathbf{S}_1 - \mathbf{T}), \end{aligned}$$

$$\begin{aligned}
\mathbf{S}_{\mathbf{Q}_2} &= \frac{1}{4}\left(\mathbf{S}_0 - \mathbf{S}_1 + \mathbf{S}_2 - \mathbf{S}_3\right), & \mathbf{S}_{\mathbf{K}_2} &= -\frac{1}{2}\left(\mathbf{S}_2 - \mathbf{T}\right), \\
\mathbf{S}_{\mathbf{Q}_3} &= \frac{1}{4}\left(\mathbf{S}_0 - \mathbf{S}_1 - \mathbf{S}_2 + \mathbf{S}_3\right), & \mathbf{S}_{\mathbf{K}_3} &= -\frac{1}{2}\left(\mathbf{S}_3 - \mathbf{T}\right).
\end{aligned} \tag{2.71}$$

If the dipolar energy is to be minimised, we have established that we expect these structure factors to be perpendicular to their corresponding wave-vector, so that the following orientational factors will vanish:

$$\begin{aligned}
A_{\mathbf{Q}_0} &\propto \mathbf{T}\cdot\mathbf{Q}_0 = \mathbf{0}, & A_{\mathbf{K}_0} &\propto \mathbf{S}_0\cdot\mathbf{K}_0, \\
A_{\mathbf{Q}_1} &\propto S_0^x + S_1^x - S_2^x - S_3^x, & A_{\mathbf{K}_1} &\propto \mathbf{S}_1\cdot\mathbf{K}_1, \\
A_{\mathbf{Q}_2} &\propto S_0^y - S_1^y + S_2^y - S_3^y, & A_{\mathbf{K}_2} &\propto \mathbf{S}_2\cdot\mathbf{K}_2, \\
A_{\mathbf{Q}_3} &\propto S_0^z - S_1^z - S_2^z + S_3^z, & A_{\mathbf{K}_3} &\propto \mathbf{S}_3\cdot\mathbf{K}_3.
\end{aligned} \tag{2.72}$$

We notice that, with the exception of $A_{\mathbf{Q}_0}$, these orientational factors are proportional to the arguments of the seven quadratics in Equation 2.35 which describes the dipole energy in the $\mathbf{k} = \mathbf{0}$ subspace. Our exact solutions (for which all seven quadratics vanish) therefore correspond to also making these seven orientational factors vanish. Finally, we note that the linear relationship between the seven arguments of Equation 2.35 (discussed in Section 2.4 is equivalent to

$$\mathbf{Q}_0\cdot\mathbf{S}_{\mathbf{Q}_0} + \mathbf{Q}_1\cdot\mathbf{S}_{\mathbf{Q}_1} + \mathbf{Q}_2\cdot\mathbf{S}_{\mathbf{Q}_2} + \mathbf{Q}_3\cdot\mathbf{S}_{\mathbf{Q}_3} = \mathbf{K}_0\cdot\mathbf{S}_{\mathbf{K}_0} - \mathbf{K}_1\cdot\mathbf{S}_{\mathbf{K}_1} - \mathbf{K}_2\cdot\mathbf{S}_{\mathbf{K}_2} - \mathbf{K}_3\cdot\mathbf{S}_{\mathbf{K}_3}, \tag{2.73}$$

which can be obtained from the four linear relationships between the pyrochlore structure factors which were given in Equation 5.17.

2.8 Experimentally observed low temperature phase transitions

In the final section of this chapter we will briefly discuss the experimentally observed low temperature phase transitions of $Gd_2Sn_2O_7$ when an external magnetic field is applied. Unfortunately, however, only powder samples of $Gd_2Sn_2O_7$ are available and as a result the experiments average over all external field directions which prevents a direct comparison with our exact solutions, as they only hold for specific highly symmetrical field directions. Powder elastic neutron scattering measurements by Stewart *et al.*[70] find that the Bragg peak intensities vary as a function of the external magnetic field strength (data was recorded at a temperature of $50mK$ and the Bragg peaks remained indexed by $\mathbf{k} = \mathbf{0}$ as the field was increased). Although the number of distinct magnetic phases is difficult to interpret from the variation of the Bragg peak intensities, Stewart *et al.* identify two phase transitions at external magnetic field strengths of approximately $2.5T$ and $5.25T$, though they do not give any interpretation of the different phases. Given that the positions of the phase boundaries proposed by Stewart *et al.* were somewhat tentative, they are consistent with those identified by Freitas *et al.*[27] using a.c. susceptibility experiments. Freitas *et al.* also find that only two phase boundaries persist down to temperatures of around $0.4K$ (though more are present at temperatures of about $0.9K$). When the two low temperature phase transitions were extrapolated down to $50mK$ by Freitas *et al.*, they were found to occur at magnetic field strengths of about $3.5T$ and $5.5T$. Furthermore, the phase transition at $B \approx 5T$ is associated with the ferromagnetic saturation of the spins[27], while the other phase transition occurs at a magnetic field strength of around half this value.

To compare the behaviour of our model with the experimental findings we need to solve the model for general field directions rather than just the highly symmetric field orientations which we found supported exact solutions. This is beyond the scope of this thesis, however, numerical minimisation calculations by M.W. Long[43] found that for general (unsymmetrical) field directions the phase transitions vanish to become crossovers

instead. One point of note, however, is that for an external field orientation of $\mathbf{B} = (1,1,1)/\sqrt{3}$, at exactly half saturation, M.W. Long found a first order phase transition (in which one of the spin orientations jumps discontinuously), although this also becomes a cross over for fields slightly mis-aligned from $\mathbf{B} = (1,1,1)/\sqrt{3}$. In addition, for all field orientations, at exactly half saturation, we found two chirally related exact solutions, whereas the general field calculations by M.W. Long found that this degeneracy vanishes for field strengths slightly away from half saturation, which could give rise to a phase transition as the field strength moves through half saturation. We therefore have two possible candidates for the experimentally observed phase transition at half saturation (assuming that it does actually occur at this magnetic field strength): firstly the first order transition for a field parallel to $\mathbf{B} = (1,1,1)/\sqrt{3}$ and secondly a transition associated with the change in degeneracy of the solutions when the field strength is exactly at half saturation. As both options, however, only involve a tiny fraction of the available orientational phase-space of the external field, it is not clear whether or not either would be experimentally observable. This concludes our discussion of $Gd_2Sn_2O_7$ in an external magnetic field. We now leave this topic and in the next chapter we will turn to considering the low temperature magnetic ordering of $Gd_2Ti_2O_7$.

CHAPTER 3

GADOLINIUM TITANATE: REAL-SPACE APPROACH (EXOTIC MULTIPLE-Q MAGNETISM)

3.1 Introduction

In this chapter we will discuss the low-temperature magnetic ordering of $Gd_2Ti_2O_7$. This compound has an identical structure to that of $Gd_2Sn_2O_7$ (which we considered in the previous Chapter) with the exception that the positions of some of the oxygen atoms differ slightly. This distortion was explained in Section 1.3 and amounts to a change in position of the O2 (shown in Fig. 1.14) of less than 3%. In the previous chapter we established that the low-temperature magnetic ordering of $Gd_2Sn_2O_7$ is controlled by the dipole interaction in the presence of a dominant nearest neighbour Heisenberg exchange interaction. Furthermore the $\mathbf{k} = \mathbf{0}$ ordering observed in $Gd_2Sn_2O_7$[75] should be robust against changes in the relative strength of the two interactions. As is the case for $Gd_2Sn_2O_7$, the only magnetic ions in $Gd_2Ti_2O_7$ are the Gd^{3+} ions. They form a pyrochlore lattice and from Hund's rules have: $S = 7/2, L = 0, J = 7/2$ leading to a theoretically expected ordered moment of $m \approx 7\mu_B$, i.e. large, classical, isotropic spins. Naively, one might therefore expect that the low-temperature magnetic ordering in $Gd_2Ti_2O_7$ would also be controlled by the same interactions as $Gd_2Sn_2O_7$ and thus also show a single transition to a long-range magnetically ordered state (with propagation vector $\mathbf{k} = \mathbf{0}$) at

a temperature with an order of magnitude of $1K$.

The Curie-Weiss temperature of $Gd_2Ti_2O_7$ is $\theta_C = -9.9K$[8]. This is within $1K$ of that observed for $Gd_2Sn_2O_7$ and indicates that as expected the antiferromagnetic Heisenberg exchange interaction dominates the low-temperature energetics. We estimate the strength of the dipole interaction coupling constant to be $|J_D|/k_B \approx 0.91K$, where we have used a lattice constant of $a = 10.46\mathring{A}$[8]. This differs by less than $0.1K$ from that estimated for $Gd_2Sn_2O_7$ (see Section 2.2). So far the energetics of the two materials appear entirely equivalent. As in $Gd_2Sn_2O_7$, this interaction is frustrated, and the onset of long-range magnetic order is also seen at a temperature scale of the order of $1K$[8, 62], indicating that the dipole interaction plays an active role in the ordering. However, as shown in Fig 3.1, the specific heat data from Petrenko *et al.*[62] actually show two phase transitions: one at $1.045K$ to an intermediate phase, and another transition at $0.75K$ to the low-temperature magnetically ordered phase. In addition elastic neutron scattering experiments by Stewart *et al.* show that the low temperature phase is indexed by the propagation vector $\mathbf{k} = (1/2, 1/2, 1/2)$[21, 69]. The energetics governing the low temperature behaviour of $Gd_2Ti_2O_7$ must differ from those controlling $Gd_2Sn_2O_7$. In our discussion of $Gd_2Sn_2O_7$ in the previous chapter we neglected the effects of further neighbour Heisenberg exchange couplings. It therefore seems natural to investigate the effects these interactions when studying the energetics of $Gd_2Ti_2O_7$.

The magnetic ordering of $Gd_2Ti_2O_7$ is much less well understood than that of $Gd_2Sn_2O_7$. In the next section we will describe two key experiments: firstly the elastic neutron scattering mentioned above and secondly Mössbauer experiments by Bonville *et al.*[8]. As we will discus, the current interpretations of these experiments provide contradictory pictures of the magnetic ordering . In particular, the only class of $\mathbf{k} = (1/2, 1/2, 1/2)$ states found to be compatible with the neutron scattering data by Stewart *et al.* [21, 69] were inconsistent with the equal-length spin constraints of a classical system. In contrast, the Mössbauer results are consistent with these constraints. In this chapter we aim to find new $\mathbf{k} = (1/2, 1/2, 1/2)$ states with equal-length spins and therefore with the potential to

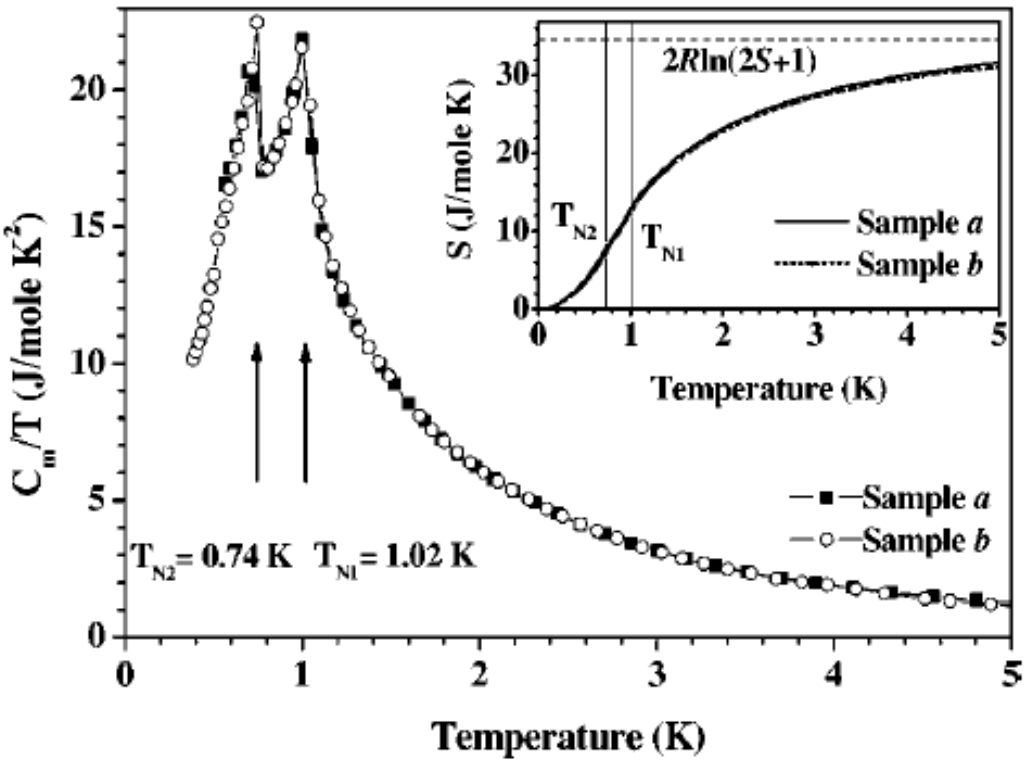

Figure 3.1: Specific heat data for $Gd_2Ti_2O_7$ from Petrenko *et al.*[62] plotted as C_p/T vs. T. The inset shows the temperature variation of the entropy and the the dashed line represents the total entropy for a spin of $S = 7/2$: $2R\ln 8 = 34.6 Jmol^{-1}K^{-1}$.

resolve the inconsistencies between the two apparently conflicting experiments.

The energetics governing the magnetic ordering is currently poorly understood. Furthermore $\mathbf{k} = (1/2, 1/2, 1/2)$ ordering is extremely complex (having sixteen independent spin degrees of freedom). For these reasons we will take the unusual approach of introducing a number of experimentally motivated real-space spin constraints in order to reduce the degeneracy of the problem to a tractable level. After solving our constrained problem on a single tetrahedron, we then look for states which also have $\mathbf{k} = (1/2, 1/2, 1/2)$ magnetic ordering. We discuss the physical interpretation of our new states and then investigate the energetics that might stabalise them; in particular we consider the role of further neighbour Heisenberg exchange couplings. Finally we discuss the extent to which these states can explain the elastic neutron scattering and Mössbauer data.

3.2 Key experiments

In this section we will discuss the two experiments which provide the most information regarding the low-temperature magnetically ordered state of $Gd_2Ti_2O_7$. The first of these is the elastic neutron scattering neutron scattering by Stewart *et al.*[21, 69]. Secondly we will consider the Mössbauer data by Bonville *et al.*[8]. As alluded to in the previous section, the current interpretations of the two experiments are contradictory.

The elastic neutron scattering data by Stewart *et al.*[21, 69] is indexed by the propagation vector $\mathbf{k} = (1/2, 1/2, 1/2)$. This means that in real space the unit cell length doubles in all three direction. As a consequence, the magnetic unit cell contains $4 \times 2^3 = 32$ spins, sixteen of which provide independent degrees of freedom, with the other sixteen being their anti-parallel counterparts. To fit the data to this many parameters, while also satisfying the sixteen equal-length spin constraints for a classical system, is a difficult task. The only states found by Stewart *et al.* that fitted the Bragg peak intensities well are the two shown in Fig 3.2. The state on the left is the single-q "Kagomé planes" state that

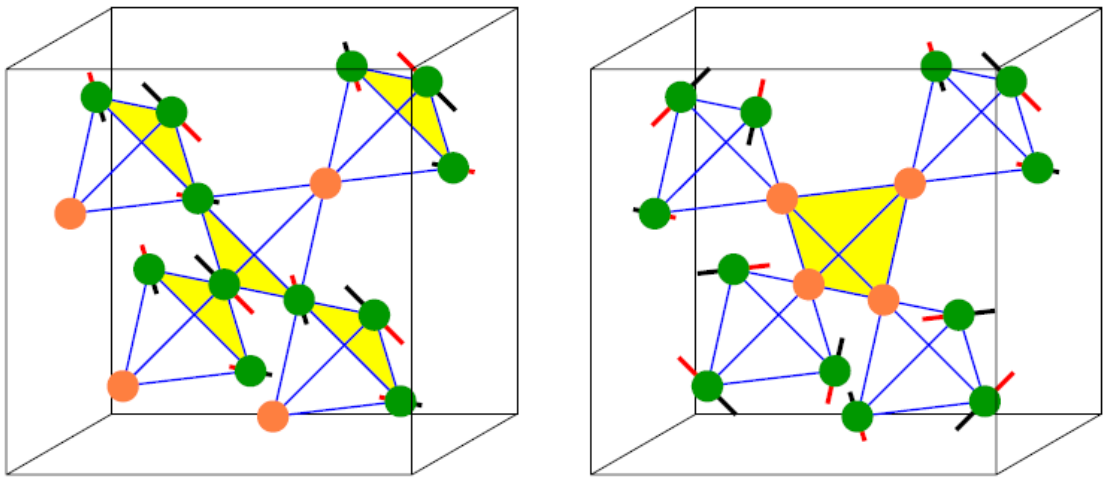

Figure 3.2: States proposed to fit elastic neutron scattering from Stewart *et al.*[69]. (left)Single-q state. (right) four-q state. The green sites carry the full $S = 7/2$ moments. For $T > 0.7K$ the moment on the orange sites averages to zero. At $T \leq 0.7K$ the orange sites develop a small ordered moment (of $m = 1.9\mu_B$) and there is a slight out of plane canting of the green moments.

was described at the end of Section 2.3.2 and the state on the right is a four-q variant of this state. In both states the green spins carry the full $S = 7/2$ ordered moment. In the intermediate-temperature phase, the orange sites have zero moment, though in the low temperature phase $T \leq 0.7K$ the data (recorded at a temperature of $250mK$) shows a good fit when fit to a small moment of $m = 1.9\mu_B$ on these sites (and additionally a slight out of plane canting of the green moments). The fit to this state by Stewart *et al.* is shown in Fig. 3.3, with the lower plot representing the error in this fit. As this error is

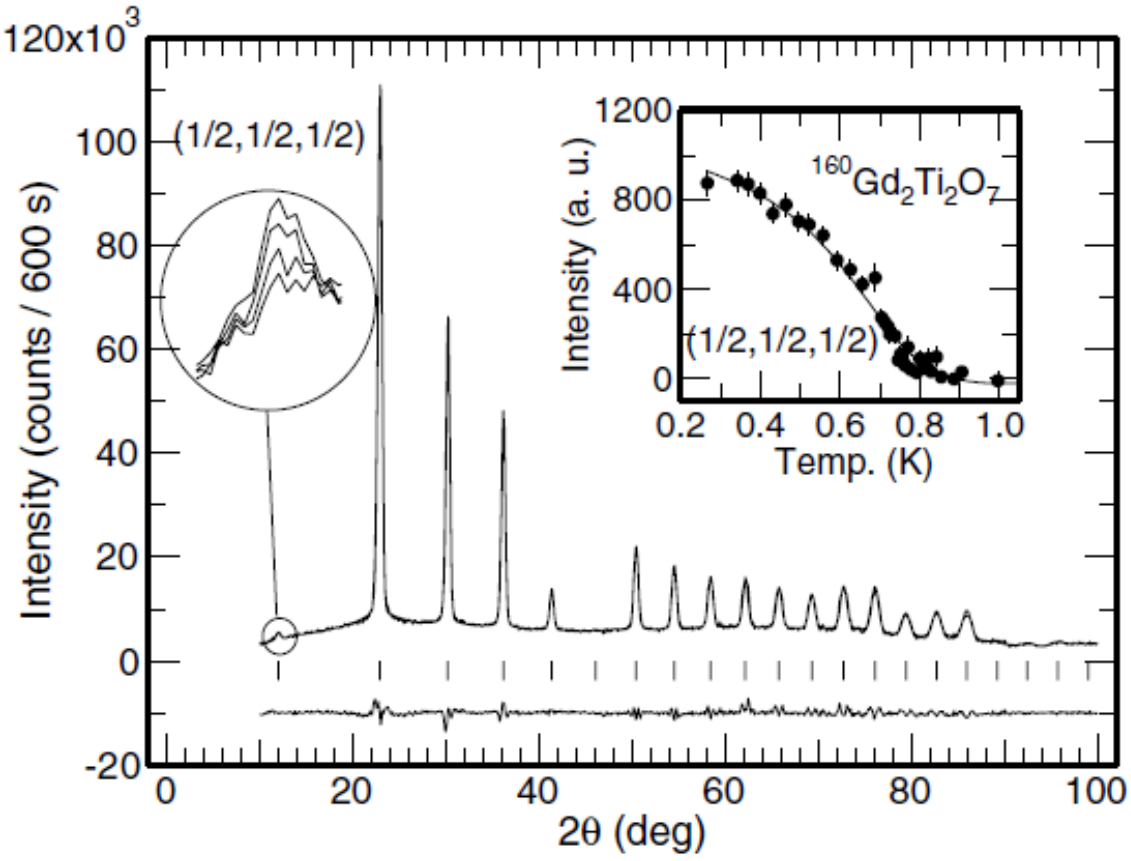

Figure 3.3: Rietveld fit at $250mK$ of the magnetic only scattering to the 'Kagomé planes' state (Fig. 3.2) from Stewart *et al.*[69]. The lower line represents the error in the fit. On the left the $\mathbf{k} = (1/2, 1/2, 1/2)$ Bragg peak intensity is enlarged. Magnetic reflections at temperatures of $420mK$, $540mK$, $670mk$ and $750mK$ in order of decreasing intensity are shown. The inset shows the temperature dependence of the intensity of this reflection, which disappears at the onset of the intermediate-temperature phase at $T \approx 0.7K$ (see Fig. 3.1).

small, the figure also provides an excellent qualitative picture of the measured Bragg peak

intensities. We notice that the intensity of the $\mathbf{k} = (1/2, 1/2, 1/2)$ Bragg spot (the one closest to the origin) is vanishingly small. The structure factor of this Bragg spot is expected to be zero if the nearest neighbour Heisenberg exchange interaction is infinite (see Section 3.5 for an explanation). In the intermediate-temperature phase this spot has zero measured intensity. In the low temperature phase, however, it develops a finite intensity of a value about one hundredth of the size of the next Bragg spot closest to the origin. The Bragg spots closest to the origin (with the exception of the $\mathbf{k} = (1/2, 1/2, 1/2)$ spot) can be seen to be dominant. Though it is not clear whether their orientational factors are actually maximal, this is indicative that the dipolar interaction is close to minimal (see discussion surrounding Equation 2.68).

As the Gd^{3+} ions have $S = 7/2$ and $L = 0$, they are expected to behave as large classical isotropic spins. The states proposed by Stewart *et al.*[69] to fit their magnetic Bragg scattering data are controversial due to the greatly reduced ordered moment on a quarter of the Gd^{3+} sites. At a temperature of $250mK$ this cannot be attributed to thermal fluctuations. Specific heat measurements can account for 90% of the expected $2R \ln 8 Jmol^{-1}K^{-1}$ of magnetic entropy when integrated up to temperatures of $5K$, and by $10K$ virtually all of the entropy is recovered (though measurements are believed to be very sensitive to the sample quality)[62, 8]. Quantum fluctuations are also highly unlikely to stabalise either of the proposed states. For the single-q state, the reduced moments lie on a sparse triangular lattice. They are therefore well separated from each other. In contrast in the four-q state, the reduced spins form tetrahedra so it is conceivable that they could fluctuate. This would however incur an energy penalty resulting from frustrating the nearest neighbour Heisenberg exchange with the neighbouring four tetrahedra. To estimate this we consider the dominant Heisenberg energy for a single tetrahedron. This is given by

$$H_0 = \frac{J}{2} \sum_{ij} \hat{\mathbf{S}}_i \cdot \hat{\mathbf{S}}_j = \frac{J}{2} \hat{\mathbf{T}} \cdot \hat{\mathbf{T}} - 2JS(S+1), \tag{3.1}$$

where we have used $\hat{\mathbf{T}}$ to represent the total spin of the tetrahedron. The ground-state

occurs when $\hat{\mathbf{T}} = \mathbf{0}$, which gives

$$E_0 = E_{Cl} - 2JS. \tag{3.2}$$

The energy of the classical ground state, E_{Cl} is obtained by summing over two bonds with parallel spins and four bonds with anti-parallel spins so that $E_{Cl} = -2JS^2$. We can therefore identify the energy gained from quantum fluctuation as $E_{qF} = -2JS$. Next we will consider the energy penalty arising from disrupting the four surrounding tetrahedra. Each of these tetrahedron (with three green sites in Fig. 3.2) have a classical energy of $-3JS^2/2$ which is equivalent to a total energy penalty $4(-JS^2/2)$. As $S = 7/2$ this energy penalty far outweighs the gain from the quantum fluctuation energy and as a result it seems implausible that quantum fluctuations could be the cause of the severely reduced moment of a quarter of the Gd^{3+} sites. The only remaining possibility is that these spins are statically disordered, however no energetic argument for this is offered.

Next we will consider the Mössbauer data by Bonville *et al.*[8]. Mössbauer is only sensitive to the local environment of the magnetic moments as opposed to elastic neutron scattering which averages over the long-range magnetic structure of the system. It therefore provides complimentary information. At temperatures of $T > 1K$ (above the ordering transition) we see only a quadrapole splitting due to the symmetry axis of the crystal-field along the local tetrahedral axis (e.g. the $\langle 1, 1, 1 \rangle$ direction). This is shown in Fig. 3.4 form Bonville *et al.*[8]. For $T < 1K$ more structure appears in the data, which is associated with the magnetic ordering of the Gd^{3+} moments. Two scenarios were used to fit the lowest temperature data ($27mK$), with the results shown in Fig. 3.5. The first is that labeled 'static'. For this fit it was assumed that every spin had the same magnetic moment, and that this moment was aligned perpendicular to the local tetrahedral axis (along with the quadrapolar background). Secondly the 'dynamic' fit consisted of a sum of two contributions. The first had a weight of 3/4 and was identical to that used in the 'static' hypothesis and the second (with a weight of 1/4) assumed there were no magnetic

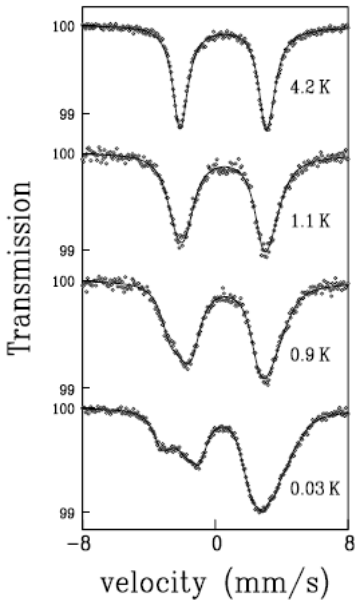

Figure 3.4: Temperature dependence of the ^{155}Gd Mössbauer absorption spectrum for $Gd_2Ti_2O_7$from Bonville *et al.*[8].

moments and only included the quadrapolar background contribution. This was done to look for consistency with the elastic neutron scattering data; in other words the 'dynamic' hypothesis was done to model the behaviour of the states shown in Fig. 3.2 in which one quarter of the moments were somehow fluctuating. It can be seen that the static fit is very good whereas the dynamic fit is completely inconsistent with the data.

Although the local spin environment in the low-temperature phase appears well explained by the simple model used for the static hypothesis, in the intermediate temperature phase the picture is not so clear cut. Though not unexpected, it turns out that the error in the fit can be reduced by adding extra parameters. The top pair of curves of Fig. 3.6[8] reproduces the fit to the static hypothesis in the intermediate temperature phase, with the top-most curve displaying the error between the data and simulation. This can be seen to spike slightly at the place indicated by the arrow in the Figure. The bottom pair of curves offers an alternative fit again using a sum of two contributions. The first contribution uses the static hypothesis weighted with 3/4 for which the moments are all orientated perpendicular to the local tetrahedral axes with a moment of $\mathbf{m} = 5.7\mu_B$; the second uses a 1/4 weighted modified dynamic hypothesis in which the spins have a

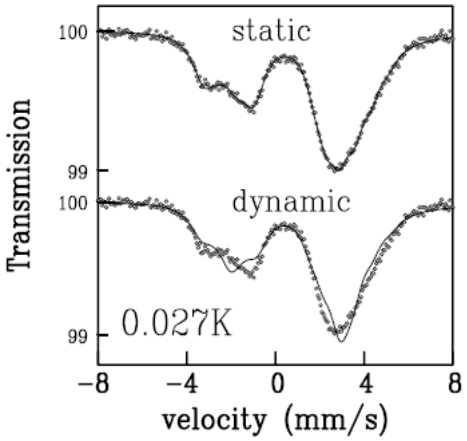

Figure 3.5: Two alternative fits to the ^{155}Gd Mössbauer spectra of $Gd_2Ti_2O_7$ at $T = 0.027K$ by Bonville *et. al*[8], using the 'static' hypothesis (top) and 'dynamic' hypothesis (bottom). The static hypothesis assumes that every Gd^{3+} site has the same magnitude magnetic moment and that they are orientated in planes perpendicular to the local tetrahedral axes. The dynamic hypothesis consists of the sum of two contributions. The first is equivalent to the static hypothesis with a weight of three-quarters, while the second contribution has a weight of one quarter and only includes the quadrapolar contribution (i.e. it assumes that there is zero moment on the Gd^{3+} sites).

reduced moment of $\mathbf{m} = 3.3\mu_B$, which is orientated at an angle of $60 \pm 10°$ to the local tetrahedral axis. This fit has a reduced error when compared to the static hypothesis, in particular at the place indicated by the arrow in Fig. 3.6. The temperature dependence of the size of the Gd^{3+} moments for the optimum models are shown in Fig. 2.5[8].

In summary the Bragg scattering intensities have been fit to states in which a quarter of the Gd^{3+} ions have a severely reduced moment in the low-temperature phase, and no moment in the intermediate-temperature phase. In contrast Mössbauer data supports the scenario that in the low-temperature phase all spins have equal magnitude moments which lie in the planes perpendicular to the local tetrahedral axis (from now on we will refer to these planes as the 'Mössbauer planes'). In addition the fit for the intermediate-temperature phase using this model is not bad, however, it can be improved upon by introducing two different magnitudes of magnetic moment and allowing those spins of reduced moment to distort out of the 'Mössbauer planes'. We are not in a position however to be able to disentangle the effects of two extra parameters introduced into the fit. Our aim is therefore to initially focus on trying to understand the low-temperature

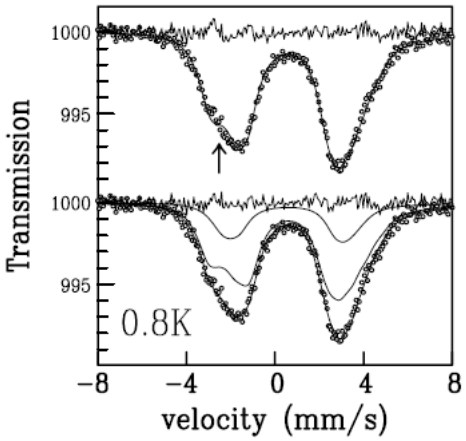

Figure 3.6: Two alternative fits to the ^{155}Gd Mössbauer data for $Gd_2Ti_2O_7$ at $T = 0.8K$ (i.e. in the intermediate temperature magnetically ordered phase) reproduced from Bonville *et. al*[8]. The upper curve shows the fit to a single hyperfine field orientated perpendicular to the local tetrahedral axes, with the error in the fit shown above. The lower curve shows the result of fitting to the sum of two 'sub-spectra'. The first, representing 75% of the transmission intensity, assumes a hyperfine field equivalent to moments of magnitude $\mathbf{m} = 5.7\mu_B$ orientated perpendicular to the local tetrahedral axes. The second contribution, which represents 25% of the transmission intensity, assumes a smaller hyperfine field, which is equivalent to magnetic moments of magnitude $\mathbf{m} = 3.3\mu_B$ which are orientated at an angle of $\sim 60^\circ$ to the local tetrahedral axes. The error in the fit at the velocity indicated by an arrow can be seen to be noticeably reduced in the lower fit.

magnetic ordering. We wish to find new $\mathbf{k} = (1/2, 1/2, 1/2)$ phases which are candidates to fit the neutron scattering intensities while also being consistent with the Mössbauer data.

3.3 Real-space spin constraints for a single tetrahedron

In this section we will enforce a number of real-space spin constraints in order to look for new magnetically ordered states with the potential to be consistent with both the elastic neutron scattering and Mössbauer data. We choose this approach because, as discussed in the previous section, to solve generally for all $\mathbf{k} = (1/2, 1/2, 1/2)$ states on the pyrochlore lattice is extremely difficult as there are sixteen independent spin degrees of freedom. We therefore require some additional constraints to reduce the size of this phase-space to a

more manageable size. Initially we will consider just a single tetrahedron and enforce three constraints:

1. Equal length (normalised) spins,

2. Total spin of the tetrahedron sums to zero,

3. Spins lying in the Mössbauer planes (i.e. perpendicular to the local tetrahedral axis).

The single tetrahedral solutions can then be combined together to generate states that are also consistent with the $\mathbf{k} = (1/2, 1/2, 1/2)$ propagation vector. These states can then be assessed by comparing their expected Bragg peak intensities to the elastic neutron scatting data.

The first constraint has both an energetic and experimental footing, as was discussed in the previous section. The second constraint is equivalent to assuming that the nearest neighbour exchange interaction is infinite (see Section 1.2.2). We note that this approximation appears well founded due to the vanishingly small observed intensity of the $\mathbf{k} = (1/2, 1/2, 1/2)$ Bragg peak intensity (see Fig. 3.2 and discussion in Section 2.7), though not perfect. Applying these first two constraints, however, only reduces the twelve degrees of freedom down to five, hence our motivation for also enforcing the third constraint which leaves us with only one degree of freedom per tetrahedron. This third constraint, however has little energetic basis. We saw in Section 2.4 that placing the spins in these planes is equivalent to partially minimising the dipolar interaction, which we believe to play an active role in the magnetic ordering. However, we also know, via comparison with $Gd_2Sn_2O_7$, that the dipolar interaction is likely to be only half the story, with further neighbour Heisenberg interact actions probably playing a key role, the result of which could be to frustrate the dipolar interaction. The basis for the third constraint is therefore purely experimental, which is risky. It is highly probably that distorting the spins slightly out of the Mössbauer plains could produce states of lower energy but which appear to fit the Mössbauer data equivalently well due to the experimental noise. We

have no way of finding such states using this approach. Ideally we would tackle this problem using the more usual approach of considering only the energetics. Unfortunately this is not possible as the magnetic ordering is likely to be highly sensitive to the precise balance between the dipolar and further neighbour Heisenberg exchange interaction (as is exhibited via the differing behaviour of $Gd_2Sn_2O_7$ and $Gd_2Ti_2O_7$), which is unknown to us.

We choose to label the four spins forming a tetrahedron as is shown in Fig. 3.7, where the planes perpendicular to the appropriate tetrahedral axes are are also shown. The axes, $\hat{\mathbf{z}}_\alpha$, corresponding to the normalised spins, $\hat{\mathbf{S}}_\alpha$, are given by:

$$\begin{aligned} \hat{\mathbf{z}}_\mathbf{0} &= (+\hat{\mathbf{x}} + \hat{\mathbf{y}} + \hat{\mathbf{z}})/\sqrt{3}, \qquad \hat{\mathbf{z}}_\mathbf{1} = (+\hat{\mathbf{x}} - \hat{\mathbf{y}} - \hat{\mathbf{z}})/\sqrt{3}, \\ \hat{\mathbf{z}}_\mathbf{2} &= (-\hat{\mathbf{x}} + \hat{\mathbf{y}} - \hat{\mathbf{z}})/\sqrt{3}, \qquad \hat{\mathbf{z}}_\mathbf{3} = (-\hat{\mathbf{x}} - \hat{\mathbf{y}} + \hat{\mathbf{z}})/\sqrt{3}. \end{aligned} \tag{3.3}$$

Initially we will focus on the first and third constraint. These are satisfied by all states

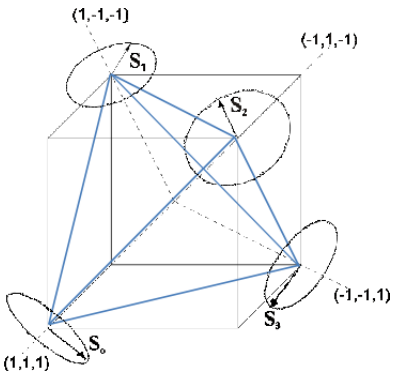

Figure 3.7: The nomenclature that we will use to describe the four spins forming a single tetrahedron. Each spin will be restricted to lie within the plane perpendicular to the local tetrahedral axis. These planes have been highlighted using the circular disks.

in which the spin orientations are described by four angles: one for each of the four planes shown in Fig. 3.7. To capture the symmetry of the problem we actually choose to represent each angle using three different bases. The three possible choices for $\hat{\mathbf{S}}_\mathbf{0}$ are shown in Fig. 3.8 which depicts the plane perpendicular to $\hat{\mathbf{z}}_\mathbf{0}$. The equivalent pictures of the other three spins can be found by rotating by π about the x, y and z-axes respectively.

This allows us to express the four spins as:

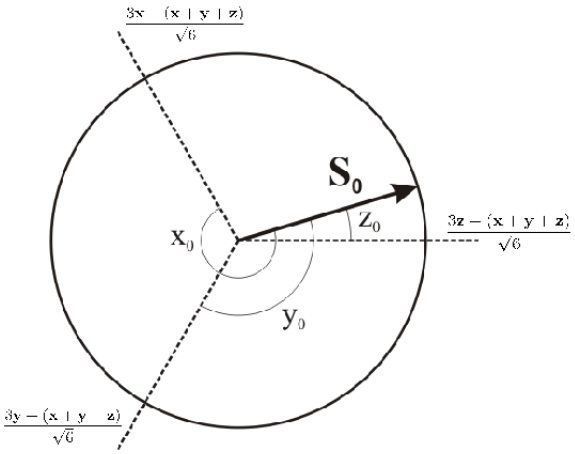

Figure 3.8: The orientation of the spin $\mathbf{S}_0$ (lying within the plane perpendicular to the $\langle 1,1,1\rangle$ direction is described using three angles: x_0, y_0 and z_0, each of which is measured using a different basis as shown.

$$\begin{aligned}
\hat{\mathbf{S}}_0 &= \frac{2}{3}\left(+\hat{\mathbf{x}}\cos x_0 + \hat{\mathbf{y}}\cos y_0 + \hat{\mathbf{z}}\cos z_0\right), \\
\hat{\mathbf{S}}_1 &= \frac{2}{3}\left(+\hat{\mathbf{x}}\cos x_1 - \hat{\mathbf{y}}\cos y_1 - \hat{\mathbf{z}}\cos z_1\right), \\
\hat{\mathbf{S}}_2 &= \frac{2}{3}\left(-\hat{\mathbf{x}}\cos x_2 + \hat{\mathbf{y}}\cos y_2 - \hat{\mathbf{z}}\cos z_2\right), \\
\hat{\mathbf{S}}_3 &= \frac{2}{3}\left(-\hat{\mathbf{x}}\cos x_3 - \hat{\mathbf{y}}\cos y_3 + \hat{\mathbf{z}}\cos z_3\right),
\end{aligned} \tag{3.4}$$

where

$$x_\alpha = z_\alpha - 2\pi/3, \qquad y_\alpha = x_\alpha - 2\pi/3, \qquad z_\alpha = x_\alpha - 2\pi/3, \tag{3.5}$$

all modulo 2π. Alternatively, if we represent the spins using a single basis to clarify how the angles relate to the Cartesian basis we get:

$$\begin{aligned}
& \hat{\mathbf{S}}_\mathbf{0} = \left[\frac{2\hat{\mathbf{x}} - \hat{\mathbf{y}} - \hat{\mathbf{z}}}{\sqrt{6}}\right]\cos x_0 + \left[\frac{\hat{\mathbf{y}} - \hat{\mathbf{z}}}{\sqrt{2}}\right]\sin x_0, \\
\text{or} \qquad & \hat{\mathbf{S}}_\mathbf{0} = \left[\frac{2\hat{\mathbf{y}} - \hat{\mathbf{z}} - \hat{\mathbf{x}}}{\sqrt{6}}\right]\cos y_0 + \left[\frac{\hat{\mathbf{z}} - \hat{\mathbf{x}}}{\sqrt{2}}\right]\sin y_0, \\
\text{or} \qquad & \hat{\mathbf{S}}_\mathbf{0} = \left[\frac{2\hat{\mathbf{z}} - \hat{\mathbf{x}} - \hat{\mathbf{y}}}{\sqrt{6}}\right]\cos z_0 + \left[\frac{\hat{\mathbf{x}} - \hat{\mathbf{y}}}{\sqrt{2}}\right]\sin z_0,
\end{aligned} \tag{3.6}$$

along with corresponding expressions for the other three spins, found by rotating by π about the x, y and z-axes respectively. It is straight forward to demonstrate that Equations 3.4 satisfy the first and third constraints. The magnitude of spin $\hat{\mathbf{S}}_\alpha$ can be found as follows:

$$\hat{\mathbf{S}}_\alpha \cdot \hat{\mathbf{S}}_\alpha = \frac{2}{3}\left[\cos^2(z_0 - 2\pi/3) + \cos^2(z_0 + 2\pi/3) + \cos^2(z_0)\right]. \tag{3.7}$$

We choose to define $z = e^{iz_0}$ and $\omega = e^{i2\pi/3}$, so that

$$\begin{aligned}
\hat{\mathbf{S}}_\alpha \cdot \hat{\mathbf{S}}_\alpha &= \frac{1}{6}\left[\left(\frac{z}{\omega} + \frac{\omega}{z}\right)^2 + \left(z\omega + \frac{1}{z\omega}\right)^2 + \left(z + \frac{1}{z}\right)^2\right], \\
&= \frac{1}{6}\left[\left(z^2 + z^{-2}\right)\left(1 + \omega + \omega^{-1}\right) + 6\right] = 1.
\end{aligned} \tag{3.8}$$

We can use the same approach to show that the third constraint is also satisfied:

$$\begin{aligned}
\hat{\mathbf{S}}_\alpha \cdot \hat{\mathbf{z}}_\alpha &= \frac{\sqrt{2}}{3}\left[\cos\left(z_0 - 2\pi/3\right) + \cos\left(z_0 - 4\pi/3\right) + \cos\left(z_0\right)\right], \\
&= \frac{1}{3\sqrt{2}}\left[\frac{z}{\omega} + \frac{\omega}{z} + z\omega + \frac{1}{z\omega} + z + \frac{1}{z}\right], \\
&= \frac{1}{3\sqrt{2}}\left[\left(z + z^{-1}\right)\left(1 + \omega + \frac{1}{\omega}\right)\right] = 0.
\end{aligned} \tag{3.9}$$

We can now consider the second constraint:

$$\hat{\mathbf{S}}_0 + \hat{\mathbf{S}}_1 + \hat{\mathbf{S}}_2 + \hat{\mathbf{S}}_3 = \mathbf{0}. \tag{3.10}$$

To solve this requires some algebra, and is shown in Appendix C. We find four types of solutions:

$$x_0 = +x_1 = +x_2 = +x_3,$$

$$x_0 = +x_1 = -x_2 = -x_3,$$

$$y_0 = -y_1 = +y_2 = -y_3,$$

$$z_0 = -z_1 = -z_2 = +z_3. \tag{3.11}$$

In the first style all spins have the same angle (and we can therefore also describe these solutions using $y_0 = y_1 = y_2 = y_3$ or $z_0 = z_1 = z_2 = z_3$). The other three solutions involve the three different ways of pairing the spins. Our reason for choosing to use the three bases is now clarified. For example, in the second style of solutions we see that the angle for spins $\hat{\mathbf{S}}_0$ and $\hat{\mathbf{S}}_1$ is reflected about the projection of the x-axis into the appropriate plane to get the angle for spins $\hat{\mathbf{S}}_2$ and $\hat{\mathbf{S}}_3$. Applying the three constraints has severely restricted the possible magnetic states for a single tetrahedron. We still have one unconstrained angle, say z_0, but once we have fixed this initial spin direction there remains only six possible orientations for each spin. These are generated by the operations: $x_\alpha \mapsto -x_\alpha$, $y_\alpha \mapsto -y_\alpha$, $z_\alpha \mapsto -z_\alpha$. An example of these six orientations for $\hat{\mathbf{S}}_0$ with an arbitrary choice of z_0 is shown in Fig. 3.9. We have used the notation 1 and

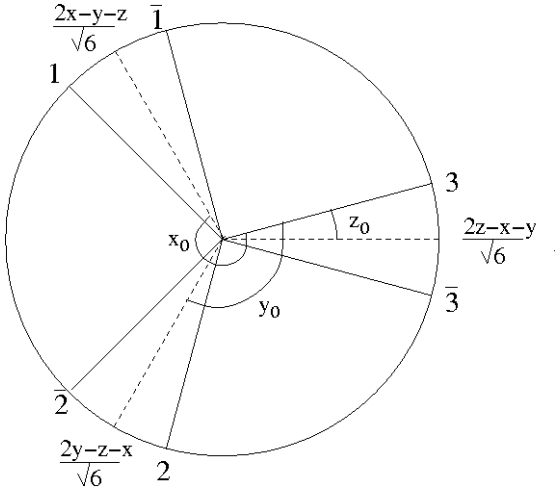

Figure 3.9: For a given initial spin orientation of $\mathbf{S}_0$, described by z_0 say, there are only six possible orientations for the other spins on this sub-lattice that are compatible with the three constraints that we have enforced. These directions are labeled by 1, $\bar{1}$, 2, $\bar{2}$, 3 and $\bar{3}$. Equivalent representations for the spins $\mathbf{S}_1$, $\mathbf{S}_2$ and $\mathbf{S}_3$ can be found be rotating by π about the x, y and z-axes respectively.

$\bar{1}$ to label the two directions related by a reflection in the projection of the x-axis onto the 'Mössbauer plane'. Equivalently, the pairs directions 2 and $\bar{2}$, and 3 and $\bar{3}$ are related via reflections in the projection of the y and z-axes respectively. There are therefore

twenty four possible choices of magnetic state for a single tetrahedron (subject to fixing the initial choice of z_0): the twelve shown in Fig. 3.10 and the analogous tetrahedra with $n \mapsto \bar{n}$. In addition, to form the pyrochlore lattice we also require the twenty-four inverted tetrahedra (with the equivalent magnetic states). Now that we have applied the three

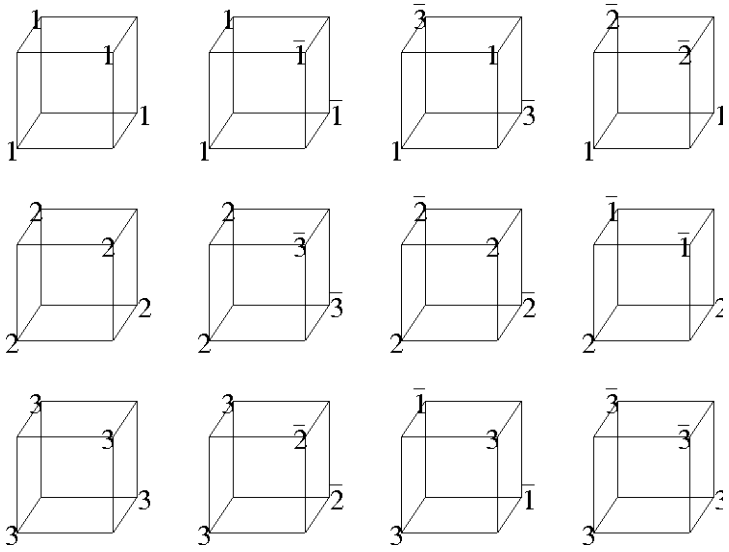

Figure 3.10: There are twenty four possible spin states for a single tetrahedron (subject to fixing the initial choice of z_0). Twelve are shown above using the notation introduced in Fig. 3.9. In addition there are another twelve found by the mapping $n \mapsto \bar{n}$.

constraints to a single tetrahedron, the next step is to use these tetrahedra as 'building blocks' from which we can construct $\mathbf{k} = (1/2, 1/2, 1/2)$. This will be discussed in the next section.

3.4 Classical $\mathbf{k} = (1/2, 1/2, 1/2)$ states

In this section we will consider how the constrained single tetrahedron states that we found in the previous section can be combined to form bulk states with $\mathbf{k} = (1/2, 1/2, 1/2)$ magnetic ordering. We need to consistently propagate the tetrahedra across the pyrochlore lattice. At each intersection between two tetrahedra superficially there is a choice of four options for the next tetrahedron, (c.f. the spin-ice two-in-two-out degenerate ground-state manifold, where if the state of one tetrahedron is fixed then there is a choice of

three out of a possible six states for each of the neighbouring tetrahedra). However, each tetrahedron is connected to four others, which places additional restrictions on the choice of tetrahedra making the macroscopic degeneracy extremely hard to assess. We, however, wish to consider the possibilities for $\mathbf{k} = (1/2, 1/2, 1/2)$ ordering. Firstly this imposes an additional restriction on our choice of direction of the initial spin. For $\mathbf{k} = (1/2, 1/2, 1/2)$ ordering we require that for every possible spin direction, the anti-parallel spin is also permitted. This leaves only three choices for the initial angle which are given by $z_0 \in \{-\pi/6, \pi/2, \pi/6\}$. For $z_0 = -\pi/6$, the pairs of anti-parallel directions are: $\{3, \bar{1}\}$, $\{1, \bar{2}\}$, $\{2, \bar{3}\}$, for $z_0 = \pi/2$ we get: $\{3, \bar{3}\}$, $\{1, \bar{1}\}$, $\{2, \bar{2}\}$ and for $z_0 = \pi/6$ we get: $\{3, \bar{2}\}$, $\{1, \bar{3}\}$ and $\{2, \bar{1}\}$. As said earlier, to specify a $\mathbf{k} = (1/2, 1/2, 1/2)$ we require the orientations of sixteen independent spins. We choose to use the sixteen sites labeled by $0, 1, ...15$ in Fig. 3.11, where the spins on sites $\bar{0}, \bar{1}, ...\bar{15}$ are anti-parallel to the spin on the equivalent un-barred state. In this figure we show successive slices through the

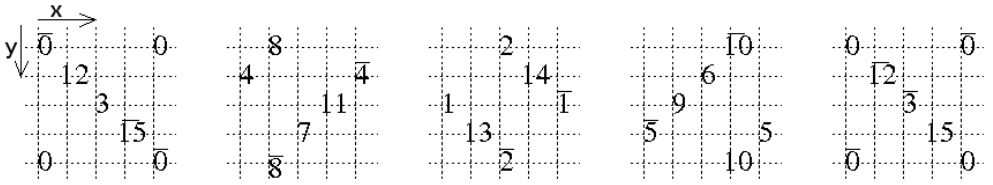

Figure 3.11: Successive slices through the pyrochlore lattice perpendicular to the z-axis (with the plane on the left being the lowest). The positions of the Gd^{3+} ions are indicated by the numbers. To describe a $\mathbf{k} = (1/2, 1/2, 1/2)$ state we need to specify the orientations of sixteen spins, which we have labeled $0, 1, ..., 15$ above. The spins on sites $\bar{0}, \bar{1}, ...\bar{15}$ are then forced by the $\mathbf{k} = (1/2, 1/2, 1/2)$ ordering to be anti-parallel to the spins on the equivalent un-barred sites. When stacked on top of each other, these planes form the section of the pyrochlore lattice shown in Fig. 3.12.

pyrochlore lattice perpendicular to the z-axis, with the plane on the left being the lowest and the plane on the right being the highest (and in which all the spins are anti-parallel to the spins in the first plane as a result of the $\mathbf{k} = (1/2, 1/2, 1/2)$ ordering). The planes are stacked to form the portion of the pyrochlore lattice shown in Fig. 3.12. To generate the full $\mathbf{k} = (1/2, 1/2, 1/2)$ magnetically ordered pyrochlore lattice, the portion of the lattice shown in Fig. 3.12 ('A') is combined with an equivalent portion in which all the spin directions are inverted ('B') using the same 'AB' ordering as is found in the NaCl

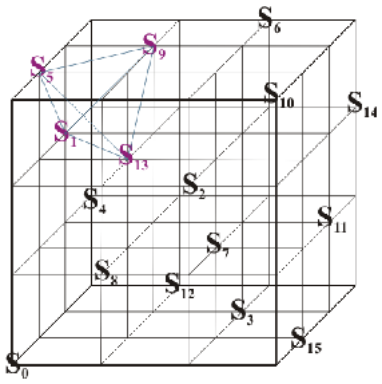

Figure 3.12: The section of the pyrochlore lattice found by consecutively stacking the planes shown in Fig. 3.11. A $\mathbf{k} = (1/2, 1/2, 1/2)$ state can then be generated by 'AB' ordering this section and an equivalent section of the lattice in which all the spin directions are reversed (in the same way as the NaCl structure is formed).

structure.

There are a number of possible ways to propagate the tetrahedra in Fig. 3.10 in such a way as to generate $\mathbf{k} = (1/2, 1/2, 1/2)$ structure. However, the majority of these are just alternative domains of the same magnetic state (being related via translational or rotational symmetry). There are actually only two classes (unrelated by symmetry operations) of $\mathbf{k} = (1/2, 1/2, 1/2)$ states which are consistent with the three constraints that we have imposed[9]. We can choose to express these using $z_0 = \pi/2$, which gives the two states shown below in Fig. 3.13. In order to interpret these states we express the

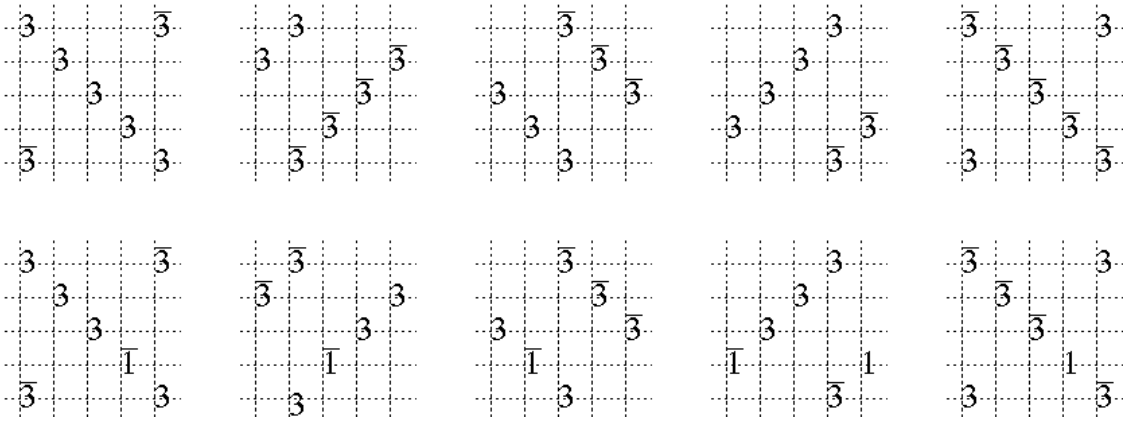

Figure 3.13: The two unique $\mathbf{k} = (1/2, 1/2, 1/2)$ states that are consistent with the three spin constraints that were enforced in the previous section. They use $z_0 = \pi/2$ to fix the direction of the vector '3'. (We note that there are a number of other domains found by translating and rotating these two states).

spin orientations in Cartesian coordinates using Equation 3.6 (along with the appropriate rotations for the other three sub-lattices), and the angles $z_0 = \pi/2$ for direction'3' and $z_0 = 7\pi/6$ for direction '1'). Spins $\hat{\mathbf{S}}_0, \hat{\mathbf{S}}_1, \hat{\mathbf{S}}_2, \hat{\mathbf{S}}_3$ lie on the 0^{th} sub-lattice, spins $\hat{\mathbf{S}}_4, \hat{\mathbf{S}}_5, \hat{\mathbf{S}}_6, \hat{\mathbf{S}}_7$ on the 1^{st} sub-lattice, spins $\hat{\mathbf{S}}_8, \hat{\mathbf{S}}_9, \hat{\mathbf{S}}_{10}, \hat{\mathbf{S}}_{11}$ on the 2^{nd} sub-lattice and spins $\hat{\mathbf{S}}_{12}, \hat{\mathbf{S}}_{13}, \hat{\mathbf{S}}_{14}, \hat{\mathbf{S}}_{15}$ on the 3^{rd} sub-lattice. In the upper state, shown in Fig. 3.13, the spins all lie in one plane with:

$$\begin{aligned}
\hat{\mathbf{S}}_0 = \hat{\mathbf{S}}_2 = \hat{\mathbf{S}}_{12} = \hat{\mathbf{S}}_{13} &= \frac{-1}{\sqrt{2}}(\hat{\mathbf{x}} - \hat{\mathbf{y}}), \\
\hat{\mathbf{S}}_1 = \hat{\mathbf{S}}_3 = \hat{\mathbf{S}}_{14} = \hat{\mathbf{S}}_{15} &= \frac{1}{\sqrt{2}}(\hat{\mathbf{x}} - \hat{\mathbf{y}}), \\
\hat{\mathbf{S}}_0 = \hat{\mathbf{S}}_2 = \hat{\mathbf{S}}_{12} = \hat{\mathbf{S}}_{13} &= \frac{1}{\sqrt{2}}(\hat{\mathbf{x}} + \hat{\mathbf{y}}), \\
\hat{\mathbf{S}}_0 = \hat{\mathbf{S}}_2 = \hat{\mathbf{S}}_{12} = \hat{\mathbf{S}}_{13} &= \frac{-1}{\sqrt{2}}(\hat{\mathbf{x}} + \hat{\mathbf{y}}).
\end{aligned} \tag{3.12}$$

This state is depicted in Fig. 3.14, and we will refer to it as the 'coplanar state'. We can see that half of the tetrahedra are in the spiral state which was shown earlier in Fig. 2.3. These tetrahedra are labeled in the figure with the circular arrows, while the other half of the tetrahedra, which are not in the dipolar ground-state are marked with crosses. In the previous chapter we established that this spiral state minimised the dipolar energy of a tetrahedron. The coplanar state, therefore, clearly only partially minimises the dipolar energy. As discussed in the previous chapter, to fully minimise the local dipolar energy we require every tetrahedra to be in the spiral state. This then gives the $\mathbf{k} = \mathbf{0}$ ground-state found in $Gd_2Sn_2O_7$. We note, however, that this state actually has a maximal energy for the third neighbour Heisenberg exchange (as every bond is ferromagnetic). We discuss this concept in more detail in Section 3.6. Here we argue that the third neighbour exchange is actually stronger than the second neighbour exchange for rare-earth pyrochlores, and that in $Gd_2Ti_2O_7$ the third neighbour exchange is in active competition with the dipolar energy (which results in the stabilisation of the $\mathbf{k} = (1/2, 1/2, 1/2)$ state over the $\mathbf{k} = \mathbf{0}$

state which is favoured by the dipole interaction). We notice that the coplaner state has regions formed of neighbouring tetrahedra in spiral states of alternating chirallity. This considerably lowers the energy of the third neighbour exchange compared to that of the $\mathbf{k} = \mathbf{0}$ state. It is not possible to consistently cover the pyrochlore lattice in this way, however, while ensuring that the total spin of each tetrahedra vanishes (as required by the dominant nearest neighbour Heisenberg exchange. Maintaining this constraint forces some of the tetrahedra to be in a higher energy dipole state (indicated by the red crosses in Fig. 3.14). The spins forming the central plane of these tetrahedra (and highlighted in blue in Fig. 3.14) can be thought of as forming a domain wall between regions of the 'ideal dipolar' spiral state. This is an idea that we return to later in the next chapter. In

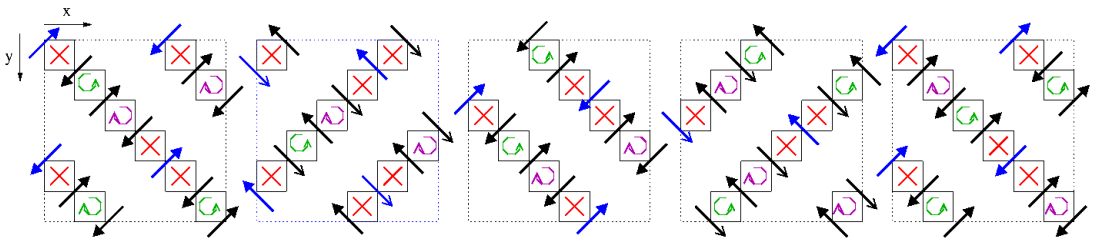

Figure 3.14: The spin orientations (shown by the black and blue arrows) of the upper (coplaner) state shown in Fig. 3.13. Half of the tetrahedra are in the spiral state which minimises the local dipolar energy. These tetrahedra are marked with green and purple 'circular' arrows (with the colour indicating the chirallity of the spiral). The other half of the states are in a high energy state of the dipole energy and are marked by a red cross. Some of the spins are highlighted in blue. These spins can be thought of as forming a domain wall between two regions in which the tetrahedra minimise the local dipolar energy (see text for more detail).

Fig. 3.15 we show a three-dimensional diagram of this state. Here we have only highlighted half of the tetrahedron. The green tetrahedron are in the spiral states and the red are in a higher energy dipolar state.

We will now describe the lower state of Fig. 3.13. For this state the spin orientations are:

$$\hat{\mathbf{S}}_0 = \hat{\mathbf{S}}_2 = \hat{\mathbf{S}}_{12} = \frac{-1}{\sqrt{2}}(\hat{\mathbf{x}} - \hat{\mathbf{y}}),$$
$$\hat{\mathbf{S}}_1 = \hat{\mathbf{S}}_3 = \hat{\mathbf{S}}_{14} = \frac{1}{\sqrt{2}}(\hat{\mathbf{x}} - \hat{\mathbf{y}}),$$

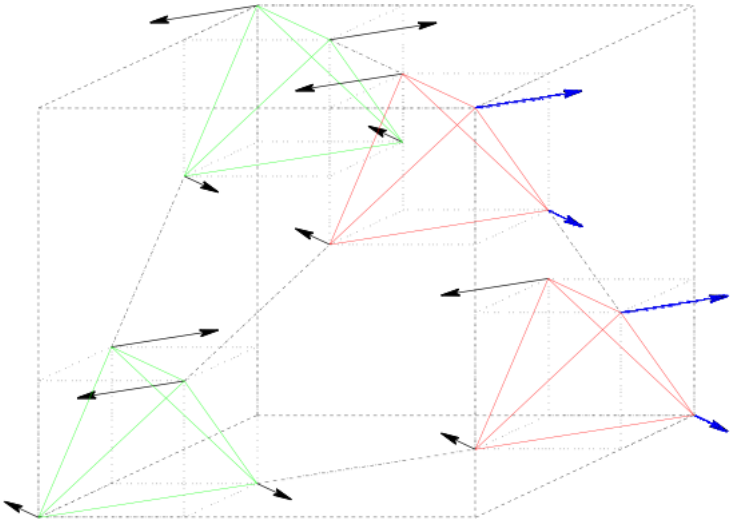

Figure 3.15: A three dimensional depiction of the coplaner state shown in Fig. 3.14. We have highlighted half of the tetrahedra. Those shown in green are in the spiral state which minimises the local dipolar energy, while those in red are in a higher energy dipolar state. We have highlighted the spins forming a 'special' plane in blue. This plane can be thought of as a domain wall between two regions in which the local dipolar energy is minimised.

$$\begin{aligned}
\hat{\mathbf{S}}_4 = \hat{\mathbf{S}}_9 = \hat{\mathbf{S}}_{11} &= \frac{-1}{\sqrt{2}}(\hat{\mathbf{x}} + \hat{\mathbf{y}}), \\
\hat{\mathbf{S}}_6 = \hat{\mathbf{S}}_8 = \hat{\mathbf{S}}_{10} &= \frac{1}{\sqrt{2}}(\hat{\mathbf{x}} + \hat{\mathbf{y}}), \\
\hat{\mathbf{S}}_5 &= \frac{-1}{\sqrt{2}}(\hat{\mathbf{y}} + \hat{\mathbf{z}}), \\
\hat{\mathbf{S}}_7 &= \frac{1}{\sqrt{2}}(\hat{\mathbf{y}} + \hat{\mathbf{z}}), \\
\hat{\mathbf{S}}_{13} &= \frac{1}{\sqrt{2}}(\hat{\mathbf{y}} - \hat{\mathbf{z}}), \\
\hat{\mathbf{S}}_{15} &= \frac{-1}{\sqrt{2}}(\hat{\mathbf{y}} - \hat{\mathbf{z}}).
\end{aligned} \tag{3.13}$$

As a quarter of the spins lie out of the xy-plane, we will refer to this state as the 'non-coplanar' state. It is depicted in Figs. 3.16 and 3.17.

Again, we see that only half of the tetrahedra are in the dipolar spiral ground-state (indicated in the same way as previously). The out-of-plane spins have been highlighted in blue. We can see that this state has an odd structure: there are three similar planes, but every fourth plane (with the out-of-plane spins) is completely different, hence the

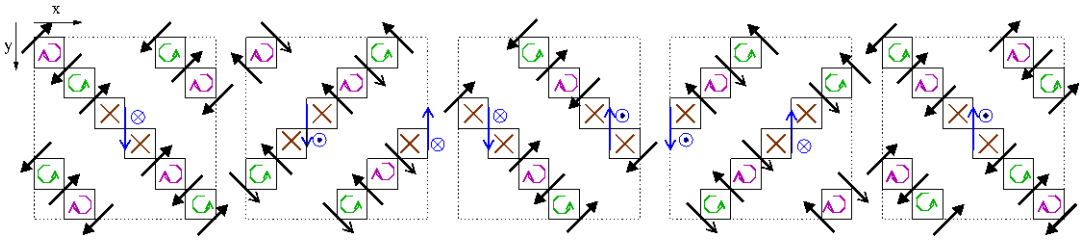

Figure 3.16: The spin orientations of the lower (non-coplaner) state shown in Fig. 3.13. The blue and black arrows show the spin components that lie within the xy-plane. The blue dots indicate a spin component out of the plane (along the positive z-direction) and the blue crosses indicate a spin component into the plane (along the negative z-direction). As in the coplaner state, half of the tetrahedra are in the spiral state which minimises the local dipolar energy. These tetrahedra are marked with green and purple 'circular' arrows (with the colour indicating the chirallity of the spiral). The other half of the states are in a high energy state of the dipole energy and are marked by a red cross. Some of the spins are highlighted in blue (which are also the full-three dimensional spins, with an out-of-plane spin component). These spins can be thought of as forming a domain wall between two regions in which the tetrahedra minimise the local dipolar energy.

highlighting the blue spins. Although it is less obvious, this is also the case for the coplanar state; the special plane is also highlighted blue in Figs. 3.14 and 3.15. As in the case of the coplaner state, this special plane can be interpreted as a domain wall between two regions of the 'ideal dipolar' spiral state. The domain wall for the non-coplaner state has a different structure, however, which turns out to have a lower dipole energy than that for the coplaner structure (which we discuss in Section 3.6.2). We will discuss the physical properties of these states further later, but first we discuss a few features of $\mathbf{k} = (1/2, 1/2, 1/2)$ ordering and then move on to a basic analysis of the energetics of the system.

3.5 Features of $\mathbf{k} = (1/2, 1/2, 1/2)$ magnetic ordering

In this section we will discuss a few consequences of the $\mathbf{k} = (1/2, 1/2, 1/2)$ which will be turn out to be useful later when we consider the energetics of the system. In Sections 3.2 and 3.3 we stated that an absent $\mathbf{k} = (1/2, 1/2, 1/2)$ Bragg peak was consistent with an infinite strength nearest neighbour Heisenberg interaction. If the nearest neigh-

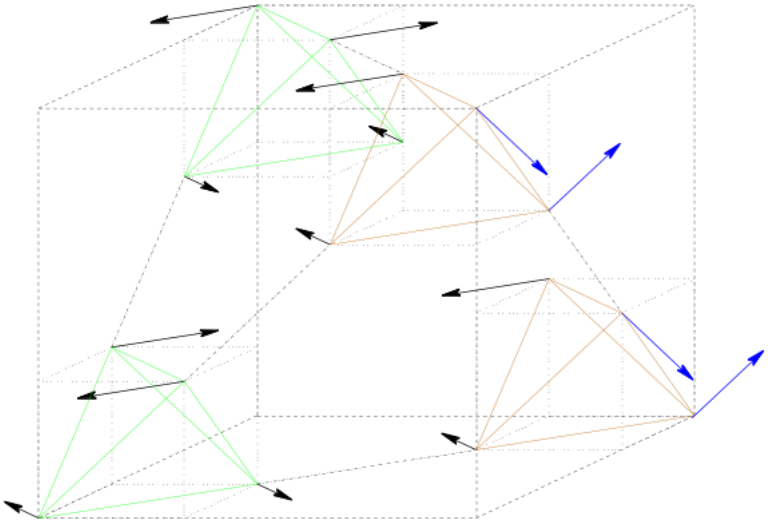

Figure 3.17: A three dimensional depiction of the con-coplaner state shown in Fig. 3.16. We have highlighted half of the tetrahedra. Those shown in green are in the spiral state that minimises the local dipolar energy, while those shown in brown are in a higher energy dipolar state. We have highlighted the spins forming a 'special' plane in blue. This plane can be thought of as forming a domain wall between two regions in which the local dipolar energy is minimised.

bour Heisenberg interaction is infinite, then every tetrahedron will have zero total spin.

The eight tetrahedra in Fig. 3.11 therefore provide us with the following relationships:

$$\begin{aligned}
\hat{\mathbf{S}}_0 + \hat{\mathbf{S}}_5 + \hat{\mathbf{S}}_{10} + \hat{\mathbf{S}}_{15} &= \mathbf{0}, \\
\hat{\mathbf{S}}_0 - \hat{\mathbf{S}}_4 - \hat{\mathbf{S}}_8 - \hat{\mathbf{S}}_{12} &= \mathbf{0}, \\
\hat{\mathbf{S}}_1 + \hat{\mathbf{S}}_4 - \hat{\mathbf{S}}_{11} - \hat{\mathbf{S}}_{14} &= \mathbf{0}, \\
\hat{\mathbf{S}}_1 - \hat{\mathbf{S}}_5 + \hat{\mathbf{S}}_9 + \hat{\mathbf{S}}_{13} &= \mathbf{0}, \\
\hat{\mathbf{S}}_2 + \hat{\mathbf{S}}_6 - \hat{\mathbf{S}}_{10} + \hat{\mathbf{S}}_{14} &= \mathbf{0}, \\
\hat{\mathbf{S}}_2 - \hat{\mathbf{S}}_7 + \hat{\mathbf{S}}_8 - \hat{\mathbf{S}}_{13} &= \mathbf{0}, \\
\hat{\mathbf{S}}_3 - \hat{\mathbf{S}}_6 - \hat{\mathbf{S}}_9 + \hat{\mathbf{S}}_{12} &= \mathbf{0}, \\
\hat{\mathbf{S}}_3 + \hat{\mathbf{S}}_7 + \hat{\mathbf{S}}_{11} - \hat{\mathbf{S}}_{15} &= \mathbf{0}.
\end{aligned} \tag{3.14}$$

We can find the structure factor for $\mathbf{S_k} = \mathbf{S}_{(\frac{1}{2},\frac{1}{2},\frac{1}{2})}$ by acquiring a phase of $\sqrt{i}$ for each unit moved (in any direction) on the grid in Fig. 3.11 to get:

$$\begin{aligned}\mathbf{S}_{(\frac{1}{2},\frac{1}{2},\frac{1}{2})} &= -(\hat{\mathbf{S}}_0 + \hat{\mathbf{S}}_1 + \hat{\mathbf{S}}_2 + \hat{\mathbf{S}}_3) + i(\hat{\mathbf{S}}_4 + \hat{\mathbf{S}}_5 - \hat{\mathbf{S}}_6 - \hat{\mathbf{S}}_7) \\ &\quad + i(\hat{\mathbf{S}}_8 - \hat{\mathbf{S}}_9 + \hat{\mathbf{S}}_{10} - \hat{\mathbf{S}}_{11}) + i(\hat{\mathbf{S}}_{12} - \hat{\mathbf{S}}_{13} - \hat{\mathbf{S}}_{14} + \hat{\mathbf{S}}_{15}). \qquad (3.15)\end{aligned}$$

Substituting in selected relationships from Equations 3.14 then gives us:

$$\mathbf{S}_{(\frac{1}{2},\frac{1}{2},\frac{1}{2})} = -(\hat{\mathbf{S}}_0 + \hat{\mathbf{S}}_1 + \hat{\mathbf{S}}_2 + \hat{\mathbf{S}}_3) - i(\hat{\mathbf{S}}_0 + \hat{\mathbf{S}}_1 + \hat{\mathbf{S}}_2 + \hat{\mathbf{S}}_3), \qquad (3.16)$$

which depends only on the spins on the 0^{th} sub-lattice. We will now pause and reconsider Equations 3.14. Manipulating these equations produces the following four relationships:

$$\begin{aligned}\hat{\mathbf{S}}_0 + \hat{\mathbf{S}}_1 + \hat{\mathbf{S}}_2 + \hat{\mathbf{S}}_3 &= \mathbf{0}, \\ \hat{\mathbf{S}}_4 + \hat{\mathbf{S}}_5 + \hat{\mathbf{S}}_6 + \hat{\mathbf{S}}_7 &= \mathbf{0}, \\ \hat{\mathbf{S}}_8 + \hat{\mathbf{S}}_9 + \hat{\mathbf{S}}_{10} + \hat{\mathbf{S}}_{11} &= \mathbf{0}, \\ \hat{\mathbf{S}}_{12} + \hat{\mathbf{S}}_{13} + \hat{\mathbf{S}}_{14} + \hat{\mathbf{S}}_{15} &= \mathbf{0}. \qquad (3.17)\end{aligned}$$

We see that the combined effect of $\mathbf{k} = (1/2, 1/2, 1/2)$ magnetic ordering and an infinite nearest neighbour Heisenberg interaction results in the total spin on each of the four sub-lattices vanishing. This in turn also allows us to see that $\mathbf{S}_{(\frac{1}{2},\frac{1}{2},\frac{1}{2})} = \mathbf{0}$. Equivalent arguments can be used to show that the structure factor also vanishes for all the other Bragg peaks which are point-symmetry related to the $\mathbf{k} = (1/2, 1/2, 1/2)$ peak.

Finally we note that there is a more physical way to see that the sum of the spins on a sub-lattice vanishes for a pyrochlore system with an infinite nearest neighbour Heisenberg exchange and $\mathbf{k} = (1/2, 1/2, 1/2)$ ordering. The pyrochlore lattice can be decomposed into alternating plane of Kagomé and sparse triangular lattices in planes perpendicular to the $\langle 1, 1, 1\rangle$. We can interpret the Kagomé lattice as a corner sharing network of two types of triangles: half pointing upwards and half downwards, as shown in Fig. 3.18. As

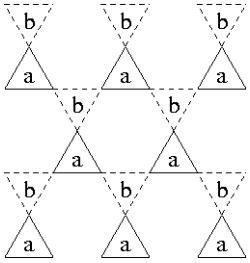

Figure 3.18: A slice through the pyrochlore lattice perpendicular to the $\langle 1,1,1\rangle$ direction, showing a Kagomé plane (the spins lie at the vertices of the triangles). The Kagomé plane can be viewed as a corner sharing network of two types of triangle: half pointing upwards (drawn with solid lines) and half pointing downwards (drawn with dashed lines). The solid triangles form the bases of tetrahedra which are completed above the plane by spins at the locations labeled 'a' (which form a sparse triangular lattice). Similarly the dashed triangles form the top faces of tetrahedra which are completed below the plane by spins at the locations labeled 'b' (which also form a sparse triangular lattice).

shown in Fig 2.8, for this projection (perpendicular to the $\langle 1,1,1\rangle$ direction), each of the triangles in the Kagomé planes is composed of one spin from each of the 1^{st}, 2^{nd}, and 3^{rd} sub-lattices (as was shown previously in Fig. 2.8 which depicted this projection), while the spins on the 0^{th} sub-lattice form the sparse triangular planes above and below the Kagomé plane. These are indicated on Fig. 3.18 by the labels 'a' and 'b', where 'a' denotes a spin above the plane, and 'b' a spin below. We can see that the upwards pointing triangles form the base of a tetrahedra which is completed above the plane by the atom at site a, and similarly for the downwards triangles which are completed below the plane. To satisfy the Heisenberg requirement that the total spin of a tetrahedron vanished, the total spin of the Kagomé plane, must therefore be exactly opposite to the total spin of each of the two neighbouring sparse triangular lattices, or equivalently the total spin on a sparse triangular plane must be opposite to the total spin on each of the two neighbouring Kagomé planes. Next we consider the $\mathbf{k} = (1/2, 1/2, 1/2)$ ordering. Perpendicular to this direction all the spins add in phase, but parallel to this direction we find that every fourth plane has the same phase and therefore the phase alternates on every second plane. This is incompatible with an alternating phase on every other plane (to satisfy the Heisenberg interaction), however, unless the total spin vanishes on every plane. As all the sites on the sparse triangular lattice planes lie on the 0^{th} sub-lattice,

we find that the total spin on this sub-lattice must vanish. Equivalent arguments that consider the planes perpendicular to the $\langle 1, \bar{1}, \bar{1} \rangle$, $\langle \bar{1}, 1, \bar{1} \rangle$ and $\langle \bar{1}, \bar{1}, 1 \rangle$ directions then find that the total spin on the 1^{st}, 2^{nd} and 3^{rd} sub-lattices respectively must also independently vanish.

3.6 Energetics

In this sections we will address two main areas. Firstly we wish to understand why $Gd_2Ti_2O_7$ is found to have $\mathbf{k} = (1/2, 1/2, 1/2)$ magnetic order. As already discussed in the introduction to this chapter, the structurally equivalent compound $Gd_2Sn_2O_7$ magnetically orders with a wave-vector of $\mathbf{k} = \mathbf{0}$. The behaviour of this material was discussed at length in the previous chapter. The experimentally observed $\mathbf{k} = \mathbf{0}$ spiral ground-state[75] is believed to minimise the classical, long-range, dipolar interaction on the pyrochlore lattice. The fact that $Gd_2Ti_2O_7$ does not magnetically order with this wave-vector implies that some other interaction must play a crucial role. Further neighbour Heisenberg interactions are a natural candidate. In the next subsection we will therefore consider the effect of second and third neighbour Heisenberg exchange couplings. Secondly, in order to better understand the two states depicted in Figs. 3.15 and 3.17 we will calculate their short-range Heisenberg and dipolar energies.

3.6.1 Further neighbour Heisenberg interactions

In Section 1.2.2 we calculated the nearest neighbour structure factor for the Heisenberg interaction on a pyrochlore lattice. The two flat low-energy bands indicate that there is a huge ground-state degeneracy (amounting to half of the phase space). Including further neighbour interactions will introduce a non-zero dispersion into these bands and lift the ground-state degeneracy.

The behaviour of further neighbour Heisenberg interactions on the pyrochlore lattice was previously studied by Wills *et al.*[75]. In this article the interaction strength was

directly dependent on the separation between the two magnetic ions. It is also important, however, to take into account the actual hopping pathways via the intermediate ions. We do not analyse this in any detail as the problem is complex. The dominant pathway for both the second and third neighbour interactions is likely to be through the O2 and Ti ions as shown in Figs. 3.19 and 3.20. The exact nature of the orbital overlaps is subtle,

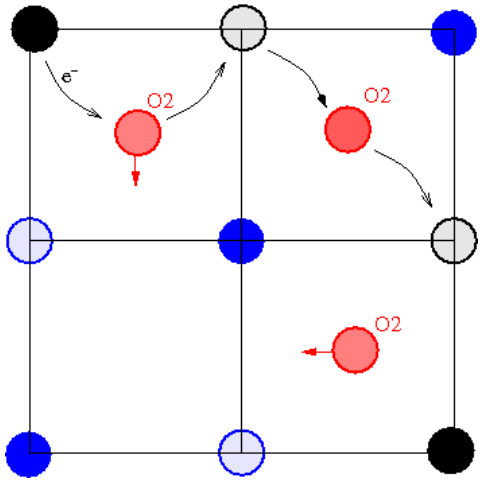

Figure 3.19: An example of one of the possible second neighbour Heisenberg exchange pathways (indicated by the curved black arrows). We show two planes of the pyrochlore lattice (perpendicular to the z-axis) projected onto the xy-plane. The filled black circles represent the Gd^{3+} ions on the lower plane, while the open black circles represent the Gd^{3+} ions on the upper plane. Similarly, the filled blue circles represent the Ti^{4+} ions on the lower plane and the open blue circles the Ti^{4+} ions on the upper plane. The O^{2-} are shown in red and lie in between the two planes (at the O2 positions shown previously in Fig. 1.14). The red arrows indicate the direction in which the O^{2-} ions are displaced away from the centre of the tetrahedra (while the O^{2-} ion without an arrow is displaced down into the plane of the diagram).

especially since the O2 ions are not situated in the center of the cubes shown, but instead are shifted towards the face containing the two Ti ion. There are two main points which we wish to highlight. Firstly we notice that both pathways exchange through the same intermediate ions, one of which is the titanium ion. We will return to this point later. Secondly, we notice that the third neighbour exchange pathway is relatively straight, while the opposite is true for the second neighbour exchange. The sharp Gd-O2-Ti bond angle is likely to significantly reduce the orbital overlaps. The result of this is that though the physical distance between ions is shorter for the second neighbour interaction,

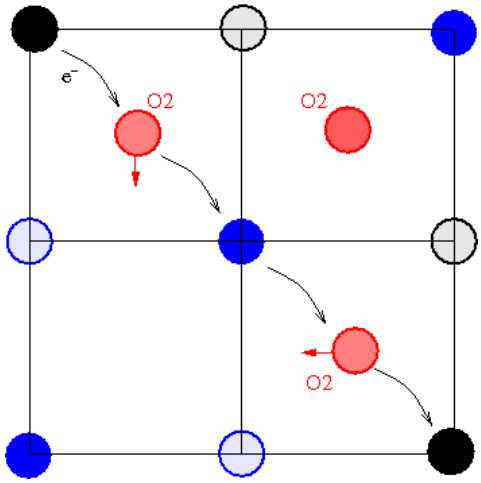

Figure 3.20: An example of the third neighbour Heisenberg exchange pathway (via an intermediate Ti^{4+} ion). We show two planes of the pyrochlore lattice (perpendicular to the z-axis) projected onto the xy-plane. The filled black circles represent the Gd^{3+} ions on the lower plane, while the open black circles represent the Gd^{3+} ions on the upper plane. Similarly, the filled blue circles represent the Ti^{4+} ions on the lower plane and the open blue circles the Ti^{4+} ions on the upper plane. The O^{2-} are shown in red and lie in between the two planes (at the O2 positions shown previously in Fig. 1.14). The red arrows indicate the direction in which the O^{2-} ions are displaced away from the centre of the tetrahedra (while the O^{2-} ion without an arrow is displaced down into the plane of the diagram). The curved black arrows show an example of the third neighbour exchange pathway through two intermediate O^{2-} ions and a Ti^{4+} ion.

the exchange constant will be smaller than that for the third neighbour interactions. We will therefore use $J_1 \gg J_3 > J_2$. In Fig. 3.21 we illustrate the positions of the first, second and third neighbours relative to the central, gray, Gd ion. There are six nearest neighbours (coloured green), twelve second neighbours (coloured blue) and twelve neighbours (coloured red). Six of the third neighbours, however, have another Gd ion as the intermediate ion rather than Ti. This blocks the third neighbour interaction for these ions, as clearly the nearest neighbour interaction will take precedence. The blocked third neighbours are indicated with the open red circles. We include only the other six unblocked third neighbours in our calculation. We parameterise the Hamiltonian using: $J_1 = J, J_3 = \lambda J, J_2 = \lambda\kappa J$, where λ and κ are small:

$$H_{\mathrm{Ex}} = \frac{J}{2}\left[\sum_{\langle ij\rangle_1} \hat{\mathbf{S}}_i \cdot \hat{\mathbf{S}}_j + \lambda\kappa \sum_{\langle ij\rangle_2} \hat{\mathbf{S}}_i \cdot \hat{\mathbf{S}}_j + \lambda \sum_{\langle ij\rangle_3} \hat{\mathbf{S}}_i \cdot \hat{\mathbf{S}}_j\right]. \tag{3.18}$$

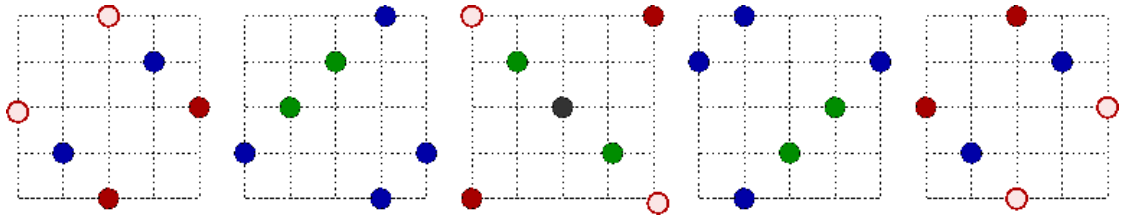

Figure 3.21: Successive slices through the pyrochlore lattice perpendicular to the z-axis. The circles represent the positions of the Gd^{3+} ions. The six green circles show the positions of the nearest neighbour ions with respect to the central black ion. Similarly, the blue circles show the positions of the twelve second neighbour ions with respect to the central black ion. Finally the twelve red circles represent the positions of the third neighbour ions. For six of these third neighbour ions, represented by the open red circles, there is another (green) Gd^{3+} ion which lies directly between it and the central black Gd^{3+} ion. These intermediate ions will 'block' the third neighbour exchange pathways for the six ions represented by the open red circles. We therefore only include the six 'unblocked' third neighbour ions, represented by the filled red circles) in the exchange Hamiltonian.

Block transforming the Hamiltonian then provides:

$$H_{\mathrm{Ex}} = \frac{J}{2} \sum_{\mathbf{k}} \mathbf{S}_{\mathbf{k}}^{\dagger} \cdot \gamma_{\mathbf{k}} \cdot \mathbf{S}_{\mathbf{k}}, \tag{3.19}$$

where $\mathbf{S}_{\mathbf{k}}$ is a twelve component vector, consisting of the four reciprocal-space spin densities (using sub-lattice representation), and setting the width of the conventional unit-cell '$a = 2$' for convenience, we find that $\gamma_{\mathbf{k}}$, the structure factor, is given by the 12×12 matrix:

$$\gamma_{\mathbf{k}} = \begin{bmatrix} \lambda(4xyz-1) & X+2\lambda\kappa x c_1 & Y+2\lambda\kappa y c_2 & Z+2\lambda\kappa z c_3 \\ X+2\lambda\kappa x c_1 & \lambda(4xYZ-1) & z+2\lambda\kappa Z c_3 & y+2\lambda\kappa Y c_2 \\ Y+2\lambda\kappa y c_2 & z+2\lambda\kappa Z c_3 & \lambda(4XyZ-1) & x+2\lambda\kappa X c_1 \\ Z+2\lambda\kappa z c_3 & y+2\lambda\kappa Y c_2 & x+2\lambda\kappa X c_1 & \lambda(4XYz-1) \end{bmatrix}, \tag{3.20}$$

and we have made the following definitions:

$$\begin{aligned} x &= \cos\left(\frac{k_y - k_z}{2}\right), & y &= \cos\left(\frac{k_z - k_x}{2}\right), & z &= \cos\left(\frac{k_x - k_y}{2}\right), \\ X &= \cos\left(\frac{k_y + k_z}{2}\right), & Y &= \cos\left(\frac{k_z + k_x}{2}\right), & Z &= \cos\left(\frac{k_x + k_y}{2}\right), \end{aligned} \tag{3.21}$$

$$c_1 = \cos k_x, \qquad c_2 = \cos k_y, \qquad c_3 = cos kz. \tag{3.22}$$

For $\lambda \mapsto 0$, the eigenenergies, Γ_k tend to the nearest neighbour band structure, with two minimum energy flat band at $\Gamma_0 = -1$. As we are treating λ as a small perturbation which lifts the degeneracy of the two flat bands, we expand the eignenenergy to first order in λ about the value of λ_0. This gives

$$\Gamma_k = -1 - \lambda - 2\lambda\epsilon_k, \tag{3.23}$$

where the function ϵ_k is determined by the equation

$$\begin{aligned}&(1-a_2)\epsilon^2 - 2\left[a_2(1+4\kappa) + 2a_2^2 - a_1(3a_1+a_3)(1+\kappa)\right]\epsilon + 2a_2^2(4\kappa^2-1) \\ &-a_3(a_3+2a_1)(1+\kappa)^2 + 9a_1^2a_2(1-\kappa^2) + 6a_1a_2a_3(1+\kappa) - 9a_2^3 = 0,\end{aligned} \tag{3.24}$$

where

$$a_1 = \frac{c_1+c_2+c_3}{3}, \qquad a_3 = \frac{c_2c_3+c_3c_1+c_1c_2}{3}, \qquad a_3 = c_1c_2c_3. \tag{3.25}$$

Minimising the above equation then predicts the magnetic ordering wave-vector for this system. We find that the ground-state ordering depends on the value of κ, and is described by

$$c_1 = c_2 = -\cos\theta, \qquad c_3 = 1, \tag{3.26}$$

where the κ dependence of θ is shown in Fig. 3.22. These k-values are compatible with a spiraling solution, where in this case $\theta = \frac{\pi}{3}$ if $\kappa = 0$ and $\theta = \frac{\pi}{2}$ for (the unphysically large) value of $\kappa = 1$. We compare the energy of this Heisenberg ground-state (black) to the $\mathbf{k} = \mathbf{0}$ solution (red) and $\mathbf{k} = (1/2, 1/2, 1/2)$ solution (green) in Figure 3.23. Firstly it is clear that further neighbour Heisenberg interactions alone cannot explain the observed $\mathbf{k} = (1/2, 1/2, 1/2)$ ordering. We notice however, that while the $\mathbf{k} = \mathbf{0}$ state is a high-energy state for the exchange interaction with $\epsilon = -2 + \kappa$, the $\mathbf{k} = (1/2, 1/2, 1/2)$ solution has an energy of $\epsilon = 0$, which is much closer in energy to exchange interaction

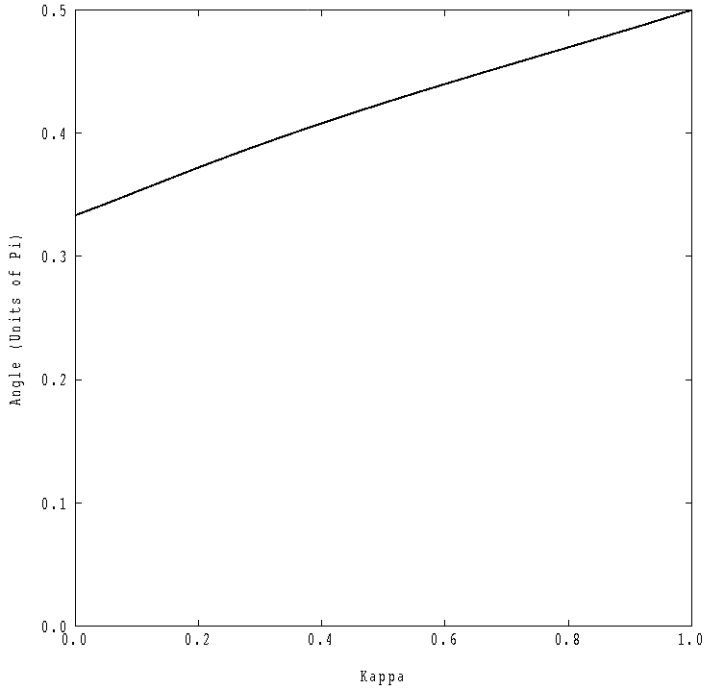

Figure 3.22: The angle, θ, (in units of π), plotted as a function of κ (which determines the strength of the second neighbour Heisenberg exchange), which specifies the periodicity of the spiraling ground-state of the first, second and third neighbour Heisenberg model on the pyrochlore lattice with $J_1 \gg J_3 \geq J_2$.

ground state. We therefore suggest that the $\mathbf{k} = (1/2, 1/2, 1/2)$ state is stabilised due to a competition between the further neighbour exchange and dipolar interaction. The dipolar interactions destabilise the ground-state of the exchange interactions in favour of the experimentally observed ordering, but are not strong enough to stabalise the $\mathbf{k} = \mathbf{0}$ state as the exchange energy of this state is too poor. This allow us to offer an explanation of the differing behaviour between $Gd_2Sn_2O_7$ and $Gd_2Ti_2O_7$. Recalling that the further neighbour Heisenberg exchange pathway is via the transition metal, we suggest that in $Gd_2Ti_2O_7$ the empty Ti $3d$-shell is close enough the chemical potential to make the further neighbour exchange large enough to compete with the dipole interaction. For $Gd_2Sn_2O_7$, however, this is not the case and the further neighbour exchange interactions are negligible.

The next question to consider is what particular style of $\mathbf{k} = (1/2, 1/2, 1/2)$ ordering is energetically favourable? Interestingly we discover that in the $\mathbf{k} = (1/2, 1/2, 1/2)$ subspace, enforcing this periodicity is enough to determine both the second and third neighbour exchange energy. We find that the second neighbour exchange energy vanishes

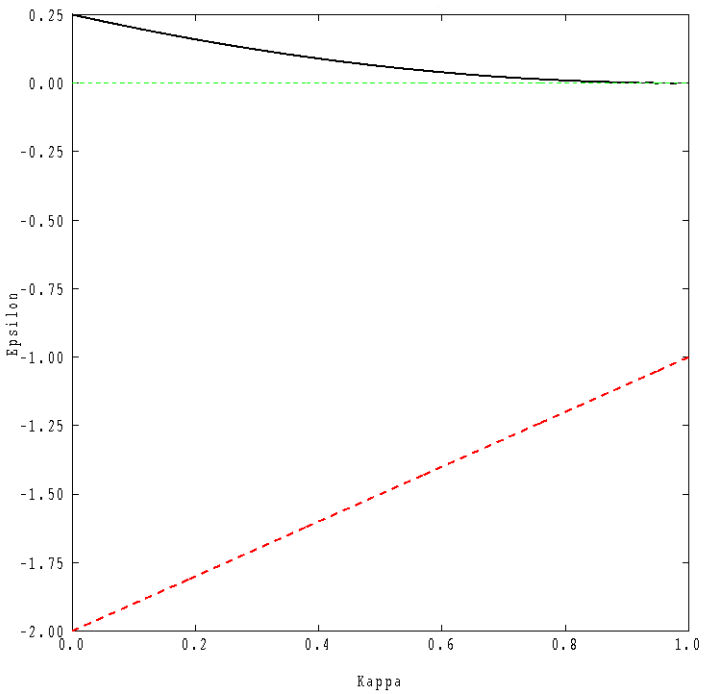

Figure 3.23: Heisenberg energy of ground-state (black), $\mathbf{k} = \mathbf{0}$ state (red) and $\mathbf{k} = (1/2, 1/2, /12)$ state (green).

for all $\mathbf{k} = (1/2, 1/2, 1/2)$ states, while the third neighbour exchange only connects spins on the same sub-lattice so that

$$\begin{aligned} H_3 &= \frac{J_3 N}{2}\left[2\mathbf{S}_0 \cdot \mathbf{S}_1 + 2\mathbf{S}_0 \cdot \mathbf{S}_2 + 2\mathbf{S}_0 \dot{\mathbf{S}}_3\right] \\ &= J_3 N \mathbf{S}_0 \cdot [\mathbf{S}_1 + \mathbf{S}_2 + \mathbf{S}_3] \\ &= -J_3 N \left|\mathbf{S}_0\right|^2 = -NS^2 J_3 \end{aligned} \tag{3.27}$$

which is a constant (we used Equation 3.17 to obtain the last equality). The further neighbour exchange interactions clearly play no part in selecting which $\mathbf{k} = (1/2, 1/2, 1/2)$ state is stabilised. The dipole interaction must therefore play the dominant role as we will consider next.

3.6.2 Local dipolar energy

We will now consider the eigenstates of the local dipole energy in order to investigate which of the two possible $\mathbf{k} = (1/2, 1/2, 1/2)$ states has the lower dipolar energy. For a single tetrahedron, this is governed by the interaction matrix:

$$\begin{bmatrix}
0 & 0 & 0 & 0 & 0 & 0 & 1 & 0 & 1 & 1 & 1 & 0 \\
0 & 0 & 0 & 0 & 1 & 1 & 0 & 0 & 0 & 1 & 1 & 0 \\
0 & 0 & 0 & 0 & 1 & 1 & 1 & 0 & 1 & 0 & 0 & 0 \\
0 & 0 & 0 & 0 & 0 & 0 & 1 & -1 & 0 & 1 & 0 & -1 \\
0 & 1 & 1 & 0 & 0 & 0 & -1 & 1 & 0 & 0 & 0 & 0 \\
0 & 1 & 1 & 0 & 0 & 0 & 0 & 0 & 0 & -1 & 0 & 1 \\
1 & 0 & 1 & 1 & -1 & 0 & 0 & 0 & 0 & 0 & 0 & 0 \\
0 & 0 & 0 & -1 & 1 & 0 & 0 & 0 & 0 & 0 & 1 & -1 \\
1 & 0 & 1 & 0 & 0 & 0 & 0 & 0 & 0 & 0 & -1 & 1 \\
1 & 1 & 0 & 1 & 0 & -1 & 0 & 0 & 0 & 0 & 0 & 0 \\
1 & 1 & 0 & 0 & 0 & 0 & 0 & 1 & -1 & 0 & 0 & 0 \\
0 & 0 & 0 & -1 & 0 & 1 & 0 & -1 & 1 & 0 & 0 & 0
\end{bmatrix}, \tag{3.28}$$

Diagonalising the above we matrix, we find the eigenenergies

$$\left\{-\frac{3}{2}(1+\sqrt{17}), -3, 3, \frac{3}{2}(\sqrt{17}-1), 12\right\}. \tag{3.29}$$

The first and third of these have 86.4 of its moments parallel, so we discount these states. The three states that are compatible with dominant nearest neighbour Heisenberg exchange are shown in Figure 3.24. The first state is triply degenerate with an energy of -3 (and is the spiral state). The second state is doubly degenerate and has an energy of 3 (we will call this the 'scissors' state). The final state has the highest eignenenergy. We find that the coplaner solution has half its tetrahedra in the spiral state (which were previously shown in green in Fig. 3.15) and half in the scissors state (which were shown

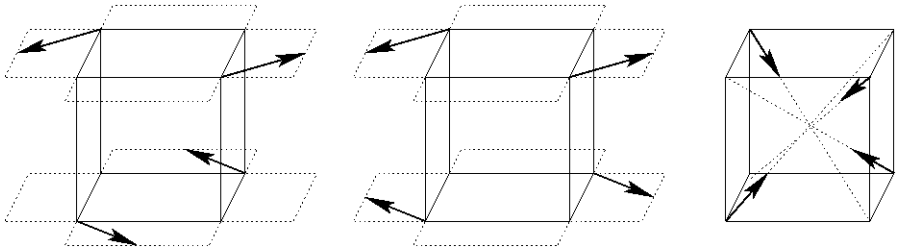

Figure 3.24: The three eigenstates of the nearest neighbour dipole interaction compatible with total spin zero.

in red in Fig. 3.15). The non-coplaner state also has half its tetrahedra in the spiral state (which were shown in green in Fig. 3.17). The other half (shown in brown in Fig. 3.17) are in a linear combination of three-quarters scissors state and one quarter spiral. The non-coplaner state therefore has a lower dipole energy.

3.7 Comparison to experimental data

We will now briefly compare the coplaner and non-coplaner states to the experimental data. We recall that two phase transitions were observed in the specific heat data. It might seem natural to ascribe the two phases to the two states that we have found. The coplaner state has a larger dipole energy but is more favourable to both quantum and thermal fluctuations (as a result of the coplaner spins). The non-coplaner has a lower dipole energy, and the three-dimensional spin orientations will be less sensitive to static magnetic disorder. First, however, we should consider whether they are compatible with the two key experiments discussed at the beginning of this chapter. By construction they were forced to be compatible with both the Mössbauer data and the $\mathbf{k} = (1/2, 1/2, 1/2)$ ordering. Unfortunately, however, the fit to the neutron scattering intensities is extremely poor. A fit by J. Gardner[28] for the coplaner state is shown in Figure 3.25. The black dots represent the data, the red line the fit to the coplaner state, and the bottom line the error in the fit. We see that the fit is terrible, and the same is true for the non-coplaner state. The only option is to relax at least one of the three constraints that we enforced. Of these, restricting the spins to lie exactly in the Mössbauer planes was the most suspect.

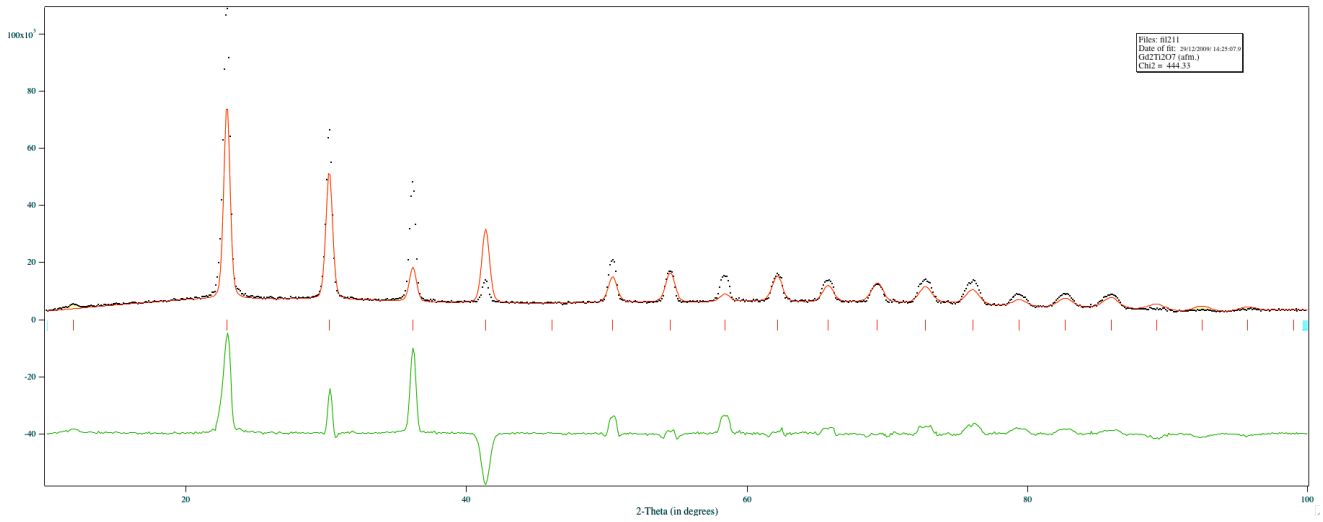

Figure 3.25: Fit of coplaner state to elastic neutron data by J. Gardner[28].

In the next chapter, therefore we will return to this problem using a reciprocal-space approach, and relax this constraint.

CHAPTER 4

GADOLINIUM TITANATE: RECIPROCAL SPACE APPROACH

4.1 Introduction

In this chapter we will continue to study the low temperature magnetic ordering of $Gd_2Ti_2O_7$. This chapter will therefore be a continuation of the previous one, in which we were looking for magnetically ordered states that were consistent with both the elastic neutron scattering and Mössbauer data (see Section 3.2). In the previous chapter we enforced constraints for equal-length classical spins confined to planes perpendicular to the local tetrahedral axes. We found that there were only two states that were consistent with both these spin constraints and $\mathbf{k} = (1/2, 1/2, 1/2)$ magnetic ordering. These two states, however, do not fit the observed neutron scattering intensities. In this chapter we therefore approach the problem from an alternative perspective. Whereas in the previous chapter we worked entirely in real-space, we will now turn to a reciprocal-space approach in order to try to find a magnetically ordered state that will also fit the neutron scattering Bragg peak intensities. In order to find new possible states we will also have to relax at least one of the assumptions made in the previous chapter. Of the three constraints that we enforced, forcing the spins to lie exactly in the planes perpendicular to the local tetrahedral axis was clearly the most dubious. We had no energetic motivation for imposing this constraint. Although orientating spins in these planes was found in Section 2.4 to

partially minimise the dipole interaction, we know that this interaction is to some degree frustrated in $Gd_2Ti_2O_7$. If this was not the case, then both $Gd_2Ti_2O_7$ and $Gd_2Sn_2O_7$ would share the $\mathbf{k} = \mathbf{0}$ spiral ground-state that is indeed observed for $Gd_2Sn_2O_7$. It therefore seems likely the spins are actually distorted slightly out of the planes perpendicular to the local tetrahedral axes forming a lower-energy state, while still being close enough to the planes to still produce a good fit to the Mössbauer data.

4.2 Relative Bragg spot intensities

In this chapter we wish to focus on the observed intensities of the elastic Bragg peaks. For $Gd_2Ti_2O_7$ they are found to be indexed by the propagation vector $\mathbf{k} = (1/2, 1/2, 1/2)$[21, 69]. We will therefore begin by discussing in some detail the reciprocal-space properties of $\mathbf{k} = (1/2, 1/2, 1/2)$ ordering on the pyrochlore lattice. We recap that the Bragg peak intensities are given by

$$I(\mathbf{Q}) \propto \left[\mathbf{S}^*_{\mathbf{Q}} \cdot \mathbf{S}_{\mathbf{Q}} - \hat{\mathbf{Q}} \cdot \mathbf{S}^*_{\mathbf{Q}} \hat{\mathbf{Q}} \cdot \mathbf{S}_{\mathbf{Q}}\right] |f(\mathbf{Q})|^2, \tag{4.1}$$

where $f(\mathbf{Q})$ is the form factor and the structure-factor, $\mathbf{S}_{\mathbf{Q}}$ is given by

$$\mathbf{S}_{\mathbf{Q}} = \sum_{\alpha} e^{i\mathbf{q}\cdot(\mathbf{R}_j + \mathbf{c}_\alpha)} \mathbf{S}_{j\alpha}, \tag{4.2}$$

where $\mathbf{c}_\alpha$ represents the positions of each of the spins in the magnetic unit cell, sixteen for the case of $\mathbf{k} = (1/2, 1/2, 1/2)$, the locations of which were shown in the previous chapter in Fig. 3.11. $\mathbf{R}_j$ is an arbitrary lattice vector, which we will choose to be the origin, located in the upper left corner of Fig. 3.11. We will first consider the different structure factors and then in the following subsection look at the orientational factors.

4.2.1 Structure Factors for $\mathbf{k} = (1/2, 1/2, 1/2)$

The structure factors have the periodicity of the magnetic reciprocal-space super-lattice:

$$\mathbf{S}_{\mathbf{Q}+\mathbf{G}} = \mathbf{S}_{\mathbf{Q}}, \tag{4.3}$$

where $\mathbf{G}$ is a magnetic reciprocal-space super-lattice vector. For the pyrochlore lattice these are given by linear combinations of the vectors

$$\mathbf{G}_1 = (-2, 2, 2)\,, \qquad \mathbf{G}_2 = (2, -2, 2)\,, \qquad \mathbf{G}_3 = (2, 2, -2)\,, \tag{4.4}$$

(see Section 5.3 for more detail). As a result there are sixteen independent structure factors. The shell of Bragg spots closest to the origin contains eight spots which are all related via the point symmetry of the lattice. We only need consider four of these as the spots at $\mathbf{S}_{\mathbf{Q}}$ and $\mathbf{S}_{-\mathbf{Q}}$ are related by $\mathbf{S}^*_{\mathbf{Q}} = \mathbf{S}_{-\mathbf{Q}}$, arising form $\mathbf{S}^*_{\mathbf{R}_j} = \mathbf{S}_{\mathbf{R}_j}$. We will use the four spots located at wave-vectors of

$$\begin{aligned} \mathbf{Q}_0 &= \left(\frac{1}{2}, \frac{1}{2}, \frac{1}{2}\right), \qquad \mathbf{Q}_4 = \left(\frac{1}{2}, -\frac{1}{2}, -\frac{1}{2}\right), \\ \mathbf{Q}_8 &= \left(-\frac{1}{2}, \frac{1}{2}, -\frac{1}{2}\right), \qquad \mathbf{Q}_{12} = \left(-\frac{1}{2}, -\frac{1}{2}, \frac{1}{2}\right). \end{aligned} \tag{4.5}$$

The next shell has twenty-four point-symmetry related Bragg spots, twelve of which are independent and we will use those located at the wave-vectors

$$\begin{aligned} \mathbf{Q}_1 &= \left(\frac{3}{2}, \frac{1}{2}, \frac{1}{2}\right), \qquad \mathbf{Q}_5 = \left(\frac{3}{2}, -\frac{1}{2}, -\frac{1}{2}\right), \\ \mathbf{Q}_9 &= \left(-\frac{3}{2}, \frac{1}{2}, -\frac{3}{2}\right), \qquad \mathbf{Q}_{13} = \left(\frac{3}{2}, -\frac{1}{2}, -\frac{1}{2}\right), \\ \mathbf{Q}_2 &= \left(\frac{1}{2}, \frac{3}{2}, \frac{1}{2}\right), \qquad \mathbf{Q}_6 = \left(\frac{1}{2}, -\frac{3}{2}, -\frac{1}{2}\right), \\ \mathbf{Q}_{10} &= \left(-\frac{1}{2}, \frac{3}{2}, -\frac{1}{2}\right), \qquad \mathbf{Q}_{14} = \left(-\frac{1}{2}, -\frac{3}{2}, \frac{1}{2}\right), \\ \mathbf{Q}_3 &= \left(\frac{1}{2}, \frac{1}{2}, \frac{3}{2}\right), \qquad \mathbf{Q}_7 = \left(\frac{1}{2}, -\frac{1}{2}, -\frac{3}{2}\right), \end{aligned}$$

$$\mathbf{Q}_{11} = \left(-\frac{1}{2}, \frac{1}{2}, -\frac{3}{2}\right), \qquad \mathbf{Q}_{10}\left(-\frac{1}{2}, -\frac{1}{2}, \frac{3}{2}\right). \tag{4.6}$$

We can relate all Bragg spots outside the first two shells back to the sixteen stated in Equations 4.5 and 4.6 using linear combinations of reciprocal super-lattice vectors. Below we demonstrate this for the first ten shells of spots. The symmetry of the lattice means that one group of point-symmetry related Bragg spots all map onto the same group of related Bragg spots in a different shell, so we only describe one Bragg spot from each group.

$$\begin{aligned}
\mathbf{Q} &= \left(\frac{3}{2}, \frac{3}{2}, \frac{1}{2}\right) = \mathbf{G}_1 + \mathbf{G}_2 + \mathbf{G}_3 - \mathbf{Q}_3, \\
\mathbf{Q} &= \left(\frac{3}{2}, \frac{3}{2}, \frac{3}{2}\right) = \mathbf{G}_1 + \mathbf{G}_2 + \mathbf{G}_3 - \mathbf{Q}_0, \\
\mathbf{Q} &= \left(\frac{5}{2}, \frac{1}{2}, \frac{1}{2}\right) = \mathbf{G}_2 + \mathbf{G}_3 - \mathbf{Q}_{13}, \\
\mathbf{Q} &= \left(\frac{5}{2}, \frac{3}{2}, \frac{1}{2}\right) = \mathbf{G}_1 + \mathbf{G}_2 + \mathbf{G}_3 + \mathbf{Q}_7, \\
\mathbf{Q} &= \left(\frac{5}{2}, \frac{3}{2}, \frac{3}{2}\right) = \mathbf{G}_1 + \mathbf{G}_2 + \mathbf{G}_3 + \mathbf{Q}_4, \\
\mathbf{Q} &= \left(\frac{5}{2}, \frac{5}{2}, \frac{1}{2}\right) = \mathbf{G}_1 + \mathbf{G}_2 + \mathbf{G}_3 - \mathbf{Q}_{15}, \\
\mathbf{Q} &= \left(\frac{7}{2}, \frac{1}{2}, \frac{1}{2}\right) = \mathbf{G}_2 + \mathbf{G}_3 - \mathbf{Q}_4, \\
\mathbf{Q} &= \left(\frac{5}{2}, \frac{5}{2}, \frac{3}{2}\right) = \mathbf{G}_1 + \mathbf{G}_2 + \mathbf{G}_3 - \mathbf{Q}_6, \\
\mathbf{Q} &= \left(\frac{7}{2}, \frac{3}{2}, \frac{1}{2}\right) = \mathbf{G}_2 + \mathbf{G}_3 - \mathbf{Q}_6, \\
\mathbf{Q} &= \left(\frac{7}{2}, \frac{3}{2}, \frac{3}{2}\right) = \mathbf{G}_1 + \mathbf{G}_2 + \mathbf{G}_3 + \mathbf{Q}_{13}, \\
\mathbf{Q} &= \left(\frac{5}{2}, \frac{5}{2}, \frac{5}{2}\right) = \mathbf{G}_1 + \mathbf{G}_2 + \mathbf{G}_3 - \mathbf{Q}_0, \\
\mathbf{Q} &= \left(\frac{7}{2}, \frac{5}{2}, \frac{1}{2}\right) = \mathbf{G}_1 + \mathbf{G}_2 + 2\mathbf{G}_3 + \mathbf{Q}_1 4,
\end{aligned} \tag{4.7}$$

which gives

$$\mathbf{S}_{\left(\frac{1}{2},\frac{1}{2},\frac{1}{2}\right)} = \mathbf{S}_{\left(\frac{3}{2},\frac{3}{2},\frac{3}{2}\right)} = \mathbf{S}_{\left(\frac{5}{2},\frac{3}{2},\frac{3}{2}\right)} = \mathbf{S}_{\left(\frac{7}{2},\frac{1}{2},\frac{1}{2}\right)} = \mathbf{S}_{\left(\frac{5}{2},\frac{5}{2},\frac{3}{2}\right)} = \mathbf{S}_{\left(\frac{5}{2},\frac{5}{2},\frac{5}{2}\right)}, \tag{4.8}$$

and

$$\mathbf{S}_{\left(\frac{3}{2},\frac{1}{2},\frac{1}{2}\right)} = \mathbf{S}_{\left(\frac{3}{2},\frac{3}{2},\frac{1}{2}\right)} = \mathbf{S}_{\left(\frac{5}{2},\frac{1}{2},\frac{1}{2}\right)} = \mathbf{S}_{\left(\frac{5}{2},\frac{3}{2},\frac{1}{2}\right)} = \mathbf{S}_{\left(\frac{5}{2},\frac{5}{2},\frac{1}{2}\right)} = \mathbf{S}_{\left(\frac{7}{2},\frac{3}{2},\frac{1}{2}\right)} = \mathbf{S}_{\left(\frac{7}{2},\frac{3}{2},\frac{3}{2}\right)} = \mathbf{S}_{\left(\frac{7}{2},\frac{5}{2},\frac{1}{2}\right)}. \tag{4.9}$$

The elastic neutron scattering studies we discussed earlier[21, 69] were powder diffraction experiments. The peak intensities are therefore the result of averaging over all Bragg spots that are the same distance from the origin. We note that there are eight spots of the form (q_1, q_1, q_1) which are mapped onto each other by the point-symmetry of the crystal, twenty-four spots of the form (q_1, q_1, q_2), and forty-eight spots of the form (q_1, q_2, q_3). In addition, for some shell there is an accidental degeneracy, where two (or more) types of Bragg spot, which are unrelated by the point-symmetry of the lattice) happen to lie at exactly the same distance from the origin. For example $\left|\left(\frac{3}{2}, \frac{3}{2}, \frac{3}{2}\right)\right| = \left|\left(\frac{5}{2}, \frac{1}{2}, \frac{1}{2}\right)\right|$. Taking these two points into account, if we neglect the orientational-factors and form-factor of the Bragg spots and focus on just the structure factors, then we find that the relative intensities of the first ten shells of Bragg spots are given by

$$I_1, \quad I_2, \quad I_2, \quad I_1 + I_2, \quad 2I_2, \quad 3I_1, \quad 3I_1 + I_2, \quad 3I_1 + 2I_2, \quad I_2, \quad I_1 + 2I_2 \tag{4.10}$$

respectively. From the neutron scattering data, however, we observe that $I_1 \approx 0$. As a result, with the exception of a couple of 'double' spots, most of the variation in the Bragg peak intensities must be due to the orientational factors. We consider this is the next subsection, however first we calculate the sixteen independent structure factors.

In the previous chapter, in Section 3.5 we calculated the structure factor for the $\mathbf{k} = (1/2, 1/2, 1/2)$ Bragg peak (see Equation 3.15). Is was shown previously, if we assume that each tetrahedron is in a perfect antiferromagnetic spin state, then the structure factor

can be written in terms of only the four spins on a single sub-lattice. The same applies for the other fifteen spots. Up to an arbitrary choice of phase, the sixteen structure factors are then given by

$$\mathbf{S}_{\mathbf{Q}_0} = \mathbf{S}_{\left(\frac{1}{2},\frac{1}{2},\frac{1}{2}\right)} \propto \mathbf{S}_0 + \mathbf{S}_1 + \mathbf{S}_2 + \mathbf{S}_3, \tag{4.11}$$

$$\mathbf{S}_{\mathbf{Q}_1} = \mathbf{S}_{\left(\frac{3}{2},\frac{1}{2},\frac{1}{2}\right)} \propto \mathbf{S}_0 + \mathbf{S}_1 - \mathbf{S}_2 - \mathbf{S}_3, \tag{4.12}$$

$$\mathbf{S}_{\mathbf{Q}_2} = \mathbf{S}_{\left(\frac{1}{2},\frac{3}{2},\frac{1}{2}\right)} \propto \mathbf{S}_0 - \mathbf{S}_1 + \mathbf{S}_2 - \mathbf{S}_3, \tag{4.13}$$

$$\mathbf{S}_{\mathbf{Q}_3} = \mathbf{S}_{\left(\frac{1}{2},\frac{1}{2},\frac{3}{2}\right)} \propto \mathbf{S}_0 - \mathbf{S}_1 - \mathbf{S}_2 + \mathbf{S}_3, \tag{4.14}$$

$$\mathbf{S}_{\mathbf{Q}_4} = \mathbf{S}_{\left(\frac{1}{2},-\frac{1}{2},-\frac{1}{2}\right)} \propto \mathbf{S}_4 + \mathbf{S}_5 + \mathbf{S}_6 + \mathbf{S}_7, \tag{4.15}$$

$$\mathbf{S}_{\mathbf{Q}_5} = \mathbf{S}_{\left(\frac{3}{2},-\frac{1}{2},-\frac{1}{2}\right)} \propto \mathbf{S}_4 + \mathbf{S}_5 - \mathbf{S}_6 - \mathbf{S}_7, \tag{4.16}$$

$$\mathbf{S}_{\mathbf{Q}_6} = \mathbf{S}_{\left(\frac{1}{2},-\frac{3}{2},-\frac{1}{2}\right)} \propto \mathbf{S}_4 - \mathbf{S}_5 + \mathbf{S}_6 - \mathbf{S}_7, \tag{4.17}$$

$$\mathbf{S}_{\mathbf{Q}_7} = \mathbf{S}_{\left(\frac{1}{2},-\frac{1}{2},-\frac{3}{2}\right)} \propto \mathbf{S}_4 - \mathbf{S}_5 - \mathbf{S}_6 + \mathbf{S}_7, \tag{4.18}$$

$$\mathbf{S}_{\mathbf{Q}_8} = \mathbf{S}_{\left(-\frac{1}{2},\frac{1}{2},-\frac{1}{2}\right)} \propto \mathbf{S}_8 + \mathbf{S}_9 + \mathbf{S}_{10} + \mathbf{S}_{11}, \tag{4.19}$$

$$\mathbf{S}_{\mathbf{Q}_9} = \mathbf{S}_{\left(-\frac{3}{2},\frac{1}{2},-\frac{1}{2}\right)} \propto \mathbf{S}_8 + \mathbf{S}_9 - \mathbf{S}_{10} - \mathbf{S}_{11}, \tag{4.20}$$

$$\mathbf{S}_{\mathbf{Q}_{10}} = \mathbf{S}_{\left(-\frac{1}{2},\frac{3}{2},-\frac{1}{2}\right)} \propto \mathbf{S}_8 - \mathbf{S}_9 + \mathbf{S}_{10} - \mathbf{S}_{11}, \tag{4.21}$$

$$\mathbf{S}_{\mathbf{Q}_{11}} = \mathbf{S}_{\left(-\frac{1}{2},\frac{1}{2},-\frac{3}{2}\right)} \propto \mathbf{S}_8 - \mathbf{S}_9 - \mathbf{S}_{10} + \mathbf{S}_{11}, \tag{4.22}$$

$$\mathbf{S}_{\mathbf{Q}_{12}} = \mathbf{S}_{\left(-\frac{1}{2},-\frac{1}{2},\frac{1}{2}\right)} \propto \mathbf{S}_{12} + \mathbf{S}_{13} + \mathbf{S}_{14} + \mathbf{S}_{15}, \tag{4.23}$$

$$\mathbf{S}_{\mathbf{Q}_{13}} = \mathbf{S}_{\left(-\frac{3}{2},-\frac{1}{2},\frac{1}{2}\right)} \propto \mathbf{S}_{12} + \mathbf{S}_{13} - \mathbf{S}_{14} - \mathbf{S}_{15}, \tag{4.24}$$

$$\mathbf{S}_{\mathbf{Q}_{14}} = \mathbf{S}_{\left(-\frac{1}{2},-\frac{3}{2},\frac{1}{2}\right)} \propto \mathbf{S}_{12} - \mathbf{S}_{13} + \mathbf{S}_{14} - \mathbf{S}_{15}, \tag{4.25}$$

$$\mathbf{S}_{\mathbf{Q}_{15}} = \mathbf{S}_{\left(-\frac{1}{2},-\frac{1}{2},\frac{3}{2}\right)} \propto \mathbf{S}_{12} - \mathbf{S}_{13} - \mathbf{S}_{14} + \mathbf{S}_{15}, \tag{4.26}$$

where we have labeled the sixteen spins required to describe the $\mathbf{k} = (1/2, 1/2, 1/2)$ ordering using the same convention as in the previous chapter, and shown in Fig. 3.11.

We saw in the previous chapter, Section 3.5, that if the nearest neighbour Heisenberg interaction is assumed to be effectively infinte, then the sum of the spins on a single sub-lattice vanishes (Equations 3.17. The experimental observation that the structure-factors of the first shell of spots vanishes (we can see in Fig. 3.3 that both the first, and also the sixth shell of spots vanish, which are both controlled by these structure-factors) is therefore consistent with this energetic argument, suggesting (thought not proving) that the nearest neighbour Heisenberg interaction is indeed dominant.

4.2.2 Orientational factors for $\mathbf{k} = (1/2, 1/2, 1/2)$

The fact that we can express the sixteen structure factors in terms on the spins on a single sub-lattice only (as shown above), considerably simplifies the orientational factors. This allows us to make some simple deductions about them. We will assume that the spins are aligned in the planes perpendicular to the local tetrahedral axes, as indicated by the Mössbauer experiments[8]. Although we do not believe that this is strictly accurate, it should serve as a useful approximation. Each sub-lattice is associated with one of the crystallographic directions (along the local tetrahedral axes) and all the spins that lie on the same sub-lattice are consequently (in our approximation) perpendicular to the same tetrahedral axis. We found in the previous subsection that each structure-factor could be expressed in terms of spins lying on only one sub-lattice, hence each of these structure-factors is also (approximately) perpendicular to the appropriate tetrahedral axis. Neutrons can only coherently scatter off the component of the reciprocal-space spin density that is perpendicular to the wave-vector $\mathbf{Q}$ (hence the orientational factor in the expression for the Bragg peak intensities). Any component of $\mathbf{Q}$ which is parallel to the local tetrahedral direction (and therefore also the reciprocal-space spin density) will therefore be visible in the scattering intensity. For each Bragg spot, we can therefore calculate the angle

$$\cos\phi\left(\mathbf{Q}\right) = \hat{\mathbf{Q}} \cdot \hat{\mathbf{z}}_{\alpha}, \tag{4.27}$$

where $\hat{\mathbf{z}}_\alpha$ is the crystallographic direction associated with sub-lattice α corresponding to the Bragg spot $\mathbf{S_Q}$. All the point-symmetry related Bragg spots in a single shell share this angle. This angle therefore places a lower bound on the expected Bragg spot strengths (as we still have no information on whether the component of $\mathbf{Q}$ lying in the 'Mössbauer' plane is perpendicular or parallel to the structure-factor). For the first ten shells we find that

$$\begin{aligned}\cos^2\phi \;=\; & 1, \quad \frac{25}{33}, \quad \frac{49}{57}, \quad 1\&\frac{1}{9}, \quad \frac{1}{105}, \quad \frac{1}{129}, \\ & \frac{25}{153}\&\frac{81}{153}, \quad \frac{49}{177}\&\frac{3}{59}, \quad \frac{1}{201}, \quad 1\&\frac{121}{225}.\end{aligned} \tag{4.28}$$

We combine the relative intensities from the structure-factors (Equation 4.10) with the lower bounds on the orientational factors (Equations 4.28) and also include that $I_1 = 0$ to find the following relative Bragg peak intensities,

$$0, \quad \frac{25}{33}, \quad \frac{49}{57}, \quad \frac{1}{9}, \quad \frac{2}{105}, \quad 0, \quad \frac{81}{153}, \quad \frac{6}{59}, \quad \frac{1}{29}, \quad \frac{242}{225} \tag{4.29}$$

for the first ten shells. We are still neglecting the form-factor; we will not consider this until towards the end of the chapter. We can compare these approximate lower bounds on Bragg peak inensites, to those experimentally observed (see Fig. 3.3. Firstly we notice that the fourth Bragg spot is observed to be strong, despite the small lower bound that we estimated. Next we notice that the fith Bragg spot has a considerably weaker observed intensity than the other Bragg spots (which is consistent with the small lower bound that we estimated). Finally we notice that the seventh, eighth, ninth and tenth Bragg spots are all observed to be of similar intensity despite having rather different lower bounds. Out of these points we choose to focus on the weak fifth Bragg spot. Bearing this in mind, we will now move on to set up some further constraints on the Bragg spot structure factors in order to look for possible magnetically ordered states to fit the neutron scattering intensities.

4.3 Modelling

As stated in the introduction to this chapter, we will relax the constraint enforced in the previous chapter that the spins must lie exactly in the planes perpendicular to the local tetrahedral axes. The energetic argument supporting the other two constraints: effectively infinite nearest neighbour Heisenberg interaction and classical equal-length spins, were however much stronger. We therefore wish to refomulate these two constraints in terms of the reciprocal-space degress of freedom: the structure-factors. We will then look for possible spin-states that obey these constraints and ideally also have a weak intensity fifth Bragg spot.

We begin with the requirement for equal-length spins and consider the four structure-factors which depend on the spins lying on the zeorth sublattice. These four structure-factors can be inverted to give:

$$\begin{aligned}
\mathbf{S}_0 &= \frac{1}{4}\left(\mathbf{S}_{\mathbf{Q}_0} + \mathbf{S}_{\mathbf{Q}_1} + \mathbf{S}_{\mathbf{Q}_2} + \mathbf{S}_{\mathbf{Q}_3}\right), \\
\mathbf{S}_1 &= \frac{1}{4}\left(\mathbf{S}_{\mathbf{Q}_0} + \mathbf{S}_{\mathbf{Q}_1} - \mathbf{S}_{\mathbf{Q}_2} - \mathbf{S}_{\mathbf{Q}_3}\right), \\
\mathbf{S}_2 &= \frac{1}{4}\left(\mathbf{S}_{\mathbf{Q}_0} - \mathbf{S}_{\mathbf{Q}_1} + \mathbf{S}_{\mathbf{Q}_2} - \mathbf{S}_{\mathbf{Q}_3}\right), \\
\mathbf{S}_3 &= \frac{1}{4}\left(\mathbf{S}_{\mathbf{Q}_0} - \mathbf{S}_{\mathbf{Q}_1} - \mathbf{S}_{\mathbf{Q}_2} + \mathbf{S}_{\mathbf{Q}_3}\right),
\end{aligned} \tag{4.30}$$

where we have chosen to use a unit proportionality constant to represent the overall phase of Equations 4.11 to 4.26. We require that

$$|\mathbf{S}_0|^2 = |\mathbf{S}_1|^2 = |\mathbf{S}_2|^2 = |\mathbf{S}_3|^2 = 1 \tag{4.31}$$

Consequently we find that

$$|\mathbf{S}_0|^2 + |\mathbf{S}_1|^2 + |\mathbf{S}_2|^2 + |\mathbf{S}_3|^2 = |\mathbf{S}_{\mathbf{Q}_0}|^2 + |\mathbf{S}_{\mathbf{Q}_1}|^2 + |\mathbf{S}_{\mathbf{Q}_2}|^2 + |\mathbf{S}_{\mathbf{Q}_3}|^2 = 1, \tag{4.32}$$

$$|\mathbf{S}_0|^2 + |\mathbf{S}_1|^2 - |\mathbf{S}_2|^2 - |\mathbf{S}_3|^2 = 2\left[\mathbf{S}_{\mathbf{Q}_0} \cdot \mathbf{S}_{\mathbf{Q}_1} + \mathbf{S}_{\mathbf{Q}_2} \cdot \mathbf{S}_{\mathbf{Q}_3}\right] = 0, \tag{4.33}$$

$$|\mathbf{S}_0|^2 - |\mathbf{S}_1|^2 + |\mathbf{S}_2|^2 - |\mathbf{S}_3|^2 = 2\left[\mathbf{S}_{\mathbf{Q}_0} \cdot \mathbf{S}_{\mathbf{Q}_2} + \mathbf{S}_{\mathbf{Q}_1} \cdot \mathbf{S}_{\mathbf{Q}_3}\right] = 0, \tag{4.34}$$

$$|\mathbf{S}_0|^2 - |\mathbf{S}_1|^2 - |\mathbf{S}_2|^2 + |\mathbf{S}_3|^2 = 2\left[\mathbf{S}_{\mathbf{Q}_0} \cdot \mathbf{S}_{\mathbf{Q}_3} + \mathbf{S}_{\mathbf{Q}_1} \cdot \mathbf{S}_{\mathbf{Q}_2}\right] = 0. \tag{4.35}$$

$$\tag{4.36}$$

We then include $\mathbf{S}_{\mathbf{Q}_0} = \mathbf{0}$ and see that the remaining three structure-factors form an orthogonal basis and their sum a normalised unit vector:

$$\mathbf{S}_{\mathbf{Q}_1} \cdot \mathbf{S}_{\mathbf{Q}_2} = \mathbf{S}_{\mathbf{Q}_2} \cdot \mathbf{S}_{\mathbf{Q}_3} = \mathbf{S}_{\mathbf{Q}_3} \cdot \mathbf{S}_{\mathbf{Q}_1} = 0, \quad |\mathbf{S}_{\mathbf{Q}_1}|^2 + |\mathbf{S}_{\mathbf{Q}_2}|^2 + |\mathbf{S}_{\mathbf{Q}_3}|^2 = 1. \tag{4.37}$$

Entirely equivalent arguments apply to the structure factors formed by the spins on the other three sub-lattices.

We will now turn our attention to the second constraint: the total spin of each tetrahedron must vanish. We have already established that this makes the four structure-factors closest to the origin vanish. These constraints, however, also give rise to four linear relationships between the structure factors. We will require the results

$$\begin{aligned}
\mathbf{S}_0 + \mathbf{S}_4 + \mathbf{S}_8 + \mathbf{S}_{12} &= \mathbf{0}, \\
\mathbf{S}_1 + \mathbf{S}_5 - \mathbf{S}_9 - \mathbf{S}_{13} &= \mathbf{0}, \\
\mathbf{S}_2 - \mathbf{S}_6 + \mathbf{S}_{10} - \mathbf{S}_{14} &= \mathbf{0}, \\
\mathbf{S}_3 - \mathbf{S}_7 - \mathbf{S}_{12} + \mathbf{S}_{15} &= \mathbf{0},
\end{aligned} \tag{4.38}$$

from Equations 3.14. Using these relationships we find that

$$\begin{aligned}
\mathbf{S}_{\mathbf{Q}_0} + \mathbf{S}_{\mathbf{Q}_5} + \mathbf{S}_{\mathbf{Q}_{10}} + \mathbf{S}_{\mathbf{Q}_{15}} &= (\mathbf{S}_0 + \mathbf{S}_1 + \mathbf{S}_2 + \mathbf{S}_3) \\
&+ (\mathbf{S}_4 + \mathbf{S}_5 - \mathbf{S}_6 - \mathbf{S}_7) \\
&+ (\mathbf{S}_8 - \mathbf{S}_9 + \mathbf{S}_{10} - \mathbf{S}_{11}) \\
&+ (\mathbf{S}_{12} - \mathbf{S}_{13} - \mathbf{S}_{14} + \mathbf{S}_{15}) \\
&= \mathbf{0}.
\end{aligned} \tag{4.39}$$

Similarly we find that

$$\begin{aligned}
\mathbf{S}_{\mathbf{Q}_1} + \mathbf{S}_{\mathbf{Q}_4} + \mathbf{S}_{\mathbf{Q}_{11}} + \mathbf{S}_{\mathbf{Q}_{14}} &= \mathbf{0}, \\
\mathbf{S}_{\mathbf{Q}_2} + \mathbf{S}_{\mathbf{Q}_7} + \mathbf{S}_{\mathbf{Q}_8} + \mathbf{S}_{\mathbf{Q}_{13}} &= \mathbf{0}, \\
\mathbf{S}_{\mathbf{Q}_3} + \mathbf{S}_{\mathbf{Q}_6} + \mathbf{S}_{\mathbf{Q}_9} + \mathbf{S}_{\mathbf{Q}_{12}} &= \mathbf{0}.
\end{aligned} \tag{4.40}$$

Any magnetic state can be specified by the values of the sixteen independent structure-factors (which can then be inverted to find the real-space spin orientations). We choose to represent these sixteen structure-factors in matrix form:

$$\begin{bmatrix}
\mathbf{S}_{\mathbf{Q}_0} & \mathbf{S}_{\mathbf{Q}_5} & \mathbf{S}_{\mathbf{Q}_{10}} & \mathbf{S}_{\mathbf{Q}_{15}} \\
\mathbf{S}_{\mathbf{Q}_1} & \mathbf{S}_{\mathbf{Q}_4} & \mathbf{S}_{\mathbf{Q}_{11}} & \mathbf{S}_{\mathbf{Q}_{14}} \\
\mathbf{S}_{\mathbf{Q}_2} & \mathbf{S}_{\mathbf{Q}_7} & \mathbf{S}_{\mathbf{Q}_8} & \mathbf{S}_{\mathbf{Q}_{13}} \\
\mathbf{S}_{\mathbf{Q}_3} & \mathbf{S}_{\mathbf{Q}_6} & \mathbf{S}_{\mathbf{Q}_9} & \mathbf{S}_{\mathbf{Q}_{12}}
\end{bmatrix} = \begin{bmatrix}
\mathbf{0} & x_1\hat{\mathbf{x}}_1 & y_2\hat{\mathbf{y}}_2 & z_3\hat{\mathbf{z}}_3 \\
x_0\hat{\mathbf{x}}_0 & \mathbf{0} & z_2\hat{\mathbf{z}}_2 & y_3\hat{\mathbf{y}}_3 \\
y_0\hat{\mathbf{y}}_0 & z_1\hat{\mathbf{z}}_1 & \mathbf{0} & x_3\hat{\mathbf{x}}_3 \\
z_0\hat{\mathbf{z}}_0 & y_1\hat{\mathbf{y}}_1 & x_2\hat{\mathbf{x}}_2 & \mathbf{0}
\end{bmatrix}, \tag{4.41}$$

where $\{\hat{\mathbf{x}}_\alpha, \hat{\mathbf{y}}_\alpha, \hat{\mathbf{z}}_\alpha\}$ form an orthonormal basis for each $\alpha \in \{0, 1, 2, 3\}$ and for each column $\hat{\mathbf{r}}_\alpha = x_\alpha\hat{\mathbf{x}} + y_\alpha\hat{\mathbf{y}}_\alpha + z_\alpha\hat{\mathbf{z}}_\alpha$ is a normalised unit vector. This satisfies the equal-length spin constraints shown for the zeroth sub-lattice in Equation 4.37. We have also included the constraint that the four first-shell structure-factors (located on the diagonals of the matrix) should vanish. The remaining four Heisenberg constraints are enforced by ensuring that the sum of the components of each row vanish.

We can also use the above representation to describe the Mössbauer restriction that spins must lie in the plane perpendicular to the local tetrahedral axis. These axes are given by

$$\begin{aligned}
\mathbf{z}_0 &= \frac{+\hat{\mathbf{x}} + \hat{\mathbf{y}} + \hat{\mathbf{z}}}{\sqrt{3}}, \qquad & \mathbf{z}_1 &= \frac{+\hat{\mathbf{x}} - \hat{\mathbf{y}} - \hat{\mathbf{z}}}{\sqrt{3}}, \\
\mathbf{z}_2 &= \frac{-\hat{\mathbf{x}} + \hat{\mathbf{y}} - \hat{\mathbf{z}}}{\sqrt{3}}, \qquad & \mathbf{z}_3 &= \frac{-\hat{\mathbf{x}} - \hat{\mathbf{y}} + \hat{\mathbf{z}}}{\sqrt{3}},
\end{aligned} \tag{4.42}$$

where spins lying on sub-lattice α are perpendicular to the direction $\hat{\mathbf{z}}_\alpha$. As $\hat{\mathbf{r}}_\alpha$ can be

expressed in term of spins lying on sub-lattice α only, we require that

$$\hat{\mathbf{r}}_\alpha \cdot \mathbf{z}_\alpha = \mathbf{0} \tag{4.43}$$

for consistency with the Mössbauer constraint.

We wish to find states which have a weak intensity for the fifth shell of Bragg spots. This shell is formed from the Bragg spots at $\mathbf{Q} = \left(\frac{5}{2}, \frac{3}{2}, \frac{1}{2}\right)$ and point-symmetry related positions, of which there are forty eight in total. The structure factors of these spots asl map onto the twenty four structure factors in the second shell of Bragg spots. There are therefore two different structure factors from the fifth shell that map onto each structure factor from the second shell. For example both $\mathbf{S}_{\left(\frac{5}{2},\frac{3}{2},\frac{1}{2}\right)}$ and $\mathbf{S}_{\left(\frac{-3}{2},\frac{-5}{2},\frac{1}{2}\right)}$ map onto the structure factor $\mathbf{S}_{\mathbf{Q}_7}$. We temporally label the two wave-vectors as $\mathbf{K}_0 = \left(\frac{5}{2}, \frac{3}{2}.\frac{1}{2}\right)$ and $\mathbf{K}_1 = \left(\frac{-3}{2}, \frac{-5}{2}, \frac{1}{2}\right)$ so that the combined intensity of the two corresponding Bragg spots is given by

$$I \propto \left|f\left(\mathbf{K}_0\right)\right|^2 \left|\mathbf{S}_{\mathbf{Q}_7}\right|^2 \left[2 - \left|\hat{\mathbf{K}}_0 \cdot \hat{\mathbf{S}}_{\mathbf{Q}_7}\right|^2 - \left|\hat{\mathbf{K}}_1 \cdot \hat{\mathbf{S}}_{\mathbf{Q}_7}\right|^2\right], \tag{4.44}$$

where we have used $\left|f\left(\mathbf{K}_1\right)\right| = \left|f\left(\mathbf{K}_0\right)\right|$ as the two Bragg spots lie within the same shell. To minimise the total scattering intensity of these two spots, we therefore need to maximise $\left|\hat{\mathbf{K}}_0 \cdot \hat{\mathbf{S}}_{\mathbf{Q}_7}\right|^2 + \left|\hat{\mathbf{K}}_1 \cdot \hat{\mathbf{S}}_{\mathbf{Q}_7}\right|^2$. Using the parameterisation

$$\hat{\mathbf{S}}_{\mathbf{Q}_7} = x\hat{\mathbf{x}} + y\hat{\mathbf{y}} + z\hat{\mathbf{z}}, \tag{4.45}$$

subject to $x^2 + y^2 + z^2 = 1$. We find the solution $x = y = \frac{1}{\sqrt{2}}, z = 0$, which gives

$$\mathbf{S}_{\mathbf{Q}_7} = \pm\frac{(\hat{\mathbf{x}} + \hat{\mathbf{y}})}{\sqrt{2}}. \tag{4.46}$$

In this way we can also individually minimise the other eleven non-zero structure factors. It is then possible to choose the relative phases of the structure factors so that the rows of Equation 4.41 so that the nearest neighbour Heisenberg interaction is also minimised.

This gives the result

$$\begin{bmatrix} \mathbf{0} & \frac{\hat{\mathbf{y}}-\hat{\mathbf{z}}}{\sqrt{2}} & \frac{\hat{\mathbf{z}}-\hat{\mathbf{x}}}{\sqrt{2}} & \frac{\hat{\mathbf{x}}-\hat{\mathbf{y}}}{\sqrt{2}} \\ \frac{\hat{\mathbf{y}}-\hat{\mathbf{z}}}{\sqrt{2}} & \mathbf{0} & -\frac{\hat{\mathbf{x}}+\hat{\mathbf{y}}}{\sqrt{2}} & \frac{\hat{\mathbf{z}}+\hat{\mathbf{x}}}{\sqrt{2}} \\ \frac{\hat{\mathbf{z}}-\hat{\mathbf{x}}}{\sqrt{2}} & \frac{\hat{\mathbf{x}}+\hat{\mathbf{y}}}{\sqrt{2}} & \mathbf{0} & -\frac{\hat{\mathbf{y}}+\hat{\mathbf{z}}}{\sqrt{2}} \\ \frac{\hat{\mathbf{x}}-\hat{\mathbf{y}}}{\sqrt{2}} & -\frac{\hat{\mathbf{z}}+\hat{\mathbf{x}}}{\sqrt{2}} & \frac{\hat{\mathbf{y}}+\hat{\mathbf{z}}}{\sqrt{2}} & \mathbf{0} \end{bmatrix}, \tag{4.47}$$

and neglecting the form-factor. We calculate the relative intensity of the fifth shell of Bragg spots using

$$I_5 = \left|f\left(\mathbf{Q}\right)\right|^2 \sum_{\mathbf{Q}} \left|\mathbf{S}_{\mathbf{Q}}\right|^2 \left[1 - \left|\hat{\mathbf{S}}_{\mathbf{Q}} \cdot \hat{\mathbf{Q}}\right|^2\right], \tag{4.48}$$

with

$$I_2 = \left|f\left(\mathbf{Q}\right)\right|^2 \sum_{\mathbf{Q}} \left|\mathbf{S}_{\mathbf{Q}}\right|^2, \tag{4.49}$$

where the sum is over all Bragg spots in the fifth shell. For the above state this gives $I_5 = \frac{6}{35} I_2 \approx 0.171 I_2$, providing a lower bound for the intensity of the fifth Bragg spot. We notice, however, that the columns of the matrix do not form an orthonormal basis and we are unable to minimise the intensity of the fifth Bragg spot while both satisfying the equal-length spin constraints and minimising the nearest neighbour Heisenberg interaction. Finally we notice that the state found by minimising the fifth Bragg spot is also consistent with orientating the spins in the Mössbauer planes. If we select just the first row of structure factors of Equation 4.47 and set all others equal to zero, then inverting the structure factors provides the real-space spin orientations:

$$\begin{aligned} \mathbf{S}_0 &= \mathbf{S}_1 = \mathbf{S}_2 = \mathbf{S}_3 = \mathbf{0}, \\ \mathbf{S}_4 &= \mathbf{S}_5 = -\mathbf{S}_6 = -\mathbf{S}_7 = \frac{\hat{\mathbf{y}} - \hat{\mathbf{z}}}{\sqrt{2}}, \\ \mathbf{S}_8 &= -\mathbf{S}_9 = \mathbf{S}_{10} = -\mathbf{S}_{11} = \frac{\hat{\mathbf{z}} - \hat{\mathbf{x}}}{\sqrt{2}}, \\ \mathbf{S}_{12} &= -\mathbf{S}_{13} = -\mathbf{S}_{14} = \mathbf{S}_{15} = \frac{\hat{\mathbf{x}} - \hat{\mathbf{y}}}{\sqrt{2}} \end{aligned} \tag{4.50}$$

This is the 'Kagomé planes' state that was shown previously in Fig. 2.9, with the non-zero spins forming a 120° phase in the plane perpendicular to $\hat{\mathbf{z}}_0$. Choosing instead one of the

other rows of structure factors provides the alternative domains of this state.

We can express the two states that we found in the previous chapter using this reciprocal space representation. For the coplaner state we find

$$\begin{bmatrix} \mathbf{0} & \mathbf{0} & \mathbf{0} & \mathbf{0} \\ \frac{\hat{\mathbf{z}}-\hat{\mathbf{x}}}{\sqrt{2}} & \mathbf{0} & -\frac{\hat{\mathbf{z}}-\hat{\mathbf{x}}}{\sqrt{2}} & \mathbf{0} \\ \mathbf{0} & \frac{\hat{\mathbf{z}}+\hat{\mathbf{x}}}{\sqrt{2}} & \mathbf{0} & -\frac{\hat{\mathbf{z}}+\hat{\mathbf{x}}}{\sqrt{2}} \\ \mathbf{0} & \mathbf{0} & \mathbf{0} & \mathbf{0} \end{bmatrix}, \tag{4.51}$$

and for the non-coplaner state

$$\begin{bmatrix} \mathbf{0} & \mathbf{0} & \mathbf{0} & \mathbf{0} \\ \frac{2\hat{\mathbf{z}}-\hat{\mathbf{x}}-\hat{\mathbf{y}}}{2\sqrt{2}} & \mathbf{0} & -\frac{\hat{\mathbf{z}}-\hat{\mathbf{x}}}{\sqrt{2}} & \frac{\hat{\mathbf{y}}-\hat{\mathbf{x}}}{2\sqrt{2}} \\ \frac{\hat{\mathbf{y}}-\hat{\mathbf{x}}}{2\sqrt{2}} & \frac{\hat{\mathbf{z}}+\hat{\mathbf{x}}}{\sqrt{2}} & \mathbf{0} & -\frac{2\hat{\mathbf{z}}+\hat{\mathbf{x}}+\hat{\mathbf{y}}}{2\sqrt{2}} \\ \mathbf{0} & \mathbf{0} & \mathbf{0} & \mathbf{0} \end{bmatrix}. \tag{4.52}$$

For these states, we can see that the structure factors are only partially aligned along the optimal directions to minimise the fifth Bragg spot (Equation 4.47. For the coplaner state we find the relative intensity of the fifth shell of Bragg spots is given by $I_5 = \frac{10}{7} I_2 \approx 1.43 I_2$ and for the non-coplaner state we get $I_5 = \frac{33}{20} \approx 1.65 I_2$. This is indicative of the poor fit to the neutron scattering data for these states (as we discussed at the end of the previous chapter).

To solve our problem in general for all states compatible with the nearest neighbour Heisenberg interaction and equal-length spin constraints and then select the state which best fits the neutron scattering data is extremely difficult. In particular we find that it is surprisingly hard to find solutions for which the intensity of the fifth Bragg spot is weak. We therefore consider a selection of highly symmetrical states and analyse their properties to see which might be the most promising.

4.4 Investigated States

We will now discuss some of the solutions we have found to the problem discussed in the previous section. First we consider a highly symmetric state in which all structure factors have equal magnitude. We begin by parameterising the matrix in Equation 4.41 using α, β and γ as follows:

$$\begin{bmatrix} \mathbf{0} & -\alpha\hat{\mathbf{y}} - \beta\hat{\mathbf{z}} + \gamma\hat{\mathbf{x}} & -\alpha\hat{\mathbf{z}} - \beta\hat{\mathbf{x}} + \gamma\hat{\mathbf{y}} & -\alpha\hat{\mathbf{x}} - \beta\hat{\mathbf{y}} + \gamma\hat{\mathbf{z}} \\ \alpha\hat{\mathbf{y}} + \beta\hat{\mathbf{z}} + \gamma\hat{\mathbf{x}} & \mathbf{0} & -\alpha\hat{\mathbf{x}} + \beta\hat{\mathbf{y}} - \gamma\hat{\mathbf{z}} & \alpha\hat{\mathbf{z}} - \beta\hat{\mathbf{x}} - \gamma\hat{\mathbf{y}} \\ \alpha\hat{\mathbf{z}} + \beta\hat{\mathbf{x}} + \gamma\hat{\mathbf{y}} & \alpha\hat{\mathbf{x}} - \beta\hat{\mathbf{y}} - \gamma\hat{\mathbf{z}} & \mathbf{0} & -\alpha\hat{\mathbf{y}} + \beta\hat{\mathbf{z}} - \gamma\hat{\mathbf{x}} \\ \alpha\hat{\mathbf{x}} + \beta\hat{\mathbf{y}} + \gamma\hat{\mathbf{z}} & -\alpha\hat{\mathbf{z}} + \beta\hat{\mathbf{x}} - \gamma\hat{\mathbf{y}} & \alpha\hat{\mathbf{y}} - \beta\hat{\mathbf{z}} - \gamma\hat{\mathbf{x}} & \mathbf{0} \end{bmatrix}, \tag{4.53}$$

where to satisfy the constraints we require that

$$\alpha + \beta - \gamma = 0, \tag{4.54}$$

$$\alpha\beta + \beta\gamma + \gamma\alpha = 0, \tag{4.55}$$

$$\alpha^2 + \beta^2 + \gamma^2 = \frac{1}{3}. \tag{4.56}$$

The above equations have the solutions:

$$\alpha = \frac{-\left(\sqrt{5} \mp 1\right)}{4\sqrt{3}}, \qquad \beta = \frac{\left(\sqrt{5} \pm 1\right)}{4\sqrt{3}}, \qquad \gamma = \frac{\pm 2}{4\sqrt{3}}, \tag{4.57}$$

(along with equivalent solutions with the opposite phase). Of these we choose the option which gives the smallest intensity for the fifth Bragg spot:

$$\begin{bmatrix} \mathbf{0} & -\frac{2}{4\sqrt{3}}\hat{\mathbf{x}} + \frac{\sqrt{5}+1}{4\sqrt{3}}\hat{\mathbf{y}} - \frac{\sqrt{5}-1}{4\sqrt{3}}\hat{\mathbf{z}} & -\frac{\sqrt{5}-1}{4\sqrt{3}}\hat{\mathbf{x}} - \frac{2}{4\sqrt{3}}\hat{\mathbf{y}} + \frac{\sqrt{5}+1}{4\sqrt{3}}\hat{\mathbf{z}} & \frac{\sqrt{5}+1}{4\sqrt{3}}\hat{\mathbf{x}} - \frac{\sqrt{5}-1}{4\sqrt{3}}\hat{\mathbf{y}} - \frac{2}{4\sqrt{3}}\hat{\mathbf{z}} \\ \frac{2}{4\sqrt{3}}\hat{\mathbf{x}} + \frac{\sqrt{5}+1}{4\sqrt{3}}\hat{\mathbf{y}} - \frac{\sqrt{5}-1}{4\sqrt{3}}\hat{\mathbf{z}} & \mathbf{0} & -\frac{\sqrt{5}+1}{4\sqrt{3}}\hat{\mathbf{x}} - \frac{\sqrt{5}+1}{4\sqrt{3}}\hat{\mathbf{y}} - \frac{2}{4\sqrt{3}}\hat{\mathbf{z}} & \frac{\sqrt{5}-1}{4\sqrt{3}}\hat{\mathbf{x}} - \frac{2}{4\sqrt{3}}\hat{\mathbf{y}} + \frac{\sqrt{5}+1}{4\sqrt{3}}\hat{\mathbf{z}} \\ -\frac{\sqrt{5}-1}{4\sqrt{3}}\hat{\mathbf{x}} + \frac{2}{4\sqrt{3}}\hat{\mathbf{y}} + \frac{\sqrt{5}+1}{4\sqrt{3}}\hat{\mathbf{z}} & \frac{\sqrt{5}+1}{4\sqrt{3}}\hat{\mathbf{x}} + \frac{\sqrt{5}-1}{4\sqrt{3}}\hat{\mathbf{y}} - \frac{2}{4\sqrt{3}}\hat{\mathbf{z}} & \mathbf{0} & -\frac{2}{4\sqrt{3}}\hat{\mathbf{x}} - \frac{\sqrt{5}+1}{4\sqrt{3}}\hat{\mathbf{y}} - \frac{\sqrt{5}-1}{4\sqrt{3}}\hat{\mathbf{z}} \\ \frac{\sqrt{5}-1}{4\sqrt{3}}\hat{\mathbf{x}} - \frac{\sqrt{5}-1}{4\sqrt{3}}\hat{\mathbf{y}} + \frac{2}{4\sqrt{3}}\hat{\mathbf{z}} & -\frac{\sqrt{5}-1}{4\sqrt{3}}\hat{\mathbf{x}} - \frac{2}{4\sqrt{3}}\hat{\mathbf{y}} - \frac{\sqrt{5}+1}{4\sqrt{3}}\hat{\mathbf{z}} & -\frac{2}{4\sqrt{3}}\hat{\mathbf{x}} + \frac{\sqrt{5}+1}{4\sqrt{3}}\hat{\mathbf{y}} + \frac{\sqrt{5}-1}{4\sqrt{3}}\hat{\mathbf{z}} & \mathbf{0} \end{bmatrix}. \tag{4.58}$$

Unfortunately, for this state the orientational factor only reduces the relative intensity of the fifth shell of Bragg spots to $I_5 = \frac{6}{7} I_2 \approx 1.65 I_2$. Although this is a considerable improvement upon the two states from the previous chapter, it is still much too large to be consistent with the neutron scattering data. The state is shown in Fig. 4.1. It is cubic-symmetric and rather similar to the triple-spin-density-wave state for face-centered-cubic magnetism. We find that three quarters of the spins lie at 70.5° to the crystallographic axes. The other quarter, however, lie parallel to the axes. These spins can be seen in the four corners of the cube shown in Fig. 4.1. As a consequence this state is not

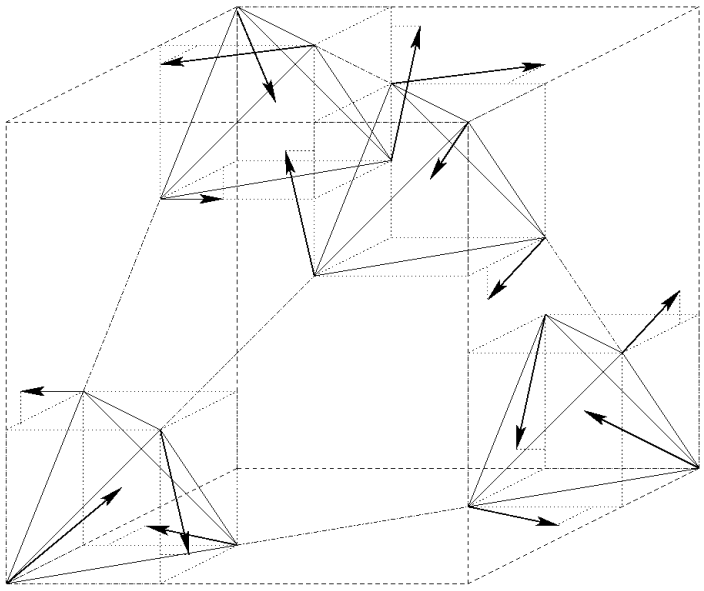

Figure 4.1: Cubic symmetry preserving state (formed from equal-magnitude structure factors).

at all useful for interpreting the experimental data. Using symmetric, equal magnitude structure factors produced fully three-dimensional spin states. To look for states that are more compatible with the Mössbauer data we therefore look for symmetry-broken states.

Next we consider generalising the coplaner state. We use the same structure as in Equation 4.51:

$$\begin{bmatrix} \mathbf{0} & \mathbf{0} & \mathbf{0} & \mathbf{0} \\ \mathbf{x}_0 & \mathbf{0} & -\mathbf{x}_0 & \mathbf{0} \\ \mathbf{0} & \mathbf{z}_1 & \mathbf{0} & -\mathbf{z}_1 \\ \mathbf{0} & \mathbf{0} & \mathbf{0} & \mathbf{0} \end{bmatrix} \tag{4.59}$$

For the moment we will focus on the choice of $\mathbf{x}_0$. We wish to maximise the orientational factor of the fifth shell for structure factors $\mathbf{S}_{\mathbf{Q}_1}$ and $-\mathbf{S}_{\mathbf{Q}_{11}}$ by making $\mathbf{x}_0$ as parallel as possible to both of the optimal structure factors given in Equation 4.47, given by

$$\mathbf{S}_{\mathbf{Q}_1} = \frac{\hat{\mathbf{y}} - \hat{\mathbf{z}}}{\sqrt{2}}, \qquad \mathbf{S}_{\mathbf{Q}_{11}} = -\frac{\hat{\mathbf{x}} + \hat{\mathbf{y}}}{\sqrt{2}}. \tag{4.60}$$

We write the two orientational factors as

$$\begin{aligned} \cos\theta &= \frac{(\hat{\mathbf{y}} - \hat{\mathbf{z}})}{\sqrt{2}} \cdot \mathbf{x}_0, \\ \cos\phi &= \frac{(\hat{\mathbf{x}} + \hat{\mathbf{y}})}{\sqrt{2}} \cdot \mathbf{x}_0, \end{aligned} \tag{4.61}$$

and notice that the two relationships are equivalent under the mapping $\hat{\mathbf{x}} \mapsto -\hat{\mathbf{z}}$. We use the parameterisation $\mathbf{x}_0 = ax + by - az$ subject to $2a^2 + b^2 = 1$. This gives

$$\cos\theta = \cos\phi = \frac{1}{\sqrt{2}}(a + b), \tag{4.62}$$

from which we can eliminate 'b' and maximise to find $a = \pm\frac{1}{\sqrt{6}}$ and $b = \pm\frac{2}{\sqrt{6}}$, and we choose

$$\mathbf{x}_0 = \frac{\hat{\mathbf{x}} + 2\hat{\mathbf{y}} - \hat{\mathbf{z}}}{\sqrt{6}}. \tag{4.63}$$

Finding $\mathbf{z}_1$ in the same way gives us the state

$$\begin{bmatrix} \mathbf{0} & \mathbf{0} & \mathbf{0} & \mathbf{0} \\ \frac{\hat{\mathbf{x}}+2\hat{\mathbf{y}}-\hat{\mathbf{z}}}{\sqrt{6}} & \mathbf{0} & \frac{-\hat{\mathbf{x}}-2\hat{\mathbf{y}}+\hat{\mathbf{z}}}{\sqrt{6}} & \mathbf{0} \\ \mathbf{0} & \frac{-\hat{\mathbf{x}}-2\hat{\mathbf{y}}-\hat{\mathbf{z}}}{\sqrt{6}} & \mathbf{0} & \frac{\hat{\mathbf{x}}+2\hat{\mathbf{y}}+\hat{\mathbf{z}}}{\sqrt{6}} \\ \mathbf{0} & \mathbf{0} & \mathbf{0} & \mathbf{0} \end{bmatrix}, \tag{4.64}$$

in which the spins are all aligned at an angle of 61.9° away form the local crystallographic axes. The relative intensity of the fifth shell of Bragg spots is given by $I_5 = \frac{22}{35} I_2 \approx 0.63 I_2$ making this the most promising state found so far. We can do better, however, so we

continue looking.

We now consider generalising the non-coplaner state and consider states with the same structure as that described in Equation 4.52. For the moment we will consider states for which the structure factors lie only in the xy plane in order to make it easier to satisfy the equal-length spin constraint. We choose the structure factors $\mathbf{S}_{\mathbf{Q}_7}$ and $\mathbf{S}_{\mathbf{Q}_{11}}$ to be optimally aligned to minimise the orientational factor of the fifth Bragg spot. We can then choose the other structure factors to take the form

$$\begin{bmatrix} \mathbf{0} & \mathbf{0} & \mathbf{0} & \mathbf{0} \\ \frac{(1-a)}{2\sqrt{2}}\hat{\mathbf{x}} + \frac{(1+b)}{2\sqrt{2}}\hat{\mathbf{y}} & \mathbf{0} & -\frac{(\hat{\mathbf{x}}+\hat{\mathbf{y}})}{\sqrt{2}} & \frac{(1+a)}{2\sqrt{2}}\hat{\mathbf{x}} + \frac{(1-b)}{2\sqrt{2}}\hat{\mathbf{y}} \\ \frac{(1+a)}{2\sqrt{2}}\hat{\mathbf{x}} + \frac{(1-b)}{2\sqrt{2}}\hat{\mathbf{y}} & -\frac{(\hat{\mathbf{x}}+\hat{\mathbf{y}})}{\sqrt{2}} & \mathbf{0} & \frac{(1-a)}{2\sqrt{2}}\hat{\mathbf{x}} + \frac{(1+b)}{2\sqrt{2}}\hat{\mathbf{y}} \\ \mathbf{0} & \mathbf{0} & \mathbf{0} & \mathbf{0} \end{bmatrix}. \tag{4.65}$$

We can see that the Heisenberg constraint is automatically satisfied and the cross terms between the two parameters cancel for the equal-length spin constraints so that we require $a^2 + b^2 = 2$. This is easily solved by selecting $a = \sqrt{2}\sin\phi$ and $b = \sqrt{2}\cos\phi$ to give

$$\begin{bmatrix} \mathbf{0} & \mathbf{0} & \mathbf{0} & \mathbf{0} \\ \frac{\left(1-\sqrt{2}\sin\phi\right)}{2\sqrt{2}}\hat{\mathbf{x}} + \frac{\left(1+\sqrt{2}\cos\phi\right)}{2\sqrt{2}}\hat{\mathbf{y}} & \mathbf{0} & -\frac{(\hat{\mathbf{x}}+\hat{\mathbf{y}})}{\sqrt{2}} & \frac{\left(1+\sqrt{2}\sin\phi\right)}{2\sqrt{2}}\hat{\mathbf{x}} + \frac{\left(1-\sqrt{2}\cos\phi\right)}{2\sqrt{2}}\hat{\mathbf{y}} \\ \frac{\left(1+\sqrt{2}\sin\phi\right)}{2\sqrt{2}}\hat{\mathbf{x}} + \frac{\left(1-\sqrt{2}\cos\phi\right)}{2\sqrt{2}}\hat{\mathbf{y}} & -\frac{(\hat{\mathbf{x}}+\hat{\mathbf{y}})}{\sqrt{2}} & \mathbf{0} & \frac{\left(1-\sqrt{2}\sin\phi\right)}{2\sqrt{2}}\hat{\mathbf{x}} + \frac{\left(1+\sqrt{2}\cos\phi\right)}{2\sqrt{2}}\hat{\mathbf{y}} \\ \mathbf{0} & \mathbf{0} & \mathbf{0} & \mathbf{0} \end{bmatrix}. \tag{4.66}$$

We can then choose ϕ to minimise the intensity of the fifth shell of Bragg spots. Two of the Bragg spots are already optimal so we need not consider them. The other four spots appear with the same 'weight' in the expression for the intensity. It is simplest therefore to maximise the projection of these four structure factors onto their ideal directions. Due to the symmetry of the problem this gives us a sum over only two contributions:

$$\left(1 + \sqrt{2}\cos\phi\right)^2 + \left(1 + \sqrt{2}\sin\phi\right)^2 = 4 + 2\sqrt{2}(\cos\phi + \sin\phi), \tag{4.67}$$

which is maximised for $\cos\phi = \sin\phi = \frac{1}{\sqrt{2}}$ or $\phi = \frac{\pi}{4}$, and so we find the state

$$\begin{bmatrix} \mathbf{0} & \mathbf{0} & \mathbf{0} & \mathbf{0} \\ \frac{1}{\sqrt{2}}\hat{\mathbf{y}} & \mathbf{0} & -\frac{(\hat{\mathbf{x}}+\hat{\mathbf{y}})}{\sqrt{2}} & \frac{1}{\sqrt{2}}\hat{\mathbf{x}} \\ \frac{1}{\sqrt{2}}\hat{\mathbf{x}} & -\frac{(\hat{\mathbf{x}}+\hat{\mathbf{y}})}{\sqrt{2}} & \mathbf{0} & \frac{1}{\sqrt{2}}\hat{\mathbf{y}} \\ \mathbf{0} & \mathbf{0} & \mathbf{0} & \mathbf{0} \end{bmatrix}. \tag{4.68}$$

The relative intensity of the fifth shell of Bragg spots is given by $I_5 = \frac{3}{5}I_2 = 0.6I_2$ which is an improvement on the previous states and half of the Bragg spots contributions are optimally aligned. We show the real-space spin orientations for this state in Fig. 4.2. It is a coplaner state with three planes containing spins parallel to $(\hat{\mathbf{x}} + \hat{\mathbf{y}})/\sqrt{2}$ and the other plane containing spins parallel to $(\hat{\mathbf{x}} - \hat{\mathbf{y}})/\sqrt{2}$. This state has a similar structure to those found in the previous chapter: one plane in every four is special. We notice that the tetrahedra bordering the plane of $(\hat{\mathbf{x}} - \hat{\mathbf{y}})/\sqrt{2}$ orientated spins are all in the local dipolar spiral ground-state that we have discussed previously. The three-quarters of the spins that are in the top three planes of Fig. 4.2 therefore also lie exactly in the Mössbauer planes. The bottom plane of spins however corrupts things. These spins are all at an angle of 35.5° from the local crystallographic directions and therefore create tetrahedra which are in a high-energy state of the dipolar interaction. We therefore need to consider a further distortion of our chosen Bragg spots.

We will now consider our final state, which we believe best describes the experimental data. We can introduce a distortion to the previously considered state in order to further reduce the intensity of the fifth shell of Bragg spots. We do this be introducing a component of $\mathbf{S}_{\mathbf{Q}_1}$ aligned along the z-axis. In order to maintain equal length spins on this sub-lattice we also have to compensate by introducing a component anti-parallel to $\hat{\mathbf{x}}$ and reducing the component parallel to $\hat{\mathbf{y}}$ so that

$$\mathbf{S}_{\mathbf{Q}_1} = -\frac{1-\cos\theta}{2\sqrt{2}}\hat{\mathbf{x}} + \frac{1+\cos\theta}{2\sqrt{2}}\hat{\mathbf{y}} - \frac{\sin\theta}{2}\hat{\mathbf{z}}. \tag{4.69}$$

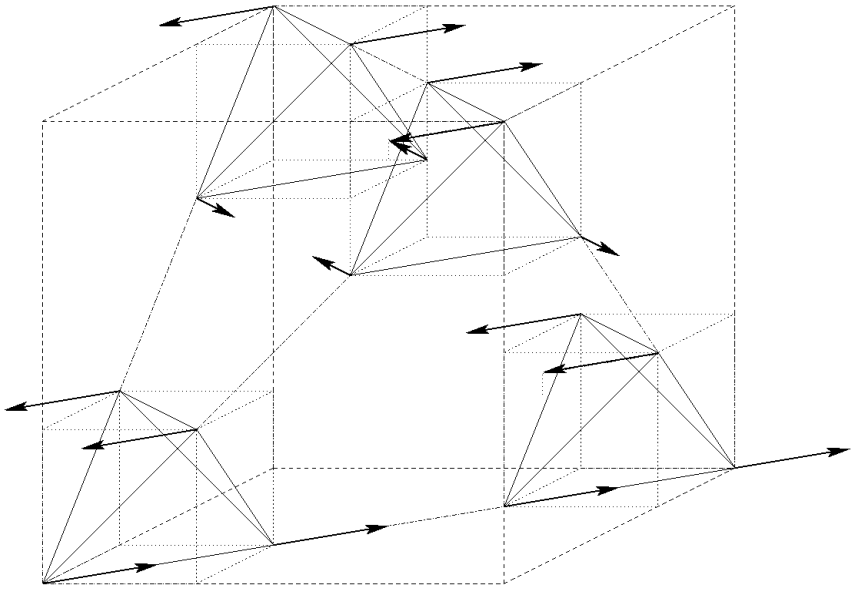

Figure 4.2: Coplaner state with special lower plane.

In order to maintain the Heisenberg constraints we also have to corrupt the two perfectly aligned structure factors by transferring some of their spin density into an empty row of the matrix, which produces the state:

$$\begin{bmatrix} \mathbf{0} & \pm\sin\theta\hat{\mathbf{z}} & \mp\sin\theta\hat{\mathbf{z}} & \mathbf{0} \\ -\frac{1-\cos\theta}{2\sqrt{2}}\hat{\mathbf{x}}+\frac{1+\cos\theta}{2\sqrt{2}}\hat{\mathbf{y}}-\frac{\sin\theta}{2}\hat{\mathbf{z}} & \mathbf{0} & -\cos\theta\frac{\hat{\mathbf{x}}+\hat{\mathbf{y}}}{\sqrt{2}} & \frac{1+\cos\theta}{2\sqrt{2}}\hat{\mathbf{x}}-\frac{1-\cos\theta}{2\sqrt{2}}\hat{\mathbf{y}}+\frac{\sin\theta}{2}\hat{\mathbf{z}} \\ \frac{1+\cos\theta}{2\sqrt{2}}\hat{\mathbf{x}}-\frac{1-\cos\theta}{2\sqrt{2}}\hat{\mathbf{y}}-\frac{\sin\theta}{2}\hat{\mathbf{z}} & -\cos\theta\frac{\hat{\mathbf{x}}+\hat{\mathbf{y}}}{\sqrt{2}} & \mathbf{0} & -\frac{1-\cos\theta}{2\sqrt{2}}\hat{\mathbf{x}}+\frac{1+\cos\theta}{2\sqrt{2}}\hat{\mathbf{y}}+\frac{\sin\theta}{2}\hat{\mathbf{z}} \\ \mathbf{0} & \mathbf{0} & \mathbf{0} & \mathbf{0} \end{bmatrix}. \tag{4.70}$$

We note that in addition to the sign degree of freedom for structure factors $\mathbf{S}_{\mathbf{Q}_5}$ and $\mathbf{S}_{\mathbf{Q}_{10}}$, alternatively we could have used $\mathbf{S}_{\mathbf{Q}_6}$ and $\mathbf{S}_{\mathbf{Q}_9}$ from the bottom row. This provides us with a choice of four domains, a point which we will discuss later. We could choose the value of the parameter θ by minimising the intensity of the fifth shell of Bragg spots was we did for the previous states. Instead however we will fix this parameter by minimising the local dipolar energy, which we address in Section 4.6. First though we will explain the real-space structure of this state.

4.5 Predicted magnetically ordered state

In this section we will briefly explain the real-space spin structure of our chosen state. We can invert the structure factors given in Equation 4.72 to find four possible states as a result of the freedom to choose whether to use two structure factors from the top row or bottom row of spots, as well as to choose their sign relative to the other six structure factors in the middle two rows. (In addition there are also many equivalent domains obtained from global translations and rotations which we will not discus). In Fig. 4.3 we show slices through the pyrochlore lattice in the xy-plane as was done in previous figures. The columns which contain two planes represent the two alternative options of using the

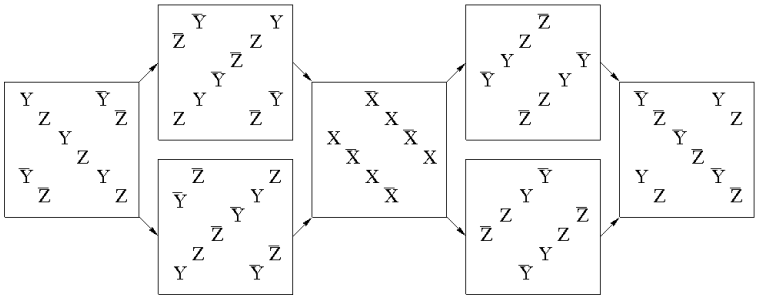

Figure 4.3: Real-space orientation of spins shown for successive planes perpendicular to the z-axis.

lower or upper pair of structure factors. In addition inverting all the spins on either of these planes also provides a solution. We have annotated the spin directions using:

$$\begin{aligned} \mathbf{X} &= \frac{\hat{\mathbf{x}} - \hat{\mathbf{y}}}{\sqrt{2}}, \\ \mathbf{Y} &= \cos\theta \frac{\hat{\mathbf{x}} + \hat{\mathbf{y}}}{\sqrt{2}} - \sin\theta \hat{\mathbf{z}}, \\ \mathbf{Z} &= \cos\theta \frac{\hat{\mathbf{x}} + \hat{\mathbf{y}}}{\sqrt{2}} + \sin\theta \hat{\mathbf{z}}, \end{aligned} \tag{4.71}$$

where a 'bar' in the figure represents the inverse of the relevant spin. A three dimensional diagram of an example of this state is shown in Fig. 4.4. In the next section we will discuss the energetics and physical properties of this state.

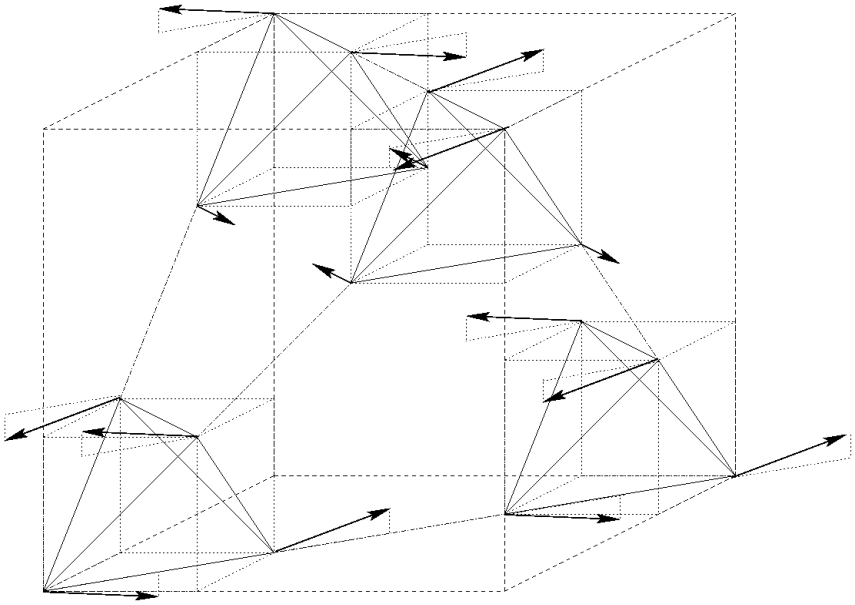

Figure 4.4: Proposed spin-state.

4.6 Energetics

We will begin by briefly summarising the general energetics arguments for the pyrochlore lattice from the previous chapter. The ground-state the dipolar interaction in the presence of dominant nearest neighbour Heisenberg exchange is the $\mathbf{k} = \mathbf{0}$ spiral ground state. However, if further neighbour Heisenberg interactions are present at a similar energy scale, they can compete with the dipole interaction to destabilise the $\mathbf{k} = \mathbf{0}$ ground-state. This spiraling state has an exchange energy of $H_{\mathrm{Ex}} = (3J_3 - 2J_2)NS^2$ and is therefore a high-energy state for this interaction (we recall that for the pyrochlore lattice we believe $J_3 > J_2$, see Section 3.6). The Heisenberg exchange energy for a $\mathbf{k} = (1/2, 1/2, 1/2)$ state is actually a constant (and therefore independent of the particular style of $\mathbf{k} = (1/2, 1/2, 1/2)$ order present): $H_{\mathrm{Ex}} = -J_3 NS^2$. We see that this is a much lower energy state than $\mathbf{k} = \mathbf{0}$ order, though it is not actually the global minimum of just the (further neighbour) Exchange energy. As a result, we therefore suggest that the presence of further neighbour exchange interaction is $Gd_2Ti_2O_7$ stabilises a $\mathbf{k} = (1/2, 1/2, 1/2)$ state over the $\mathbf{k} = \mathbf{0}$ state, but does not influence which $\mathbf{k} = (1/2, 1/2, 1/2)$ is chosen. This must depend on the dipolar energy of the different $\mathbf{k} = (1/2, 1/2, 1/2)$ states (we will neglect all weaker

interactions). For this reason we will therefore use the dipole energy to fix our choice of the parameter θ for our proposed ground state (see Fig. 4.3).

For simplicity we will consider only the local (i.e. nearest neighbour) contribution to the dipole energy for our chosen state. Longer-range correlations will be much weaker and unlikely to be relevant to this argument anyway as a result of other assumptions that we have made, in particular that the nearest neighbour Heisenberg exchange is infinite. For states indexed by $\mathbf{k} = (1/2, 1/2, 1/2)$ there are eight different tetrahedra that we need to consider (the four highlighted in Fig. 4.4 and also four inverted tetrahedra that we did not draw attention to). We will consider the state:

$$\begin{bmatrix} \mathbf{0} & \pm\sin\theta\hat{\mathbf{z}} & \mp\sin\theta\hat{\mathbf{z}} & \mathbf{0} \\ -\frac{\sqrt{2}\sin\phi-\cos\theta}{2\sqrt{2}}\hat{\mathbf{x}}+\frac{\sqrt{2}\cos\phi+\cos\theta}{2\sqrt{2}}\hat{\mathbf{y}}-\frac{\sin\theta}{2}\hat{\mathbf{z}} & \mathbf{0} & -\cos\theta\frac{\hat{\mathbf{x}}+\hat{\mathbf{y}}}{\sqrt{2}} & \frac{\sqrt{2}\sin\phi+\cos\theta}{2\sqrt{2}}\hat{\mathbf{x}}-\frac{\sqrt{2}\cos\phi-\cos\theta}{2\sqrt{2}}\hat{\mathbf{y}}+\frac{\sin\theta}{2}\hat{\mathbf{z}} \\ \frac{\sqrt{2}\sin\phi+\cos\theta}{2\sqrt{2}}\hat{\mathbf{x}}-\frac{\sqrt{2}\cos\phi-\cos\theta}{2\sqrt{2}}\hat{\mathbf{y}}-\frac{\sin\theta}{2}\hat{\mathbf{z}} & -\cos\theta\frac{\hat{\mathbf{x}}+\hat{\mathbf{y}}}{\sqrt{2}} & \mathbf{0} & -\frac{\sqrt{2}\sin\phi-\cos\theta}{2\sqrt{2}}\hat{\mathbf{x}}+\frac{\sqrt{2}\cos\phi+\cos\theta}{2\sqrt{2}}\hat{\mathbf{y}}+\frac{\sin\theta}{2}\hat{\mathbf{z}} \\ \mathbf{0} & \mathbf{0} & \mathbf{0} & \mathbf{0} \end{bmatrix}, \tag{4.72}$$

where we have included both θ and also ϕ as parameters. We sum the local dipole energy for the eight independent tetrahedra (choosing those shown in Fig. 3.11) to find

$$E_D \propto \frac{1}{4} - \frac{\cos\phi\sin\phi}{2} - \frac{\sin\phi+\cos\phi}{2\sqrt{2}}\cos\theta - \frac{\sin\theta\cos\theta}{\sqrt{2}}. \tag{4.73}$$

This is minimised by

$$\phi = \frac{\pi}{4}, \qquad \sin\theta = \frac{\sqrt{17}-1}{4\sqrt{2}}, \tag{4.74}$$

with an energy of

$$E_D \propto -\frac{3+\sqrt{17}}{32}\left(7+\sqrt{17}\right)^{\frac{1}{2}} \approx -0.742, \tag{4.75}$$

where we have chosen the units so that the $\mathbf{k} = \mathbf{0}$ ground-state to the local dipole interaction has an energy of $E_D = -1$. Our proposed state therefore has a local dipole energy of nearly three-quarters of that of the ground-state. It also has the lowest local dipole energy of all the possible $\mathbf{k} = (1/2, 1/2, 1/2)$ states that we have considered in this

chapter (with the obvious exception of the Kagomé planes state that does not satisfy the equal-length spin constraints). Furthermore we note that this value of θ is also surprisingly close to where the intensity of the fifth shell of Bragg spots is minimised for solutions of this style.

We notice another important consequence of the above local dipole energy calculation. As we discussed in the previous section, for two of the planes [see Figure 4.3) we have a choice of four possible states for each of the planes. We find that the local dipole energy does not distinguish between these states. Although weaker interactions would lift this degeneracy it seems likely that when the system magnetically orders, these planes will be incoherently frozen into the structure at random. If this is the case, then the z-component of the spins in these two planes will show no periodicity and therefore will not contribute to the neutron scattering intensities. These spin components are controlled by the two structure factors in the top (or bottom) rows of the matrix in Equation 4.72. These two structure factors therefore do not contribute to the scattering intensity. Taking this into account and using the values of θ and ϕ from Equation 4.74 we find that the intensity of the fifth shell of Bragg spots is given by $I_5 \approx 0.268 I_2$ where we have used $I_2 = \sum_{\mathbf{Q}} |\mathbf{S}_{\mathbf{Q}}|^2 = 4$. This value of I_5 is encouragingly close to the lower bound of $I_5 \approx 0.171 I_2$. We will assess the fit to the neutron scattering data in a later section, however, where we will also take into account the form-factor.

4.7 Physical Properties of proposed state.

In this section we return to considering the real-space spin orientations of our proposed state (see Figure 4.4) in order to provide some physical insight into the magnetic ordering. We begin by considering to what extent this state can be built up form the three dipolar tetrahedral ground-states shown in Fig. 2.3, along with their inverses. As these three spirals have no co-parallel spins, we cannot join the different styles of tetrahedra together without incurring a dipolar energy penalty. We begin therefore by just considering one

of these three solutions. The planes of the pyrochlore lattice show lines of Gd^{3+} ions along the directions $x = \pm y$. Starting with a line along the $x = y$ direction, we choose a dipolar ground-state spiral in which the spin directions are parallel to $(\hat{\mathbf{x}} - \hat{\mathbf{y}})/\sqrt{2}$. If we place these spins in alternating directions along the line and also between the lines, then we maintain the $\mathbf{k} = (1/2, 1/2, 1/2)$ ordering while minimising the dipole energy so far. We can place every tetrahedra connected to this plane in a spiral state, thus also fixing the spin orientations of the two neighbouring planes. This can be seen in Figure 4.5 which projects the spin orientations of our proposed state onto successive xy-planes. The

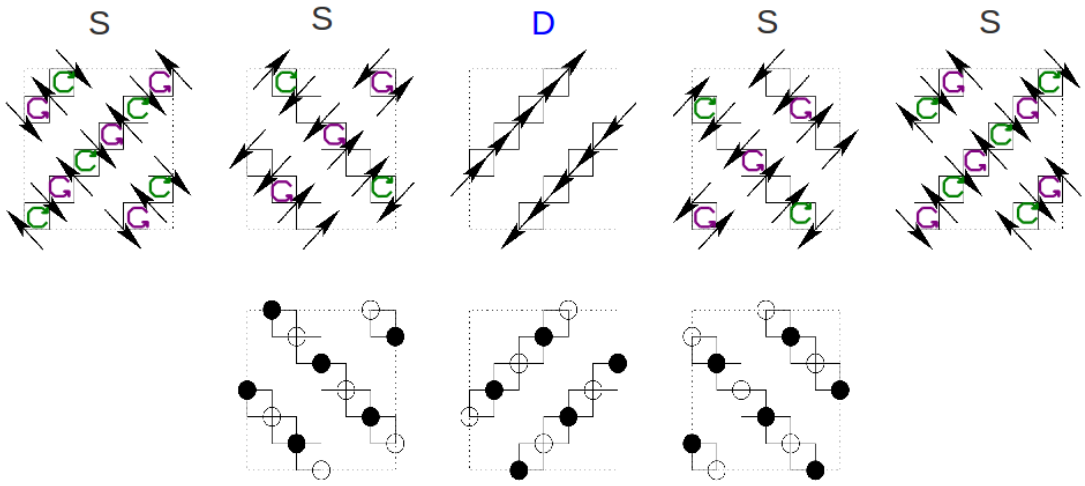

Figure 4.5: The real-space spin orientations of our proposed state. We show five consecutive planes (perpendicular to the z-axis) of the pyrochlore lattice. The arrows in the top row of diagrams show the spin components which lie within the xy-plane, while the bottom row of diagrams depict the S^z components of the spins (note that for the first and fifth planes the spins lie entirely within the xy-plane). The black circles represent a spin component into the page and the while circles a spin component out of the page. The tetrahedron formed by the Gd^{3+} ions are shown as black squares, with those in the spiral state (which minimises the local dipole energy) are marked with a purple or green arrow (with the colour indicating the chirallity of the spiral), while th e unmarked tetrahedra are in a higher energy state of the dipole interaction. If we neglect the S^z components of the spins then the planes labeled 'S' consist of spins which are forming tetrahedra in the perfect spiral state. the plane labeled 'D' can then be interpreted as a domain wall separating two regions of spiral-tetrahedra.

top panels show the x and y components of the spins and the lower panels show the z components. The tetrahedra in perfect spiral states are indicated by the green and purple arrows (with the colour representing the chirallity). If we neglect the z component for

the moment then we can see that in the first plane every tetrahedron forms a perfect spiral. (The fifth plane is forced to be the inverse of the first by the periodicity of the system.) The planes neighbouring the perfect spiral plane contain pairs of parallel spins. Minimising the nearest neighbour Heisenberg interaction then uniquely specifies the final plane of spins, forcing them to form parallel lines. For this plane the dipole energy is terrible. We note that this state is the one shown in Figure 4.2, i.e. $\theta = 0$. It is very reminiscent of the two states found in the previous chapter. We have three planes in which the spins form the dipole spirals (labeled by 'S' in Figure 4.5). The fourth plane, however, is completely different and can by viewed as a domain wall between two different regions of the spiral phase (hence we have labeled it with a 'D' in Figure 4.5). We now consider the introduction of the z components of the spins (i.e. $\theta > 0$). This has the effect of lowering the dipole energy of high energy tetrahedra. It is easiest to see this in Figure 4.4. If we project the bottom left tetrahedron onto the front face of the cube then we see a spiral around the y-axis, while projecting the bottom right tetrahedron onto the right-hand face produces a spiral around the x-axis. Although this distortion corrupts the perfect tetrahedra somewhat, the overall effect is to significantly reduce the total dipole energy when using the optimum choice of θ. We can view this distortion as a relaxing of the domain wall into the two neighbouring planes in order to reduce the total dipole energy of the system.

Finally we return to the two phase transitions observed in the specific heat data (see Figure 3.1[62]). As we discuss in the next section, we believe that our proposed state has the potential to show an excellent fit to the neutron scattering data for the low temperature phase. This state consists of two independent styles of magnetic order. The first is the six-q state described by the matrix in Equation 4.68 and the second is the addition of the two extra Bragg spots to form the eight-q state described by the matrix in Equation 4.72. We suggest that as the temperature is raised, the first transition represents the loss of magnetic order associated with the domain wall relaxation to give the coplaner state of Figure 4.2 as the intermediate phase. It is possible that this state

could be favoured in the higher temperature phase as a result of coplaner spins being more compatible with thermal fluctuations,though this is just a conjecture that would require experimental investigation. We will now move onto the final section in which we will revisit the key experiments.

4.8 Comparison with Experimental Data

In this section we will consider to what extent our proposed state is consistent with the elastic neutron scattering and Mössbauer data. We will begin with the Mössbauer. Firstly, by construction, all the spins have an equal magnitude. This was one of the key requirements for consistency with the Mössbauer data. The other was that the spins are orientated at an angle of 90° to the local crystallographic axes. Our proposed state has one quarter of the spins exactly consistent with this. We find that another quarter are close, at an angle of 83.7° and the final half (forming the incoherent planes) are orientated at 70.1°. These orientations are quite close, though not perfect. It would be interesting to see the fit of the Mössbauer data to the state in Fig. 4.4.

Next we will turn to the neutron scattering intensities. The only available data is from powder samples. We therefore need to average over the Bragg spots in each shell, as we did when investigating the intensity of the fifth Bragg spot for the various states discussed in Section 4.4. Taking care not to include the contributions from the incoherent spin components we find, still neglecting at present the form factor scaling, the relative intensities shown in Table 4.8. Next we turn to the form factor, though we will only use a very crude estimate. As Gd^{3+} has a half filled, spherically symmetric f-shell, we can obtain an approximate fit by using a hydrogenic $4f$ wavefunction. This gives us the normalised form factor

$$\frac{f(Q)}{f(0)} = \frac{\left[1-\left(\frac{Q}{\alpha}\right)^2\right]\left[\left(\frac{Q}{\alpha}\right)^2-3-2\sqrt{2}\right]\left[\left(\frac{Q}{\alpha}\right)^2-3+\sqrt{2}\right]}{\left[1+\left(\frac{Q}{\alpha}\right)^2\right]^8}, \tag{4.76}$$

Table 4.1: The predicted relative Bragg spot intensities for our proposed state, neglecting the form factors.

Bragg Spot	Intensity	Bragg Spot	Intensity
1	0.0000000000	17	2.0215609823
2	0.8441048900	18	0.2675940491
3	0.7886702835	19	0.3305764354
4	0.8311627867	20	0.4097293918
5	0.2677220592	21	0.0000000000
6	0.0000000000	22	2.9975460129
7	0.7752968633	23	1.8622664466
8	0.7979986130	24	0.7765690827
9	0.8127382051	25	1.9756766395
10	1.0159312338	26	1.4363639095
11	1.0976887018	27	1.4192743142
12	1.0878370211	28	2.2669112828
13	1.6704615147	29	1.6211537903
14	1.9201549353	30	0.7852255348
15	1.2498532874	31	3.0317246897
16	1.6511165533		

where we estimate the parameter, 'α', by eye in order to attempt to match the relative Bragg spot intensities observed experimentally[69]. The decay of the form factor and the calculated Bragg spot intensities for our proposed state are shown in Fig. 4.6 Firstly we note that the relative intensities are consistent with the experimental data. In particular, the weak fifth spot is now clear, while the following few spots all have a similar intensity to each other. These features are also present in the experimentally observed data. We do not offer a more detailed comparison to the data, however, as our calculation of the relative Bragg spot intensities for our predicted state neglected many subtleties. For example, the hydrogenic wavefunction decays more slowly than a correctly screened analogue for gadolinium would. The result of this is that the first few Bragg spots appear rather weak in our fit. We have also neglected Lorentz factors. These account for the fact that the scattering intensity can have some angular dependence, for example, from the design of the detector or because in a powder sample the number of crystals orientated to satisfy Bragg's scattering law tend to be greater for low angle scattering. As in the case of the Mössbauer data, we are therefore interested in seeing an accurate fit to our proposed state.

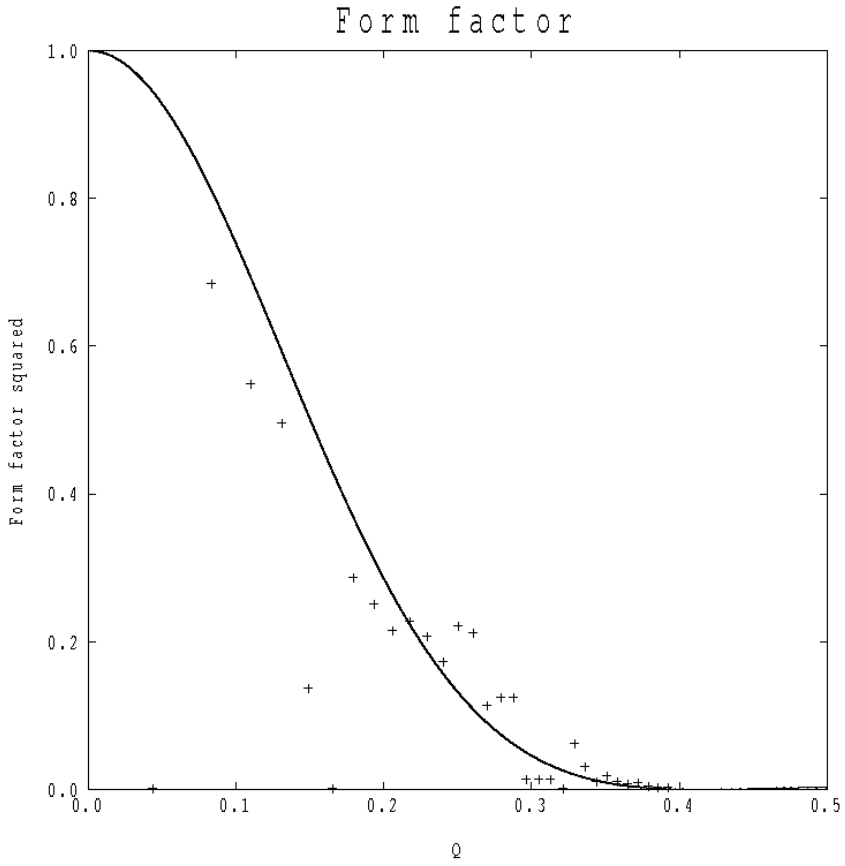

Figure 4.6: Data Points: predicted Bragg peak intensities for our proposed state. Curve: the hydrogenic form factor used.

CHAPTER 5

ERBIUM TITANATE: UNCONVENTIONAL MAGNETIC ORDER AND GAPLESS SPIN-WAVES

5.1 Introduction

In this chapter we consider the low temperature magnetic ordering of a different rare earth pyrochlore: erbium titanate. This material is very different from the gadolinium pyrochlores, as the crystal-field interaction plays a key role (something we could neglect for $Gd_2Sn_2O_7$ and $Gd_2Ti_2O_7$). In this chapter we begin by reviewing existing elastic neutron scattering experiments and their current interpretation in the literature. We argue that the magnetically ordered state currently proposed in the literature is inconsistent with the magnetic elastic neutron scattering data. We offer an alternative state which resolves this inconsistency. This state is physically very different to the previously proposed state. In particular the spins do not lie along symmetry directions of crystal lattice. Although very unusual for systems with strong spin obit coupling, this state is also consistent with gapless spin-wave mode reported by Ruff *et al.*[66] as we will discuss. We begin by reviewing the behaviour of erbium titanate by discussing the different energy scales of the system in the next section. We will then move on to discuss the elastic neutron scattering data and our interpretation of it. Finally we use a phenomenological approach to investigate how such a state might be energetically stabilised along with a semi-classical analysis of the corresponding spin-wave spectrum.

5.2 Energy scales and degeneracy lifting

In this section we will consider the degeneracies present in the electronic structure of erbium titanate. In addition we will also discuss the energy scales at which these degeneracies are lifted. As already explained in Section 1.2.3, the active ions are the Er^{3+} which form a pyrochlore lattice. The other ions: Ti^{4+} and O^{2-} are closed-shell and therefore have no electronic degeneracy. Er^{3+} has an electronic structure of: $[Xe]\,4f^{11}$, which is equivalent to three holes in the f-shell. From Hund's first and second rules, we find that the Er^{3+} ions have $S = \frac{3}{2}$ and $L = 6$. For f-block ions the third Hund's rule is also dominant over the crystal-field interaction so that in its ground-state the Er^{3+} ions have $J = \frac{15}{2}$. There is an energy separation of the order of $1eV$ (or 10^4K)[59] to the next excited state. As we are interested in the low-temperature behaviour of erbium titanate we will assume that the Er^{3+} always have $J = \frac{15}{2}$. In this case, theoretically, the maximum possible ordered moment for the erbium ions is therefore $\mu \approx g(JLS)\sqrt{J(J+1)}\mu_B = 9.58\mu_B$, where $g(JLS)$ is the Landé g factor which for the case of Er^{3+} has the value $g(JLS) = 6/5$.

Erbium ions with $J = \frac{15}{2}$ have a degeneracy of $2J + 1 = 16$ and the states are labeled by: $J_z = \frac{-15}{2}, \frac{-13}{2}, ..., \frac{15}{2}$. The sixteen degenerate states are then further split by the crystal-field interaction into up to eight pairs of (at least) doubly degenerate states. The pairs are time-reversal symmetry related and are commonly called Kramer's doublets. The doublets have been observed by inelastic neutron scattering[19]. A powder spectrum, measured at $1.8K$ is shown in Fig 5.1. There is an energy gap of $6.3meV$ between the ground-state, and first excited Kramer's doublets. The excited-state doublets, therefore, become frozen out at temperatures less than of order $100K$. We will only consider the low temperature ($T \ll 1K$) behaviour of erbium titanate. The Er^{3+} ions can therefore be modeled as having a pseudo-spin $\frac{1}{2}$.

The degeneracy of the J_z states is usually lifted by the crystal-field interaction. To gain a simple picture of which J_z eigenstates might form the ground-state Kramer's doublet we will briefly consider the geometry of the oxygen ions surrounding an erbium. There are two types of oxygen ion, which we label O1 and O2. O1 ions lie in the center of the Er^{3+}

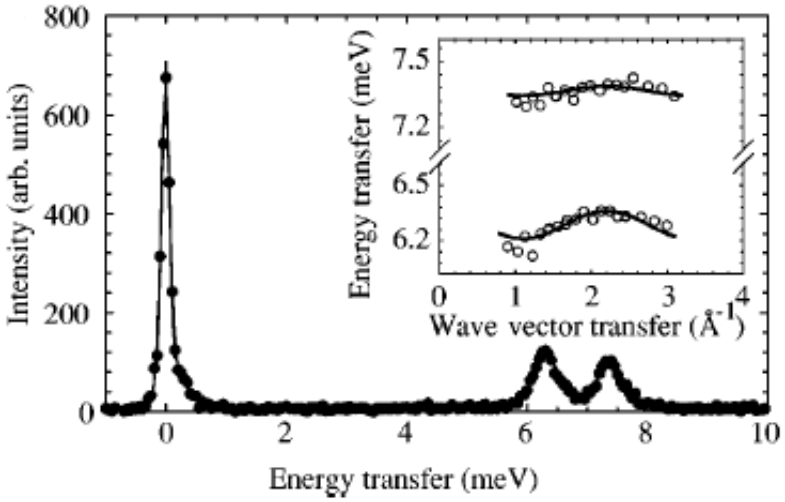

Figure 5.1: Inelastic powder spectrum measured at $T = 1.8K$. Inset: wave-vector dependence of the excitation energies. From Champion *et. al*[19].

tetrahedra, as shown earlier in Fig. 1.14. The six O2 ions form a corrugated ring (with three-fold rotation symmetry) around the plane perpendicular to the axis joining the two O1 ions (see Fig. 5.2). The O1 ions are about 12% closer to the Er^{3+} ion than the O2 ions[5]. As the radial wavefunctions decay exponentially with distance, the crystal-field energy is dominated by the O1 ions. We therefore choose to quantize the Er^{3+} angular momenta along the lines connecting the two O1 ions. These lines are also the local axes of the Er^{3+} tetrahedra (e.g. $\frac{\langle 1,1,1\rangle}{\sqrt{3}}$). To maximise the overlap between the Er^{3+} holes and O1 ion we require orbitals with low J_z values. In the previous chapter we did not have to consider this issue, as the Gd^{3+} ions are spherically symmetric and therefore isotropic. To illustrate the effect of the crystal-field interaction, we therefore briefly the case of Yb^{3+} which is particularly simple as the ion has only one hole in its outer-shell. The Yb^{3+} hole is therefore expected to be in the state $|J, \pm J_z\rangle = \left|\frac{7}{2}, \pm\frac{1}{2}\right\rangle$ in order to maximise the overlap with the O1 ions. Although this argument becomes more complicated in the case of multiple holes, however, it is likely that the ground-state of Kramer's doublet of erbium titanate will consist of a linear combination of predominately low J_z states.

We will next turn to the heat capacity data to discuss the lifting of Kramer's doublet degeneracy. The specific heat data recorded by Blöte *et al.*[5] is shown in Fig. 5.3. There

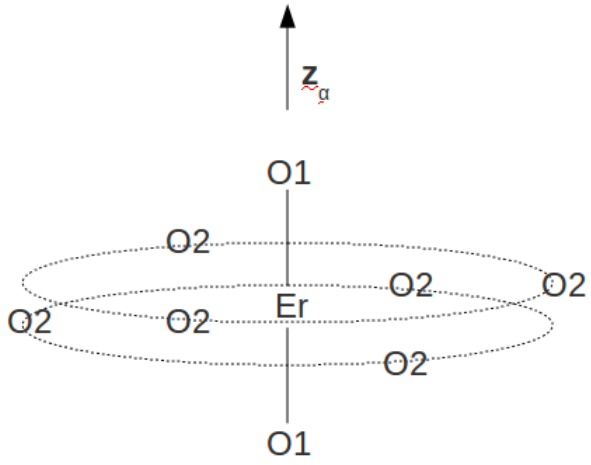

Figure 5.2: The eight O^{2-} ions surrounding the Er^{3+} ion. The O1 type oxygen ions dominate the crystal-field potential experienced by the erbium ion. $\mathbf{z}_\alpha$ is one of the local tetrahedral axes.

is a a clear singularity at $T = 1.25K$[5], which is associated with the long-range magnetic ordering of the erbium ions. An upturn in the specific heat for temperatures of $T > 0.2K$ is also visible. This upturn is associated with the onset of the ordering of the nuclear magnetic moments (and unfortunately limits the accuracy to which the magnetic entropy can be determined). As stated earlier, transitions to excited-state Kramer's doublets only become active at an energy scale of about $60K$ and the specific heat peak at T_N is therefore well isolated. Blöte *et al.* therefore integrated the extrapolated heat capacity peak to both high and low temperatures and found that it corresponded to an entropy change of $0.675 \approx 0.97R \ln 2$. This is consistent with interpretation that the transition is the ordering of a Kramer's doublet: a pseudo-spin $\frac{1}{2}$.

The low temperature magnetically ordered phase has been studied using elastic neutron scattering. Single crystal data will be discussed later, however, we will briefly mention the powder data from Champion *et al.*[19]. The powder spectrum (measured at $50mK$ show Bragg peaks indexed by a $\mathbf{k} = \mathbf{0}$ propagation vector. The ordered moment is observed to have a magnitude of $3.01 \pm 0.05\mu_B$ per erbium ion. This is of note, as it is only a third of the single-ion erbium moment. Returning to the pseudo-spin representation,

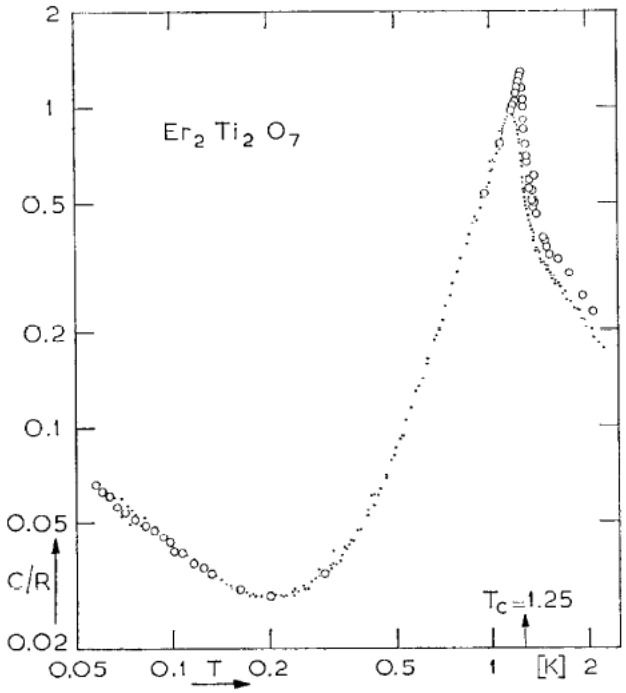

Figure 5.3: Specific heat data for erbium titanate by Blöte *et. al*[5].

we can choose to orientate the pseudo-spin in any direction. The long-range magnetic ordering is equivalent to fixing this orientation for each erbium ion, and the small observed ordered moment can provide some indication of which directions the spins are likely to align along. Sticking with our previous example of using the two $J_z = \pm\frac{1}{2}$ states to describe the Kramer's doublet, a pseudo-spin of arbitrary orientation can be described using the basis

$$\left|\psi^{\pm}\right\rangle = e^{\mp\frac{i\phi}{2}}\cos\frac{\theta}{2}\left|J, \pm\frac{1}{2}\right\rangle \pm e^{\pm\frac{i\phi}{2}}\sin\frac{\theta}{2}\left|J, \mp\frac{1}{2}\right\rangle, \tag{5.1}$$

where θ is the angle between the quantisation direction and the local tetrahedral axis, for example $\frac{\langle 111\rangle}{\sqrt{3}}$, and ϕ is the azimuthal angle. For a spin orientated parallel to this quantisation direction $|\psi^{+}\rangle = \left|\frac{15}{2}, \frac{1}{2}\right\rangle$ and

$$\langle \mathbf{J}\rangle = \langle\frac{15}{2}, \frac{1}{2} \mid J_z \left|\frac{15}{2}, \frac{1}{2}\right\rangle \hat{\mathbf{z}} = \frac{1}{2}\hat{\mathbf{z}}. \tag{5.2}$$

If the spin is orientated perpendicular to the quantisation direction, then we can choose

$|\psi^+\rangle = \frac{1}{\sqrt{2}}\left(\left|\frac{15}{2},\frac{1}{2}\right\rangle + \left|\frac{15}{2},-\frac{1}{2}\right\rangle\right)$. Using

$$J^{\pm} = J^x \pm iJ^y \tag{5.3}$$

and

$$J^{\pm}\,|J, J_z\rangle = \sqrt{(J \mp J_z)\,(J \pm J_z + 1)}\,|J, J_z \pm 1\rangle, \tag{5.4}$$

then

$$\langle \mathbf{J} \rangle = \frac{1}{4}\left(\langle \frac{15}{2},\frac{1}{2} \mid J^+ \left| \frac{15}{2},-\frac{1}{2}\right\rangle + \langle \frac{15}{2},-\frac{1}{2} \mid J^- \left| \frac{15}{2},\frac{1}{2}\right\rangle\right)\hat{\mathbf{x}} = \frac{\sqrt{63}}{2}\hat{\mathbf{x}}. \tag{5.5}$$

The magnetic moment can be calculated using $\mu = g(JLS)\sqrt{J(J+1)}\mu_B$, where the Landé g-factor is given by

$$g(JLS) \approx \frac{3}{2} + \frac{1}{2}\left[\frac{S\,(S+1) - L\,(L+1)}{J\,(J+1)}\right] = \frac{6}{5}. \tag{5.6}$$

For our chosen crystal-field state, spins orientated parallel to the quantisation direction are expected to have an ordered moment of $\mu_{\parallel} \approx 1.04\mu_B$ per spin, and spins ordered perpendicular to the quantisation direction are expected to have an ordered moment of $\mu_{\perp} \approx 5.33\mu_B$ per spin. As discussed earlier, the actual ground-state Kramer's doublet for erbium titanate is likely to be the $J_z = \pm\frac{1}{2}$ with some larger $|J_z|$ eigenstates mixed in. This will increase the values of both $\mu_{\parallel}$ and $\mu_{\perp}$. If the spins were orientated close to (though not necessarily exactly along) the local quantisation direction, in a linear combination of low J_z eigenstates, this would give rise to a low value of the ordered moment, perhaps consistent with the experimentally observed value of $\mu \approx 3\mu_B$.

5.3 Magnetic ordering

5.3.1 Reciprocal-space description

We will now turn to the long-range magnetically ordered state and the corresponding elastic neutron scattering experiments. In order to discuss the observed Bragg spots using a notation consistent with that in the relevant literature, in this section we will begin by describing the reciprocal-space representation of erbium titanate. In addition we will also highlight four linear dependencies which exist between the observed magnetic Bragg spots in this system. These linear relationships are a result of the titanium ions having zero magnetic moment. We will then go on to consider the relevant experiments and the magnetically ordered state that is currently proposed in the literature in the following sections.

$Er_2Ti_2O_7$ has a face-centered cubic lattice with four Er and four Ti atoms per unit cell. If the conventional unit cell has sides of length 'a' then the principle lattice vectors are given by

$$\mathbf{a}_1 = \frac{a}{2}\left(\hat{\mathbf{y}} + \hat{\mathbf{z}}\right), \qquad \mathbf{a}_2 = \frac{a}{2}\left(\hat{\mathbf{z}} + \hat{\mathbf{x}}\right), \qquad \mathbf{a}_3 = \frac{a}{2}\left(\hat{\mathbf{x}} + \hat{\mathbf{y}}\right). \tag{5.7}$$

The full set of lattice vectors, $\mathbf{R}_j$, is generated using $\mathbf{R}_j = n_1\mathbf{a}_1 + n_2\mathbf{a}_2 + n_3\mathbf{a}_3$, where $n_1, n_2, n_3 \in \mathcal{Z}$. The corresponding reciprocal space lattice is body centered and the reciprocal lattice vector, $\mathbf{G}$, which corresponds to the lattice site at $\mathbf{R}$ satisfies the Bragg condition

$$e^{i\mathbf{G}\cdot\mathbf{R}} = 1. \tag{5.8}$$

The principle body-centred reciprocal lattice vectors are given by

$$\mathbf{b}_1 = \frac{2\pi}{a}\left(\hat{\mathbf{y}} + \hat{\mathbf{z}} - \hat{\mathbf{x}}\right), \qquad \mathbf{b}_2 = \frac{2\pi}{a}\left(\hat{\mathbf{z}} + \hat{\mathbf{x}} - \hat{\mathbf{y}}\right), \qquad \mathbf{b}_3 = \frac{2\pi}{a}\left(\hat{\mathbf{x}} + \hat{\mathbf{y}} - \hat{\mathbf{z}}\right), \tag{5.9}$$

and describe the positions of the nuclear Bragg spots. As the magnetic elastic neutron

diffraction powder data is indexed by a propagation vector of $\mathbf{k} = \mathbf{0}$[19], the magnetic Bragg peaks appear on top of the nuclear ones. As discussed in Section 1.4.1, the Bragg spot intensities are given by

$$I\left(\mathbf{k}, \mathbf{S_k}\right) \sim \left|\mathbf{f}\left(\mathbf{k}\right)\right|^2 \left[1 - \left|\hat{\mathbf{k}} \cdot \hat{\mathbf{S}}_\mathbf{k}\right|^2\right] \left|\mathbf{S_k}\right|^2, \tag{5.10}$$

where $\left|\mathbf{f}\left(\mathbf{k}\right)\right|^2$ is the form factor (which we assume to be spherically symmetric), $\left[1 - \left|\hat{\mathbf{k}} \cdot \hat{\mathbf{S}}_\mathbf{k}\right|^2\right]$ is the orientational factor and $\mathbf{S_k}$ is the structure factor. The structure factor can be calculated using

$$\mathbf{S_k} = \frac{1}{N_0} \sum_\alpha e^{i\mathbf{k}\cdot(\mathbf{c}_\alpha)} \mathbf{S}_{j\alpha}, \tag{5.11}$$

where the sub-lattice vectors, $\mathbf{c}_\alpha$, describe the locations of the atoms in the unit cell and $\mathbf{S}_{j\alpha}$ is the spin on the appropriate site and N_0 is the number of atoms per unit cell. We will choose the four atoms in a single tetrahedron to describe the basis of the lattice such that

$$\mathbf{c}_0 = \langle 000 \rangle, \qquad \mathbf{c}_1 = \frac{a}{4}\langle 011 \rangle, \qquad \mathbf{c}_2 = \frac{a}{4}\langle 101 \rangle, \qquad \mathbf{c}_3 = \frac{a}{4}\langle 110 \rangle. \tag{5.12}$$

For consistency with the neutron scattering literature, we will set $a = 1$. In addition from this point we will now quote reciprocal lattice vectors (Equation 5.9) in units of 2π so that they become

$$\mathbf{b_1} = (\hat{\mathbf{y}} + \hat{\mathbf{z}} - \hat{\mathbf{x}}), \qquad \mathbf{b_2} = (\hat{\mathbf{z}} + \hat{\mathbf{x}} - \hat{\mathbf{y}}), \qquad \mathbf{b_3} = (\hat{\mathbf{x}} + \hat{\mathbf{y}} - \hat{\mathbf{z}}). \tag{5.13}$$

As $Er_2Ti_2O_7$ has multiple atoms per unit cell, the structure factors (and therefore also the intensities) will vary between Bragg spots. This structure factor variation will also form a periodic lattice in reciprocal space, which we will call the magnetic super-lattice, so that

$$\mathbf{S}_{\mathbf{k}+\mathcal{G}} = \mathbf{S_k}, \tag{5.14}$$

where $\mathcal{G}$ is some element of the magnetic super-lattice. The simplest way to specify this

lattice is to consider all Bragg spots which have the same structure factor as the (000) spot, i.e. all the spins add in phase. For a Bragg spot labeled by $\mathbf{K}$, this occurs when $\mathbf{K}\cdot(\mathbf{R}_j+\mathbf{c}_\alpha)=2n\pi$, where n is some integer and consequently, from the Bragg condition (Equation 5.8), we require that every $\mathbf{R}_j+\mathbf{c}_\alpha$, and therefore every Er^{3+} ion, must lie on a lattice site of the real-space super-lattice. The real-space super-lattice is therefore formed by adding just enough 'extra' erbium ions so that they exactly form a Bravais lattice (with one erbium atom per unit cell). It turns out that for the pyrochlore structure, this is achieved by considering the titanium atoms as equivalent to erbium atoms and the reciprocal-space magnetic super-lattice can therefore be generated using the vectors: $\{(2\bar{2}\bar{2}),(\bar{2}2\bar{2}),(\bar{2}\bar{2}2)\}$.

In each Brillouin zone of the magnetic super-lattice there are eight Bragg spots. We will consider the ones at:

$$\begin{aligned}
&\mathbf{Q}_0=(000), \qquad \mathbf{Q}_1=(200), \qquad \mathbf{Q}_2=(020), \qquad \mathbf{Q}_3=(002),\\
&\mathbf{K}_0=(111), \qquad \mathbf{K}_1=(1\bar{1}\bar{1}), \qquad \mathbf{K}_2=(\bar{1}1\bar{1}), \qquad \mathbf{K}_3=(\bar{1}\bar{1}1).
\end{aligned} \tag{5.15}$$

As the magnetic Bragg spots lie exactly on top of the chemical Bragg spots they have the same periodicity. This means that every tetrahedron will have the same spin orientations, or equivalently the spins on each of the four sub-lattices will be parallel, i.e. $\mathbf{S}_{j\alpha}=\mathbf{S}_\alpha$. The structure factors (normalised to the number of Er atoms in the unit cell) then simplify to

$$\begin{aligned}
\mathbf{S}_{\mathbf{Q}_0}&=\frac{1}{4}\left(\mathbf{S}_0+\mathbf{S}_1+\mathbf{S}_2+\mathbf{S}_3\right), & \mathbf{S}_{\mathbf{Q}_1}&=\frac{1}{4}\left(\mathbf{S}_0+\mathbf{S}_1-\mathbf{S}_2-\mathbf{S}_3\right),\\
\mathbf{S}_{\mathbf{Q}_2}&=\frac{1}{4}\left(\mathbf{S}_0-\mathbf{S}_1+\mathbf{S}_2-\mathbf{S}_3\right), & \mathbf{S}_{\mathbf{Q}_3}&=\frac{1}{4}\left(\mathbf{S}_0-\mathbf{S}_1-\mathbf{S}_2+\mathbf{S}_3\right),\\
\mathbf{S}_{\mathbf{K}_0}&=\frac{1}{4}\left(\mathbf{S}_0-\mathbf{S}_1-\mathbf{S}_2-\mathbf{S}_3\right), & \mathbf{S}_{\mathbf{K}_1}&=\frac{1}{4}\left(\mathbf{S}_0-\mathbf{S}_1+\mathbf{S}_2+\mathbf{S}_3\right),\\
\mathbf{S}_{\mathbf{K}_2}&=\frac{1}{4}\left(\mathbf{S}_0+\mathbf{S}_1-\mathbf{S}_2+\mathbf{S}_3\right), & \mathbf{S}_{\mathbf{K}_3}&=\frac{1}{4}\left(\mathbf{S}_0+\mathbf{S}_1+\mathbf{S}_2-\mathbf{S}_3\right).
\end{aligned} \tag{5.16}$$

We can see that for the pyrochlore lattice there are eight Bragg spots but only four spin

variables, resulting in the following linear relationships between the Bragg spots

$$\mathbf{S}_{\mathbf{K}_0} = \frac{1}{2}\left(-\mathbf{S}_{\mathbf{Q}_0} + \mathbf{S}_{\mathbf{Q}_1} + \mathbf{S}_{\mathbf{Q}_2} + \mathbf{S}_{\mathbf{Q}_3}\right), \qquad \mathbf{S}_{\mathbf{K}_1} = \frac{1}{2}\left(+\mathbf{S}_{\mathbf{Q}_0} - \mathbf{S}_{\mathbf{Q}_1} + \mathbf{S}_{\mathbf{Q}_2} + \mathbf{S}_{\mathbf{Q}_3}\right),$$
$$\mathbf{S}_{\mathbf{K}_2} = \frac{1}{2}\left(+\mathbf{S}_{\mathbf{Q}_0} + \mathbf{S}_{\mathbf{Q}_1} - \mathbf{S}_{\mathbf{Q}_2} + \mathbf{S}_{\mathbf{Q}_3}\right), \qquad \mathbf{S}_{\mathbf{K}_3} = \frac{1}{2}\left(+\mathbf{S}_{\mathbf{Q}_0} + \mathbf{S}_{\mathbf{Q}_1} + \mathbf{S}_{\mathbf{Q}_2} - \mathbf{S}_{\mathbf{Q}_3}\right), \quad (5.17)$$

which provide extra phase information about the ordered state. To have this extra information is very unusual and it considerably simplifies the interpretation of the elastic neutron scattering data. Normally there are the same number of different Structure factors as there are spin degrees of freedom. This is indeed the case for erbium titanate, if the titanium spins are included in the structure factor. The four linear relationships shown in Equation 5.17 therefore only hold if the titanium spins are zero. This is expected to be true from the chemistry of the system and is also found to be the case experimentally[19].

5.3.2 Elastic Scattering data by Ruff *et al.*[66]

We will now consider the relative intensities of the observed elastic Bragg peaks. In this section we discuss the data reported by Ruff *et at.*[66], though we will also look at some complimentary data by Cao *et al.*[14] in Section 5.3.4 after considering the magnetic state currently proposed in the literature.

Ruff *et al.*[66] use single crystal experiments to study the scattering within the the $[H, H, L]$ plane in reciprocal space. Fig. 5.4 shows their measurements of the intensities of the five Bragg spots closest to the origin as a function of the external magnetic field strength. These are in order: $(1,1,1)$, $(0,0,2)$, $(2,2,0)$, $(1,1,3)$ and $(2,2,2)$. The data was collected at a temperature of $50mK$. The magnetic scattering was isolated by subtracting the nuclear scattering measured at $2K$ (which is above T_N). Assuming that the magnetic ordering breaks the cubic symmetry of the crystal, then there will be multiple magnetic domains present within a single crystal. The relative proportions of these domains may be altered by application of the external field. To interpret the details of this polarisation, however, the intensities of corresponding Bragg spots in the $[L, H, H]$

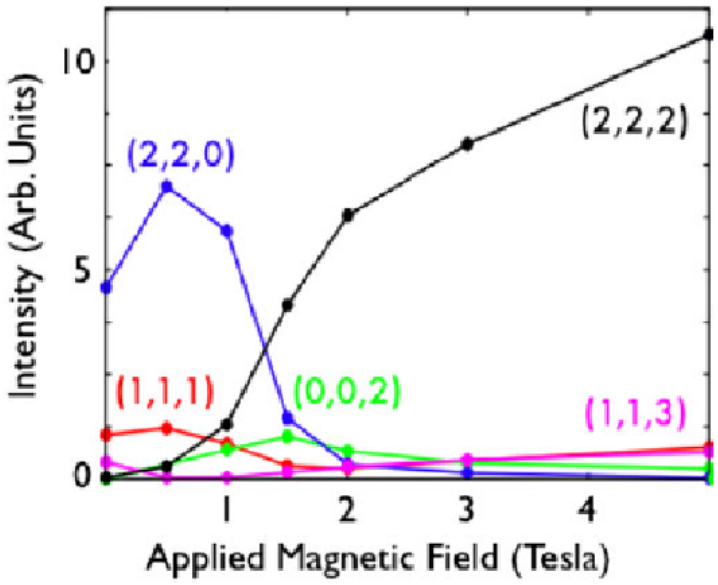

Figure 5.4: Single crystal elastic magnetic Bragg peak intensities measured as a function of the external magnetic field strength. the applied field was parallel to the $\langle 1, 1, 0\rangle$ direction and the $\mathbf{Q} = \mathbf{0}$ peaks lying within the $[H, H, L]$ plane were measured at a temperature of $50mK$ (with the nuclear component of the scattering removed by subtracting data measured at $2K$). Data reproduced from Ruff *et. al*[66].

and $[H, L, H]$ planes are required. We will therefore focus on the zero-field intensities of the spots. We first mention, however, that the application of the external field induces a ferromagnetic moment, indicated by the growing intensity of the $(2, 2, 2)$ peak. This peaks becomes dominant and an applied field of approximately $1.5T$ and we associate this point with a saturation of the ferromagnetism. When there is no external field, we can see that the $(2, 2, 0)$ peak is clearly dominant[66]. Its intensity can also be seen to increase by a factor of one third upon application of a small external field. In the paper by Ruff *et al.* this is attributed to a decrease in the diffuse scattering due to short range correlations. In other publications[19, 14], however, it is attributed to the formation of a single domain, which we will discuss later. The next most prominent Bragg spot is the $(1, 1, 1)$, which is around a factor of four smaller (although it will have a larger form-factor). There is also a tiny $(1, 1, 3)$ spot present (with an intensity of less than one tenth of the dominant $(2, 2, 0)$ spot at zero applied field). The zero field intensities of the $(0, 0, 2)$ and $(2, 2, 2)$ spots are both negligible.

First we will consider the absent $(2,2,2)$ Bragg spot. As mentioned in the previous paragraph, this Bragg spot controls the ferromagnetism. This is because the reciprocal lattice vector $(2,2,2)$ is related to the origin $(0,0,0)$ by a superlattice vector. The absent Bragg spot is therefore consistent with

$$\mathbf{S}_{\mathbf{Q}_0} = \frac{1}{4}(\mathbf{S}_0 + \mathbf{S}_1 + \mathbf{S}_2 + \mathbf{S}_3) = \mathbf{0}. \tag{5.18}$$

To confirm that the structure factor $\mathbf{S}_{\mathbf{Q}_0} = 0$ and therefore that there is no ferromagnetic component in the the system, it is necessary to check that at least three Bragg spots which share this structure factor (i.e. are related by a magnetic superlattice vector) are also absent. This rules out the possibility that the $(2,2,2)$ Bragg spot is absent as a result of the orientational factor. In the case of erbium titanate there is no ferromagnetism observed[19]. In addition, this is consistent with the dominant antiferromagnetic interactions indicated by the negative Curie-Weiss temperature of $\theta_{CW} \sim -22K$[5]. A dominant antiferromagnetic Heisenberg interaction on the pyrochlore lattice is consistent with the constraint that the total spin on a tetrahedron sums to zero (see Section 1.2.2), which is in turn equivalent to $\mathbf{S}_{\mathbf{Q}_0} = \mathbf{0}$. This allows us to simplify the four $\mathbf{S}_{\mathbf{K}_\alpha}$ structure factors to

$$\mathbf{S}_{\mathbf{K}_0} = \frac{1}{2}\mathbf{S}_0, \qquad \mathbf{S}_{\mathbf{K}_1} = \frac{1}{2}\mathbf{S}_1, \qquad \mathbf{S}_{\mathbf{K}_2} = \frac{1}{2}\mathbf{S}_2, \qquad \mathbf{S}_{\mathbf{K}_3} = \frac{1}{2}\mathbf{S}_3. \tag{5.19}$$

The next point of interest is the absent $(0,0,2)$ and dominant $(2,2,0)$ spots. These spots are also linked by a superlattice vector, and therefore share the same structure factor. The $(0,0,2)$ spot must therefore have negligible intensity as a result of the orientational factor. We assume that at zero applied field, the crystal contains equal proportions of all magnetic domains such that by symmetry, if the $(0,0,2)$ spot is absent, so are the related $(2,0,0)$ and $(0,2,0)$ spots. We will, however, return to this point later. For the orientational factors of these spots to vanish we require that $\hat{\mathbf{k}} \cdot \hat{\mathbf{S}}_{\mathbf{k}} = 1$ for each spot,

which is equivalent to

$$\mathbf{S}_{\mathbf{Q}_1} = S_x\hat{\mathbf{x}} \qquad \mathbf{S}_{\mathbf{Q}_2} = S_y\hat{\mathbf{y}} \qquad \mathbf{S}_{\mathbf{Q}_3} = S_z\hat{\mathbf{z}}, \tag{5.20}$$

where S_x, S_y and S_z are currently arbitrary coefficients. We also note that for $\mathbf{k} = (2, 2, 0)$ then $\hat{\mathbf{k}}\cdot\hat{\mathbf{S}}_{\mathbf{Q}_3} = 0$, which results in a maximal orientational factor and is therefore consistent with a dominant $(2, 2, 0)$ Bragg spot.

We can recover the real space spin directions by back transforming the structure factors (Equations 5.18 and 5.19). This provides

$$\begin{aligned}
\mathbf{S}_0 &= \mathbf{S}_{\mathbf{Q}_0} + \mathbf{S}_{\mathbf{Q}_1} + \mathbf{S}_{\mathbf{Q}_2} + \mathbf{S}_{\mathbf{Q}_3} \\
&= S_x\hat{\mathbf{x}} + S_y\hat{\mathbf{y}} + S_z\hat{\mathbf{z}}, && (5.21) \\
\mathbf{S}_1 &= \mathbf{S}_{\mathbf{Q}_0} + \mathbf{S}_{\mathbf{Q}_1} - \mathbf{S}_{\mathbf{Q}_2} - \mathbf{S}_{\mathbf{Q}_3} \\
&= S_x\hat{\mathbf{x}} - S_y\hat{\mathbf{y}} - S_z\hat{\mathbf{z}}, && (5.22) \\
\mathbf{S}_2 &= \mathbf{S}_{\mathbf{Q}_0} - \mathbf{S}_{\mathbf{Q}_1} + \mathbf{S}_{\mathbf{Q}_2} - \mathbf{S}_{\mathbf{Q}_3} \\
&= -S_x\hat{\mathbf{x}} + S_y\hat{\mathbf{y}} - S_z\hat{\mathbf{z}}, && (5.23) \\
\mathbf{S}_3 &= \mathbf{S}_{\mathbf{Q}_0} - \mathbf{S}_{\mathbf{Q}_1} - \mathbf{S}_{\mathbf{Q}_2} + \mathbf{S}_{\mathbf{Q}_3} \\
&= -S_x\hat{\mathbf{x}} - S_y\hat{\mathbf{y}} + S_z\hat{\mathbf{z}}. && (5.24)
\end{aligned}$$

As we require the spins to have equal magnitudes, there are therefore two degrees of freedom remaining. The magnetism ($\mathbf{m}$) is characterised by three independent components of spin density, which are parallel to the Cartesian directions. This can be expressed mathematically as

$$\mathbf{m}(\mathbf{R}) = |\mathbf{m}| \left[e^{\hat{\mathbf{x}}\cdot\mathbf{R}2\pi i} \sin\theta\cos\phi\hat{\mathbf{x}} + e^{\hat{\mathbf{y}}\cdot\mathbf{R}2\pi i} \sin\theta\sin\phi\hat{\mathbf{y}} + e^{\hat{\mathbf{z}}\cdot\mathbf{R}2\pi i} \cos\theta\hat{\mathbf{z}} \right], \tag{5.25}$$

where $\mathbf{R}$ is the position of the atom in units of $\frac{a}{2}$. The angles θ and ϕ are currently unconstrained and are shown in Fig. 5.5 which depicts the magnetic state for one tetra-

hedron. Basing our arguments solely on the elastic scattering data presented in the paper

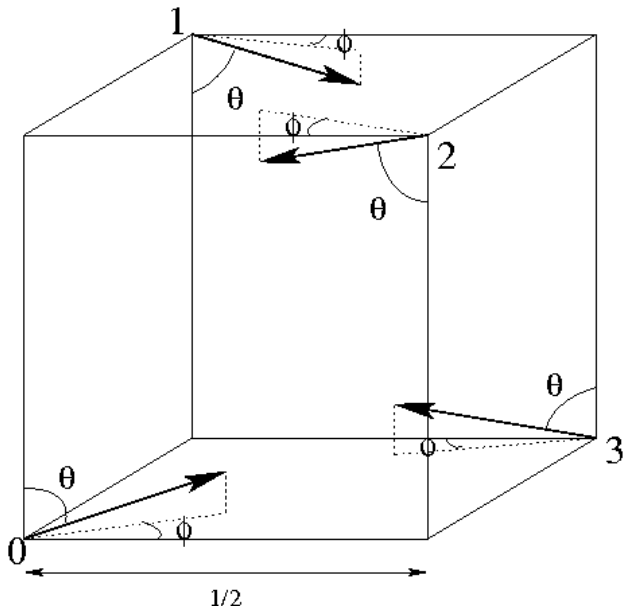

Figure 5.5: The spin states (parameterised by the angles 'θ' and 'ϕ') which are consistent with the vanishingly small measured intensity of the (200), (020) and (002) Bragg spots.

by Ruff *et al.*[66] does not provide enough information to determine the angles θ and ϕ that correspond to the low temperature magnetically ordered state of erbium titanate. We will therefore consider this issue in Section 5.3.4 when we discuss the measurements made by Cao *et al.*[14]. The intensity of the $(1,1,1)$ Bragg spot however does provide some clues which we will discuss in the next subsection where we will also consider the magnetic state currently proposed in the literature.

5.3.3 Current experimentally proposed state

We will now take time to discuss the state currently proposed in the literature to explain the elastic neutron scattering data. In this section we will demonstrate that it is actually inconsistent with the experimentally observed intensity of the $(1,1,1)$ Bragg peak.

In the initial elastic neutron studies[19], the magnetic scattering data was interpreted using the state shown in Fig. 5.6. The magnetic state is equivalent to $\mathbf{S}_0 = \frac{1}{\sqrt{6}}\langle 1,1,-2\rangle$, (although as this structure breaks the cubic symmetry, there are two other symmetrically related domains with $\mathbf{S}_0 = \frac{1}{\sqrt{6}}\langle -2,1,1\rangle$ and $\mathbf{S}_0 = \frac{1}{\sqrt{6}}\langle 1,-2,2\rangle$). This state is therefore

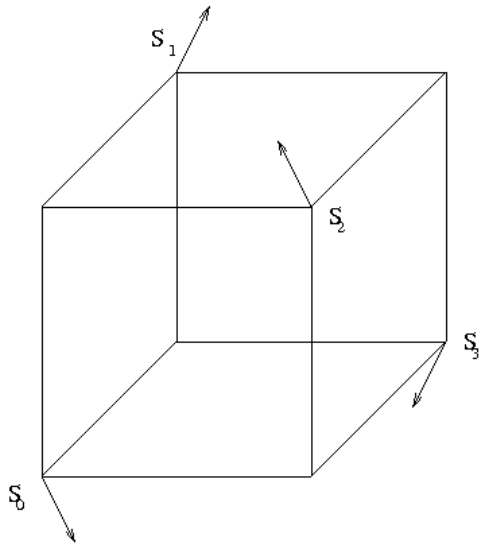

Figure 5.6: A single tetrahedron (of one domain) of the $\mathbf{k} = \mathbf{0}$ state used by Champion *et. al* to interpret their elastic neutron scattering data of the magnetically ordered state[19]. The spins are orientated in the planes perpendicular to the local tetrahedral axes.

consistent with the observed high intensity $(2, 2, 0)$ Bragg spot and the negligible intensity $(2, 2, 2)$ and $(0, 0, 2)$ Bragg spots. If we refer back to Fig. 5.5, the angles defined in this figure are chosen to be: $\theta \approx 144.7°$ and $\phi = 45°$. This choice of θ orientates the spins in the planes perpendicular to the local tetrahedral $\langle 1, 1, 1\rangle$ type axes (which were shown previously in Fig. 3.7). The choice of ϕ is consistent with the direction of one of the O_2 ions, when projected onto the plane perpendicular to the $\langle 1, 1, 1\rangle$ axis. This means that the spins point along crystallographically significant directions (in this case towards the O2 ions shown in Fig. 1.14) as is usual for compounds with strong crystal-field interactions.

Next we will use Equation 5.10 to estimate the expected relative intensities for the $(1, 1, 1)$ and $(2, 2, 0)$ Bragg peaks for this state, in order to compare them with the elastic scattering data from the paper by Ruff *et al.*[66]. For the $(1, 1, 1)$ peak the appropriate structure factor is $\mathbf{S}_{\mathbf{K}_0} = \frac{1}{2}\mathbf{S}_0$, which gives $|\mathbf{S}_{\mathbf{K}_0}|^2 = \frac{1}{4}$ for all three domains. The orientational factor is maximal because, for each of the domains, $\mathbf{K}_0 \cdot \mathbf{S}_0 = 0$. The intensity of this Bragg spot is therefore given by

$$I\left((1, 1, 1)\right) \sim \frac{1}{4}\left|\mathbf{f}\left(\sqrt{3}\right)\right|^2. \tag{5.26}$$

The appropriate structure factor for the $(2,2,0)$ Bragg peak is $\mathbf{S}_{\mathbf{Q}_3} = S_z\hat{\mathbf{z}}$ which, after averaging over the three domains, gives $|\mathbf{S}_{\mathbf{Q}_3}|^2 = \frac{1}{3}$. The orientational factor is again maximal for all three domains. The intensity of this peak is therefore

$$I\left((2,2,0)\right) \sim \frac{1}{3}\left|\mathbf{f}\left(2\sqrt{2}\right)\right|^2. \tag{5.27}$$

The contribution from that form factor is crucial. We will only consider a very crude estimate here and assume a spherically symmetrical form factor (neglecting the angular dependency of the erbium ions). This allows us to use the form factor shown in Fig. 4.6 in Section 4.8 which was scaled to fit the predicted Bragg spot intensities for $Gd_2Ti_2O_7$. We have therefore also neglected the contraction of the 4-f orbitals along the series of the lanthanides. Using Fig. 4.6 we find a ratio of

$$\frac{\left|\mathbf{f}\left(\sqrt{3}\right)\right|^2}{\left|\mathbf{f}\left(2\sqrt{2}\right)\right|^2} \sim \frac{3}{2}, \tag{5.28}$$

which provides

$$\frac{I\left((1,1,1)\right)}{I\left((2,2,0)\right)} \sim \frac{9}{8}. \tag{5.29}$$

This predicts that the $(1,1,1)$ peak should be slightly larger than the $(2,2,0)$, which is clearly inconsistent with the data by Ruff *et al.*, shown in Fig 5.4, where the $(2,2,0)$ peak is dominant with an approximate intensity ration of

$$\frac{I\left((1,1,1)\right)}{I\left((2,2,0)\right)} \sim \frac{1}{5}. \tag{5.30}$$

To propose a new state, which does not suffer from this inconsistency with the data, we will now turn to the experiments by Cao *et al.*[14].

5.3.4 Elastic Scattering data by Cao *et al.*[14]

In this section we will discuss the single crystal elastic scattering data presented by Cao *et al.*[14] which is shown in Fig. 5.7. Unlike the data by Ruff *et al.*[66], their investigation

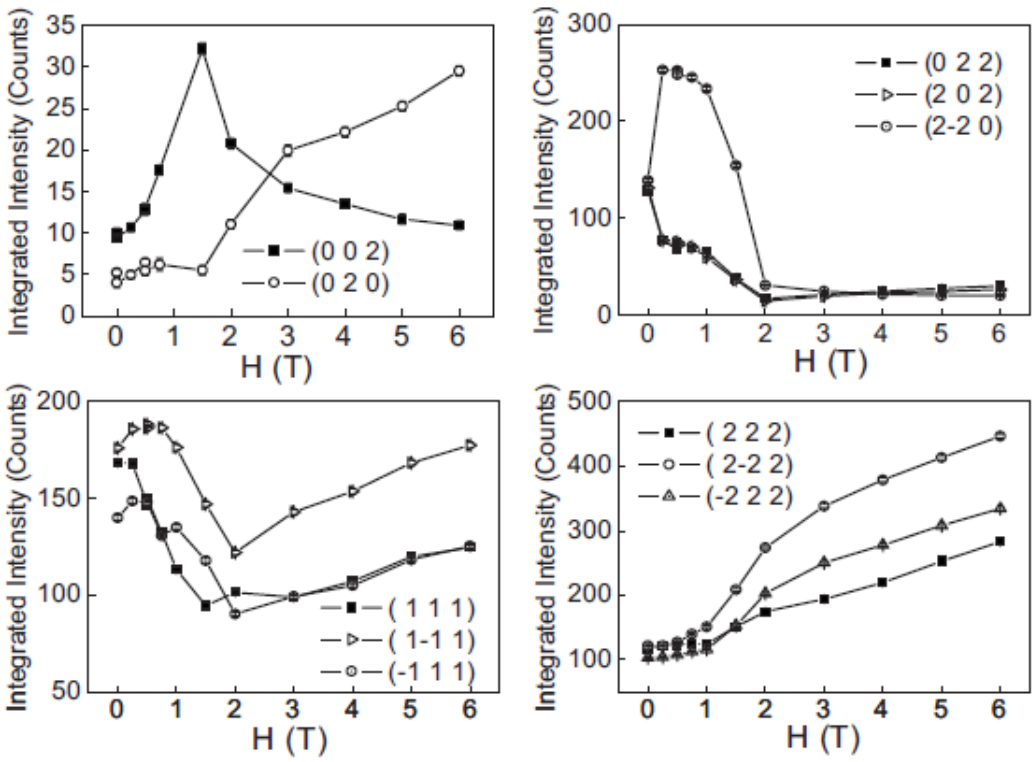

Figure 5.7: Single crystal elastic scattering data from Cao *et. al*[14]. Selected Bragg peak intensities were measured as a function of external magnetic field strength, with the field applied along the $\langle 1, 1, 0\rangle$ direction, at a temperature of $0.3K$.

is not restricted to Bragg spots which lie within the $[H, H, L]$ plane. They compare the intensities of symmetrically related Bragg peaks as a function of an applied magnetic field parallel to $\langle 1, 1, 0\rangle$. It is not possible to directly compare the intensities of the four types of Bragg peak, however, as the intensity scales on the four graphs do not appear to be calibrated. We will focus on the low-field behaviour: $B \ll 1T$, where the ferromagnetic Bragg peak has a negligible intensity, as we are interested in the zero-field magnetically ordered state, which will distort in the presence of an external field. As we can see in Fig. 5.7, four types of Bragg spot were investigated. These are the $(0, 0, 2)$, $(0, 2, 2)$, $(1, 1, 1)$ and $(2, 2, 2)$ as was studied by Ruff *et al.*[66]. We first note that for zero

applied field all the symmetrically related Bragg spots appear with approximately the same intensity. This is most precise for the $(0,2,2)$, $(2,0,2)$ and $(2,-2,0)$ Bragg spots as these spots have been seen to be dominant by Ruff *et al.* and will therefore be the easiest to resolve above the background nuclear scattering. The $(1,1,1)$ and $(2,2,2)$ type spots change little upon application of the field, but because for these types of Bragg spot, each domains will have identical structure factors and also orientational factors, this is unsurprising. The intensity of the $(0,0,2)$ and $(0,2,0)$ peaks can be seen to be an order of magnitude smaller than other three intensity scales. This is therefore consistent with evidence from Ruff *et al.*[66] that the intensity of these spots is negligible.

We will now discuss the most interesting feature of this data. When a small external field is applied, the intensity of the $(2,-2,0)$ peak increases dramatically (from about 130 counts to about 260 counts). This increase in intensity is also seen in Fig. 5.4 by Ruff *et al.*[66], however, the data by Cao *et al.*[14] shows a simultaneous decrease in the intensity of the $(2,0,2)$ and $(0,2,2)$ peaks. We can now interpret (as was proposed by Cao *et al.*) that this change in intensity is a result of the external-field polarising the different magnetic domains, so that the sample now contains only a single domain. As the field is applied along the $\langle 110 \rangle$ direction, it will select the z-direction as special which is consistent with the behaviour of the three Bragg spots. This also confirms our earlier assumption that the magnetic state breaks the cubic symmetry, ruling out the possibility of a triple-q state, with all spins-pointing towards the center of the tetrahedron. All three Bragg spots have the same form factor. Using the magnetic superlattice vectors, their structure factors can be seen to be equivalent to those in Equations 5.19 and are given by

$$\mathbf{S}_{(0,2,2)} = S_x\hat{\mathbf{x}} \qquad \mathbf{S}_{(2,0,2)} = S_y\hat{\mathbf{y}} \qquad \mathbf{S}_{(2,-2,0)} = S_z\hat{\mathbf{z}}, \tag{5.31}$$

where

$$\mathbf{S}_0 \;=\; S_x\hat{\mathbf{x}} + S_y\hat{\mathbf{y}} + S_z\hat{\mathbf{z}}$$

$$= \sin\theta\cos\phi\hat{\mathbf{x}} + \sin\theta\sin\phi\hat{\mathbf{y}} + \cos\theta\hat{\mathbf{z}}. \tag{5.32}$$

The orientational factor for all three of these Bragg spots is maximal. When comparing the intensity of the three Bragg spots, we therefore need only consider the structure factors. We will first consider the $(0,2,2)$ and $(2,0,2)$ spots as these have equal intensities, which enforces

$$\sin^2\theta\left(\cos^2\phi - \sin^2\phi\right) = 0. \tag{5.33}$$

If $\sin\theta = 0, \pi$ then the $(0,2,2)$ and $(2,0,2)$ would be absent which is not the case. We are therefore able to deduce that $\tan^2\phi = 1$ and $\phi = \pm\frac{\pi}{4}, \pm\frac{3\pi}{4}$. To obtain an extremely crude estimate for θ we use the intensities ratio of the $(2,-2,0)$ and $(0,2,2)$ peaks from Fig. 5.7 which gives

$$\frac{I\left((2,-2,0)\right))}{I\left((0,2,2)\right)} = 2\cot^2\theta \approx \frac{260}{80}, \tag{5.34}$$

so that $\theta \approx \pm 0.2\pi, \pm 1.2\pi$. These values of θ and ϕ are equivalent to $\mathbf{S}_0 \approx \frac{1}{\sqrt{6}}\langle\pm1,\pm1,\pm2\rangle$. Now all that remains is to fix the signs of components of $\mathbf{S}_0$, which we will discuss in the next section.

5.3.5 New magnetically ordered state

In this section we will propose a new magnetically ordered state, which, as far as we can tell, is consistent with the elastic scattering neutron data and physically distinct from the state discussed in the current literature. In the previous section we established that $\mathbf{S}_0 \approx \frac{1}{\sqrt{6}}\langle\pm1,\pm1,\pm2\rangle$, with the relative orientation of the spins shown in Fig. 5.5. The choice of $\mathbf{S}_0 = \frac{1}{\sqrt{6}}\langle1,1,-2\rangle$ is the state currently proposed in the literature, however, as we discussed in Section 5.3.3 this is inconsistent with the $(1,1,1)$ Bragg peak. This peak provides the complementary information that for the intensity of the $(1,1,1)$ spot to be low, as is experimentally observed, $\mathbf{S}_0$ must be orientated close to the $\frac{1}{\sqrt{3}}\langle1,1,1\rangle$ crystallographic axis. There are two other possible styles of choices for $\mathbf{S}_0$. These are: $\mathbf{S}_0 = \frac{1}{\sqrt{6}}\langle-1,1,2\rangle$ or $S_0 = \frac{1}{\sqrt{6}}\langle1,1,2\rangle$. First we will consider the state for which $\mathbf{S}_0 =$

$\frac{1}{\sqrt{6}}\langle -1,1,2\rangle$. The intensity of the $(2,2,0)$ Bragg peak remains unchanged from that calculated in Section 5.3.3. The structure factor for the $(1,1,1)$ Bragg peak also remains unchanged, however, its orientational factor does not. This is now given by $1-\left|\hat{\mathbf{K}}_0\cdot\hat{\mathbf{S}}_0\right|^2=\frac{7}{9}$, so that the Bragg peak intensities ration is

$$\frac{I\left((2,2,0)\right)}{I\left((1,1,1)\right)}\sim\frac{8}{7}. \tag{5.35}$$

For this state, the $(1,1,1)$ and$(2,2,0)$ are expected to be of similar intensity, which is not the case. We now therefore consider the state with $S_0=\frac{1}{\sqrt{6}}\langle 1,1,2\rangle$. Again, the only quantity which differs from previous calculations is the orientational factor of the $(1,1,1)$ peak which is given by $1-\left|\hat{\mathbf{K}}_0\cdot\hat{\mathbf{S}}_0\right|^2=\frac{1}{9}$, giving

$$\frac{I\left((2,2,0)\right)}{I\left((1,1,1)\right)}\sim 8. \tag{5.36}$$

This is closer to the ratio observed by Ruff *et al.*[66] and as $\mathbf{S}_0$ is orientated relatively close to the $\frac{1}{\sqrt{3}}\langle 1,1,1\rangle$ crystallographic axis, the choice of this state is supported by the observation of the small ordered moment discussed in Section 5.2. We therefore propose the magnetic state with

$$\mathbf{S}_0=\frac{1}{\sqrt{6}}\langle 1,1,2\rangle,\quad \mathbf{S}_1=\frac{1}{\sqrt{6}}\langle 1,-1,-2\rangle,\quad \mathbf{S}_2=\frac{1}{\sqrt{6}}\langle -1,1,-2\rangle,\quad \mathbf{S}_3=\frac{1}{\sqrt{6}}\langle -1,-1,2\rangle, \tag{5.37}$$

which is depicted in Fig. 5.8.

We can rewrite this state as:

$$\begin{aligned}\mathbf{S}_0 &= \frac{1}{\sqrt{6}}\langle 1,1,1\rangle+\frac{1}{\sqrt{6}}\langle 0,0,1\rangle, \qquad \mathbf{S}_1=\frac{1}{\sqrt{6}}\langle 1,-1,-1\rangle+\frac{1}{\sqrt{6}}\langle 0,0,-1\rangle,\\ \mathbf{S}_2 &= \frac{1}{\sqrt{6}}\langle -1,1,-1\rangle+\frac{1}{\sqrt{6}}\langle 0,0,-1\rangle, \qquad \mathbf{S}_3=\frac{1}{\sqrt{6}}\langle -1,-1,1\rangle+\frac{1}{\sqrt{6}}\langle 0,0,1\rangle\end{aligned} \tag{5.38}$$

The first term for each spin forms the triple-q state with all spins pointing towards the center of the tetrahedron, while the second forms an additional antiferromagnetic contri-

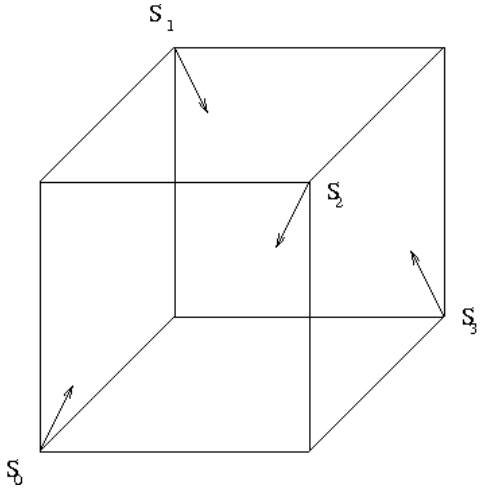

Figure 5.8: A single tetrahedron (of one domain) of our $\mathbf{k} = \mathbf{0}$ state (with $\mathbf{S}_0 = \langle 1, 1, 2\rangle/\sqrt{6}$) proposed to fit the elastic neutron scattering data by Ruff *et al.*[66] and Cao *et al.*[14].

bution with the magnetic moment orientated parallel to the z-axis. Two other symmetrically domains will also be present in the sample when there is no external field present. These other domains will have the additional antiferromagnetic contribution parallel to the x-axis or the y-axis. The application of an external-field parallel to $\langle 1, 1, 0\rangle$ results in the dominance of the domain described in Equation 5.38 and we can see that the additional antiferromagnetic contribution is perpendicular to the direction of the external field. This is consistent with a spin-flop transition and enables the spins to cant towards the applied field direction, gaining energy from the field with minimum disruption to the antiferromagnetic spin arrangement.

Finally, we wish to note that our proposed magnetic state is physically very different to the state currently discussed in the literature. The state currently discussed in the literature (which was described in Section 5.3.3) consisted of spins orientated along $\mathbf{S}_0 = \frac{1}{\sqrt{6}}\langle 1, 1, -2\rangle$ and other symmetrically related directions. As was discussed earlier, these directions lie along crystallographic axis. However, in the state that we propose there is no crystallographic significance to the spin orientations, which is very surprising. In the next section, we will therefore go on to investigate whether this state might be stabilised energetically.

5.4 Energetic Modeling

5.4.1 The Hamiltonians

Modeling rare-earth magnets is complicated. As was discussed in Section 5.2 Hund's rules are dominant over crystal-field considerations. The erbium ions also have three holes which results in a Kramer's doublet ground state for each ion which is a non-trivial linear combination of spin and orbital eigenstates. In addition, the orbital character of the erbium wavefunction will give rise to an anisotropic exchange interaction. For these reasons we will not attempt to calculate the precise erbium wavefunction of the Kramer's doublet ground-state from a crystal-field analysis. Instead we will develop a phenomenological Hamiltonian.

We will first briefly summarise the energy scales that were discussed in Section 5.2. Hund's rules are dominant and predict that the Er^{3+} ions have $J = \frac{15}{2}$ with a degeneracy of $2J + 1 = 16$. This degeneracy is then lifted by the crystal-field interaction to produce Kramer's doublet ground-state at an energy scale of about $60K$. Finally there is a transition at $T = 1.25K$ which is associated with the magnetic ordering of the Kramer's doublet which we wish to model. The interactions that are likely to lift the degeneracy of the Kramer's doublet are Heisenberg exchange and dipolar exchange. Blöte *et al.* obtain a value of $|J_{\mathrm{Ex}}/k_B| \approx 0.6K$ for the strength of nearest neighbour Heisenberg exchange coupling constant[5]. We can estimate the strength of the dipolar coupling constant, J_D, using:

$$|J_D/k_B| = \frac{\mu_0 \mu^2}{4\pi r^3 k_B} \approx 1.1K, \tag{5.39}$$

with $\mu = g(JLS)J\mu_B$, $g(JLS) = \frac{6}{5}$, $J = \frac{15}{2}$ and the Er$-$Er nearest neighbour separation is given by $r = 3.56\mathring{A}$[5]. We can see that although the Heisenberg interaction is expected to be the stronger of the two, they exist at a similar energy scale. In the rest of this section we will describe the Hamiltonians for the Heisenberg and Dipolar exchange interactions. To account for the crystal-field interaction, in the following section,we will then project these

Hamiltonians onto a pseudo-spin half subspace chosen to estimate the actual Kramer's doublet ground state.

We will now consider Heisenberg exchange. In Section 1.2.2 we showed that the nearest neighbour isotropic Heisenberg interaction on a pyrochlore lattice could be expressed, up to a constant, as:

$$H_{\mathrm{Ex}} = \frac{J_{\mathrm{Ex}}}{2} \sum_t \left(\sum_\alpha \hat{\mathbf{J}}_\alpha \right)^2, \tag{5.40}$$

where we sum over the tetrahedra in the lattice (t) and the four atoms in a tetrahedron (α) and $\hat{\mathbf{J}}_\alpha$ represents the angular momentum operator of the atom at position $\mathbf{c}_\alpha$. Defining the total spin of a tetrahedron as $\hat{\mathbf{T}} = \hat{\mathbf{J}}_0 + \hat{\mathbf{J}}_1 + \hat{\mathbf{J}}_2 + \hat{\mathbf{J}}_3$ gives:

$$H_{\mathrm{Ex}} = \frac{J_{\mathrm{Ex}}}{2} \sum_t \hat{\mathbf{T}} \cdot \hat{\mathbf{T}}. \tag{5.41}$$

We will now consider the anisotropic character of the Heisenberg exchange. The exchange pathway is via the O_1 ion at the centre of the tetrahedron (see Fig. 1.14), and the strength of the interaction is determined by the size of the overlap between the orbital components of the oxygen and erbium wavefunctions. From Hund's rules we know that the spin component of the magnetic moment is parallel to the orbital component. If for the moment we focus on the exchange interaction between between $\hat{\mathbf{J}}_0$ and $\hat{\mathbf{J}}_3$, then, temporarily using the Cartesian basis, we can express this interaction as: $J_x \hat{J}_0^x \hat{J}_3^x + J_y \hat{J}_0^y \hat{J}_3^y + J_z \hat{J}_0^z \hat{J}_3^z$ where we have introduced an anisotropic exchange constant. The tetrahedron has a symmetry axis along the direction $x = y$ so that the spin operators $\hat{J}_0^x$ and $\hat{J}_0^y$ experience the same environment (as do $\hat{J}_3^x$ and $\hat{J}_3^y$). We can therefore set $J_x = J_y$. In contrast the spin operator $\hat{J}_0^z$ feels a completely different environment to $\hat{J}_0^y$ and $\hat{J}_0^x$ (and the same applies to the components of $\hat{\mathbf{J}}_3$), due to the position of the O_1 ion in the center of the tetrahedron. As a result, $J_x = J_y \neq J_z$, and we choose to introduce the parameters $a_{\mathrm{Ex}} = (J_x + J_z)/2$ and $b_{\mathrm{Ex}} = (J_x - J_z)/2$ such that the interaction between $\hat{\mathbf{J}}_0$ and $\hat{\mathbf{J}}_3$ can be written as: $(a_{\mathrm{Ex}} + b_{\mathrm{Ex}})\, \hat{J}_0^x \hat{J}_3^x + (a_{\mathrm{Ex}} + b_{\mathrm{Ex}})\, \hat{J}_0^y \hat{J}_3^y + (a_{\mathrm{Ex}} - b_{\mathrm{Ex}})\, \hat{J}_0^z \hat{J}_3^z$. We will discuss the sign of b_{Ex} at the end of this section. Using the same approach for the

interactions between the other pairs of spins, for a single tetrahedron we have the following anisotropic nearest neighbour exchange Hamiltonian (again neglecting constant terms):

$$\begin{aligned} H_{\mathrm{Ex}} &= (a_{\mathrm{Ex}} - b_{\mathrm{Ex}}) \left[\hat{J}_0^x \hat{J}_1^x + \hat{J}_2^x \hat{J}_3^x \right] \\ &+ (a_{\mathrm{Ex}} + b_{\mathrm{Ex}}) \left[\hat{J}_0^y \hat{J}_1^y + \hat{J}_2^y \hat{J}_3^y + \hat{J}_0^z \hat{J}_1^z + \hat{J}_2^z \hat{J}_3^z \right] \\ &+ (a_{\mathrm{Ex}} - b_{\mathrm{Ex}}) \left[\hat{J}_0^y \hat{J}_2^y + \hat{J}_1^y \hat{J}_3^y \right] \\ &+ (a_{\mathrm{Ex}} + b_{\mathrm{Ex}}) \left[\hat{J}_0^z \hat{J}_2^z + \hat{J}_1^z \hat{J}_3^z + \hat{J}_0^x \hat{J}_2^x + \hat{J}_1^x \hat{J}_3^x \right] \\ &+ (a_{\mathrm{Ex}} - b_{\mathrm{Ex}}) \left[\hat{J}_0^z \hat{J}_3^z + \hat{J}_1^z \hat{J}_2^z \right] \\ &+ (a_{\mathrm{Ex}} + b_{\mathrm{Ex}}) \left[\hat{J}_0^x \hat{J}_3^x + \hat{J}_1^x \hat{J}_2^x + \hat{J}_0^y \hat{J}_3^y + \hat{J}_1^y \hat{J}_2^y \right] \\ &= a_{\mathrm{Ex}} H_1 - b_{\mathrm{Ex}} H_4, \end{aligned} \tag{5.42}$$

where we have made the following definitions:

$$H_1 = \frac{1}{2} \hat{\mathbf{T}} \cdot \hat{\mathbf{T}}, \tag{5.43}$$

$$H_4 = \frac{1}{2} \hat{\mathbf{A}} \cdot \hat{\mathbf{A}}, \tag{5.44}$$

and

$$\hat{\mathbf{A}} = \left(\hat{J}_0^x + \hat{J}_1^x - \hat{J}_2^x - \hat{J}_2^x \right) \hat{\mathbf{x}} + \left(\hat{J}_0^y - \hat{J}_1^y + \hat{J}_2^y - \hat{J}_3^y \right) \hat{\mathbf{y}} + \left(\hat{J}_0^z - \hat{J}_1^z - \hat{J}_2^z + \hat{J}_3^z \right) \hat{\mathbf{z}}. \tag{5.45}$$

Finally, we will consider the dipolar interaction. Using the factorisation of the dipole interaction described in Appendix B (Equation B.9), the nearest neighbour dipolar interaction for a single tetrahedron can be expressed as:

$$H_D = \frac{J_D}{2} \left\{ \frac{1}{4} \hat{\mathbf{T}} \cdot \hat{\mathbf{T}} + \frac{3}{4} \hat{\mathbf{A}} \cdot \hat{\mathbf{A}} + \frac{9}{2} \sum_{\alpha} \left(\hat{\mathbf{J}}_{\alpha} \cdot \hat{\mathbf{z}}_{\alpha} - \frac{1}{2} \hat{\mathbf{T}} \cdot \hat{\mathbf{z}}_{\alpha} \right)^2 \right\}, \tag{5.46}$$

where $\hat{\mathbf{z}}_\alpha \in \{0,1,2,3\}$ represents the four tetrahedral axis:

$$\begin{aligned}\hat{\mathbf{z}}_0 &= \frac{1}{\sqrt{3}}\left(\hat{\mathbf{x}}+\hat{\mathbf{y}}+\hat{\mathbf{z}}\right), \qquad \hat{\mathbf{z}}_1 = \frac{1}{\sqrt{3}}\left(\hat{\mathbf{x}}-\hat{\mathbf{y}}-\hat{\mathbf{z}}\right), \\ \hat{\mathbf{z}}_2 &= \frac{1}{\sqrt{3}}\left(-\hat{\mathbf{x}}+\hat{\mathbf{y}}-\hat{\mathbf{z}}\right), \qquad \hat{\mathbf{z}}_3 = \frac{1}{\sqrt{3}}\left(-\hat{\mathbf{x}}-\hat{\mathbf{y}}+\hat{\mathbf{z}}\right). \end{aligned} \tag{5.47}$$

This can be simplified using:

$$\sum_\alpha \left(\hat{\mathbf{z}}_\alpha \cdot \hat{\mathbf{T}}\right)^2 = \frac{4}{3}\hat{\mathbf{T}}\cdot\hat{\mathbf{T}} \tag{5.48}$$

to give

$$\begin{aligned} H_D &= \frac{J_D}{4}\left\{\frac{7}{2}\hat{\mathbf{T}}\cdot\hat{\mathbf{T}} + \frac{3}{2}\hat{\mathbf{A}}\cdot\hat{\mathbf{A}} + 9\sum_\alpha\left(\hat{\mathbf{J}}_\alpha\cdot\hat{\mathbf{z}}_\alpha\right)^2 - 9\sum_\alpha\left(\hat{\mathbf{J}}_\alpha\cdot\hat{\mathbf{z}}_\alpha\right)\left(\hat{\mathbf{T}}\cdot\hat{\mathbf{z}}_\alpha\right)\right\} \\ &= J_D\left\{\frac{7}{4}H_1 + \frac{3}{4}H_4 + \frac{9}{2}H_0 - \frac{9}{4}H_2\right\}, \end{aligned} \tag{5.49}$$

where we have defined the following Hamiltonians:

$$H_0 = \frac{1}{2}\sum_\alpha\left(\hat{\mathbf{z}}_\alpha\cdot\hat{\mathbf{J}}_\alpha\right)^2, \tag{5.50}$$

$$H_2 = \hat{\mathbf{T}}\cdot\hat{\mathbf{z}}_\alpha\sum_\alpha\left(\hat{\mathbf{z}}_\alpha\cdot\hat{\mathbf{J}}_\alpha\right). \tag{5.51}$$

At this point we will also define the final Hamiltonian that will be considered:

$$H_3 = \frac{1}{8}\left(\sum_\alpha \hat{\mathbf{z}}_\alpha\cdot\hat{\mathbf{J}}_\alpha\right)^2, \tag{5.52}$$

although this Hamiltonian will not arise until the next section.

Finally we return to the choice of sign for the phenomenological coefficient b_{Ex} introduced in Equation 5.42. In Section 2.3.2 and Appendix A we showed that in reciprocal

space the dipolar interaction could be expressed using sub-band representation as

$$H_D = \frac{J_D}{2} \sum_{\mathbf{k}} \sum_{\mathbf{G}} \left| (\mathbf{k} + \mathbf{G}) \cdot \hat{\mathbf{J}}_{\mathbf{k}} \right|^2 \tilde{V} \left(|\mathbf{k} + \mathbf{G}| \right). \tag{5.53}$$

$\tilde{V}(K)$ is the Fourier transform of $V(X) = \frac{1}{X}$ at lattice sites, but also vanishes as $X \mapsto 0$. The vectors $\mathbf{G}$ range over the reciprocal-space magnetic super-lattice and $\mathbf{k}$ ranges over one Brillouin zone of the superlattice. As $\tilde{V}(K)$ is a monotonically decaying function, minimising the dipolar interaction is therefore equivalent to minimising the factor $\left| (\mathbf{k} + \mathbf{G}) \cdot \hat{\mathbf{J}}_{\mathbf{k}} \right|$, or equivalently, maximising the orientational factors for the Bragg spots nearest the origin. As was said earlier these are the $(1, 1, 1)$ type spots, and the $(0, 0, 2)$ type spots, which as can be seen in the elastic neutron scattering data by Ruff *et al.* reproduced in Fig 5.4[66] are either small or vanishingly small intensity. This is therefore evidence that in erbium titanate the dipolar interaction is actually intrinsically frustrated. We notice that in Equations 5.42 and 5.49 for the exchange and dipolar interactions H_1 appears with the same sign, however, if $b_{\mathrm{Ex}} > 0$ then H_4 appears with a competing sign. We choose to consider a phenomenological Hamiltonian with $b_{\mathrm{Ex}} > b_D = \frac{3}{4} J_D$ to model the behaviour of erbium titanate.

5.4.2 Pseudo-spin projection

In the previous section we discussed the from of the exchange and dipolar Hamiltonians in the absence of a crystal-field interaction. We will now go on to mathematically formulate the pseudo-spin mapping that we will use to project the Hamiltonians onto the subspace of the Kramer's doublet. There are two natural limits which we can project onto: maximal with $J_z = \pm J$ and minimal with $J_z = \pm \frac{1}{2}$. Although we expect erbium titanate to be closest to the minimal pseudo-spin projection (as was discussed in Section 5.2), we will also consider the maximal projection as this is somewhat simpler.

The spin operators: $\hat{J}^x = (\hat{J}^+ + \hat{J}^-)/2$, $\hat{J}^y = (\hat{J}^+ - J^-)/2i$ and $\hat{J}^z$, where

$$\begin{aligned} \hat{J}^+ \left|J, J_z\right\rangle &= \sqrt{(J - J_z)(J + J_z + 1)}\left|J, J_z + 1\right\rangle, \\ \hat{J}^- \left|J, J_z\right\rangle &= \sqrt{(J + J_z)(J - J_z + 1)}\left|J, J_z - 1\right\rangle, \\ \hat{J}^z &= J_z \left|J, J_z\right\rangle, \end{aligned} \tag{5.54}$$

which can be represented explicitly in matrix form as shown below:

$$\hat{\mathbf{J}}^z = \begin{bmatrix} J & 0 & 0 & & & & & & & 0 & 0 & 0 \\ 0 & J-1 & 0 & \cdots & \cdots & \cdots & \cdots & \cdots & \cdots & 0 & 0 & 0 \\ 0 & 0 & J-2 & & & & & & & 0 & 0 & 0 \\ & \vdots & & \ddots & \cdots & \cdots & \cdots & \cdots & 0 & & \vdots & \\ & \vdots & & \vdots & \frac{3}{2} & 0 & 0 & 0 & \vdots & & \vdots & \\ & \vdots & & \vdots & 0 & \frac{1}{2} & 0 & 0 & \vdots & & \vdots & \\ & \vdots & & \vdots & 0 & 0 & -\frac{1}{2} & 0 & \vdots & & \vdots & \\ & \vdots & & \vdots & 0 & 0 & 0 & -\frac{3}{2} & \vdots & & \vdots & \\ & \vdots & & 0 & \cdots & \cdots & \cdots & \cdots & \ddots & & \vdots & \\ 0 & 0 & 0 & & & & & & & 2-J & 0 & 0 \\ 0 & 0 & 0 & \cdots & \cdots & \cdots & \cdots & \cdots & \cdots & 0 & 1-J & 0 \\ 0 & 0 & 0 & & & & & & & o & 0 & -J \end{bmatrix}, \tag{5.55}$$

$$\hat{\mathbf{J}}^{+} = \begin{bmatrix}
0 & \sqrt{2J} & 0 & & & & & & & 0 & 0 & 0 \\
0 & 0 & \sqrt{2(2J-1)} & \cdots & \cdots & \cdots & \cdots & \cdots & \cdots & 0 & 0 & 0 \\
0 & 0 & 0 & & & & & & & 0 & 0 & 0 \\
 & \vdots & & \ddots & \cdots & \cdots & \cdots & \cdots & 0 & & \vdots & \\
 & \vdots & & \vdots & 0 & \sqrt{(J+\frac{3}{2})(J-\frac{1}{2})} & 0 & 0 & \vdots & & \vdots & \\
 & \vdots & & \vdots & 0 & 0 & J+\frac{1}{2} & 0 & \vdots & & \vdots & \\
 & \vdots & & \vdots & 0 & 0 & 0 & \sqrt{(J+\frac{3}{2})(J-\frac{1}{2})} & \vdots & & \vdots & \\
 & \vdots & & \vdots & 0 & 0 & 0 & 0 & \vdots & & \vdots & \\
 & \vdots & & 0 & \cdots & \cdots & \cdots & \cdots & \ddots & & \vdots & \\
0 & 0 & 0 & & & & & & & 0 & \sqrt{2(2J-1)} & 0 \\
0 & 0 & 0 & \cdots & \cdots & \cdots & \cdots & \cdots & \cdots & 0 & 0 & \sqrt{2J} \\
0 & 0 & 0 & & & & & & & 0 & 0 & 0
\end{bmatrix}, \tag{5.56}$$

and

$$\hat{\mathbf{J}}^{-} = \begin{bmatrix}
0 & 0 & 0 & & & & & & & 0 & 0 & 0 \\
\sqrt{2J} & 0 & 0 & \cdots & \cdots & \cdots & \cdots & \cdots & \cdots & 0 & 0 & 0 \\
0 & \sqrt{2(2J-1)} & 0 & & & & & & & 0 & 0 & 0 \\
 & \vdots & & \ddots & \cdots & \cdots & \cdots & \cdots & 0 & & \vdots & \\
 & \vdots & & \vdots & 0 & 0 & 0 & 0 & \vdots & & \vdots & \\
 & \vdots & & \vdots & \sqrt{(J+\frac{3}{2})(J-\frac{1}{2})} & 0 & 0 & 0 & \vdots & & \vdots & \\
 & \vdots & & \vdots & 0 & J+\frac{1}{2} & 0 & 0 & \vdots & & \vdots & \\
 & \vdots & & \vdots & 0 & 0 & \sqrt{(J+\frac{3}{2})(J-\frac{1}{2})} & 0 & \vdots & & \vdots & \\
 & \vdots & & 0 & \cdots & \cdots & \cdots & \cdots & \ddots & & \vdots & \\
0 & 0 & 0 & & & & & & & 0 & 0 & 0 \\
0 & 0 & 0 & \cdots & \cdots & \cdots & \cdots & \cdots & \cdots & \sqrt{2(2J-1)} & 0 & 0 \\
0 & 0 & 0 & & & & & & & 0 & \sqrt{2J} & 0
\end{bmatrix}. \tag{5.57}$$

Projecting onto $J_z = \pm J$ subspace then gives:

$$\hat{\mathbf{J}}^z \mapsto \begin{bmatrix} J & 0 \\ 0 & -J \end{bmatrix} = 2J\hat{\mathbf{S}}^z, \qquad \hat{\mathbf{J}}^+ \mapsto \mathbf{0}, \qquad \hat{\mathbf{J}}^- = \mathbf{0}, \tag{5.58}$$

so that

$$\hat{J}^x \mapsto 0, \qquad \hat{J}^y \mapsto 0, \qquad \hat{J}^z \mapsto 2J\hat{S}^z \tag{5.59}$$

where we have introduced the pseudo-spin $\frac{1}{2}$ operators: $\hat{S}^x$, $\hat{S}^y$ and $\hat{S}^z$. This maximal pseudo-spin mapping can be written in a basis-independent from as:

$$\hat{\mathbf{J}}_\alpha \mapsto 2J\left(\hat{\mathbf{S}}_\alpha \cdot \hat{\mathbf{z}}_\alpha\right)\hat{\mathbf{z}}_\alpha. \tag{5.60}$$

This projection is not valid for all Hamiltonians; if there is a term with $\left(\hat{\mathbf{J}}\right)^{2J}$ it will give rise to a coupling between the state with $J_z = +J$ and the state with $J_z = -J$, which is not included in the projection. As we are only considering Hamiltonians which are quadratic in $\hat{\mathbf{J}}$, however, this is not an issue.

Alternatively we could project onto the subspace of $J_z = \pm\frac{1}{2}$, which provides:

$$\hat{\mathbf{J}}^z \mapsto \begin{bmatrix} \frac{1}{2} & 0 \\ 0 & -\frac{1}{2} \end{bmatrix} = \hat{\mathbf{S}}^z, \tag{5.61}$$

$$\hat{\mathbf{J}}^+ \mapsto \begin{bmatrix} 0 & J+\frac{1}{2} \\ 0 & 0 \end{bmatrix} = \left(J+\frac{1}{2}\right)\hat{\mathbf{S}}^+, \tag{5.62}$$

and

$$\hat{\mathbf{J}}^- \mapsto \begin{bmatrix} 0 & 0 \\ J+\frac{1}{2} & 0 \end{bmatrix} = \left(J+\frac{1}{2}\right)\hat{\mathbf{S}}^-, \tag{5.63}$$

which gives:

$$\hat{J}^x \mapsto \left(J+\frac{1}{2}\right)\hat{S}^x, \qquad \hat{J}^y \mapsto \left(J+\frac{1}{2}\right)\hat{S}^y, \qquad \hat{J}^z \mapsto \hat{S}^z. \tag{5.64}$$

We therefore arrive at the minimal pseudo-spin mapping:

$$\hat{\mathbf{J}}_\alpha \mapsto \left(J + \frac{1}{2}\right) \hat{\mathbf{S}}_\alpha - \left(J - \frac{1}{2}\right) \left(\hat{\mathbf{S}}_\alpha \cdot \hat{\mathbf{z}}_\alpha\right) \hat{\mathbf{z}}_\alpha. \tag{5.65}$$

Finally we note that pseudo-spin 1/2 projections to states with intermediate J_z values have the same structure as Equation 5.65. They only differ in the relative size of the coefficients of the two terms. So although we only calculate the maximal and minimal projections (in the following sections) we should bear in mind that generalising the coefficients of the resulting Hamiltonians is equivalent to projecting onto some (unspecified) linear combination of J_z states.

5.4.3 Maximal pseudo-spin projection

As the maximal pseudo-spin projection is the simplest of the two limits we will discuss this case first and then move on to the minimal pseudo-spin projection in the next section. The maximal pseudo-spin projection is also of interest, however, because it accurately describes the behaviour of the spin-ice materials. As discussed in the introduction (Section 1.3.2), in holmium and dysprosium titanate the spins have an Ising-like character (orientated along the local tetrahedral axes) and carrying the full moment of $J_z = \pm J$[35]. This is precisely the scenario captured by the maximal pseudo-spin projection.

The maximal pseudo-spin projection consists of applying the mapping:

$$\hat{\mathbf{J}}_\alpha \mapsto 2J \left(\hat{\mathbf{S}}_\alpha \cdot \hat{\mathbf{z}}_\alpha\right) \hat{\mathbf{z}}_\alpha, \tag{5.66}$$

to the five Hamiltonians derived in Section 5.4.1. Making use of the identity:

$$\hat{\mathbf{z}}_\alpha \cdot \hat{\mathbf{z}}_\beta = \frac{4}{3}\delta_{\alpha\beta} - \frac{1}{3}, \tag{5.67}$$

we get:

$$\begin{aligned} H_0 &= \frac{1}{2}\sum_{\alpha}\left(\hat{\mathbf{z}}_\alpha\cdot\hat{\mathbf{J}}_\alpha\right)^2 \\ &\mapsto \frac{1}{2}(2J)^2\sum_{\alpha}\left(\left[\hat{\mathbf{z}}_\alpha\cdot\hat{\mathbf{z}}_\alpha\right]\left[\hat{\mathbf{z}}_\alpha\cdot\hat{\mathbf{S}}_\alpha\right]\right)^2 \\ &= 4J^2H_0, \end{aligned} \tag{5.68}$$

$$\begin{aligned} H_1 &= \frac{1}{2}\sum_{\alpha\beta}\hat{\mathbf{J}}_\alpha\cdot\hat{\mathbf{J}}_\beta \\ &\mapsto \frac{1}{2}(2J)^2\left\{\frac{4}{3}\sum_{\alpha}\left(\hat{\mathbf{z}}_\alpha\cdot\hat{\mathbf{S}}_\alpha\right)^2-\frac{1}{3}\left(\sum_{\alpha}\hat{\mathbf{z}}_\alpha\cdot\hat{\mathbf{S}}_\alpha\right)^2\right\} \\ &= \frac{16}{3}J^2(H_0-H_3) \end{aligned} \tag{5.69}$$

$$\begin{aligned} H_2 &= \sum_{\alpha}\hat{\mathbf{J}}_\alpha\cdot\sum_{\beta}\hat{\mathbf{z}}_\beta\left(\hat{\mathbf{z}}_\beta\cdot\hat{\mathbf{J}}_\beta\right) \\ &\mapsto \frac{32}{3}J^2(H_0-H_3) \end{aligned} \tag{5.70}$$

$$\begin{aligned} H_3 &= \frac{1}{8}\left(\sum_{\alpha}\hat{\mathbf{z}}_\alpha\cdot\hat{\mathbf{J}}_\alpha\right)^2 \\ &\mapsto 4J^2H_3 \end{aligned} \tag{5.71}$$

$$\begin{aligned} H_4 &= \frac{1}{2}\hat{\mathbf{A}}\cdot\hat{\mathbf{A}} \\ &\mapsto \frac{1}{2}(2J)^2\left(\sum_{\alpha}\hat{\mathbf{z}}_\alpha\cdot\hat{\mathbf{S}}_\alpha\right)^2 \\ &= 16J^2H_3. \end{aligned} \tag{5.72}$$

Substituting the projected Hamiltonians into Equations 5.42 and 5.49 then gives:

$$H_{\mathrm{Ex}} = J^2\left\{16b_{\mathrm{Ex}}H_0-\left(\frac{16}{3}a_{\mathrm{Ex}}+16b_{\mathrm{Ex}}\right)H_3\right\}, \tag{5.73}$$

$$H_D \;=\; J_D J^2 \left\{ \frac{10}{3} H_0 + \frac{80}{3} H_3 \right\}. \tag{5.74}$$

For a spin-1/2 operator we note that

$$\left\langle \left(\hat{\mathbf{r}} \cdot \hat{\mathbf{S}} \right)^2 \right\rangle = 1/4, \tag{5.75}$$

for an arbitrary unit vector $\hat{\mathbf{r}}$. This means that H_0 just reduces to a constant. The exchange and dipolar Hamiltonians only depend on H_3, which (for $b_{\mathrm{Ex}} > 0$) appears with a competing sign in the two Hamiltonians. We choose to quantise the four spins parallel to their local tetrahedral axes so that $\hat{\mathbf{z}}_\alpha \cdot \hat{\mathbf{S}}_\alpha = S^z_\alpha$. The Hamiltonian for this system then has the particularly simple form of

$$H \propto H_3 = \frac{J^2}{2} \left(\sum_\alpha \hat{S}^z_\alpha \right)^2 \tag{5.76}$$

and the eigenstates of the Hamiltonian are just the eigenstates of the $\hat{S}^z_\alpha$ operators, with eigenvalues $S^z_\alpha = \pm\frac{1}{2}$. If $H_{\mathrm{Ex}} + H_D \propto -H_3$ (i.e. the exchange term dominating) then we wish to maximise H_3. This occurs when $\sum_\alpha S^z_\alpha = \pm 2$, i.e. the triple-$\mathbf{q}$ state with all four spins pointing into the centre of the tetrahedron or all four spins pointing out of the centre. In contrast if the dipolar term dominates the Hamiltonian: $H_{\mathrm{Ex}} + H_D \propto +H_3$, then we with to minimise H_3. We now require that $\sum_\alpha S^z_\alpha = 0$, which occurs when two of the spins point into the centre of the tetrahedron and two point out of the tetrahedron. This second case is equivalent to the 'two-in-two-out' ground-state experimentally observed in the spin ice materials[35]. Furthermore the dipolar interactions are dominant over the exchange interaction in spin ice. For example in $Dy_2Ti_2O_7$ the ratio of the nearest neighbour exchange interaction (J_{Ex}) to dipolar interaction (J_D) strength has been estimated to by $J_{\mathrm{Ex}}/J_D \approx 0.7$ from magnetic susceptibility data[51]. Now that we have demonstrated the use of the maximal pseudo-spin 1/2 projection in understanding the behaviour of the spin-ice material $Dy_2Ti_2O_7$, we will go on to consider the minimal pseudo-spin projection

in the next section.

5.4.4 Minimal pseudo-spin projection

We will now consider the minimal pseudo-spin 1/2 projection. As discussed in Section 5.2, the exact projection onto the $J_z = \pm 1/2$ subspace is most relevant, to Yb^{3+} based materials. We also expect it to be a good approximation to describe $Er_2Ti_2O_7$ due to the hole-like character of the Er^{3+} ions and the largely reduced ordered magnetic moment which is experimentally observed[19]. However, we will generalise this approximation (see the end of Section 5.4.2) in the later spin-wave calculations by using phenomenological parameters for the coefficients in the Hamiltonian.

We now apply the minimal pseudo-spin 1/2 projection:

$$\hat{\mathbf{J}}_\alpha \mapsto \left(J + \frac{1}{2}\right) \hat{\mathbf{S}}_\alpha - \left(J - \frac{1}{2}\right) \left(\hat{\mathbf{S}}_\alpha \cdot \hat{\mathbf{z}}_\alpha\right) \hat{\mathbf{z}}_\alpha. \tag{5.77}$$

to our five Hamiltonians to get:

$$H_0 \mapsto H_0 \tag{5.78}$$

$$H_1 \mapsto \left(J + \frac{1}{2}\right)^2 H_1 - \left(J + \frac{1}{2}\right)\left(J - \frac{1}{2}\right) H_2 + \frac{4}{3}\left(J - \frac{1}{2}\right)^2 (H_0 - H_3) \tag{5.79}$$

$$H_2 \mapsto \left(J + \frac{1}{2}\right) H_2 - \frac{8}{3}\left(J - \frac{1}{2}\right)(H_0 - H_3) \tag{5.80}$$

$$H_3 \mapsto H_3 \tag{5.81}$$

$$H_4 \mapsto \left(J + \frac{1}{2}\right)^2 H_4 - 4\left[2\left(J + \frac{1}{2}\right)\left(J - \frac{1}{2}\right) - \left(J - \frac{1}{2}\right)^2\right] H_3. \tag{5.82}$$

We notice that the Hamiltonian H_0 (and also H_3) projects onto itself. Although the isotropic exchange, H_1, maps onto a number of Hamiltonians, the isotropic exchange term still remains dominant. H_4 also maps onto itself, but with an additional term in $-H_3$ (which is dominant over the term in H_4). The mapping of H_1 and H_2 also introduces

a term in $(H_0 - H_3)$ which can be written as:

$$H_0 - H_3 = \frac{1}{16} \sum_{\alpha\beta} \left(\hat{\mathbf{z}}_\alpha \cdot \hat{\mathbf{S}}_\alpha - \hat{\mathbf{z}}_\beta \cdot \hat{\mathbf{S}}_\beta \right)^2, \tag{5.83}$$

and so could be considered as another 'natural' Hamiltonian.

Applying the above mappings to the exchange interaction gives:

$$\begin{aligned} H_{\rm Ex} &= a_{\rm Ex} H_1 - b_{\rm Ex} H_4 \\ &\mapsto \lambda_{\rm Ex1} H_1 - \lambda_{\rm Ex2} H_2 + \lambda_{\rm Ex3} H_3 - \lambda_{\rm Ex4} H_4 + \lambda_{\rm Ex5} \left(H_0 - H_3 \right), \end{aligned} \tag{5.84}$$

where we have introduced the phenomenological parameters: $\lambda_{\rm Ex1}, \lambda_{\rm Ex2}, \lambda_{\rm Ex3}, \lambda_{\rm Ex4}, \lambda_{\rm Ex5}$ which we chose to be positive. Similarly the dipole interaction transforms to:

$$\begin{aligned} H_D &= J_D \left(\frac{7}{4} H_1 + \frac{3}{4} H_4 + \frac{9}{2} H_0 - \frac{9}{4} H_2 \right) \\ &\mapsto \lambda_{D0} H_0 + \lambda_{D1} H_1 - \lambda_{D2} H_2 + \lambda_{D4} H_4 + \lambda_{D5} \left(H_0 - H_3 \right), \end{aligned} \tag{5.85}$$

where $\lambda_{D0}, \lambda_{D1}, \lambda_{D2}, \lambda_{D4}$ and λ_{D5} are also positive phenomenological parameters. Only the Hamiltonians H_3 and H_4 appear with competing signs. We discussed earlier that we require the dipolar interaction to be intrinsically frustrated to explain the Bragg peak intensities observed by elastic neutron scattering. We therefore choose $\lambda_{Ex4} > \lambda_{D4}$. We also choose to incorporate the term in H_3 into the Hamiltonian $(H_0 - H_3)$. As a result, we allow the coefficients of both the term in H_0 (λ_0) and also in $(H_0 - H_3)$ (λ_3) to be positive or negative at present. Consequently we arrive at our final Hamiltonian:

$$H = \lambda_0 H_0 + \lambda_1 H_1 - \lambda_2 H_2 + \lambda_3 (H_0 - H_3) - \lambda_4 H_4, \tag{5.86}$$

with λ_1, λ_2 and λ_4 all positive parameters. This Hamiltonian is far more complex than the one found via the maximal pseudo-spin projection. As a result we have no way to find the fully quantum solution of the above Hamiltonian and instead are limited to

using a semi-classical approach. In the next section we therefore discuss possible classical ground-states of the various component Hamiltonians with a view to later calculating the spin-wave dispersion (and quantum fluctuation energy contribution) by using the Holstein-Primakoff transformation.

5.4.5 Classical ground-states

In this section we will discuss the possible classical ground-states of our phenomenological Hamiltonian in order to assess whether they are compatible with the long-range magnetic ordering observed by elastic scattering experiments. We will begin by considering H_1 as this represents the isotropic antiferromagnetic exchange interaction. This is minimised by enforcing the constraint that the moments of the four spins forming a tetrahedron sum to zero (for every tetrahedron). Mathematically this is equivalent to $\hat{\mathbf{T}} = \mathbf{0}$. As discussed in Section 5.3.2 the elastic scattering data is consistent with this constraint (the $(2,2,2)$ Bragg peak being of negligible intensity[66]) and so we can assume that the ground-state of erbium titanate miminises the Hamiltonian H_1.

We will next consider the Hamiltonian $-H_4$. This is clearly minimised (for normalised spins) by requiring that:

$$S^x = S_0^x = S_1^x = -S_2^x = -S_3^x, \tag{5.87}$$

$$S^y = S_0^y = -S_1^y = S_2^y = -S_3^y, \tag{5.88}$$

$$S^z = S_0^z = -S_1^z = -S_2^z = S_3^z, \tag{5.89}$$

where $(S^x)^2 + (S^y)^2 + (S^z)^2 = 1$. We see that this is exactly equivalent to the states described by Equations 5.21 to 5.24, and therefore consistent with the observed intensities of both the $(2,2,2)$ and $(2,2,0)$ type peaks. Substituting the above relationships into the Hamiltonian gives $-H_4 = 8$, and is therefore independent of the relative sizes of the spin components S^x, S^y and S^z. As these states are also compatible with $\hat{\mathbf{T}} = 0$, the classical ground-state to $\lambda_1 H_1 - \lambda_4 H_4$ is that previously depicted in Fig. 5.5 , with two degrees of

freedom (which can be thought of as specifying the orientation of the spin $\mathbf{S}_0$).

Now turning to the term $\lambda_3(H_0-H_3)$, we allowed for the possibility that the parameter λ_3 could be positive of negative. We will first consider the possibility that $\lambda_3 < 0$, in which case we wish to maximise the Hamiltonian:

$$H_0 - H_3 = \frac{1}{16}\sum_{\alpha\beta}\left(\hat{\mathbf{z}}_\alpha \cdot \hat{\mathbf{S}}_\alpha - \hat{\mathbf{z}}_\beta \cdot \hat{\mathbf{S}}_\beta\right)^2. \tag{5.90}$$

We therefore require that $\hat{\mathbf{z}}_\alpha \cdot \hat{\mathbf{S}}_\alpha = -\hat{\mathbf{z}}_\beta \cdot \hat{\mathbf{S}}_\beta$ for as many of the pairs of spins in a tetrahedron as possible, with the spins orientated along the tetrahedral axis. This gives us the 'two-in-two-out' states seen in spin-ice. These clearly have a ferromagnetic component and are therefore not consistent with elastic neutron scattering data. We will therefore restrict our phenomenological Hamiltonian to include $\lambda_3 > 0$ only. To minimise $(H_0 - H_3)$ we require that $\hat{\mathbf{z}}_\alpha \cdot \hat{\mathbf{S}}_\alpha = \hat{\mathbf{z}}_\beta \cdot \hat{\mathbf{S}}_\beta = const.$ for all α and β. This set of states is precisely the same one that minimises the Hamiltonian $\lambda_1 H_1 - \lambda_4 H_4$.

Next we will consider the Hamiltonian H_0, which we could appear with either a positive or negative coefficient. $+H_0$ is minimised by requiring that $\hat{\mathbf{z}} \cdot \hat{\mathbf{S}}_\alpha = 0$ for all α, i.e. the spins are orientated perpendicular to the tetrahedral axes. This is consistent with the state currently proposed in the literature, and discussed in Section 5.3.3. Alternatively $-H_0$ is minimised by $\hat{\mathbf{z}} \cdot \hat{\mathbf{S}}_\alpha = \pm 1$, for all α. Examples of this are the triple-q state with all spins pointing either inwards or outwards of the tetrahedron, or the 'two-in-two-out' spin-ice states. Combining $-H_0$ with the previous Hamiltonians, the classical ground-state of $\lambda_1 H_1 + \lambda_3(H_0 - H_3) - \lambda_4 H_4 - \lambda_0 H_0$ is the triple-q state.

Finally we mention the Hamiltonian $H_2 = \mathbf{T} \cdot \sum_\alpha \hat{\mathbf{z}}_\alpha(\hat{\mathbf{z}}_\alpha \cdot \hat{\mathbf{S}}_\alpha)$. The classical ground state for this Hamiltonian is less obvious, though we note that the Hamiltonian can be factorised in terms of H_0 and H_1. In Section 5.6 we will use the classical ground state for H_1 to apply the Holstein-Primakoff transformation. It turns out that the terms in $S^{\frac{3}{2}}$ and S then vanish indicating that we have indeed used a classical-ground state of H_2.

The elastic neutron scattering data, however, appears consistent with $\mathbf{S}_0 = \langle 1, 1, 2\rangle/\sqrt{6}$

(and symmetry related domains), as was discussed in Section 5.3.5, rather than $\mathbf{S}_0 = \langle 1,1,1\rangle/\sqrt{3}$ as is the case for the triple-q state. As we are modeling the system using a pseudo-spin 1/2 representation, quantum fluctuations are likely to be significant. We have no way to approach the fully quantum Hamiltonian, so in Section 5.6 we will offer a semi-classical spin-wave analysis of the model. As erbium titanate has been observed to exhibit long-range magnetic order (albeit of reduced magnitude) this seems a reasonable approach, though not perfect. Furthermore, as we will discuss in the next section, $Er_2Ti_2O_2$ appears to have an extremely unusual spin wave spectrum: an additional motivation for a semi-classical spin-wave analysis of the model.

5.5 Gapless spin-waves

One particularly interesting feature of $Er_2Ti_2O_2$ is that it has been observed to have a gapless spin wave spectrum. This will be the topic of discussion for this section. In Fig. 5.9 we reproduce the inelastic neutron scattering data by Ruff *et. al*[66]. The data are measured for a slice through k-space along the direction $(2,2,k)$. At a temperature of $2K$ (which is above the magnetic ordering temperature) only the background scattering is visible (see panel 'a'). However, at $T = 50mK$ (panel 'b') what appears to be a gapless dispersive mode is visible. In addition, there is also a relatively dispersionless mode at an energy of about $0.4meV$. The remainder of the data shows how the spin-wave spectrum changes on application of a magnetic field. We do not attempt to understand the details of the scattering in the presence of the external field as the system is too complex. Strangely the gapless spin-wave branch disappears on application of a field strength of around $1T$ and is seen by Ruff *et. al* to reappear at a different point in k-space. Further more, the dispersionless mode can be seen to soften until at a temperature of $T = 1.5K$ it becomes temporally gapless. This is the field at which there is a transition to the saturated ferromagnetic state[10], which would appear to be linked to the softening of dispersionless mode.

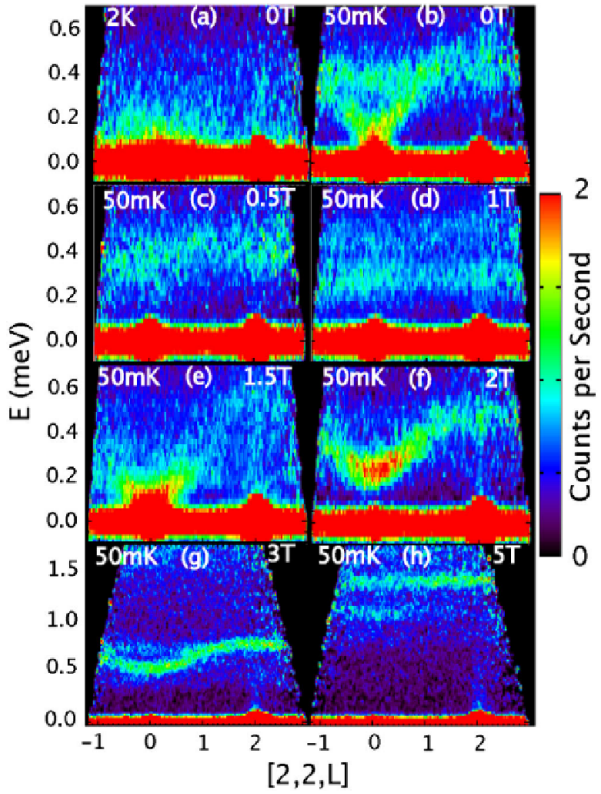

Figure 5.9: Spin-wave dispersion spectrum plotted along the reciprocal-space line $\mathbf{k} = (2, 2, k)$, with the temperature and external field strength indicated on figure. Data by Ruff *et. al*[66].

The (zero-field) gapless spin-wave mode is also compatible with specific heat data. It appears that $C_v \propto T^3$ at low temperatures as shown in Fig. 5.10 from Champion *et. al*[19]. Unfortunately, this trend cannot easily be followed below $T \sim 1K$ as there

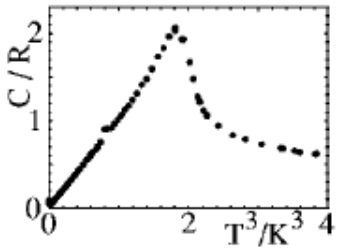

Figure 5.10: The specific heat plotted as a function of T^3 from Champion *et. al*[19].

is then an upturn in the specific heat due to the onset of the ordering of the nuclear magnetic moments. Assuming that the contribution to the specific heat from the rare-earth moments is indeed proportional to T^3 as $T \mapsto 0$ however, this implies that the

energy dependency of the density of states goes like $g(\epsilon) \propto \epsilon^2$ at leading order, i.e. there is no energy gap to creating magnetic excitations.

Naively gapless spin-wave modes are not expected to occur for magnetically ordered rare-earth oxides. This is because the crystal-field interaction is usually dominant. As a result, when combined with the strong spin-orbit coupling present in f-block ions, there exists a significant single-ion anisotropy (except for the case of Gd^{3+} which has $L = 0$). The spins are therefore expected to be orientated along the minima of the crystal-field potential. Creating a spin-wave incurs a finite energy penalty associated with the introduction of a (non-vanishing) component of spin that is no longer orientated along the crystal field minimum. For this reason it is highly unlikely that the gapless spin-wave mode could be associated with the usual Goldstone mode describing a global spin rotation.

We propose an alternative explanation for the origin of the gapless spin-wave mode. We suggest that it is actually an unusual form of 'longitudinal' spin-wave associated with the transferal of (reciprocal-space) spin-density between different Bragg spots. In this case we are referring to the $(0, 2, 2), (2, 0, 2)$ and $(2, 2, 0)$ spots, which are the three active spots for $Er_2Ti_2O_7$. As we use the phrase 'longitudinal spin-wave' in a very particular way, we will try to clarify our meaning. Naturally the spins still fluctuate transversely and maintain a constant length. Instead, changes in θ and ϕ for the spin state shown previously in Fig. 5.5 (while maintaining the rotational symmetries which map the four spin onto each other), is in turn equivalent to changing the relative intensities of the three active Bragg spots. Consequently, if the scattering intensity at a single Bragg spot is observed, this will change longitudinally. When the behaviour of all three Bragg spots is combined, however, it corresponds to transverse oscillations of equal-length spins. A similar idea is discussed in the paper by Jensen *et. al*[38].

We will illustrate the difference between the longitudinal spin-waves described above and the usual transverse spin-waves with the following examples. First we consider an isotropic single-$\mathbf{q}$ state with spins orientated along the z-axis ($\theta = 0$ in Fig. 5.5). Magnetic

scattering should then be visible at $(2,2,0)$, though not at $(2,2,0)$ or $(2,0,2)$. Gapless spin-wave modes are also expected around the $(0,2,2)$ spot (and the other spots related by the magnetic reciprocal-space superlattice) due to the Goldstone modes associated with global spin rotations, i.e. they create a small amount of magnetism indexed by the same **k**-vector but in a perpendicular direction. Spin-waves at $(2,0,0)$ and $(0,2,0)$ (and at superlattice related positions) should be gapped, however, as these styles of magnetism are not currently low energy states. Populating these modes corresponds to creating small amounts of this type of magnetism (and therefore changing θ and ϕ slightly). If these modes soften to become gapless, it corresponds to a phase transition between the original single-**q** state and a new multiple-**q** state. Normal rare-earth magnets, however, have a large spin anisotropy (arising from the combination of the crystal field and spin-orbit interactions). This will open up a large gap in the transverse modes (associated with global spin rotations). The longitudinal spin-wave modes, which link to other multiple- **q** magnetic states can remain gapless. The rare-earth magnet CeAs is believed to show this behaviour. It has been observed to have a spin-wave mode with an extremely small energy gap of $\sim 0.03meV$[34].

Qualitatively it is not unreasonable that $Er_2Ti_2O_7$ will exhibit this kind of gapless spin-wave mode. Elastic neutron scattering experiments indicate that the spins lie along crystallographically insignificant directions, i.e. they do not lie along minima of the crystal-field interaction. Presumably this is due to competing interactions in the Hamiltonian (and an indication that the system is extremely frustrated). Crudely speaking, the magnetic ground-state could be thought of as already 'paying' a spin-anisotropy energy penalty and therefore vanishingly small distortions to this state correspond to only vanishingly small changes in the cost of this energy penalty, hence the absence of an anisotropy gap.

In the following section we will calculate the semi-classical spin-wave dispersion of our model to see to what extent it can qualitatively reproduce the gapless spin-waves observed in $Er_2Ti_2O_7$.

5.6 Spin-wave calculations

In this section we will calculate the semi-classical spin-wave spectrum and quantum fluctuation energy of our phenomenological Hamiltonian. We will use a bosonic representation for the spins in the form of a Holstein-Primakoff Transformation[36, 1]:

$$\begin{aligned} \hat{S}^z &= S - b^\dagger b \\ \hat{S}^- &= b^\dagger \sqrt{(2S - b^\dagger b)} \\ \hat{S}^+ &= \sqrt{(2S - b^\dagger b)}\; b, \end{aligned} \tag{5.91}$$

for a spin quantised parallel to the z-axis, where $b^\dagger$ and b are bosonic creation and annihilation operators respectively. Expanding to lowest non-trivial order in these operators then give:

$$\hat{\mathbf{S}} = \begin{bmatrix} \hat{S}^x \\ \hat{S}^y \\ \hat{S}^z \end{bmatrix} \mapsto \begin{bmatrix} \sqrt{S/2}\;(b^\dagger + b) \\ \sqrt{S/2}\;(b^\dagger - b)i \\ S - b^\dagger b \end{bmatrix}. \tag{5.92}$$

We begin by considering the following Hamiltonian for a single tetrahedron:

$$H = J_0(H_1 - \delta H_4 - \eta H_0 + \xi(H_0 - H_3) - \mu H_2, \tag{5.93}$$

where we have extracted the natural energy scale, J_0 so that the parameters δ, η, ξ and μ are all scale free parameters. To stabalise the required classical ground-state we will require that these parameters are all positive and less than unity. For the case of $\eta = 0$ the classical ground-state manifold is shown in Fig. 5.5 with four spins per unit cell (where the angles θ and ϕ can take any value). If $\eta > 0$ then the cubic symmetric triple-$\mathbf{q}$ state with all spins pointing into the centre of the tetrahedron is stabilised. We need to quantise the spins along a direction which corresponds to a minimum of the classical energy and

therefore chose the directions shown in Fig. 5.5:

$$\hat{\mathbf{S}}_0 = \begin{bmatrix} \hat{\mathbf{x}} & \hat{\mathbf{y}} & \hat{\mathbf{z}} \end{bmatrix} \begin{bmatrix} \cos\theta\cos\phi & -\sin\phi & \sin\theta\cos\phi \\ \cos\theta\sin\phi & \cos\phi & \sin\theta\sin\phi \\ -\sin\theta & 0 & \cos\theta \end{bmatrix} \begin{bmatrix} \sqrt{S/2}\ (b_0^\dagger + b_0) \\ \sqrt{S/2}\ (b_0^\dagger - b_0)i \\ S - b_0^\dagger b_0 \end{bmatrix}, \quad (5.94)$$

$$\hat{\mathbf{S}}_1 = \begin{bmatrix} \hat{\mathbf{x}} & \hat{\mathbf{y}} & \hat{\mathbf{z}} \end{bmatrix} \begin{bmatrix} \cos\theta\cos\phi & -\sin\phi & \sin\theta\cos\phi \\ -\cos\theta\sin\phi & -\cos\phi & -\sin\theta\sin\phi \\ \sin\theta & 0 & -\cos\theta \end{bmatrix} \begin{bmatrix} \sqrt{S/2}\ (b_1^\dagger + b_1) \\ \sqrt{S/2}\ (b_1^\dagger - b_1)i \\ S - b_1^\dagger b_1 \end{bmatrix}, \quad (5.95)$$

$$\hat{\mathbf{S}}_2 = \begin{bmatrix} \hat{\mathbf{x}} & \hat{\mathbf{y}} & \hat{\mathbf{z}} \end{bmatrix} \begin{bmatrix} -\cos\theta\cos\phi & \sin\phi & -\sin\theta\cos\phi \\ \cos\theta\sin\phi & \cos\phi & \sin\theta\sin\phi \\ \sin\theta & 0 & -\cos\theta \end{bmatrix} \begin{bmatrix} \sqrt{S/2}\ (b_2^\dagger + b_2) \\ \sqrt{S/2}\ (b_2^\dagger - b_2)i \\ S - b_2^\dagger b_2 \end{bmatrix}, \quad (5.96)$$

$$\hat{\mathbf{S}}_3 = \begin{bmatrix} \hat{\mathbf{x}} & \hat{\mathbf{y}} & \hat{\mathbf{z}} \end{bmatrix} \begin{bmatrix} -\cos\theta\cos\phi & \sin\phi & -\sin\theta\cos\phi \\ -\cos\theta\sin\phi & -\cos\phi & -\sin\theta\sin\phi \\ -\sin\theta & 0 & \cos\theta \end{bmatrix} \begin{bmatrix} \sqrt{S/2}\ (b_3^\dagger + b_3) \\ \sqrt{S/2}\ (b_3^\dagger - b_3)i \\ S - b_3^\dagger b_3 \end{bmatrix}, \quad (5.97)$$

where θ and ϕ are the angles shown in Fig. 5.5. We then notice that:

$$\begin{aligned} \hat{\mathbf{z}}_\alpha \cdot \hat{\mathbf{S}}_\alpha &= \frac{1}{\sqrt{3}} \begin{bmatrix} 1 & 1 & 1 \end{bmatrix} \begin{bmatrix} \mathrm{c}_\theta\mathrm{c}_\phi & -\mathrm{s}_\phi & \mathrm{s}_\theta\mathrm{c}_\phi \\ \mathrm{c}_\theta\mathrm{s}_\phi & \mathrm{c}_\phi & \mathrm{s}_\theta\mathrm{s}_\phi \\ -\mathrm{s}_\theta & 0 & \mathrm{c}_\theta \end{bmatrix} \begin{bmatrix} \sqrt{S/2}\ (b_\alpha^\dagger + b_\alpha) \\ \sqrt{S/2}\ (b_\alpha^\dagger - b_\alpha)i \\ S - b_\alpha^\dagger b_\alpha \end{bmatrix} \\ &= \frac{1}{\sqrt{3}} \left[\sqrt{S/2}\ \left(R b_\alpha^\dagger + \overline{R} b_\alpha \right) + \left(S - b_\alpha^\dagger b_\alpha \right) \left(\mathrm{s}_\theta\mathrm{c}_\phi + \mathrm{s}_\theta\mathrm{s}_\phi + \mathrm{c}_\theta \right) \right] \end{aligned} \quad (5.98)$$

for all α, where we have made a number of definitions:

$$\mathrm{s}_\theta = \sin\theta, \qquad \mathrm{c}_\theta = \cos\theta, \qquad \mathrm{s}_\phi = \sin\phi, \qquad \mathrm{c}_\phi = \cos\phi, \quad (5.99)$$

and

$$R = X + Y + Z, \quad (5.100)$$

$$X = \mathrm{c}_\theta \mathrm{c}_\phi - i\mathrm{s}_\phi, \qquad Y = \mathrm{c}_\theta \mathrm{s}_\phi + i\mathrm{c}_\phi, \qquad Z = -\mathrm{s}_\theta, \tag{5.101}$$

with the 'bar' denoting the complex conjugate. At this point we also note that:

$$X^2 + Y^2 + Z^2 = 0 \qquad \text{and} \qquad |X|^2 + |Y|^2 + |Z|^2 = 2. \tag{5.102}$$

We will now go on to express our five, single-tetrahedron Hamiltonians in terms of the bosonic operators $b_\alpha^\dagger$ and b_α, by considering decreasing powers of S. The first Hamiltonian that we will look at is:

$$H_0 = \frac{1}{2} \sum_\alpha \left(\hat{\mathbf{z}}_\alpha \cdot \hat{\mathbf{s}}_\alpha \right)^2 . \tag{5.103}$$

The term at $\mathcal{O}(S^2)$ gives the classical ground-state energy:

$$H_0 \left[\mathcal{O}(S^2) \right] = \frac{2}{3} S^2 \left(\mathrm{s}_\theta \mathrm{c}_\phi + \mathrm{s}_\theta \mathrm{s}_\phi + \mathrm{c}_\theta \right)^2 , \tag{5.104}$$

and the term at $\mathcal{O}(S^{3/2})$ gives:

$$H_0 \left[\mathcal{O}(S^{3/2}) \right] = \frac{1}{6} S \sqrt{S/2} \ \left(\mathrm{s}_\theta \mathrm{c}_\phi + \mathrm{s}_\theta \mathrm{s}_\phi + \mathrm{c}_\theta \right) \sum_\alpha \left(R b_\alpha^\dagger + \overline{R} b_\alpha \right) , \tag{5.105}$$

which is linear in the bosonic operators. This term should be zero if we have chosen the correct classical-ground state. As discussed in Section 5.4.5, if the coefficient of H_0 is positive, then the classical ground-state manifold has $\hat{\mathbf{z}}_\alpha \cdot \mathbf{S}_\alpha = 0$. For the spin $\mathbf{S}_0$ this gives $S_x + S_y + S_z = \mathrm{s}_\theta \mathrm{c}_\phi + \mathrm{s}_\theta \mathrm{s}_\phi + \mathrm{c}_\theta = 0$, so that the term at $\mathcal{O}(S^{2/3})$ is zero as expected. Alternatively, if the coefficient of H_0 is negative, then the classical ground-state has $\hat{\mathbf{z}}_\alpha \cdot \mathbf{S}_\alpha = \pm 1$ for all α. In this case we get $R = 0$ (using $\mathrm{s}_\theta = \sqrt{2/3}$, $\mathrm{c}_\theta = 1/\sqrt{3}$ and $\mathrm{s}_\phi = \mathrm{c}_\phi = 1/\sqrt{2}$), which again makes the term at $\mathcal{O}(S^{2/3})$ vanish. Finally we will calculate the term at order $\mathcal{O}(S)$:

$$\begin{aligned} H_0 \left[\mathcal{O}(S) \right] \ = \ & \frac{1}{6} S \sum_\alpha \left\{ \frac{1}{2} \left[R^2 b_\alpha^\dagger b_\alpha^\dagger + \overline{R}^2 b_\alpha b_\alpha + R\overline{R} \left(b_\alpha^\dagger b_\alpha + b_\alpha b_\alpha^\dagger \right) \right] \right. \\ & \left. -2 \left(\mathrm{s}_\theta \mathrm{c}_\phi + \mathrm{s}_\theta \mathrm{s}_\phi + \mathrm{c}_\theta \right) b_\alpha^\dagger b_\alpha \right\} . \end{aligned} \tag{5.106}$$

To calculate $H_1 = \frac{1}{2}\hat{\mathbf{T}} \cdot \hat{\mathbf{T}}$, we use:

$$\begin{aligned}
T^x &= \left(\sqrt{S/2}\; X \left[b_0^\dagger + b_1^\dagger - b_2^\dagger - b_3^\dagger\right] + h.c.\right) - \mathrm{s}_\theta \mathrm{c}_\phi \left[b_0^\dagger b_0 + b_1^\dagger b_1 - b_2^\dagger b_2 - b_3^\dagger b_3\right] \\
T^y &= \left(\sqrt{S/2}\; Y \left[b_0^\dagger - b_1^\dagger + b_2^\dagger - b_3^\dagger\right] + h.c.\right) - \mathrm{s}_\theta \mathrm{s}_\phi \left[b_0^\dagger b_0 - b_1^\dagger b_1 + b_2^\dagger b_2 - b_3^\dagger b_3\right] \\
T^z &= \left(\sqrt{S/2}\; Z \left[b_0^\dagger - b_1^\dagger - b_2^\dagger + b_3^\dagger\right] + h.c.\right) - \mathrm{c}_\theta \left[b_0^\dagger b_0 - b_1^\dagger b_1 - b_2^\dagger b_2 + b_3^\dagger b_3\right] . \quad (5.107)
\end{aligned}$$

This then provides us with:

$$\begin{aligned}
H_1\left[\mathcal{O}(S^2)\right] &= 0 \\
H_1\left[\mathcal{O}(S^{3/2})\right] &= 0 \\
H_1\left[\mathcal{O}(S)\right] &= \frac{1}{4}S\Bigg\{\left(X^2+Y^2+Z^2\right)\sum_\alpha \left[b_\alpha^\dagger b_\alpha^\dagger\right] + 2\left(X^2-Y^2-Z^2\right)\left[b_0^\dagger b_1^\dagger + b_2^\dagger b_3^\dagger\right] \\
&\quad +2\left(-X^2+Y^2-Z^2\right)\left[b_0^\dagger b_2^\dagger + b_1^\dagger b_3^\dagger\right] + 2\left(-X^2-Y^2+Z^2\right)\left[b_0^\dagger b_3^\dagger + b_1^\dagger b_2^\dagger\right]\Bigg\} + h.c. \\
&\quad +\frac{1}{4}S\Bigg\{\left(X\overline{X}+Y\overline{Y}+Z\overline{Z}\right)\sum_\alpha \left[b_\alpha^\dagger b_\alpha + b_\alpha b_\alpha^\dagger\right] \\
&\quad +2\left(X\overline{X}-Y\overline{Y}-Z\overline{Z}\right)\left[b_0^\dagger b_1 + b_2^\dagger b_3 + h.c.\right] \\
&\quad +2\left(-X\overline{X}+Y\overline{Y}-Z\overline{Z}\right)\left[b_0^\dagger b_2 + b_1^\dagger b_3 + h.c.\right] \\
&\quad +2\left(-X\overline{X}-Y\overline{Y}+Z\overline{Z}\right)\left[b_0^\dagger b_3 + b_1^\dagger b_2 + h.c.\right]\Bigg\} \\
&= S\left\{X^2\left[b_0^\dagger b_1^\dagger + b_2^\dagger b_3^\dagger\right] + Y^2\left[b_0^\dagger b_2^\dagger + b_1^\dagger b_3^\dagger\right] + Z^2\left[b_0^\dagger b_3^\dagger + b_1^\dagger b_2^\dagger\right] + h.c.\right\} \\
&\quad \frac{1}{2}S\Bigg\{\sum_\alpha \left[b_\alpha^\dagger b_\alpha + b_\alpha b_\alpha^\dagger\right] + 2\left(X\overline{X}-1\right)\left[b_0^\dagger b_1 + b_2^\dagger b_3 + h.c.\right] \\
&\quad +2\left(Y\overline{Y}-1\right)\left[b_0^\dagger b_2 + b_1^\dagger b_3 + h.c.\right] + 2\left(Z\overline{Z}-1\right)\left[b_0^\dagger b_3 + b_1^\dagger b_2 + h.c.\right]\Bigg\} .
\end{aligned} \quad (5.108)$$

Next we will calculate $H_2 = \hat{\mathbf{T}} \cdot \sum_\alpha \hat{\mathbf{z}}_\alpha(\hat{\mathbf{z}}_\alpha \cdot \hat{\mathbf{S}}_\alpha)$. Making use of the fact that $\hat{\mathbf{T}}$ was

previously calculated to find H_1, we get

$$\sum_\alpha \hat{\mathbf{z}}_\alpha(\hat{\mathbf{z}}_\alpha\cdot\hat{\mathbf{s}}_\alpha)=\frac{1}{3}\begin{bmatrix} \sqrt{\frac{S}{2}}\left(R\left[b_0^\dagger+b_1^\dagger-b_2^\dagger-b_3^\dagger\right]+h.c.\right)-\left(\mathrm{s}_\theta\mathrm{c}_\phi+\mathrm{s}_\theta\mathrm{s}_\phi+\mathrm{c}_\theta\right)\left[b_0^\dagger b_0+b_1^\dagger b_1-b_2^\dagger b_2-b_3^\dagger b_3\right] \\ \sqrt{\frac{S}{2}}\left(R\left[b_0^\dagger-b_1^\dagger+b_2^\dagger-b_3^\dagger\right]+h.c.\right)-\left(\mathrm{s}_\theta\mathrm{c}_\phi+\mathrm{s}_\theta\mathrm{s}_\phi+\mathrm{c}_\theta\right)\left[b_0^\dagger b_0-b_1^\dagger b_1+b_2^\dagger b_2-b_3^\dagger b_3\right] \\ \sqrt{\frac{S}{2}}\left(R\left[b_0^\dagger-b_1^\dagger-b_2^\dagger+b_3^\dagger\right]+h.c.\right)-\left(\mathrm{s}_\theta\mathrm{c}_\phi+\mathrm{s}_\theta\mathrm{s}_\phi+\mathrm{c}_\theta\right)\left[b_0^\dagger b_0-b_1^\dagger b_1-b_2^\dagger b_2+b_3^\dagger b_3\right] \end{bmatrix}. \quad (5.109)$$

The terms in S^2 and $S^{3/2}$ are zero and the term in S gives:

$$\begin{aligned} H_2 &= \frac{S}{6}\left\{\left[R^2\sum_\alpha b_\alpha^\dagger b_\alpha^\dagger+2R\left(X-Y-Z\right)\left(b_0^\dagger b_1^\dagger+b_2^\dagger b_3^\dagger\right)+2R\left(-X+Y-Z\right)\left(b_0^\dagger b_2^\dagger+b_1^\dagger b_3^\dagger\right)\right.\right. \\ &\quad \left.+2R\left(-X-Y+Z\right)\left(b_0^\dagger b_3^\dagger+b_1^\dagger b_2^\dagger\right)+h.c.\right]+R\overline{R}\sum_\alpha\left(b_\alpha^\dagger b_\alpha+b_\alpha b_\alpha^\dagger\right) \\ &\quad +\left[\overline{R}\left(X-Y-Z\right)+R\left(\overline{X}-\overline{Y}-\overline{Z}\right)\right]\left(b_0^\dagger b_1+b_2^\dagger b_3+h.c.\right) \\ &\quad +\left[\overline{R}\left(-X+Y-Z\right)+R\left(-\overline{X}+\overline{Y}-\overline{Z}\right)\right]\left(b_0^\dagger b_2+b_1^\dagger b_3+h.c.\right) \\ &\quad \left.+\left[\overline{R}\left(-X-Y+Z\right)+R\left(-\overline{X}-\overline{Y}+\overline{Z}\right)\right]\left(b_0^\dagger b_3+b_1^\dagger b_2+h.c.\right)\right\} \\ &= \frac{S}{6}\left\{\left[R^2\sum_\alpha b_\alpha^\dagger b_\alpha^\dagger-4YZ\left(b_0^\dagger b_1^\dagger+b_2^\dagger b_3^\dagger\right)-4ZX\left(b_0^\dagger b_2^\dagger+b_1^\dagger b_3^\dagger\right)-4XY\left(b_0^\dagger b_3^\dagger+b_1^\dagger b_2^\dagger\right)+h.c.\right]\right. \\ &\quad +R\overline{R}\sum_\alpha\left(b_\alpha^\dagger b_\alpha+b_\alpha b_\alpha^\dagger\right) \\ &\quad +4\left[X\overline{X}-1-\frac{Y\overline{Z}+Z\overline{Y}}{2}\right]\left(b_0^\dagger b_1+b_2^\dagger b_3+h.c.\right) \\ &\quad +4\left[Y\overline{Y}-1-\frac{Z\overline{X}+X\overline{Z}}{2}\right]\left(b_0^\dagger b_2+b_1^\dagger b_3+h.c\right) \\ &\quad \left.+4\left[Z\overline{Z}-1-\frac{X\overline{Y}+Y\overline{X}}{2}\right]\left(b_0^\dagger b_3+b_1^\dagger b_2+h.c.\right)\right\}. \end{aligned} \quad (5.110)$$

Turning to $H_3=\frac{1}{8}\left(\sum_\alpha\hat{\mathbf{z}}_\alpha\cdot\hat{\mathbf{s}}_\alpha\right)^2$, we get

$$\begin{aligned} H_3[\mathcal{O}(S^2)] &= \frac{2}{3}S^2\left(\mathrm{s}_\theta\mathrm{c}_\phi+\mathrm{s}_\theta\mathrm{s}_\phi+\mathrm{c}_\theta\right)^2 \\ H_3[\mathcal{O}(S^{3/2})] &= \frac{1}{6}S\sqrt{\frac{S}{2}}R\sum_\alpha b_\alpha^\dagger\left(\mathrm{s}_\theta\mathrm{c}_\phi+\mathrm{s}_\theta\mathrm{s}_\phi+\mathrm{c}_\theta\right)+h.c. \\ H_3[\mathcal{O}(S)] &= \frac{S}{48}\sum_{\alpha\beta}\left\{\left[R^2b_\alpha^\dagger b_\beta^\dagger+h.c.\right]+R\overline{R}\left[b_\alpha^\dagger b_\beta+b_\alpha b_\beta^\dagger\right]\right\} \end{aligned}$$

$$
\begin{aligned}
& -\frac{S}{3}\sum_\alpha b_\alpha^\dagger b_\alpha \left(\mathrm{s}_\theta \mathrm{c}_\phi + \mathrm{s}_\theta \mathrm{s}_\phi + \mathrm{c}_\theta\right) \\
= \; & \frac{S}{48}\left\{\left[R^2\sum_\alpha b_\alpha^\dagger b_\alpha^\dagger + 2R^2\left(b_0^\dagger b_1^\dagger + b_0^\dagger b_2^\dagger + b_0^\dagger b_3^\dagger + b_1^\dagger b_2^\dagger + b_1^\dagger b_3^\dagger + b_2^\dagger b_3^\dagger\right) + h.c.\right]\right. \\
& \left. + R\overline{R}\sum_\alpha\left[b_\alpha^\dagger b_\alpha + b_\alpha b_\alpha^\dagger\right] + 2R\overline{R}\left[b_0^\dagger b_1 + b_0^\dagger b_2 + b_0^\dagger b_3 + b_1^\dagger b_2 + b_1^\dagger b_3 + b_2^\dagger b_3 + h.c.\right]\right\} \\
& -\frac{S}{3}\sum_\alpha b_\alpha^\dagger b_\alpha \left(\mathrm{s}_\theta \mathrm{c}_\phi + \mathrm{s}_\theta \mathrm{s}_\phi + \mathrm{c}_\theta\right)
\end{aligned}
\tag{5.111}
$$

$$
\begin{aligned}
(H_0 - H_3)[\mathcal{O}(S^2)] &= 0 \\
(H_0 - H_3)[\mathcal{O}(S^{3/2})] &= 0 \\
(H_0 - H_3)[\mathcal{O}(S)] &= \frac{S}{16}\left\{\left[\sum_\alpha R^2 b_\alpha^\dagger b_\alpha^\dagger - \frac{2}{3}R^2\left(b_0^\dagger b_1^\dagger + b_0^\dagger b_2^\dagger + b_0^\dagger b_3^\dagger + b_1^\dagger b_2^\dagger + b_1^\dagger b_3^\dagger + b_2^\dagger b_3^\dagger\right) + h.c.\right]\right. \\
& \quad -\frac{2}{3}R\overline{R}\left[b_0^\dagger b_1 + b_0^\dagger b_2 + b_0^\dagger b_3 + b_1^\dagger b_2 + b_1^\dagger b_3 + b_2^\dagger b_3 + h.c.\right] \\
& \quad \left. + R\overline{R}\sum_\alpha\left(b_\alpha^\dagger b_\alpha + b_\alpha b_\alpha^\dagger\right)\right\}.
\end{aligned}
\tag{5.112}
$$

Finally we consider $H_4 = \frac{1}{2}\hat{\mathbf{A}}\cdot\hat{\mathbf{A}}$, for which we use

$$
\begin{aligned}
A^x &= \sqrt{\frac{S}{2}}\left(X\sum_\alpha b_\alpha^\dagger + h.c.\right) + \mathrm{s}_\theta\mathrm{c}_\phi\left(4S - \sum_\alpha b_\alpha^\dagger b_\alpha\right), \\
A^y &= \sqrt{\frac{S}{2}}\left(Y\sum_\alpha b_\alpha^\dagger + h.c.\right) + \mathrm{s}_\theta\mathrm{s}_\phi\left(4S - \sum_\alpha b_\alpha^\dagger b_\alpha\right), \\
A^z &= \sqrt{\frac{S}{2}}\left(Z\sum_\alpha b_\alpha^\dagger + h.c.\right) + \mathrm{c}_\theta\left(4S - \sum_\alpha b_\alpha^\dagger b_\alpha\right).
\end{aligned}
\tag{5.113}
$$

Therefore, we find that

$$
\begin{aligned}
H_4[\mathcal{O}(S^2)] &= 8S^2 \\
H_4[\mathcal{O}(S^{3/2})] &= 2S\sqrt{\frac{S}{2}}\left(X\mathrm{s}_\theta\mathrm{c}_\phi + Y\mathrm{s}_\theta\mathrm{s}_\phi + Z\mathrm{c}_\theta\right)\sum_\alpha b_\alpha^\dagger + h.c.
\end{aligned}
$$

$$
\begin{aligned}
&= 0 \\
H_4[\mathcal{O}(S)] &= \frac{S}{4}\left\{\sum_{\alpha\beta}\left[(X^2+Y^2+Z^2)b_\alpha^\dagger b_\beta^\dagger + h.c.\right] + (X\overline{X}+Y\overline{Y}+Z\overline{Z})\sum_{\alpha\beta}\left[b_\alpha^\dagger b_\beta + b_\alpha b_\beta^\dagger\right]\right\} \\
&\quad -4S\left[\mathrm{s}_\theta^2\mathrm{c}_\phi^2 + \mathrm{s}_\theta^2\mathrm{s}_\phi^2 + \mathrm{c}_\theta^2\right]\sum_\alpha b_\alpha^\dagger b_\alpha \\
&= \frac{S}{2}\sum_{\alpha\beta}\left[b_\alpha^\dagger b_\beta + b_\alpha b_\beta^\dagger\right] - 4S\sum_\alpha b_\alpha^\dagger b_\alpha \\
&= \frac{S}{2}\left\{\sum_\alpha (b_\alpha^\dagger b_\alpha + b_\alpha b_\alpha^\dagger) + 2\left(b_0^\dagger b_1 + b_0^\dagger b_2 + b_0^\dagger b_3 + b_1^\dagger b_2 + b_1^\dagger b_3 + b_2^\dagger b_3 + h.c.\right)\right\} \\
&\quad -4S\sum_\alpha b_\alpha^\dagger b_\alpha. \qquad (5.114)
\end{aligned}
$$

5.6.1 Bloch transforming the Hamiltonian

In this section we make use of the periodicity of the lattice by Bloch transforming the Hamiltonian. This Hamiltonian for the full system is given by

$$H = J_0\sum_t \left[H_1 - \delta H_4 - \eta H_0 + \xi(H_0 - H_3) - \mu H_2\right], \qquad (5.115)$$

where we have summed over the tetrahedra ('t'). We find that there are two kinds of terms that we have to consider. Firstly there are the local terms: $b_\alpha^\dagger b_\alpha^\dagger$, $b_\alpha b_\alpha$, $b_\alpha^\dagger b_\alpha$ and $b_\alpha b_\alpha^\dagger$. Secondly we have the non-local terms: $\alpha \neq \beta$: $b_\alpha^\dagger b_\beta^\dagger$, $b_\alpha b_\beta$, $b_\alpha^\dagger b_\beta$ and $b_\alpha b_\beta^\dagger$. We begin by converting the sum over tetrahedra into a sum over lattice sites. For non-local terms this gives

$$\sum_t b_\alpha^\dagger b_\beta = \sum_{\mathbf{R}_j}\left[b_\alpha^\dagger\left(\mathbf{R}_j + \mathbf{c}_\alpha\right) b_\beta\left(\mathbf{R}_j + \mathbf{c}_\beta\right) + b_\alpha^\dagger\left(\mathbf{R}_j - \mathbf{c}_\alpha\right) b_\beta^\dagger\left(\mathbf{R}_j - \mathbf{c}_\beta\right)\right], \qquad (5.116)$$

which is a sum over nearest neighbour bonds (along with equivalent expressions for the other three terms). As each Gd^{3+} ion is in two tetrahedra, for the local terms we find:

$$\sum_t b_\alpha^\dagger b_\alpha = \sum_{\mathbf{R}_j} 2b_\alpha^\dagger\left(\mathbf{R}_j + \mathbf{c}_\alpha\right) b_\alpha\left(\mathbf{R}_j + \mathbf{c}_\alpha\right), \qquad (5.117)$$

as each atom is in two tetrahedra.

To Block transform Hamiltonians use:

$$b_\alpha\left(\mathbf{R}_j+\mathbf{c}_\alpha\right)=\frac{1}{\sqrt{N_\alpha}}\sum_{\mathbf{k}}\mathbf{b}_{\alpha,\mathbf{k}}e^{i\mathbf{k}\cdot\left(\mathbf{R}_j+\mathbf{c}_\alpha\right)}, \tag{5.118}$$

$$b_{\alpha,\mathbf{k}}=\frac{1}{\sqrt{N_\alpha}}\sum_{\mathbf{R}_j}b_\alpha\left(\mathbf{R}_j+\mathbf{c}_\alpha\right)e^{-i\mathbf{k}\cdot\left(\mathbf{R}_j+\mathbf{c}_\alpha\right)}, \tag{5.119}$$

$$\frac{1}{N_\alpha}\sum_{\mathbf{R}_j}e^{i(\mathbf{k}-\mathbf{k}')\cdot\mathbf{R}_j}=\delta_{\mathbf{k},\mathbf{k}'}, \tag{5.120}$$

where $\mathbf{R}_j$ and $\mathbf{c}_\alpha$ are defined in Section 5.3 (with the rescaling that $a=4$ for simplicity), and we will use $\mathbf{c}_\alpha-\mathbf{c}_\beta=\mathbf{c}_{\alpha\beta}$. N_α is the number of atoms on one sub-lattice. The terms transform as:

$$\begin{aligned}\sum_t b_\alpha^\dagger b_\alpha^\dagger &= 2\sum_{\mathbf{R}_j}b_\alpha^\dagger\left(\mathbf{R}_j+\mathbf{c}_\alpha\right)b_\alpha^\dagger\left(\mathbf{R}_j+\mathbf{c}_\alpha\right)\\ &= \frac{2}{N_\alpha}\sum_{\mathbf{R}_j}\sum_{\mathbf{k}\mathbf{k}'}b_{\alpha,\mathbf{k}}^\dagger b_{\alpha,\mathbf{k}'}^\dagger e^{-i(\mathbf{k}+\mathbf{k}')\cdot\left(\mathbf{R}_j+\mathbf{c}_\alpha\right)}\\ &= 2\sum_{\mathbf{k}\mathbf{k}'}b_{\alpha,\mathbf{k}}^\dagger b_{\alpha,\mathbf{k}'}^\dagger\delta_{\mathbf{k},-\mathbf{k}'}e^{-i(\mathbf{k}+\mathbf{k}')\cdot\mathbf{c}_\alpha}\\ &= 2\sum_{\mathbf{k}}b_{\alpha,\mathbf{k}}^\dagger b_{\alpha,-\mathbf{k}}^\dagger\end{aligned} \tag{5.121}$$

$$\begin{aligned}\sum_t b_\alpha^\dagger b_\alpha &= 2\sum_{\mathbf{R}_j}b_\alpha^\dagger\left(\mathbf{R}_j+\mathbf{c}_\alpha\right)b_\alpha\left(\mathbf{R}_j+\mathbf{c}_\alpha\right)\\ &= \frac{2}{N_\alpha}\sum_{\mathbf{R}_j}\sum_{\mathbf{k},\mathbf{k}'}b_{\alpha,\mathbf{k}}^\dagger b_{\alpha,\mathbf{k}'}e^{-i(\mathbf{k}-\mathbf{k}')\cdot\left(\mathbf{R}_j+\mathbf{c}_\alpha\right)}\\ &= 2\sum_{\mathbf{k}\mathbf{k}'}b_{\alpha,\mathbf{k}}^\dagger b_{\alpha,\mathbf{k}'}\delta_{\mathbf{k},\mathbf{k}'}e^{-i(\mathbf{k}-\mathbf{k}_\prime)\cdot\mathbf{c}_\alpha}\\ &= 2\sum_{\mathbf{k}}b_{\alpha,\mathbf{k}}^\dagger b_{\alpha,\mathbf{k}}\end{aligned} \tag{5.122}$$

For $\alpha \neq \beta$

$$\begin{aligned}
\sum_t b_\alpha^\dagger b_\beta &= \sum_{\mathbf{R}_j} \left[b_\alpha^\dagger \left(\mathbf{R}_j + \mathbf{c}_\alpha \right) b_\beta \left(\mathbf{R}_j + \mathbf{c}_\beta \right) + b_\alpha^\dagger \left(\mathbf{R}_j - \mathbf{c}_\alpha \right) b_\beta \left(\mathbf{R}_j - \mathbf{c}_\beta \right) \right] \\
&= \frac{1}{N_\alpha} \sum_{\mathbf{R}_j} \sum_{\mathbf{k}\mathbf{k}'} \left[b_{\alpha,\mathbf{k}}^\dagger b_{\beta,\mathbf{k}'} e^{-i(\mathbf{k}-\mathbf{k}')\cdot\mathbf{R}_j} e^{-i\mathbf{k}\cdot\mathbf{c}_\alpha} e^{i\mathbf{k}'\cdot\mathbf{c}_\beta} + b_{\alpha,\mathbf{k}}^\dagger b_{\beta,\mathbf{k}'} e^{-i(\mathbf{k}-\mathbf{k}')\cdot\mathbf{R}_j} e^{i\mathbf{k}\cdot\mathbf{c}_\alpha} e^{-i\mathbf{k}'\cdot\mathbf{c}_\beta} \right] \\
&= \sum_{\mathbf{k}} b_{\alpha,\mathbf{k}}^\dagger b_{\beta,\mathbf{k}} \left[e^{i\mathbf{k}\cdot\left(\mathbf{c}_\alpha - \mathbf{c}_\beta\right)} + e^{-i\mathbf{k}\cdot\left(\mathbf{c}_\alpha - \mathbf{c}_\beta\right)} \right] \\
&= 2 \sum_{\mathbf{k}} b_{\alpha,\mathbf{k}}^\dagger b_{\beta,\mathbf{k}} \cos\left(\mathbf{k} \cdot \mathbf{c}_{\alpha\beta} \right) \qquad (5.123)
\end{aligned}$$

Similarly we find that:

$$\sum_t b_\alpha b_\alpha = \sum_{\mathbf{k}} b_{\alpha,-\mathbf{k}} b_{\alpha,\mathbf{k}} \qquad (5.124)$$

$$\sum_t b_\alpha b_\alpha^\dagger = 2 \sum_{\mathbf{k}} b_{\alpha,\mathbf{k}} b_{\alpha,\mathbf{k}}^\dagger \qquad (5.125)$$

$$\sum_t b_\alpha b_\beta^\dagger = 2 \sum_{\mathbf{k}} b_{\alpha,\mathbf{k}} b_{\alpha,\mathbf{k}}^\dagger \cos\left(\mathbf{k} \cdot \mathbf{c}_{\alpha\beta} \right) \qquad (5.126)$$

$$\sum_t b_\alpha^\dagger b_\beta^\dagger = 2 \sum_{\mathbf{k}} b_{\alpha,\mathbf{k}}^\dagger b_{\beta,-\mathbf{k}}^\dagger \cos\left(\mathbf{k} \cdot \mathbf{c}_{\alpha\beta} \right) \qquad (5.127)$$

$$\sum_t b_\alpha b_\beta = 2 \sum_{\mathbf{k}} b_{\alpha,-\mathbf{k}} b_{\beta,\mathbf{k}} \cos\left(\mathbf{k} \cdot \mathbf{c}_{\alpha\beta} \right) \qquad (5.128)$$

We define $\mathbf{b}_{\alpha,\mathbf{k}}^\dagger = \left[b_{0,\mathbf{k}}^\dagger,\ b_{1,\mathbf{k}}^\dagger,\ b_{2,\mathbf{k}}^\dagger,\ b_{3,\mathbf{k}}^\dagger \right]$ and write the Hamiltonians in matrix form:

$$H = J_0 \sum_{\mathbf{k}>0} \left\{ 4E_{Cl} + E_{Com} + \begin{bmatrix} \mathbf{b}_{\alpha,\mathbf{k}}^\dagger & \mathbf{b}_{\alpha,-\mathbf{k}} \end{bmatrix} \begin{bmatrix} \mathbf{A}\left(\mathbf{k}\right) & \mathbf{B}\left(\mathbf{k}\right) \\ \overline{\mathbf{B}}\left(\mathbf{k}\right) & \mathbf{A}\left(\mathbf{k}\right) \end{bmatrix} \begin{bmatrix} \mathbf{b}_{\alpha,\mathbf{k}} \\ \mathbf{b}_{\alpha,-\mathbf{k}}^\dagger \end{bmatrix} \right\}, \qquad (5.129)$$

where $\mathbf{A}\left(\mathbf{k}\right)$ and $\mathbf{B}\left(\mathbf{k}\right)$ are 4×4 matrices, which we will specify for each Hamiltonian below. E_{Com} is a constant term arising from reordering ordering the operators appropriately, E_{Cl} is the classical ground-state energy for a single tetrahedron and we have used $\sum_t = 4 \sum_{\mathbf{k}>0}$.

The matrix $\mathbf{A}(\mathbf{k})$ takes the form:

$$\mathbf{A}(\mathbf{k}) = \begin{bmatrix} f_x + f_y + f_z & -f_x C_{y+z} & -f_y C_{z+x} & -f_z C_{x+y} \\ -f_x C_{y+z} & f_x + f_y + f_z & -f_z C_{x-y} & -f_y C_{z-x} \\ -f_y C_{z+x} & -f_z C_{x-y} & f_x + f_y + f_z & -f_x C_{y-z} \\ -f_z C_{x+y} & -f_y C_{z-x} & -f_x C_{y-z} & f_x + f_y + f_z \end{bmatrix} \tag{5.130}$$

and similarly $\mathbf{B}(\mathbf{k})$ can be expressed as:

$$\mathbf{B}(\mathbf{k}) = \begin{bmatrix} g_x + g_y + g_z & -g_x C_{y+z} & -g_y C_{z+x} & -g_z C_{x+y} \\ -g_x C_{y+z} & g_x + g_y + g_z & -g_z C_{x-y} & -g_y C_{z-x} \\ -g_y C_{z+x} & -g_z C_{x-y} & g_x + g_y + g_z & -g_x C_{y-z} \\ -g_z C_{x+y} & -g_y C_{z-x} & -g_x C_{y-z} & g_x + g_y + g_z \end{bmatrix}, \tag{5.131}$$

where value of the parameters: $\{f_x, f_y, f_z\}$ and $\{g_x, g_y, g_z\}$ depends on the Hamiltonian being considered and $C_{\alpha\pm\beta} = \cos(k_\alpha \pm k_\beta)$ where we have set $a = 4$ to simplify the notation. For H_1 we find the parameters:

$$\begin{aligned} f1_x = 2S(1 - X\overline{X}), \qquad f1_y = 2S(1 - Y\overline{Y}) \qquad f1_z = 2S(1 - Z\overline{Z}) \\ g1_x = -2SX^2, \qquad g1_y = -2SY^2, \qquad g1_z = -2SZ^2, \end{aligned} \tag{5.132}$$

and also $E_{Cl} = E_{Com} = 0$.

H_2 has:

$$\begin{aligned} f2_x &= \frac{4}{3}S\left(1 + \frac{Y\overline{Z} + Z\overline{X}}{2} - X\overline{Y}\right), \\ f2_y &= \frac{4}{3}S\left(1 + \frac{Z\overline{X} + X\overline{Y}}{2} - Y\overline{Z}\right), \\ f2_z &= \frac{4}{3}S\left(1 + \frac{X\overline{Y} + Y\overline{Z}}{2} - Z\overline{X}\right), \\ g2_x = \frac{4}{3}SYZ, \qquad g2_y = \frac{4}{3}SZX, \qquad g2_z &= \frac{4}{3}SXY, \end{aligned} \tag{5.133}$$

and $E_{Cl} = E_{Com} = 0$. $(H_0 - H_3)$ has:

$$f3_x = f3_y = f3_z = \frac{S}{12}R\overline{R}, \qquad g3_x = g3_y = g3_z = \frac{S}{12}R^2, \tag{5.134}$$

and $E_{Cl} = E_{Com} = 0$. H_4 has:

$$f4_x = f4_y = f4_z = -2S. \qquad g4_x = g4_y = g4_z = 0, \tag{5.135}$$

$E_{Cl} = 8S^2$ and $E_{Com} = 32S$. For H_0, however, we use the classical ground-state with $\hat{\mathbf{z}} \cdot \hat{\mathbf{s}}_\alpha = 1$ ($\mathrm{s}_\theta = \sqrt{2/3}$, $\mathrm{c}_\theta = 1/\sqrt{3}$ and $\mathrm{s}_\phi = \mathrm{c}_\phi = 1/\sqrt{2}$), which gives:

$$H_0 = \sum_{\mathbf{k}>0} \left\{ 8S^2 - \frac{2}{\sqrt{3}} S\mathcal{I} + \frac{8}{\sqrt{3}} S \right\}, \tag{5.136}$$

where $\mathcal{I}$ represents the identity matrix.

The next step is to diagonalise the Hamiltonians. To do this we are required to use a Bogoliubov transform as we discuss in the next section.

5.6.2 Bogoliubov Transforms

To calculate the quantum fluctuation energy and spin-wave spectrum we need to express the Hamiltonian in a diagonal representation. We must, however, ensure that the commutation relations of the operators are preserved. If we define

$$\mathbf{X}^\dagger = \begin{bmatrix} \mathbf{b}^\dagger_{\alpha,\mathbf{k}} & \mathbf{b}_{\alpha,-\mathbf{k}} \end{bmatrix}, \tag{5.137}$$

then the commutation relations take the form

$$\left[X_\alpha, X^\dagger_\beta \right] = L_{\alpha\beta}, \tag{5.138}$$

where

$$\mathbf{L} = \begin{bmatrix} \mathcal{I} & 0 \\ 0 & -\mathcal{I} \end{bmatrix}, \tag{5.139}$$

which describes Bogoliubov transformation. As a result we need to solve the generalised eigenvalue problem:

$$\mathbf{H} \cdot \mathbf{u} = \epsilon \mathbf{L} \cdot \mathbf{u}, \tag{5.140}$$

where the eigenvectors, $\mathbf{u}$, are subject to the normalisation condition

$$\mathbf{u}_i^\dagger \cdot \mathbf{L} \cdot \mathbf{u}_j = L_{ij}. \tag{5.141}$$

In other words we need to solve the characteristic equation given by

$$|\mathbf{H} - \epsilon \mathbf{L}| = \left| \tilde{\mathbf{H}} - \epsilon \mathbf{L} \right| = 0, \tag{5.142}$$

where we have defined

$$\tilde{\mathbf{H}} = \mathbf{U}^\dagger \cdot \mathbf{H} \cdot \mathbf{U}. \tag{5.143}$$

We can express $\tilde{\mathbf{H}}$ in terms of the eigenvectors and corresponding eigenvalues as

$$\tilde{H}_{\alpha\beta} = \delta_{\alpha\beta} \epsilon_\alpha \mathbf{u}_\alpha^\dagger \cdot \mathbf{L} \cdot \mathbf{u}_\beta. \tag{5.144}$$

Using this transformation, the Hamiltonian then takes the following form (where we will temporally supress the terms E_{Cl} and E_{Com})

$$\begin{aligned} H &= J_0 \sum_{\mathbf{k}>0} \mathbf{X}^\dagger \cdot \mathbf{H} \cdot \mathbf{X} = J_0 \sum_{\mathbf{k}>0} \tilde{\mathbf{X}}^\dagger \cdot \tilde{\mathbf{H}} \cdot \tilde{\mathbf{X}} \\ &= J_0 \sum_{\mathbf{k}>0} \sum_\alpha \tilde{X}^*_{\mathbf{k},\alpha} \mathbf{u}_\alpha^\dagger \cdot \mathbf{L} \cdot \mathbf{u}_\alpha \epsilon_\alpha \tilde{X}_{\mathbf{k},\alpha} \\ &= J_0 \sum_{\mathbf{k}>0} \sum_\alpha \left[\tilde{b}^\dagger_{\alpha,\mathbf{k}} \tilde{b}_{\alpha,\mathbf{k}} \mathbf{u}_\alpha^\dagger \cdot \mathbf{L} \cdot \mathbf{u}_\alpha \epsilon_\alpha + b_{\alpha,-\mathbf{k}} \tilde{b}^\dagger_{\alpha,-\mathbf{k}} \mathbf{u}_\alpha^\dagger \cdot \mathbf{L} \cdot \mathbf{u}_\alpha \epsilon_\alpha \right]. \end{aligned} \tag{5.145}$$

As it turns out that the eigenvalues always occur in pairs of $\pm\epsilon$, then we can define

$$\omega_\alpha(\mathbf{k}) = \mathbf{u}_\alpha^\dagger \cdot \mathbf{L} \cdot \mathbf{u}_\alpha > 0 \qquad \forall \quad \omega_\alpha(\mathbf{k}). \tag{5.146}$$

Finally, we reinstate the terms E_{Cl} and E_{Com} which we had suppressed earlier to get

$$H = J_0 \sum_{\mathbf{k}} \left[\frac{1}{2} \sum_\alpha \omega_\alpha(\mathbf{k}) + \sum_\alpha \tilde{b}_{\alpha,\mathbf{k}}^\dagger \tilde{b}_{\alpha,\mathbf{k}} \omega_\alpha(\mathbf{k}) + 2E_{Cl} + \frac{1}{2} E_{Com} \right], \tag{5.147}$$

where the spin-wave dispersion spectrum has four branches described by the '$\omega_\alpha(\mathbf{k})$'. The quantum fluctuation energy is given by

$$Q = J_0 \frac{1}{2} \sum_{\mathbf{k}} \left[E_{Com} + \sum_\alpha \omega_\alpha(\mathbf{k}) \right]. \tag{5.148}$$

In order to find the spin-wave spectrum and quantum fluctuation energy we need to calculate $\epsilon(\mathbf{k})$ from

$$|\mathbf{H} - \epsilon\mathbf{L}| = \begin{vmatrix} \mathbf{A} - \epsilon\mathcal{I} & \mathbf{B} \\ \overline{\mathbf{B}} & \mathbf{A} + \epsilon\mathcal{I} \end{vmatrix} = 0, \tag{5.149}$$

where the matrices $\mathbf{A}$ and $\mathbf{B}$ were defined in Equation 5.129. We note, however, that

$$|\mathbf{H} - \epsilon\mathbf{L}| = |(\mathbf{H} - \epsilon\mathbf{L})\mathbf{L}| = \begin{vmatrix} \mathbf{A} - \epsilon\mathcal{I} & -\mathbf{B} \\ \overline{\mathbf{B}} & -\mathbf{A} - \epsilon\mathcal{I} \end{vmatrix}, \tag{5.150}$$

allowing us to just find the eigenvalues of the matrix

$$\begin{bmatrix} \mathbf{A} & -\mathbf{B} \\ \overline{\mathbf{B}} & -\mathbf{A} \end{bmatrix}, \tag{5.151}$$

in the usual way. This allows us to use the standard numerical NAG Fortran routines to both calculate the eigenvalues and (taking the limit that $N \mapsto \infty$) integrate the $\omega_\alpha(\mathbf{k})$ over $\mathbf{k}$ to find the quantum fluctuation energy.

5.6.3 Calculated spin-wave dispersion relations

In this section we will discuss the spin-wave dispersion relations and the quantum fluctuation energies that we calculated for our phenomenological model using the method described in the previous sections. We will attempt to find the minimal model based upon the previously discussed Hamiltonians which can qualitatively reproduce the general features of the system. In particular we wish to find a model with the potential to stabalise spins which are orientated along crystallographically insignificant directions and which has a a gapless spin-wave mode.

We begin by considering the simplified model, in which H_1 dominates, given by $H = J_0 \sum_t (H_1 - \delta H_4)$, where the parameter, δ, satisfies $1 \gg \delta > 0$. The corresponding spin-wave spectrum for $\delta = 1 \times 10^{-4}$ is shown in Fig. 5.11. We have used our experimentally

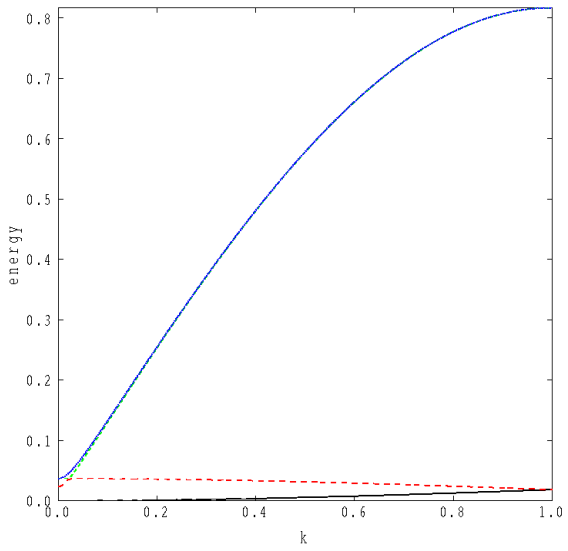

Figure 5.11: The four spin-wave branches calculated for $\delta = 1 \times 10^{-4}$, plotted for wave-vectors parallel to one of the Cartesian axes. We have used our experimentally proposed classical ground-state of $\theta \approx 0.2\pi = \Theta$ and $\phi = \pi/4$ and plotted the energy in units of $2J_0S$.

proposed classical ground-state to specify the values of $\theta \approx 0.2\pi = \Theta$ and $\phi = \pi/4$ (as defined in Fig. 5.5) plotted the dispersion relation parallel to one of the Cartesian axes. Two approximately dispersionless bands can be seen at an energy scale of about $2JS\sqrt{\delta}$. In addition there are two strongly dispersive bands. We note that for this case it is one

of the approximately flat bands which control the degeneracy of the Hamiltonian. This produces a band which tends to zero quadratically (as the classical ground-state of H_1 contains tow degrees of freedom (described by θ and ϕ). As Fig. 5.11 does not match the experimentally observed spectrum shown previously Fig. 5.9.

Next we consider the same Hamiltonian as previously, but with a larger value of δ. For the example of $\delta = 0.2$, this produces the dispersion relation shown in Fig. 5.12. This time we see that there is one very weakly dispersing mode and two with a moderate

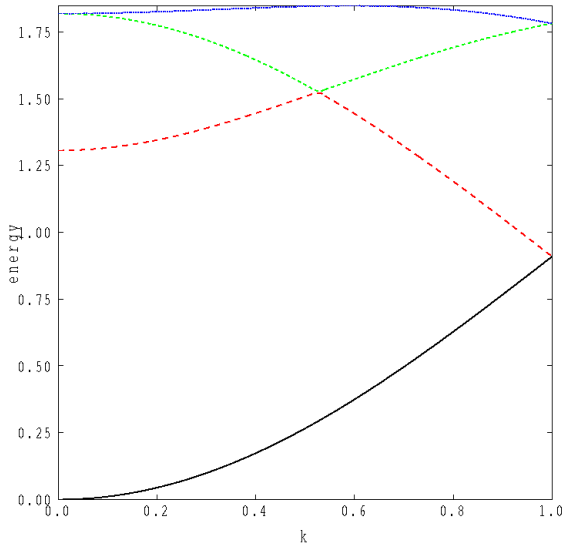

Figure 5.12: The four spin-wave branches calculated for $\delta = 0.2$ and plotted for wave-vectors parallel to one of the Cartesian axes. We have used $\theta = \Theta$ and $\phi = \pi/4$ and plotted the energy in units of $2J_0S$.

dispersion. These three bands have become the high energy excitations (at an energy of around $3JS$). Instead, the gapless mode is now strongly dispersive. Qualitatively, this picture is very similar to that seen in Fig. 5.9.

As the classical ground-state for the Hamiltonian $H = J_0 \sum_t (H_1 - \delta H_4)$ is degenerate for all angles θ and ϕ, the next step is to consider how this degeneracy is lifted by the quantum fluctuations. In Fig. 5.13 we plot the quantum fluctuation energy per spin as a function of theta for $\delta = 0.2$.

This is represented by the black curve (we will return to discuss the other two curves in this figure a little later). We have assumed the experimentally observed value of $\phi = \pi/4$,

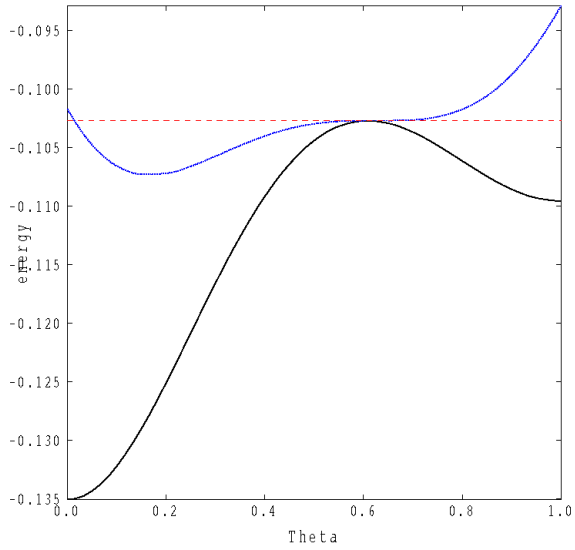

Figure 5.13: Black curve: the quantum fluctuation energy for the case $\delta = 0.2$, plotted as function of θ in units of $\pi/2$ and with $\phi = \pi/4$. Blue curve: Produced by including both the quantum fluctuation energy and a classical contribution arising from the term in η (for $1 \ll \eta > 0$). Red curve: The value of θ which minimises the blue curve jumps discontinuously when the minimum of the blue curve reaches this line.

which would be stabilised by including a term in the Hamiltonian which produces a weak locally hexagonally-symmetric crystal-field potential to lift the azimuthal symmetry around the local tetrahedral axes (arising from the presence of the O2 ions in Fig. 5.2). We will return to discuss the other two curves in this figure a little later. As expected we find that the quantum fluctuation energy is minimum for $\theta = 0$, which is equivalent to a colinear single-**q** spin state (in which the spins are aligned along one of the Cartesian axes). This is not however consistent with the elastic neutron scattering data by Cao *et. al*[14] and Ruff *et. al*[66]. We must therefore consider a more complex model.

We next try incorporating a term proportional to H_0 in the Hamiltonian. As discussed previously, the classical ground-state for this Hamiltonian: $H = J_0 \sum_t (H_1 - \delta H_4 - \eta H_0)$, is the triple-**q** state with all the spins pointing along the local crystallographic axes into the centre of the tetrahedron. The classical-ground state is no longer degenerate and has all the spins pointing along crystallographically symmetrical directions. As expected, we therefore find that, even for an infinitesimally small value of η, the spin-wave spectrum becomes gapped. In Fig. 5.14 we plot this for the case of $\delta = \eta = 0.2$. Qualitatively

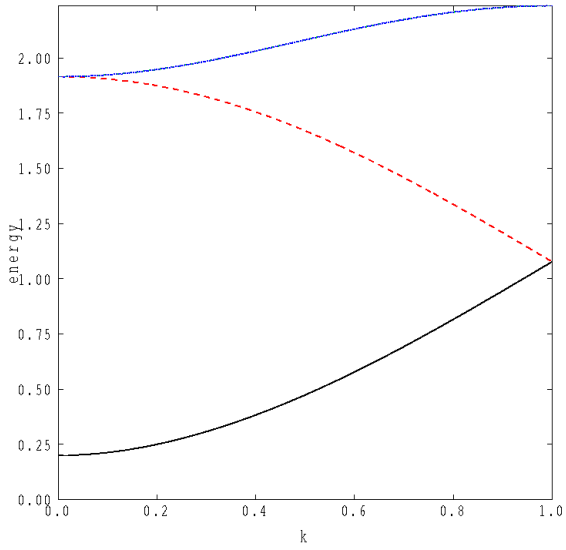

Figure 5.14: The four spin-wave branches when $\delta = \eta = 0.2$ for the cubic triple-**q** state ($\theta = \Theta$ and $\phi = \pi/4$). The energy is plotted in units of $2J_0S$ for wave-vectors parallel to one of the Cartesian axes.

the spectrum looks like that for $\eta = 0$, except that there is a spin-wave gap of an energy $\delta \sim \eta$. This picture therefore is still not consistent with the experimental observations.

The final part of our argument is a little crude. We note that our model describes a pseudo-spin half. This means that the quantum fluctuation energy is actually of the same order as the classical energy. We therefore suggest that it is possible that the quantum fluctuation energy of $H_1 - \delta H_4$, promoting the single-**q** colinear state, could be in competition with a classical contribution from H_0 which stabilises the cubic triple-**q** state. These two contributions to the energy could then happen to be balanced in such a way as to stabilise the intermediate value of θ which we proposed earlier on experimental grounds as a compromise solution. We illustrate this idea using the example shown in Fig. 5.13. As discussed earlier, the black curve represents the quantum fluctuation energy for $\delta = 0.2$. We can then also add a carefully scaled classical contribution from the term in H_0 by using a small non-zero value of η to produce the blue curve. We see that the minimum energy spin state now occurs when the angle θ has no particular crystallographic significance. With this model we can tune the position of the minimum over a finite range of θ, depending on the particular balance between the two contributions to the energy.

Unfortunately the energetics of the above model are not completely stable. When the minimum value of θ approaches the cubic triple-**q** state (and the minimum of the blue curve becomes level with the red line in Fig. 5.13) it actually jumps discontinuously to this value. We do not discuss this point in any detail, however, as our model is too crude to provide any prediction of the experimentally observed value of θ. Firstly we note that any value of θ calculated from the model describes the angle of the pseudo-spin. To relate this to the orientation of the observed moment is subtle because the effective g-factors depend on the crystal-field state of the ground-state Kramer's doublet, which we have not attempted to calculate. Furthermore, as our model Hamiltonian was only obtained on phenomenological grounds, experimentally realistic values of the coefficients of the various terms are unknown. Finally we note that our use of a semi-classical spin-wave analysis to model a pseudo-spin half is dubious anyway, although we have no way to tackle the fully quantum problem.

To summarise, we offer the following qualitative argument to suggest a possible method of stabilising the magnetically ordered state that we proposed on experimental grounds. The quantum fluctuation energy of $H_1 + \delta H_4$ stabilises a single-**q** colinear spin-state, while the classical energy of H_0 favours the cubic symmetric triple-**q** state. A competition between these two energy contributions could give rise to a value θ which does not describe a crystallographically symmetrical direction. This is an indication that the effective crystal-field interaction (which in turn gives rise to a spin anisotropy) is frustrated and therefore expected to result in a gapless spin-wave mode (see Section 5.5).

CHAPTER 6

CONCLUSIONS

This thesis focuses on investigating the low temperature magnetic ordering of rare-earth pyrochlores. In these materials the rare-earth magnetic ion forms a pyrochlore lattice. We concentrated on three compounds: $Gd_2Sn_2O_7$, $Gd_2Ti_2O_7$ and $Er_2Ti_2O_7$. The first two compounds are isotropic, whereas in the final one the crystal-field interaction plays a crucial role.

In the first chapter we focused on $Gd_2Sn_2O_7$. Its behavior is governed by the dipole interaction in the presence of a dominant Heisenberg exchange. We began by reviewing the existing (mainly theoretical) studies of this problem and found that despite some initial confusion in the literature, the global minimum of the dipolar interaction matrix has a periodicity of $\mathbf{k} = (1/2, 1/2, 1/2)$, but does not satisfy the classic equal-length spin constraints and therefore is not a physical solution to the classical problem. The actual minimum is believed to the $\mathbf{k} = \mathbf{0}$ states observed in $Gd_2Sn_2O_7$.

We then move on to investigate the behaviour of this model in the presence of an external field. We discover that for two types of special highly symmetrical field direction it is possible to find exact solutions to the long-range dipole interaction problem by expressing the Hamiltonian as a sum over quadratic terms, the arguments of these quadratics providing natural variables for the problem. For the special field directions we can make all ten of these quadratics vanish (despite the fact that the problem is actually over-constrained), and the solutions are therefor not sensitive to the relative strength of

the dipole and exchange energies. Finally we consider our exact solutions and discuss how the spins distort as a function of field (within the subspace that the solution is valid) and look for possible phase transition.

Additionally, expressing the Hamiltonian using the ten quadratic terms is also physically instructive. Four of the ten terms provide an effective local crystal-field interaction which explains the Mössbauer observation that the spins lie in planes perpendicular to the local crystallographic axis. The 'ten quadratics' representation also highlights a direct link between minimising the dipole interaction and maximising the intensity of the first shell of Bragg spots (closest to the origin) for elastic neutron scattering. (This can also be seen through the reciprocal-space sub-band representation of the problem).

In the following two chapters we discuss the magnetic ordering of $Gd_2Ti_2O_7$. Superficially one would expect this material to show the same behaviour as $Gd_2Sn_2O_7$, however the ground-state actually has $\mathbf{k} = (1/2, 1/2, 1/2)$. We conclude that this is because further neighbour exchange interactions (whose pathway is via the transition metal ion) are active for $Gd_2Ti_2O_7$, but not in $Gd_2Sn_2O_7$. The further neighbour exchange interactions destabilise the dipolar ground-state in favour of $\mathbf{k} = (1/2, 1/2, 1/2)$ ordering.

One of our original motivations for studying gadolinium titanate was that the Mössbauer and elastic neutron scattering data describing the magnetic ordering are presented with contradictory interpretations in the literature, which we attempt to resolve. We decided against using the standard of approach of minimising a model Hamiltonian to find the ground-state. This is because we believe that the energetics are governed by a number of competing interactions, and without prior knowledge of their relevant strengths we have know way to judge whether our model is representative of the material in question. For this reason we instead use the rather unusual approach of using the experimental evidence to motivate enforcing four constraints on the spin-orientations of the system. This removes enough of the degrees of freedom to allow us to tackle the problem. In the first of the two chapters on this subject, we first enforce the three constraints: equal-length spins; vanishing total spin on each tetrahedron and spins confined to the observed

Mössbauer planes. We then also demand that the solutions are also compatible with $\mathbf{k} = (1/2, 1/2, 1/2)$ ordering. This reduces the degeneracy of the problem to such an extent that there are only two (unrelated by symmetry) solutions to our model. Both these state have an unusual structure. Every fourth plane behaves like a domain wall between different regions formed of tetrahedra in the dipolar ground-state spirals. These two states however show an extremely poor fit to the neutron scattering intensities, an issue that we address in the next chapter.

In the following chapter we relax the planer spin constraint and use a reciprocal-space approach to look for other solutions which are more compatible with the neutron scattering intensity. Although we cannot solve the problem exhaustively, our favoured state has the same domain wall structure as the two states from the previous chapter. This state appears to fit the neutron scattering intensities extremely well and has a low dipolar energy, which can be further reduced by allowing the domain wall to relax into the two neighbouring planes. Without the domain wall relaxation the state is a multiple-q state of six Bragg spots. When the domain wall relaxes it gives rise to an additional magnetic order (described by an extra two Bragg spots). The two phase transitions in $Gd_2Ti_2O_7$ could therefore be explained by the vanishing of this additional order in the higher temperature phase. An accurate fit of the two states to the neutron scattering data is required, however.

In the final chapter we discuss $Er_2Ti_2O_7$ and notice that the state currently proposed in the literature is inconsistent with the elastic neutron scattering data. We therefore propose an alternative state which is consistent with the data. This state is of interest because the spins are not aligned along any significant crystallographic direction which is highly unusual. This multiple-q state is, however, consistent with the observed gapless spin-wave. Gapless spin-waves are extremely unusual for highly anisotropic compounds, like $Er_2Ti_2O_7$. The gapless mode is expected, however for a multiple-q state and can be viewed as transferring spin-density between the three different q-points. The spin-wave is gapless because the ground-state spins do not aligned along the minima of the

crystal field potential and the energy penalty for small distortions of the spin directions is only quadratic rather than linear. We suggest the spin state could be stabilised by a competition between the quantum fluctuation energy of a Hamiltonian stabilising a single-q state and the classical energy of a Hamiltonian stabilising a triple-q state though we cannot offer any rigorous arguments.

APPENDIX A

THE DIPOLE INTERACTION EXPRESSED USING SUB-BAND REPRESENTATION

In this appendix we describe how sub-band representation can be used to express dipole energy as a sum over k-space. We begin by a standard Bloch transform to describe the spin degrees of freedom:

$$\begin{aligned} \tilde{\mathbf{S}}_{\mathbf{k}} &= \frac{1}{\sqrt{N}} \sum_{j} e^{i\mathbf{k}\cdot\mathbf{R}_j} \mathbf{S}_j \\ \mathbf{S}_j &= \frac{1}{\sqrt{N}} \sum_{\mathbf{k}} e^{-i\mathbf{k}\cdot\mathbf{R}_j} \tilde{\mathbf{S}}_{\mathbf{k}}, \end{aligned} \tag{A.1}$$

where $\mathbf{R}_j$ ranges over the (small-scale) face-centre-cubic superlattice, $\mathbf{k}$ ranges over the associated body-centre-cubic reciprocal lattice and N represents the number of lattice sites. We start from the expression of the dipole energy given in Equation 1.71:

$$E_D = -\frac{\mu}{2} \sum_{jj'} \mathbf{S}_j \cdot \frac{\partial}{\partial \mathbf{X}} \mathbf{S}_{j'} \cdot \frac{\partial}{\partial \mathbf{X}} V\left(|\mathbf{x}|\right)|_{\mathbf{x}=\mathbf{R}_j-\mathbf{R}_{j'}}, \tag{A.2}$$

where the potential is given by

$$V\left(X\right) = \frac{1}{X} \tag{A.3}$$

for all lattice vectors, except that $V(X) \mapsto 0$ as $X \mapsto 0$, including sufficient spatial derivatives to ensure that there is no self-interaction contribution, and $\mu = \frac{\mu_0}{4\pi}$. Bloch

transforming the spins gives

$$E_D = -\frac{\mu}{2N}\sum_{jj'}\sum_{\mathbf{k}\mathbf{k}'}\mathbf{S}_{\mathbf{k}}\cdot\frac{\partial}{\partial\mathbf{X}}\mathbf{S}_{\mathbf{k}'}\cdot\frac{\partial}{\partial\mathbf{X}}\,V\left(|\mathbf{x}|\right)\big|_{\mathbf{x}=\mathbf{R}_j-\mathbf{R}_{j'}}\,e^{i(\mathbf{k}+\mathbf{k}')\cdot\mathbf{R}_j}e^{i\mathbf{k}'\cdot\left(\mathbf{R}_j-\mathbf{R}_{j'}\right)}. \tag{A.4}$$

Then using $\mathbf{R}_j - \mathbf{R}_{j'} = \mathbf{R}_i$ and

$$\frac{1}{N}\sum_{j}e^{i(\mathbf{k}+\mathbf{k}')\cdot\mathbf{R}_j} = \sum_{\mathbf{G}}\delta_{(\mathbf{k}+\mathbf{k}'),\mathbf{G}}, \tag{A.5}$$

where $\mathbf{G}$ ranges over the reciprocal-space superlattice, we find

$$E_D = -\frac{\mu}{2}\sum_{i}\sum_{\mathbf{G}\mathbf{k}\mathbf{k}'}\mathbf{S}_{\mathbf{k}}\cdot\frac{\partial}{\partial\mathbf{X}}\mathbf{S}_{\mathbf{k}'}\cdot\frac{\partial}{\partial\mathbf{X}}\,V\left(|\mathbf{x}|\right)\big|_{\mathbf{x}=\mathbf{R}_i}\,e^{i\mathbf{k}'\cdot\mathbf{R}_i}\delta_{\mathbf{k}+\mathbf{k}',\mathbf{G}}. \tag{A.6}$$

Then because the sum over $\mathbf{k}$ and $\mathbf{k}'$ is restricted to the first Brillouin zone, only the term $\mathbf{G} = \mathbf{0}$ contributes to the sum over the reciprocal-space superlattice, so that

$$E_D = -\frac{\mu}{2}\sum_{i}\sum_{\mathbf{k}}\mathbf{S}_{\mathbf{k}}\cdot\frac{\partial}{\partial\mathbf{X}}\mathbf{S}_{-\mathbf{k}}\cdot\frac{\partial}{\partial\mathbf{X}}\,V\left(|\mathbf{x}|\right)\big|_{\mathbf{x}=\mathbf{R}_i}\,e^{-i\mathbf{k}\cdot\mathbf{R}_i}. \tag{A.7}$$

We will now pause for a moment to consider how a discrete summation can be transformed into Fourier space. If a function $f(\mathbf{r})$ has the Fourier transform $\tilde{f}(\mathbf{k})$ such that

$$f(\mathbf{r}) = \int_{-\infty}^{+\infty}\frac{\mathbf{d}^3\mathbf{k}}{(2\pi)^3}\;\tilde{f}(\mathbf{k})e^{i\mathbf{k}\cdot\mathbf{r}}, \tag{A.8}$$

then we can write

$$\sum_{i}f(\mathbf{R}_i) = N\sum_{\mathbf{G}}\int_{-\infty}^{+\infty}\frac{\mathbf{d}^3\mathbf{k}}{(2\pi)^3}\;\tilde{f}(\mathbf{k})\delta_{\mathbf{k},\mathbf{G}}, \tag{A.9}$$

having used:

$$\sum_{i}\frac{e^{i\mathbf{k}\cdot\mathbf{R}_i}}{N} = \sum_{\mathbf{G}}\delta_{\mathbf{k},\mathbf{G}}. \tag{A.10}$$

Noting that

$$\int_{-\infty}^{+\infty}\mathbf{d}^3\mathbf{k} \mapsto \sum_{\mathbf{k}}\frac{\mathcal{V}(\tilde{\Omega})}{N}, \tag{A.11}$$

where $\mathcal{V}(\tilde{\Omega})$ denotes the volume of the Brillouin zone, we get

$$\begin{aligned}\sum_i f(\mathbf{R}_i) &= \frac{\mathcal{V}(\tilde{\Omega})}{(2\pi)^3}\sum_{\mathbf{Gk}}\tilde{V}(\mathbf{k})\delta_{\mathbf{k},\mathbf{G}} \\ &= \frac{1}{\mathcal{V}(\Omega)}\sum_{\mathbf{G}}\tilde{V}(\mathbf{G}),\end{aligned} \tag{A.12}$$

with $\mathcal{V}(\Omega)$ denoting the volume of the Wigner-Seitz cell and $\mathcal{V}(\Omega)\mathcal{V}(\tilde{\Omega}) = (2\pi)^3$. To apply the above relationship to EquationA.7 we therefore require the Fourier transform of

$$f_{\alpha\beta}(\mathbf{x}) = e^{-i\mathbf{k}\cdot\mathbf{x}}\frac{\partial}{\partial x_\alpha}\frac{\partial}{\partial x_\beta}V(|\mathbf{x}|), \tag{A.13}$$

where $V(\infty) \mapsto 0$ and $\left.\frac{\partial V(|\mathbf{x}|)}{\partial \mathbf{x}}\right|_{|\mathbf{x}|=\infty} \mapsto \mathbf{0}$ and integrate by parts twice to get

$$\tilde{f}_{\alpha\beta}(\mathbf{q}) = -(k_\alpha + q_\alpha)(k_\beta + q_\beta)\tilde{V}(|\mathbf{k}+\mathbf{q}|), \tag{A.14}$$

which gives

$$\begin{aligned}E_D &= \frac{\mu}{2\mathcal{V}(\Omega)}\sum_{\mathbf{k}}\sum_{\mathbf{G}}\left[\mathbf{S}_k\cdot(\mathbf{k}+\mathbf{G})\right]\left[\mathbf{S}_{-\mathbf{k}}\cdot(\mathbf{k}+\mathbf{G})\right]\tilde{V}(|\mathbf{k}+\mathbf{G}|) \\ &= \frac{\mu}{2\mathcal{V}(\Omega)}\sum_{\mathbf{k}}\sum_{\mathbf{G}}\left|\mathbf{S}_{\mathbf{k}}\cdot(\mathbf{k}+\mathbf{G})\right|^2\tilde{V}(|\mathbf{k}+\mathbf{G}|),\end{aligned} \tag{A.15}$$

where in the last line we have used $\mathbf{S}^*_{\mathbf{k}} = \mathbf{S}_{-\mathbf{k}}$ (as a result of $\mathbf{S}^*_{\mathbf{R}_j} = \mathbf{S}_{\mathbf{R}_j}$).

APPENDIX B

FACTORISING THE DIPOLE INTERACTION

The dipolar interaction is given by: In this appendix we will demonstrate how the expression for the dipole interaction can be refactorised in terms of ten natural arguments to provide the result given in Equation 2.35. We will make use of the definition:

$$\mathbf{T} = \frac{1}{2}\left[\mathbf{S}_0 + \mathbf{S}_1 + \mathbf{S}_2 + \mathbf{S}_3\right]. \tag{B.1}$$

Starting from the expression given in Equation 2.34:

$$\begin{aligned} H_{D1} &= -\frac{\mu}{2}\left\{\left(S_0^y + S_0^z\right)\left(S_1^y + S_1^z\right) + \left(S_2^y - S_2^z\right)\left(S_3^y - S_3^z\right)\right. \\ &\quad + \left(S_0^z + S_0^x\right)\left(S_2^z + S_2^x\right) + \left(S_1^z - S_1^x\right)\left(S_3^z - S_3^x\right) \\ &\quad \left. + \left(S_0^x + S_0^y\right)\left(S_3^x + S_3^y\right) + \left(S_1^x - S_1^y\right)\left(S_2^x - S_2^y\right)\right\}, \end{aligned} \tag{B.2}$$

this can be rewritten as:

$$\begin{aligned} H_{D1} &= -\frac{\mu}{2}\left\{\left(S_0^x + S_1^x\right)\left(S_2^x + S_3^x\right) + \left(S_0^y + S_2^y\right)\left(S_1^y + S_3^y\right) + \left(S_0^z + S_3^z\right)\left(S_1^z + S_2^z\right)\right. \\ &\quad \left(S_0^y + S_1^y\right)\left(S_0^z + S_1^z\right) + \left(S_0^z + S_2^z\right)\left(S_0^x + S_2^x\right) + \left(S_0^x + S_3^x\right)\left(S_0^y + S_3^y\right) \\ &\quad - \left(S_2^y + S_3^y\right)\left(S_2^z + S_3^z\right) - \left(S_1^z + S_3^z\right)\left(S_1^x + S_3^x\right) - \left(S_1^x + S_2^x\right)\left(S_1^y + S_2^y\right) \\ &\quad - \left(S_0^y S_0^z + S_0^z S_0^x + S_0^x S_0^y\right) - \left(S_1^y S_1^z - S_1^z S_1^x - S_1^x S_1^y\right) \\ &\quad \left. - \left(-S_2^y S_2^z + S_2^z S_2^x - S_2^x S_2^y\right) - \left(-S_3^y S_3^z - S_3^z S_3^x + S_3^x S_3^y\right)\right\}. \end{aligned} \tag{B.3}$$

We notice that:

$$(S_0^x + S_1^x)(S_2^x + S_3^x) = \frac{1}{4}\left[(S_0^x + S_1^x + S_2^x + S_3^x)^2 - (S_0^x + S_1^x - S_2^x - S_3^x)^2\right], \qquad \text{(B.4)}$$

and temporally defining $y = (S_0^y + S_1^y - S_2^y - S_3^y)/2$ and $z = (S_0^z + S_1^z - S_2^z - S_3^z)/2$ we have:

$$\begin{aligned}(S_0^y + S_1^y)(S_0^z + S_1^z) - (S_2^y + S_3^y)(S_2^z + S_3^z) &= (T^y + y)(T^z + z) - (T^y - y)(T^z - z) \\ &= 2(T^y z + T^z y) \\ &= T^y (S_0^z + S_1^z - S_2^z - S_3^z) + T^z (S_0^y + S_1^y - S_2^y - S_3^y),\end{aligned} \qquad \text{(B.5)}$$

and finally,

$$S_0^y S_0^z + S_0^z S_0^x + S_0^x S_0^y = \frac{1}{2}\left[(S_0^x + S_0^y + S_0^z)^2 - S^2\right], \qquad \text{(B.6)}$$

so that,

$$\begin{aligned}H_{D1} = &-\frac{\mu}{2}\Big\{(T^x)^2 - (S_0^x + S_1^x - S_2^x - S_3^x)^2/4 + (T^y)^2 - (S_0^y - S_1^y + S_2^y - S_3^y)^2/4 \\ &+(T^z)^2 - (S_0^z - S_1^z - S_2^z + S_3^z)^2/4 \\ &+T^y (S_0^z + S_1^z - S_2^z - S_3^z) + T^z (S_0^y + S_1^y - S_2^y - S_3^y) \\ &+T^z (S_0^x - S_1^x + S_2^x - S_3^x) + T^x (S_0^z - S_1^z + S_2^z - S_3^z) \\ &+T^x (S_0^y - S_1^y - S_2^y + S_3^y) + T^y (S_0^x - S_1^x - S_2^x + S_3^x) \\ &-(S_0^x + S_0^y + S_0^z)^2 - (S_1^x - S_1^y - S_1^z)^2 - (-S_2^x + S_2^y - S_2^z)^2 - (-S_3^x - S_3^y + S_3^z)^2 - 2S^2\Big\}.\end{aligned} \qquad \text{(B.7)}$$

We then notice that:

$$\begin{aligned}&T^z (S_0^x - S_1^x + S_2^x - S_3^x) + T^z (S_0^y + S_1^y + S_2^y - S_3^y) + T^z (S_0^z + S_1^z + S_2^z + S_3^z - 2T^z) \\ &= T^z ([S_0^x + S_0^y + S_0^z] - [S_1^x - S_1^y - S_1^z] - [-S_2^x + S_2^y - S_2^z] + [-S_3^x - S_0^y + S_0^z] - 2T^z)\end{aligned} \qquad \text{(B.8)}$$

which gives:

$$
\begin{aligned}
H_{D1} &= \frac{\mu}{2}\Big\{\left(S_0^x+S_1^x-S_2^x-S_3^x\right)^2/4+\left(S_0^y-S_1^y+S_2^y-S_3^y\right)^2/4+\left(S_0^z-S_1^z-S_2^z+S_3^z\right)^2/4 \\
&\quad +\left(S_0^x+S_0^y+S_0^z\right)^2/2+\left(S_1^x-S_1^y-S_1^z\right)^2/2+\left(-S_2^x+S_2^y-S_2^z\right)^2/2+\left(-S_3^x-S_3^y+S_3^z\right)^2/2 \\
&\quad -\left(S_0^x+S_0^y+S_0^z\right)\left(T^x+T^y+T^z\right)-\left(S_1^x-S_1^y-S_1^z\right)\left(T^x-T^y-T^z\right) \\
&\quad -\left(-S_2^x+S_2^y-S_2^z\right)\left(-T^x+T^y-T^z\right)-\left(-S_3^x-S_3^y+S_3^z\right)\left(-T^x-T^y+T^z\right) \\
&\quad +\left((T^x)^2+(T^y)^2+(T^z)^2\right)-2S^2\Big\} \\
&= \frac{\mu}{2}\Big\{\left(S_0^x+S_1^x-S_2^x-S_3^x\right)^2/4+\left(S_0^y-S_1^y+S_2^y-S_3^y\right)^2/4+\left(S_0^z-S_1^z-S_2^z+S_3^z\right)^2/4 \\
&\quad +\left(S_0^x+S_0^y+S_0^z-[T^x+T^y+T^z]\right)^2/2+\left(S_1^x-S_1^y-S_1^z-[T^x-T^y-T^z]\right)^2/2 \\
&\quad +\left(-S_2^x+S_2^y-S_2^z-[-T^x+T^y-T^z]\right)^2/2+\left(-S_3^x-S_3^y+S_3^z-[-T^x-T^y+T^z]\right)^2/2 \\
&\quad -\left((T^x)^2+(T^y)^2+(T^z)^2\right)\Big\}, \qquad \text{(B.9)}
\end{aligned}
$$

where we have dropped the constant in the last line. We have shown that H_{D1} can be expressed as a sum of seven quadratic terms. The nearest neighbour dipolar interaction on the pyrochlore lattice in the presence of a dominant antiferromagnetic nearest neighbour

APPENDIX C

SOLVING THE REAL-SPACE SPIN CONSTRAINTS

In this appendix we will solve the Heisenberg constraint

$$\hat{\mathbf{S}}_0 + \hat{\mathbf{S}}_1 + \hat{\mathbf{S}}_2 + \hat{\mathbf{S}}_3 = \mathbf{0}, \tag{C.1}$$

for the normalised spins defined previously in Equation 3.4 and reproduced below:

$$\begin{aligned}
\mathbf{S}_0 &= \left(\frac{2}{3}\right)^{\frac{1}{2}} \left(\hat{\mathbf{x}} \cos x_0 + \hat{\mathbf{y}} \cos y_0 + \hat{\mathbf{z}} \cos z_0\right), \\
\mathbf{S}_1 &= \left(\frac{2}{3}\right)^{\frac{1}{2}} \left(\hat{\mathbf{x}} \cos x_1 - \hat{\mathbf{y}} \cos y_1 - \hat{\mathbf{z}} \cos z_1\right), \\
\mathbf{S}_2 &= \left(\frac{2}{3}\right)^{\frac{1}{2}} \left(-\hat{\mathbf{x}} \cos x_2 + \hat{\mathbf{y}} \cos y_2 - \hat{\mathbf{z}} \cos z_2\right), \\
\mathbf{S}_3 &= \left(\frac{2}{3}\right)^{\frac{1}{2}} \left(-\hat{\mathbf{x}} \cos x_3 - \hat{\mathbf{y}} \cos y_3 + \hat{\mathbf{z}} \cos z_3\right),
\end{aligned} \tag{C.2}$$

where each spin is confined to the plane perpendicular to the local tetrahedral axis in which it lies. Substituting these expressions into the constraint provides:

$$\begin{aligned}
\cos x_0 + \cos x_1 - \cos x_2 - \cos x_3 = 0, \\
\cos y_0 - \cos y_1 + \cos y_2 - \cos y_3 = 0, \\
\cos z_0 - \cos z_1 - \cos z_2 + \cos z_3 = 0.
\end{aligned} \tag{C.3}$$

We choose to break the symmetry of these equations by expressing everything in terms of z_α only as follows:

$$\begin{aligned}
\cos x_0 - \cos x_3 &= -\cos x_1 + \cos x_2, \\
\cos y_0 - \cos y_3 &= \cos y_1 - \cos y_2, \\
\cos z_0 + \cos z_3 &= \cos z_1 + \cos z_2,
\end{aligned} \tag{C.4}$$

becomes

$$\begin{aligned}
\sin\left(\frac{x_0+x_3}{2}\right)\sin\left(\frac{x_0-x_3}{2}\right) &= -\sin\left(\frac{x_1+x_2}{2}\right)\sin\left(\frac{x_1-x_2}{2}\right), \\
\sin\left(\frac{y_0+y_3}{2}\right)\sin\left(\frac{y_0-y_3}{2}\right) &= \sin\left(\frac{y_1+y_2}{2}\right)\sin\left(\frac{y_1-y_2}{2}\right), \\
\cos\left(\frac{z_0+z_3}{2}\right)\cos\left(\frac{z_0-z_3}{2}\right) &= \cos\left(\frac{z_2+z_2}{2}\right)\cos\left(\frac{z_1-z_2}{2}\right),
\end{aligned} \tag{C.5}$$

where we have used the identities:

$$\begin{aligned}
\cos A - \cos B &= -2\sin\left(\frac{A+B}{2}\right)\sin\left(\frac{A-B}{2}\right), \\
\cos A + \cos B &= 2\cos\left(\frac{A+B}{2}\right)\cos\left(\frac{A-B}{2}\right),
\end{aligned} \tag{C.6}$$

and finally we make the substitution $x_\alpha = z_\alpha - 2\pi/3$ and $y_\alpha = z_\alpha - 4\pi/3$ (from Equation 3.5) so that

$$\begin{aligned}
\sin\left(\frac{z_0+z_3-4\pi/3}{2}\right)\sin\left(\frac{z_0-z_3}{2}\right) &= -\sin\left(\frac{z_1+z_2-4\pi/3}{2}\right)\sin\left(\frac{z_1-z_2}{2}\right), \\
\sin\left(\frac{z_0+z_3-8\pi/3}{2}\right)\sin\left(\frac{z_0-z_3}{2}\right) &= \sin\left(\frac{z_1+z_2-8\pi/3}{2}\right)\sin\left(\frac{z_1-z_2}{2}\right), \\
\cos\left(\frac{z_0+z_3}{2}\right)\cos\left(\frac{z_0-z_3}{2}\right) &= \cos\left(\frac{z_1+z_2}{2}\right)\cos\left(\frac{z_1-z_2}{2}\right),
\end{aligned} \tag{C.7}$$

which simplifies to give

$$\begin{aligned}
&\left[\sin\left(\frac{z_0+z_3}{2}\right)+\sqrt{3}\cos\left(\frac{z_0+z_3}{2}\right)\right]\sin\left(\frac{z_0-z_3}{2}\right)\\
&=-\left[\sin\left(\frac{z_1+z_2}{2}\right)+\sqrt{3}\cos\left(\frac{z_1+z_2}{2}\right)\right]\sin\left(\frac{z_1-z_2}{2}\right),\\
&\left[\sin\left(\frac{z_0+z_3}{2}\right)-\sqrt{3}\cos\left(\frac{z_0+z_3}{2}\right)\right]\sin\left(\frac{z_0-z_3}{2}\right)\\
&=\left[\sin\left(\frac{z_1+z_2}{2}\right)-\sqrt{3}\cos\left(\frac{z_1+z_2}{2}\right)\right]\sin\left(\frac{z_1-z_2}{2}\right),\\
&\cos\left(\frac{z_0+z_3}{2}\right)\cos\left(\frac{z_0-z_3}{2}\right)=\cos\left(\frac{z_1+z_2}{2}\right)\cos\left(\frac{z_1-z_2}{2}\right). \qquad \text{(C.8)}
\end{aligned}$$

The first two of the above equations can the be recombined so that:

$$\sin\left(\frac{z_0+z_3}{2}\right)\sin\left(\frac{z_0-z_3}{2}\right) = -\sqrt{3}\cos\left(\frac{z_1+z_2}{2}\right)\cos\left(\frac{z_1-z_2}{2}\right), \qquad \text{(C.9)}$$

$$\sqrt{3}\cos\left(\frac{z_0+z_3}{2}\right)\sin\left(\frac{z_0-z_3}{2}\right) = -\sin\left(\frac{z_1+z_2}{2}\right)\sin\left(\frac{z_1-z_2}{2}\right), \qquad \text{(C.10)}$$

$$\cos\left(\frac{z_0+z_3}{2}\right)\cos\left(\frac{z_0-z_3}{2}\right) = \cos\left(\frac{z_1+z_2}{2}\right)\cos\left(\frac{z_1-z_2}{2}\right). \qquad \text{(C.11)}$$

Next we wish to eliminate the variables z_1 and z_2. In order to compress the notation we define:

$$s_\pm = \sin\left(\frac{z_0 \pm z_3}{2}\right), \qquad c_\pm = \cos\left(\frac{z_0 \pm z_3}{2}\right) \qquad \text{(C.12)}$$

The squares of Equations C.9 and C.11 can then be combined to give

$$\frac{1}{3}s_+^2 s_-^2 + c_+^2 c_-^2 = \cos^2\left(\frac{z_1+z_2}{2}\right) \qquad \text{(C.13)}$$

and the squares of Equations C.9 and C.10 can be combined to give

$$\frac{1}{3}s_+^2 s_-^2 + 3c_+^2 s_-^2 = 1 - \cos^2\left(\frac{z_1-z_2}{2}\right), \qquad \text{(C.14)}$$

and then the above two equations can be substituted into Equation C.11 to provide

$$c_+^2 c_-^2 = \left[\frac{1}{3}s_+^2 s_-^2 + c_+^2 c_-^2\right]\left[1 - \frac{1}{3}s_+^2 s_-^2 - 3c_+^2 s_-^2\right], \tag{C.15}$$

from which we eliminate c_+ and c_- to find

$$s_-^2\left[\frac{32}{9}s_+^4 s_-^2 + 6s_+^2 - \frac{20}{3}s_+^2 s_-^2 - 3 - \frac{8}{3}s_+^4 + 3s_-^2\right] = 0. \tag{C.16}$$

The above equation can be factorised as a product of three terms:

$$s_-^2\left(4s_+^2 - 3\right)\left[\left(9 - 8s_+^2\right)\left(1 - s_-^2\right) + 2s_+^2\right] = 0. \tag{C.17}$$

The solutions arising from the final (complicated) term are unphysical). From the first term we find:

$$\sin\left(\frac{z_0 - z_3}{2}\right) = 0, \tag{C.18}$$

and therefore

$$\sin\left(\frac{z_1 - z_2}{2}\right) = 0, \tag{C.19}$$

leading to the two possible sets of solutions:

$$z_0 = z_1 = z_2 = z_3, \qquad z_0 = -z_1 = -z_2 = z_3. \tag{C.20}$$

Next we consider the second term:

$$\sin^2\left(\frac{z_0 + z_3}{2}\right) = \frac{3}{4} \tag{C.21}$$

and substituting into Equations C.9 and C.10 provides

$$\sin\left(\frac{z_1 - z_2}{2}\right)\sin\left(\frac{z_0 + z_3}{2} - \frac{z_1 + z_2}{2}\right) = 0. \tag{C.22}$$

As the solution $z_0 + z_3$ just provides a subset of the previous solutions, the new option is $z_0 + z_3 = z_1 + z_2$, which gives two new solutions. Firstly we can have

$$z_0 + z_3 = \frac{4\pi}{3} = z_1 + z_2 \Rightarrow x_0 + x_3 = x_1 + x_3, \tag{C.23}$$

which using Equations C.3 provides the solutions

$$x_0 = x_1 = -x_2 = -x_3. \tag{C.24}$$

Finally we can use the alternative option of

$$z_0 + z_3 = -\frac{4\pi}{3} = z_1 + z_2 \Rightarrow y_0 + y_3 = 0 = y_1 + y_2. \tag{C.25}$$

which can be substituted into Equations C.3 to provide the final solution:

$$y_0 = -y_1 = y_2 = -y_3. \tag{C.26}$$

LIST OF REFERENCES

[1] A. Altland and S. Simons. *Condensed Matter Field Theory*. Cambridge University Press, 2006.

[2] P. W. Anderson. New approach to the theory of superexchange interactions. *Phys. Rev.*, 115:2–13, Jul 1959.

[3] Ashcroft and Mermin. *Solid State Physics*. Holt Rinehard Winston, 1976.

[4] Per Bak and R. Bruinsma. One-dimensional Ising model and the complete devil's staircase. *Phys. Rev. Lett.*, 49:249, 1982.

[5] H.W.J. Blöte, R.F. Wielinga, and W.J. Huiskamp. Heat-capacity measurements on rare-earth double oxides $R_2M_2O_7$. *Physica*, 43(4):549–568, 1969.

[6] S. Blundell. *Magnetism in Condensed Matter*. Oxford University Press, 2009.

[7] V. Bondah-Jagalu and S. T. Brammwell. Magnetic susceptibility study of the heavy rare-earth stannate pyrochlores. *Canadian Journal of Physics*, 79:1381, 2001.

[8] P. Bonville, J. A. Hodges, M. Ocio, J. P. Sanchez, P. Vulliet, S. S. Sosin, and D. Braithwaite. Low temperature magnetic properties of geometrically frustrated $Gd_2Sn_2O_7$ and $Gd_2Ti_2O_7$. *Journal of Physics: Condensed Matter*, 15(45):7777, 2003.

[9] M. I. Brammall, A. K. R. Briffa, and M. W. Long. Magnetic structure of $Gd_2Ti_2O_7$. *Phys. Rev. B*, 83:054422, Feb 2011.

[10] S. T. Bramwell, M. N. Field, M. J. Harris, and I. P. Parkin. Bulk magnetization of the heavy rare earth titanate pyrochlores - a series of model frustrated magnets. *J. Phys. Condens. Matter*, 12:483–495, 2000.

[11] S. T. Bramwell, S. R. Giblin, S. Calder, R. Aldus, D. Prabhakaran, and T. Fennell. Measurement of the charge and current of magnetic monopoles in spin ice. *Nature*, 461:956, 2009.

[12] S. T. Bramwell, M. J. Harris, B. C. den Hertog, M. J. P. Gingras, J. S. Gardner, D. F. McMorrow, A. R. Wildes, A. L. Cornelius, J. D. M. Champion, R. G. Melko, and T. Fennell. Spin correlations in $Ho_2Ti_2O_7$: a dipolar spin ice system. *Phys. Rev. Lett.*, 87:047205, Jul 2001.

[13] Steven T. Bramwell and Michel J. P. Gingras. Spin ice state in frustrated magnetic pyrochlore materials. *Science*, 294(5546):1495–1501, 2001.

[14] H. B. Cao, I. Mirebeau, A. Gukasov, P. Bonville, and C. Decorse. Field evolution of the magnetic structures in $Er_2Ti_2O_7$ through the critical point. *Phys. Rev. B*, 82:104431, Sep 2010.

[15] C. Castelnovo, R. Moessner, and S. L. Sondhi. Magnetic monopoles in spin ice. *Nature*, 451:42, 2008.

[16] O. Cépas, A. P. Young, and B. S. Shastry. Degeneracy and strong fluctuation-induced first-order phase transition in the dipolar pyrochlore antiferromagnet. *Phys. Rev. B*, (72):184408, 2005.

[17] J. T. Chalker. *Introduction to Frustrated Magnetism: Materials, Experiments, Theory, Chapter 1.* Springer Series in Solid-State Sciences. Springer, 2011. arXiv:0901.3492v1.

[18] J.T. Chalker, P.C.W. Holdsworth, and E.F. Shender. Hidden order in a frustrated system: properties of the Heisenberg Kagomé antiferromagnet. *Phys. Rev. Lett.*, 68(6):855, 1992.

[19] J. D. M. Champion, M. J. Harris, P. C. W. Holdsworth, A. S. Wills, G. Balakrishnan, S. T. Bramwell, E. Čižmár, T. Fennell, J. S. Gardner, J. Lago, D. F. McMorrow, M. Orendáč, A. Orendáčová, D. McK. Paul, R. I. Smith, M. T. F. Telling, and A. Wildes. Evidence of quantum order by disorder in a frustrated antiferromagnet $Er_2Ti_2O_7$. *Phys. Rev. B*, 68:020401, Jul 2003.

[20] J D M Champion and P C W Holdsworth. Soft modes in the easy plane pyrochlore antiferromagnet. *Journal of Physics: Condensed Matter*, 16(11):S665, 2004.

[21] J. D. M. Champion, A. S. Wills, T. Fennell, S. T. Bramwell, J. S. Gardner, and M. A. Green. Order in the Heisenberg pyrochlore: The magnetic structure of $Gd_2Ti_2O_7$. *Phys. Rev. B*, 64:140407, Sep 2001.

[22] P. Dalmas de Réotier, A. Yaouanc, L. Keller, A. Cervellino, B. Roessli, C. Baines, A. Forget, C. Vaju, P. C. M. Gubbens, A. Amato, and P. J. C. King. Spin dynamics and magnetic order in magnetically frustrated $Tb_2Sn_2O_7$. *Phys. Rev. Lett.*, 96:127202, Mar 2006.

[23] Byron C. den Hertog and Michel J. P. Gingras. Dipolar interactions and origin of spin ice in Ising pyrochlore magnets. *Phys. Rev. Lett.*, 84:3430–3433, Apr 2000.

[24] H. T. Diep, editor. *Frustrated spin systems.* World Scientific Publishing Co., 2004.

[25] T. Fennell, P. P. Deen, A. R. Wildes, K. Schmalzl, D. Prabhakaran, A. T. Boothroyd, R. J. Aldus, D. F. McMorrow, and S. T. Bramwell. Magnetic Coulomb phase in the spin ice $Ho_2Ti_2O_7$. *Science*, 326(5951):415–417, 2009.

[26] T. Fennell, O. A. Petrenko, B. Fåk, J. S. Gardner, S. T. Bramwell, and B. Ouladdiaf. Neutron scattering studies of the spin ices $Ho_2Ti_2O_7$ and $Dy_2Ti_2O_7$ in an applied magnetic field. *Phys. Rev. B*, 72:224411, Dec 2005.

[27] R. S. Freitas and J. S. Gardner. The magnetic phase diagram of $Gd_2Sn_2O_7$. *J. Phys. Condens. Matter*, 23:164215, 2011.

[28] J. S. Gardner.

[29] J. S. Gardner, S. R. Dunsiger, B. D. Gaulin, M. J. P. Gingras, J. E. Greedan, R. F. Kiefl, M. D. Lumsden, W. A. MacFarlane, N. P. Raju, J. E. Sonier, I. Swainson, and Z. Tun. Cooperative paramagnetism in the geometrically frustrated pyrochlore antiferromagnet $Tb_2Ti_2O_7$. *Phys. Rev. Lett.*, 82(5):1012, 1999.

[30] J. S. Gardner, M. J. P. Gingras, and J. E. Greedan. Magnetic pyrochlore oxides. *Reviews of Modern Physics*, 82:53, 2010.

[31] M. J. P. Gingras, B. C. den Hertog, M. Faucher, J. S. Gardner, S. R. Dunsiger, L. J. Chang, B. D. Gauling, NewAuthor5, and J. E. Greedan. Thermodynamic and single-ion properties of Tb^{3+} within the collective paramagnetic-spin liquid state of the frustrated pyrochlore antiferromagnet $Tb_2Ti_2O_7$. *Phys. Rev. B*, 62:6496, 2000.

[32] V. N. Glazkov, M. E. Zhitomirsky, A. I. Smirnov, H.-A. Krug von Nidda, A. Loidl, C. Marin, and J.-P. Sanchez. Single-ion anisotropy in the gadolinium pyrochlores studied by electron paramagnetic resonance. *Phys. Rev. B*, 72:020409, Jul 2005.

[33] D. Goldschmidt and H. L. Tuller. Small-polaron conduction in $Y_2Ti_2O_7$. *Phys. Rev. B*, 34(8):5558, 1986.

[34] B. Hälg and A. Furrer. Anisotropic exchange and spin dynamics in the type-I (-IA) antiferromagnets CeAs, CeSb, and USb: A neutron study. *Phys. Rev. B*, 34:6258–6279, Nov 1986.

[35] M. J. Harris, S. T. Bramwell, D. F. McMorrow, T. Zeiske, and K. W. Godfrey. Geometrical frustration in the ferromagnetic pyrochlore $Ho_2Ti_2O_7$. *Phys. Rev. Lett.*, 79(13):2554, 1997.

[36] T. Holstein and H. Primakoff. Field dependence of the intrinsic domain magnetization of a ferromagnet. *Phys. Rev.*, 58:1098–1113, Dec 1940.

[37] Naoki Honda, Yasunori Tanji, and Yasuaki Nakagawa. Lattice distortion and elastic properties of anitferromagnetic γ $Mn-Ni$ alloys. *J. Phys. Soc. Jpn.*, 41:1931–1937, 1976.

[38] Jens Jensen and Per Bak. Spin waves in triple-q structures. Application to USb. *Phys. Rev. B*, 23:6180–6183, Jun 1981.

[39] Jens Jensen and Allan Mackintosh. *Rare earth magnetism: structures and excitations.* Clarendon Press, 1991.

[40] C. Kittel. *Introduction to Solid State Physics.* John Wiley and Sons, eighth edition, 2004.

[41] L.D. Landau and E. M. Lifshitz. *Vol. 3: Quantum Mechanics - Non-relativistic Theory.* Robert Maxwell, MC, 1958.

[42] L.D. Landau and E. M. Lifshitz. *Vol. 2: The Classical Theory of Fields*. Robert Maxwell, MC, 1975.

[43] M. W. Long. Unpublished.

[44] M W Long. Effects that can stabilise multiple spin-density waves. *Journal of Physics: Condensed Matter*, 1(17):2857, 1989.

[45] M. W. Long, R. D. Lowde, and M. Sakata. Technical Report RAL-88-022.

[46] M W Long and O Moze. Magnetic diffuse scattering and the triple-q structure in fcc -MnNi. *Journal of Physics: Condensed Matter*, 2(27):6013, 1990.

[47] M. W. Long and S. Siak. An exactly soluble two-dimensional quantum mechanical Heisenberg model: quantum fluctuations versus magnetic order. *J. Phys. Condens. Matter*, 2:10321, 1990.

[48] M.W. Long. Multiple-q structures in frustrated antiferromagnets. *International Journal of Modern Physics B*, 7:2981–3002, 1993.

[49] M.W. Long and A. Bayri. Spin impurities in non-collinear antiferromagnets with Mn_3Pt as an example. *J. Phys. Condens. Matter*, 5:7719, 1993.

[50] S. W. Lovesey. *Theory of neutron scattering from condensed matter*. Oxford, 1984.

[51] B. Z. Malkin, T. T. A. Lummen, P. H. M. van Loosdrecht, G. Dhalenne, and A. R. Zakirov. Static magnetic susceptibility, crystal field and exchange interactions in rare earth titanate pyrochlores. *J. Phys. Condens. Matter*, 22:276003, 2010.

[52] R. J. Mason and M. W. Long. Controlling spin-ice with a $(1\bar{1}0)$ magnetic field. *unpublished*.

[53] K. Matsuhira, Y. Hinatsu, H. Amitsuak, and T. Sakakibara. Low-temperature magnetic properties of pyrochlore stannates. *J. Phys. Soc. Jpn.*, 71:1576, 2002.

[54] Leopold May, editor. *An Introduction To Mössbauer Spectroscopy*. Adam Hilger, 1971.

[55] I. Mirebeau, A. Apetrei, J. Rodríguez-Carvajal, P. Bonville, A. Forget, D. Colson, V. Glazkov, J. P. Sanchez, O. Isnard, and E. Suard. Ordered spin ice state and magnetic fluctuations in $Tb_2Sn_2O_7$. *Phys. Rev. Lett.*, 94:246402, Jun 2005.

[56] I. Mirebeau and I. Goncharenko. Spin liquid and spin ice under high pressure: a neutron study of $R_2Ti_2O_7$ ($R = Tb, Ho$). *J. Phys. Condens. Matter*, 16:S653, 2004.

[57] I. Mirebeau, H. Mutka, P. Bonville, A. Apetrei, and A. Forget. Investigation of magnetic fluctuations in $Tb_2Sn_2O_7$ ordered spin ice by high-resolution energy resolved neutron scattering. *Phys. Rev. B*, 78:2008, 174416.

[58] R. Moessner and J. T. Chalker. Low-temperature properties of classical geometrically frustrated antiferromagnets. *Phys. Rev. B*, 58(18):12 049, 1998.

[59] R. Osborn, S. W. Lovesey, and A. D. Taylor. Intermultiplet transitions using neutron spectroscopy. *Handbook on the Physics and Chemistry of Rare Earths*, 14, 1991.

[60] S. E. Palmer and J. T. Chalker. Order induced by dipolar interactions in a geometrically frustrated antiferromagnet. *Phys. Rev. B*, 62:488–492, Jul 2000.

[61] L. Pauling. The structure and entropy of ice and of other crystals with some randomness of atomic arrangement. *Jornal of the American Chemical Society*, 57:2680–2684, 1935.

[62] O. A. Petrenko, M. R. Lees, G. Balakrishnan, and D. McK Paul. Magnetic phase diagram of the antiferromagnetic pyrochlore $Gd_2Ti_2O_2$. *Phys. Rev. B*, 70:012402, Jul 2004.

[63] N. P. Raju, M. Dion, M. J. P. Gingras, T. E. Mason, and J. E. Greedan. Transition to long-range magnetic order in the highly frustrated insulating pyrochlore antiferromagnet $Gd_2Ti_2O_7$. *Phys. Rev. B*, 59:14489–14498, Jun 1999.

[64] A. P. Ramirez, A. Hayashi, R. J. Cava, R. Siddharthan, and B. S. Shastry. Zero-point entropy in 'spin ice'. *Nature*, 399:333, 1999.

[65] D. H. Reich, B. Ellman, J. Yang, T. F. Rosenbaum, G. Aeppli, and D. P. Belanger. Dipolar magnets and glasses: neutron-scattering, dynamical, and calorimetric studies of randomly distributed Ising spins. *Phys. Rev. B*, 42:4631, 1990.

[66] J. P. C. Ruff, J. P. Clancy, A. Bourque, M. A. White, M. Ramazanoglu, J. S. Gardner, Y. Qiu, J. R. D. Copley, M. B. Johnson, H. A. Dabkowska, and B. D. Gaulin. Spin waves and quantum criticality in the frustrated XY pyrochlore antiferromagnet $Er_2Ti_2O_7$. *Phys. Rev. Lett.*, 101:147205, Oct 2008.

[67] J. Snyder, J. S. Slusky, R. J. Cava, and P. Schiffer. How 'spin ice' freezes. *Nature*, 413:48, 2001.

[68] R. R. Sobral and C. Lacroix. Order by disorder in the pyrochlore antiferromagnets. *Solid State Communications*, 103(7):407, 1997.

[69] J. R. Stewart, G. Ehlers, A. S. Wills, S .T. Bramwell, and J S Gardner. Phase transitions, partial disorder and multi- k structures in $Gd_2Ti_2O_7$. *Journal of Physics: Condensed Matter*, 16(28):L321, 2004.

[70] J. R. Stewart, J. S. Gardner, Y. Qiu, and G. Ehlers. Collective dynamics in the Heisenberg pyrochlore antiferromagnet $Gd_2Sn_2O_7$. *Phys. Rev. B*, 78:132410, 2008.

[71] Y. Tabira, R. L. Withers, L. Minervini, and R. W. Grimes. Systematic structural change in selected rare earth oxide pyrochlores as determined by wide-angle CBED and a comparison with the results of atomistic computer simulation. *Jornal of Solid State Chemistry*, 153:16, 2000.

[72] J. Villain, R. Bidaux, J. P. Carton, and R. J. Conte. *J. Phys. - Paris*, 41:1263, 1980.

[73] G. H. Wannier. *Elements of Solid State Theory.* Cambridge University Press, 1960.

[74] Gunther K. Werthein. *Mössbauer Effect: Principles and Applications.* Academic Press, 1964.

[75] A. S. Wills, M. E. Zhitomirsky, B. Canals, J. P. Sanchez, P. Bonville, P. Dalmas de Réotier, and A Yaouanc. Magnetic ordering in $Gd_2Sn_2O_7$: the archetypal Heisenberg pyrochlore antiferromagnet. *Journal of Physics: Condensed Matter*, 18(3):L37, 2006.

[76] Y. Yasui, M. Kanada, M. Ito, H. Harashina, M. Sato, H. Okumura, K. Kakurai, and H. Kadowaki. Static correlation and dynamical properties of Tb^{3+} moments in $Tb_2Ti_2O_7$ - neutron scattering study. *J. Phys. Soc. Jpn.*, 71:599–606, 2002.